



HAL
open science

Study of Dense Assemblies of Active Colloids : collective Behavior and Rheological Properties

Natsuda Klongvessa

► **To cite this version:**

Natsuda Klongvessa. Study of Dense Assemblies of Active Colloids : collective Behavior and Rheological Properties. Mechanics of materials [physics.class-ph]. Université de Lyon, 2020. English. NNT : 2020LYSE1146 . tel-03282035

HAL Id: tel-03282035

<https://theses.hal.science/tel-03282035>

Submitted on 8 Jul 2021

HAL is a multi-disciplinary open access archive for the deposit and dissemination of scientific research documents, whether they are published or not. The documents may come from teaching and research institutions in France or abroad, or from public or private research centers.

L'archive ouverte pluridisciplinaire **HAL**, est destinée au dépôt et à la diffusion de documents scientifiques de niveau recherche, publiés ou non, émanant des établissements d'enseignement et de recherche français ou étrangers, des laboratoires publics ou privés.



N° d'ordre NNT: 2020LYSE1146

THÈSE DE DOCTORAT DE L'UNIVERSITÉ DE LYON

Opérée au sein de

l'Université Claude Bernard Lyon 1

Ecole Doctorale N° 52
Physique et Astrophysique de Lyon

Spécialité de doctorat : Physique

Soutenue publiquement le 29/09/2020, par :

Natsuda KLONGVESSA

**Étude d'assemblées denses de colloïdes auto-propulsés:
Comportement collectif et propriétés rhéologiques**

Devant le jury composé de :

Emanuela ZACCARELLI Senior Researcher, Sapienza University of Rome	Rapporteure
Olivier DAUCHOT Directeur de Recherche, CNRS	Rapporteur
Axelle AMON Maître de Conférences, Université de Rennes 1	Examinatrice
David RODNEY Professeur, Université Claude Bernard Lyon 1	Examineur
Cécile COTTIN-BIZONNE Directrice de Recherche, CNRS	Directrice de thèse
Mathieu LEOCMACH Chargé de Recherche, CNRS	Co-Directeur de thèse
Christophe YBERT Directeur de Recherche, CNRS	Invité
Takeshi KAWASAKI Lecturer, Nagoya University	Invité



N° d'ordre NNT: 2020LYSE1146

THESIS SUBMITTED TO THE UNIVERSITY OF LYON

Operated within

Claude Bernard University Lyon 1

Doctoral school N° 52
Physics and Astrophysics

Doctoral specialty : Physics

Publicly defended on 29/09/2020, by :

Natsuda KLONGVESSA

Study of Dense Assemblies of Active Colloids: Collective Behavior and Rheological Properties

The jury members :

Emanuela ZACCARELLI Senior Researcher, Sapienza University of Rome	Reviewer
Olivier DAUCHOT Directeur de Recherche, CNRS	Reviewer
Axelle AMON Maître de Conférences, Université de Rennes 1	Examiner
David RODNEY Professeur, Université Claude Bernard Lyon 1	Examiner
Cécile COTTIN-BIZONNE Directrice de Recherche, CNRS	PhD supervisor
Mathieu LEOCMACH Chargé de Recherche, CNRS	PhD co-supervisor
Christophe YBERT Directeur de Recherche, CNRS	Invited member
Takeshi KAWASAKI Lecturer, Nagoya University	Invited member

Abstract

In the last decades, active matter has stepped up from a fascination about mesmerizing animal collective movements to well-controlled experiments in the laboratory. Abiotic active systems have been used as a model to develop new knowledge in non-equilibrium physics and it has been done extensively in rather dilute systems. However, investigation in crowded conditions is still lacking especially in experiments. This leads to the key objective of this study: to perform an experimental investigation of active systems at high density and to relate the observation to our knowledge in glassy physics. Besides, by considering such a system as a new kind of active material, we also aim to investigate it via microrheology. In both cases, the main question is to examine how activity influences a system whose passive counterpart is already out of equilibrium.

Our experimental system is a monolayer of gold-platinum Janus colloids, which become self-propelled upon adding a solution of hydrogen peroxide (H_2O_2). The monolayer is slightly inclined to cause an in-plane density gradient. We characterize the activity level from the sedimentation length and define an effective temperature, which monotonically increases with H_2O_2 concentration. With this setup, we can investigate a full range of densities from dilute to ergodic supercooled and to non-ergodic glass regime. We find that standard glassy physics describes well the active supercooled regime provided the replacement of the temperature by the effective one. However, beyond the glass transition, we find that relaxation responds non-monotonically to activity. We observe a dramatic slowdown of the relaxation when particles are weakly self-propelled; followed by faster relaxation at high enough activity level. By analyzing correlation of displacement orientations, we propose that directed motion makes cage exploration less efficient and thus slows down cooperative relaxation comparing to a passive glass. We, therefore, name this phenomenon "Deadlock from the Emergence of Active Directionality (DEAD)".

To perform microrheology, we apply two types of actuation on a probe particle immersed in the sediment. The first actuation is a small amplitude oscillation controlled by optical tweezers. The resulting complex shear modulus gives us a hint that activity makes the sediment more elastic. However, activity-dependent interaction between the optical tweezers and the colloids makes the analysis difficult. We thus switch to gravitational force to pull the probe through the sediment. We first find that there is more flux of the colloids that push the probe forward in the passive sediment than in the active one. This can be understood by the sedimentation length and it results in a stark difference in the probe falling motion. Next, we find that the advection of the colloids around the probe quantitatively agree with a Stokes flow. This leads to a possibility to extract an effective viscosity. As we need a better-controlled setup, we developed a magnetic microrheometer for our future study.

We also start a numerical investigation using a model of active Brownian particles. Unlike in experiment, we can precisely fix the density in simulation. We find a motility induced phase separation at moderate densities and high propulsion forces. Apart from this, the simulation well agrees with our experimental result at least up to the supercooled regime. In this way, we can study the glassy regime where we expect the DEAD phenomenon and gain a better insight into the active glassy system.

Résumé (en français)

Cette thèse se situe à la convergence de deux grands domaines de la physique hors équilibre: la physique des verres et la matière active. Dans le premier domaine, l'état d'équilibre serait un solide cristallin qui n'est pas atteint à cause d'un refroidissement trop rapide. L'état du système est métastable et les fluctuations thermiques ne lui permettent pas de se réorganiser en un temps raisonnable vers l'état qu'équilibre. Un tel système dense est coincé dans un état amorphe appelé verre.

Dans le domaine de la matière active, le système est poussé hors équilibre par une injection locale d'énergie. La source de la dynamique n'est plus seulement l'énergie thermique, mais aussi l'autopropulsion des sous-unités du système. Un vol d'oiseaux et une colonie de bactéries sont des exemples typiques de matière active dans la nature. Grâce aux progrès des techniques d'ingénierie, les systèmes actifs abiotiques ont été utilisés comme système modèle pour étudier la dynamique collective et le comportement d'émergence de la matière active. Au cours des dernières années, le comportement des assemblages d'objets auto-propulsés est passé d'une simple curiosité zoologique à un champ florissant de la physique hors équilibre. Le but de la plupart des études est de tester s'il est possible de trouver une correspondance entre le système actif hors équilibre et un système passif à l'équilibre. Si une telle correspondance n'est pas possible, alors s'ouvre la question des ingrédients physiques manquants pour décrire le système, menant à une nouvelle compréhension de la physique hors d'équilibre.

Des études de systèmes actifs plutôt dilués ont été menées ces dernières années de manière approfondie à la fois par des expériences et des simulations numériques. On constate que le comportement d'un système actif dilué peut être expliqué en utilisant la physique à l'équilibre si on remplace la température ambiante par une température effective. À des densités plus élevées, certaines études numériques ont signalé un décalage de la transition vitreuse lorsque le système devient actif, mais sans phénoménologie nouvelle. Néanmoins, un tel régime à haute densité reste inexploré expérimentalement et cette exploration constitue l'objectif principal de ma thèse.

Pendant cette thèse, nous avons réalisé des expériences sur des assemblées denses de particules artificielles autopropulsées, à des régimes où un système passif de même densité est dans un état vitreux. Il s'agit du premier système modèle expérimental à une densité assez élevée pour permettre d'étudier la réponse de la dynamique spontanée d'un système vitreux à une augmentation du niveau d'activité. Nous avons analysé ces expériences dans le cadre de la physique des verres. Nous considérons également ce système comme un matériau. Ainsi, le second objectif de cette thèse a été d'étudier ce système actif dense via une approche microrhéologique afin de sonder comment l'activité modifie la réponse rhéologique du système.

Notre étude se compose de trois parties. Dans la première partie, qui constitue le cœur de la thèse, nous avons réalisé des expériences sur des assemblées denses de particules actives. Nous avons étudié l'influence du niveau d'activité sur la dynamique du système et nous avons trouvé un comportement non trivial à l'état vitreux. La deuxième partie est une étude de microrhéologie sur un sédiment actif, pendant laquelle nous avons agi sur le système par deux méthodes différentes : des oscillations de petite amplitude contrôlées par des pinces optiques d'une part, et d'autre part un fluage sous l'action de la gravité sur un intrus mobile. Nous avons également développé un microrhéomètre magnétique pour une étude future. La dernière partie de cette thèse est une approche de simulation numérique pour étudier le comportement non trivial que nous avons trouvé dans la première partie.

Dans nos expériences, les particules actives sont constituées de colloïdes Janus Or-Platine de taille micronique dispersés dans l'eau. Ces particules coulent au fond de la chambre expérimentale, ce qui en fait un modèle parfait pour étudier les mouvements des particules en 2D. Les particules suivent un mouvement brownien diffusif jusqu'à ce que nous activions le système en ajoutant une solution de peroxyde d'hydrogène (H_2O_2). La décomposition asymétrique de H_2O_2 sur la surface du platine et de l'or conduit à des mécanismes auto-phorétiques, ce qui entraîne une auto-propulsion des particules. Nous avons caractérisé le mouvement des particules individuelles dans une phase diluée. Le déplacement carré moyen (MSD) affiche un mouvement aléatoire persistant, c'est à dire un mouvement balistique aux temps courts et une diffusion effective aux temps longs. La vitesse de propulsion mesurée et le coefficient de diffusion effectif augmentent de façon monotone avec la concentration de H_2O_2 , tandis que le temps de diffusion en rotation reste inchangé. Dans notre système, nous pouvons atteindre des vitesses de propulsion de 10 micromètres par seconde au maximum.

Pour l'étude de la phase dense, nous utilisons la gravité pour confiner les particules en inclinant la configuration avec un petit angle de $\theta \sim 0.1^\circ$. Cela permet de conserver une monocouche qui sédimente dans son plan, avec un gradient de densité allant d'une phase diluée en partie haute à une phase dense en partie basse. Nous avons caractérisé le niveau d'activité à partir de la partie diluée du profil de sédimentation. Nous avons mesuré la longueur de sédimentation et défini une température effective, qui augmente de façon monotone avec la concentration en H_2O_2 . En nous concentrant sur la partie dense, nous avons observé de manière inattendue un comportement non monotone. À basse température effective, les réarrangements du système sont étonnamment plus lents qu'avant l'introduction de l'activité. À des niveaux d'activité plus élevés, on retrouve un comportement plus attendu avec une dynamique plus rapide sous l'effet de l'activité. En profitant du sédiment pour explorer différentes densités, nous avons montré que le comportement non monotone apparaît lorsque la densité dépasse la densité de transition vitreuse. Nous avons constaté qu'en dessous de la densité de transition vitreuse, le temps de relaxation en fonction de la densité suit la forme Vogel-Tamman-Fulcher (VTF). Les sédiments à tout niveau d'activité se superposent à cette courbe maîtresse une fois la densité mise à l'échelle d'une densité de transition vitreuse efficace, qui augmente de façon monotone avec les niveaux d'activité. Cela signifie qu'il existe une correspondance des systèmes actifs au système passif lorsque le système reste en dessous de la transition vitreuse. Cependant, cette correspondance n'est plus valide dans le verre, où on a rupture de l'ergodicité. En effet, dans ce cas, la dynamique du système répond à l'activité de manière non monotone.

Pour expliquer l'invalidité de cette correspondance, nous nous sommes intéressés à l'état polycristallin que nous trouvons au fond de notre sédiment. Cet état est lui aussi non ergodique et a l'avantage d'être relativement homogène, ce qui permet d'avoir accès à des corrélations à longue distance. Ainsi, nous avons pu corréler l'orientation du déplacement des particules et calculer la taille moyenne des domaines corrélés. Cette taille diminue puis augmente avec la température effective. En particulier, la température effective qui correspond au minimum de taille des domaines corrélés correspond aussi à la relaxation la plus lente. Cela suggère que la relaxation dans un système non ergodique suffisamment actif se produit par des mécanismes de mouvement collectif, tandis que les mouvements coopératifs dominent à zéro et à faible activité. Nous avons proposé que la directionnalité du mouvement auto-propulsé rende la relaxation coopérative moins efficace. Dans

un système non ergodique dense (verre ou polycristal), les particules sont piégées à l'intérieur d'une cage formée par leurs voisins. Une particule passive soumise uniquement au mouvement brownien explore la cage de façon isotrope et la diffusion rotationnelle ne joue pas un rôle important dans l'exploration de la cage. Au contraire, le mouvement d'une particule même légèrement active est biaisé dans une direction aux temps courts devant la diffusion rotationnelle. Par conséquent, la particule continue de pousser sa cage toujours au même endroit jusqu'à ce que la diffusion rotationnelle la réoriente vers d'autres directions. Cette exploration de la cage est inefficace, ce qui explique que le réarrangement du système actif soit plus lent que le système vitreux passif. Nous avons modélisé et nommé ce phénomène «Deadlock from the Emergence of Active Directionality (DEAD)». Lorsque l'activité est suffisamment élevée, la particule parvient à pousser son voisin vers l'avant et entraîne un mouvement collectif. C'est à ce moment que la dynamique augmente avec le niveau d'activité.

Nous étudions ensuite la microrhéologie du sédiment actif. Nous avons introduit une particule sonde dans le sédiment et y avons appliqué un stimulus mécanique. Nous avons appliqué deux types de stimulus : un déplacement oscillant de petite amplitude (SAOS) et une force gravitationnelle constante. Une troisième expérience que nous avons développée devrait permettre d'étendre la gamme des stimuli mécaniques possibles et d'améliorer leur contrôle. Pour le SAOS, nous avons contrôlé le mouvement de la sonde à l'aide d'une pince optique. Nous avons ainsi pu mesurer un module de cisaillement complexe qui montre que la réponse du sédiment passif est plus élastique que visqueuse. De plus, cette rigidité augmente avec le niveau d'activité. Cependant, les pinces optiques engendrent des interactions parasites entre la sonde, et les particules colloïdales, et ces interactions semblent dépendre de l'activité, ce qui rend difficile l'interprétation des résultats. Nous concluons donc que les pinces optiques ne sont pas un outil adapté à notre système.

Le deuxième stimulus mécanique consiste à laisser la force gravitationnelle tirer la particule sonde à l'intérieur du sédiment. Nous avons remarqué une différence significative entre le mouvement de la sonde à l'intérieur des sédiments passif et actif. Dans le sédiment passif, la vitesse de la sonde en fonction de la densité colloïdale est presque constante tout au long de la chute, puis accélère avant un arrêt brusque. En revanche, la sonde dans le sédiment actif passe par une phase de décélération suivie d'une phase à vitesse constante, qui se produit à des densités plus élevées que celle du sédiment passif, puis une deuxième décélération jusqu'à son arrêt. On note que l'évolution du mouvement de la sonde est monotone avec les niveaux d'activité, c'est-à-dire que la phase à vitesse constante semble se déplacer vers des densités plus élevées lorsque le niveau d'activité augmente. L'analyse des trajectoires colloïdales nous aide à comprendre l'origine d'une telle différence. Le flux dipolaire des particules colloïdales provoque une poussée sur le dessus de la sonde. En comparant à la même profondeur, la sonde dans le sédiment actif est soumise à moins de poussée que la sonde dans le sédiment passif, et c'est pourquoi la phase à vitesse constante se produit plus tard dans le sédiment actif. Nous avons poursuivi l'analyse en étudiant le mouvement relatif des particules avec leurs voisins à l'aide d'un outil statistique. Cette analyse révèle que les particules colloïdales autour de la sonde sphérique sont advectées selon un flux de Stokes. Cette observation ouvre la possibilité d'extraire une viscosité effective dépendante de l'activité à travers un terme de traînée de type Stokes. Malheureusement, cette configuration expérimentale ne permet pas un contrôle suffisant pour une modélisation quantitative.

Dans cette perspective, nous avons développé un microrhéomètre magnétique. Cet appareil est composé de quatre bobines autour de la chambre expérimentale, permettant de contrôler le mouvement d'une sonde aimantée en rotation ou en translation. Ce développement expérimental bénéficiera à la prochaine étape de la caractérisation microrhéologique de notre système actif.

La dernière partie de ma thèse est une investigation numérique de la phénoménologie « DEAD » découverte expérimentalement dans la première partie, et plus généralement des mécanismes de réarrangements spontanés d'un assemblage dense de colloïdes actifs. Nous avons modélisé un système de particules browniennes actives (ABP) en utilisant une équation de Langevin avec une force active supplémentaire, dont nous avons fixé le temps de rotation et varié l'amplitude. Le MSD résultant des particules individuelles montre bien un mouvement aléatoire persistant, ce qui est en accord avec l'expérience. Dans un système de nombreuses particules de potentiel d'interaction Weeks-Chandler-Anderson (WCA), nous avons retrouvé une séparation de phase induite par la motilité (MIPS) à des densités modérées et à un régime de forces de propulsion élevées. Qu'il y ait MIPS ou non, le temps de relaxation en fonction de la densité suit une forme VTF pour tous les niveaux d'activité. Comme dans les expériences, la transition vitreuse se déplace vers les densités plus élevées et la superposition de la dynamique des différentes activités sous la densité de transition vitreuse semble possible. Il est ainsi possible d'étudier le régime vitreux où nous avons trouvé expérimentalement le phénomène DEAD. Grâce aux simulations numériques, nous pourrions pousser l'analyse plus loin que dans les expériences. Par exemple, nous aurons accès aux corrélations à longue distance et pourront mesurer directement les orientations des particules. Bien sûr, cela nous permettra de mieux comprendre les systèmes vitreux actifs.

Mots clés: Matière active, Colloïdes actifs, Comportement collectif, Liquide surfondu, Verre, Polycristal, Ergodicité, Microrhéologie

Acknowledgements

After three years of my PhD life in France and more than a half year in Japan, I have gained tons of knowledge and experience more than I could ever imagine. It is such a great opportunity to encounter all the amazing people who later become an important part of my life.

First of all, I would like to express the deepest gratitude to both of my thesis supervisors, Dr. Cécile Cottin-Bizonne and Dr. Mathieu Leocmach, for their continuous support in both scientific and personal aspects. I would like to thank them for their help and encouragement during this research and thesis writing. I hope someday I can be a great supervisor as they are.

I particularly acknowledge Dr. Cécile Cottin-Bizonne for her profound knowledge in active matter and her expertise in the experimental system that are extremely helpful for this research. Personally, I deeply appreciate her true spirit of being a teacher who always encourages her students and promotes them in any direction that they want. Besides, I would like to thank her for placing her trust and confidence in me since the beginning when I first contacted her for a PhD position. Without her generous acceptance, this story could never happen.

I also would like to express my great appreciation to my co-supervisor, Dr. Mathieu Leocmach. Thanks to his help and very useful suggestions that make me progress a lot, especially in the knowledge of glassy physics and computational skills. Thanks to his strong connection with the Japanese research groups, I had opportunities to conduct a research in Japan twice during my PhD. Moreover, I truly appreciate his patience and willingness to help during our discussion. I would like to thank him for always listening to any of my requests and issues.

Apart from both official supervisors, I would like to thank Dr. Christophe Ybert, whom I consider as my third supervisor. He joined most of the discussion and he often brought out new ideas that three of us had never thought about. With his sharp eyes, he could point out a weak spot in our work that was sometimes overlooked. I believe that this thesis would not come this far without his contribution.

It is also my great honor to work with Prof. Takeshi Kawasaki at Nagoya University during the last period of my PhD. I could learn a lot from his expertise in glassy systems via a simulation approach. I also appreciate his great spirit of an instructor and his intention to explain difficult stuff in an easy way. In addition, living alone in a foreign country could be more difficult, especially during the pandemic (COVID-19). I would like to thank him for his great hospitality and kindness that made things much easier for me.

During my PhD, it was a great opportunity and great honor for me to have small discussions with Dr. François Graner, Dr. Ludovic Berthier, Prof. Hajime Tanaka, and Prof. Kunimasa Miyazaki. Despite we had only a little discussion, the suggestions from their expertise could enhance a lot the quality of our research.

I would like to thank my thesis referees, Dr. Emanuela Zaccarelli and Dr. Olivier Dauchot, for reporting my PhD manuscript and for attending my PhD thesis defense together with the rest of the jury, Dr. Axelle Amon and Prof. David Rodney. I would like to thank them for the fruitful discussion, comments, and suggestions that could be useful in my future work.

I would like to sincerely thank Dr. Félix Ginot for being my experimental mentor at the beginning of my PhD. Also, he helped me to get familiar with the environment and people in the lab when I first arrived in France, and I always thank him for that.

I also would like to thank Dr. Isaac Theurkauff for our collaboration in Tokyo during my 2nd year. Despite my research stay was short and intense, we managed

to obtain the results in time thanks to his expertise and very useful suggestions. I also appreciate his great hospitality during my stay in Tokyo.

I would like to acknowledge Dr. Rémy Fulcrand, Mr. Gilles Simon and Mr. Ruben Mascart for their technical support throughout the thesis. I thank Rémy for the platinum deposition and microfabrication, and thank Gilles for large-scale fabrication in the experimental setup. Apart from the technical treatment and fabrication, they had also given advice and suggestion to improve the experiments. I could learn a lot from them in terms of various engineering techniques. I also thank Ruben for his skills in computer that can always rescue my computer whenever it breaks down.

I would like to thank all of the students whom I co-advised in my PhD: Mickaël Dos Santos, Selvamugesh Rajmohan, Thomas Boquet, and Adérito Fins Carreira. It was a great opportunity for me to advise and teach them because I could also practice to be a future advisor. I especially acknowledge Mickaël and Selvamugesh for their hard work and their internship results, which are included in a part of this thesis.

It has been a real pleasure to be a part of the team 'liquid and interface' at iLM. Apart from the great availability of experimental equipment, I am impressed by the organization of the team together with the biophysics team (ranging from scientific stuff to BBQ party and Christmas dinner). Also, I really like the working environment here where people are super friendly and supportive.

I wish to thank all of my friends from iLM for being a part of this journey beside me. We came from different parts of the world to share our moment in France. I will always remember our lunchtime, coffee break, and activities that we have done together: hiking, skiing, restaurant exploring, etc. Without all of you, I could not imagine how I can make it through my PhD.

I must also thank my Thai friends in Lyon and in France. We are far from our home country, but we could build our warm community to support and spend time with each other. I would like to especially thank P'Foam/Foamie (Dr. Kritsadi Thetraphi). I was very lucky to have you as my flatmate, my friend, my sister, and my travel buddy. Thanks to your sense of humor and positive attitude that can always cheer me up. My PhD life in France would be totally different without you.

In this last paragraph, I would like to express my gratitude to my supporters from a distance. I would like to thank my boyfriend, P'Champ (Dr. Sutthipong Noisagool), for his continuous support since my Master's degree until the present. Thank you for always encouraging me and for listening to any of my decision even though it made us far apart (and thank you for your patience as well). Lastly but most importantly, I would like to thank my family for their endless care and support.

This thesis was supported by a doctoral grant from Physics and Astrophysics doctoral school of Lyon (PHAST). For an additional research experience, I was supported by a pre-doctoral fellowship from the Japan Society for the Promotion of Science (JSPS) to spend the last 8.5 months of my PhD in Nagoya, Japan. The three months gap between both grants were filled by ANR GelBreak (managed by CNRS) of Dr. Mathieu Leocmach. Besides, I was also supported by his PICS-CNRS budget for two months of a research stay in Tokyo when I was in the second year.

Contents

1	Introduction	1
1.1	Active matter and why it matters?	2
1.1.1	Natural/biotic active matter	2
1.1.2	Physical description of active matter	6
1.1.3	Abiotic active particles	8
1.2	Colloidal particles and how they make statistical physics visible	10
1.2.1	Perrin's sedimentation experiment of passive colloids	10
1.2.2	Sedimentation of active colloids	11
1.3	Active dense systems in experiments	12
1.4	Passive dense system with thermal agitation	13
1.4.1	Equilibrium path: crystalline, hexatic and polycrystalline phases	14
1.4.2	Nonequilibrium path: from supercooled to glass	16
1.5	How self-propulsion influences dense systems?	18
1.5.1	Simulation works	19
1.6	Objectives	21
1.7	Thesis outline	22
2	Experimental configuration and characterization in a dilute regime	23
2.1	Active Colloids	23
2.1.1	Gold-platinum Janus particle	23
	Propulsion mechanism	24
2.1.2	Making of the gold-platinum Janus particle	25
	Gold particles	25
	Platinum deposition and detachment of the Janus particles	27
2.2	Experimental setup	29
	(a) Experimental chamber	29
	(b) Imaging and data acquisition	30
	(c) Motorized stage	30
	(d) Lightning condition: dark-field microscopy	31
	(e) Angle control	31
2.3	Characterization in the dilute regime	32
2.3.1	Van Hove function	33
2.3.2	Mean square displacement and effective diffusion	36
2.3.3	Propulsion velocity	38
2.4	Alternative gold particles for making active colloids	40
2.4.1	Latex(AuNP)-platinum Janus particle	41
3	Analysis tools for the dense regime	45
3.1	Particle tracking in a dilute regime	45
	Step 1: Detecting particles	45
	Step 2: Reconstructing trajectories	47
	Step 3: Filtering spurious trajectories	48
	Step 4: Subtracting the drift	48

3.2	Particle tracking in a dense regime	48
3.2.1	Tracking parameters	49
3.2.2	Data streaming with hierarchical data format (HDF)	49
3.3	Structure investigation	50
3.3.1	Radial-pair correlation function, $g(r)$	51
3.3.2	Static structure factor, $S(q)$	53
3.3.3	Hexatic order parameter, ψ_6	54
3.4	Dynamical analysis	57
3.4.1	Mean square displacement, MSD	57
3.4.2	Overlap function, $F(\Delta t)$	58
3.4.3	Four-point structure factor, $S_4(q, \Delta t)$	59
3.5	Network analysis	61
3.5.1	Defining neighbors	61
	6-nearest neighbors (6-NNs)	61
	Voronoi neighbors	62
3.5.2	Defining graph and connected components	63
3.5.3	Broken bonds and bonds life time	64
4	Experimental Investigation on Dense Assemblies of Active Colloids	67
4.1	Experimental configuration and characterization	67
4.1.1	Creating the dense phase	67
4.1.2	Minimizing the drift	68
4.1.3	Introducing H_2O_2 and data acquisition	69
4.1.4	Effective diameter and density definition	69
4.1.5	Hexatic order parameter, $\psi_{6,i}$	69
4.2	My first observation of the non-monotonic behavior	70
4.3	Sedimentation of active colloids	71
4.3.1	Characterization of activity levels: Effective temperature	71
4.3.2	Compaction	73
4.4	Density control experiment	74
4.4.1	Slicing the profile	74
4.4.2	Density-dependent dynamics of the passive sediment	75
4.4.3	Glass or crystalline?	77
4.4.4	Activity-dependent dynamics at fixed densities	78
4.5	Identify the non-monotonic behavior condition	80
4.5.1	Liquid-glass phase diagram	80
4.5.2	VTF relation	80
4.5.3	Ergodicity breaking	82
4.5.4	Particle motion before and after ergodicity breaking	82
4.6	Polycrystalline slice: probing the relaxation mechanism	84
4.6.1	Checking the structure order	84
4.6.2	Relaxation of the wide polycrystalline slice	84
4.6.3	Orientation of displacement	86
4.6.4	Directional correlation map	88
4.6.5	Broken bonds	88
4.6.6	Defining characteristic length ℓ	90
4.7	Simple model for the efficiency drop in cooperative rearrangements	91
	Propulsion-diffusion in a cage	92
4.8	Conclusions	94
	Appendices	96

5	Microrheology of Active Colloids Sediment	103
5.1	Key concept of rheology and microrheology	103
	Yield stress fluid	104
	Viscoelastic material	104
	Oscillatory test	104
	Creep testing	105
	Microrheology	106
5.2	Actuation by optical tweezers: Periodic motion of a tracer	107
5.2.1	Optical tweezers and its application to microrheology	108
5.2.2	Our experimental setup	108
	Optical tweezers setup	109
	Microscope setup and our sample	109
	Probe particle	109
	Actuation	111
5.2.3	Result	112
5.3	Actuation by gravity: An intruder falls through the sediment	113
5.3.1	Experimental configuration and procedure	113
	Unconventional H_2O_2 variation	114
	Defining the reference position and time	114
5.3.2	Qualitative observation	116
5.3.3	Glass bead trajectory	117
5.3.4	Colloidal particle trajectories	121
5.3.5	Network analysis and broken bonds	124
5.3.6	Texture analysis: statistical tools to investigate bonds deformation	126
	Principle of the texture analysis	126
	Representation of matrices	127
	Texture analysis in our experiment	128
5.4	Perspective towards magnetic actuation	132
5.4.1	Key concept of magnetic microrheometer	132
5.4.2	Making of the magnetic microrheometer	133
5.4.3	Preliminary output	134
5.4.4	Further development	136
6	Numerical simulation approach	139
6.1	Previous numerical studies	139
6.2	Setting up the simulation for Active Brownian particles	140
6.2.1	Langevin equation for ABP	140
6.2.2	Nondimensionalized equation of motion	141
6.2.3	Numerical integration of the equations of motion	142
6.2.4	Relevant numerical simulation techniques	143
	Box-Muller method for Gaussian random generator	143
	Verlet list and cell lists method for neighbors search	143
	Initial configuration	143
	Logarithmic sampling	144
	Zero-mode subtraction	145
6.2.5	Our ABP simulation	146
6.3	Dynamic of an individual ABP	146
6.3.1	Verify the simulation	146
6.3.2	Individual dynamics of our system	147
6.4	Ergodic supercooled regime	148

6.4.1	Passive WCA simulation	148
	Effective hard sphere diameters in WCA system	148
	Self-intermediate scattering function and relaxation time	149
	Approaching the glass transition from supercooled regime	150
	Temperature dependence	151
6.4.2	Active supercooled	152
	How activity influences the glass transition?	153
	Motility-Induced Phase Separation	153
	VTF fitting	155
6.5	Beyond the glass transition	157
7	Conclusions and perspectives	161
	Bibliography	165

Chapter 1

Introduction

Being fascinated by a murmuration of bird flocks, I chose to conduct a research on it during my master's degree¹ and this is how I entered the field of active matter. The work was purely numerical because of limitations to obtain empirical data from a natural flock². While I was prospecting for a possible PhD topic, I came across several articles about synthetic active matter. I still remember the feeling of excitement I had when I found that scientists can create and study a 'real' active system on laboratory scale. I decided to pursue this motivation and finally obtained a PhD position in liquid and interfaces team of Institut Lumière Matière (iLM), which had published a series of very nice experimental works on synthetic active particles in the past few years. The team had successfully explored the system at low [7, 8, 9] and intermediate [10, 11] densities. Some of these works are now milestones of the field of active matter. However, what was still missing at that time was the investigation at high density, in which the passive counterpart exhibits glassy dynamics. This was exactly what I was looking for. Staring at the astonishing movement of active particles and then interpret their motion into new knowledge of physics. The baton has been passed to me since then and now it has been 4 years of my PhD journey, which I have condensed it into this 163 pages manuscript.

In this chapter, I will provide the key concepts of my PhD work. There are two pillars that I am standing on: active systems and glassy physics. I will present the state of the art in both fields and how they merged at the time I started my PhD (including some works that have been published recently, parallel to my PhD work). I will start by introducing active matter in both natural and abiotic systems, including how physicists model active systems. Then, I will review the mapping from passive (equilibrium) systems to active (non-equilibrium) systems, which is demonstrated using active colloids at low density, following by some recent experimental works on active systems at high density. After that, I will give a full review of passive dense systems (both crystal and glass) and finally end the review with simulation works showing how activity influences the classical phenomenology of dense systems. The aim is not to cite every single study in these flourishing fields, but to emphasis our standing point among the sea of literature. In the end of this chapter, I will state the objectives of my PhD work and provide a brief description of each chapter in this manuscript.

¹In my master's degree, I investigated a 3D bird flock model proposed by Cavagna et al. [1] which is an extension from the famous Vicsek model [2]. I extended the model further and analyzed its stability combined with network theory. I showed that the stability of this model relates to topology of a flock network. This finding could lead to a further analysis on flock shape and bird distribution [3].

²At that time, there was only one real field measurement on starling flocks in Rome that could extract bird's individual trajectory for physical interpretation [4, 5, 6].

1.1 Active matter and why it matters?

‘What is active matter?’ is always the following question when someone (with none or different scientific background) asks me what is my PhD research. Because of the novelty of the field, I always have to start my answer from a classical feature of general matter. A molecule of any state of matter always undergoes Brownian (random) motion, which is a result from thermal energy. The term ‘active’ refers to a special scenario when each unit can harvest energy from its environment and convert into motion [12, 13, 14]. From a thermodynamic point of view, such system is out-of-equilibrium because of energy injection at a local scale. This is why active matter has been used as a model to probe new physics out of the scope of thermal equilibrium. It is a new path towards novel type of material [15], and also a bridge from material science to cell biology [16]. Because many biological processes in a cell are non-equilibrium [17], with a framework of active matter we can try to understand cell mechanics and collective motion. From this point, there are numerous further studies regarding health care issues such as epithelial self-healing [18, 19, 20], cancer cell metastasis [21, 22] and tumor growth [23, 24]. Remarkably, a very recent study reveals that tumor cell expansion is better explained using active matter model rather than equilibrium physics [25]. Besides, apart from trying to understand it, such active biomaterial is a great inspiration for bioengineering to control molecular motors of living material [26, 27, 28].

The term active matter does not only apply to living tissues and cell biology. It can apply to any length scale as long as the energy injection is at the level of an individual unit. Fig. 1.1 shows various examples of active matter on different length scales from a few hundred meters down to microns scale of unicellular organisms. Studying their fascinating movement is not only just for pleasure, but also for unexpected outcomes that could lead to innovation. For example by studying a suspension of swimming *Escherichia coli* (*E. coli*) with asymmetric boundaries, a tiny microgear was designed to be powered by these microswimmers [32] (see Fig. 1.2a). Later on, the 2D ratchet has been improved to be a 3D micromotor and *E. Coli.* was engineered so that its swimming speed can be tuned by light intensity [33] (see Fig. 1.2b). Alternatively, instead of using living swimmers, the microgear can be powered by artificial microswimmers [34] (see Fig. 1.2c) or even self-assembled directly from abiotic microswimmers [35] (see Fig. 1.2d).

All of the above examples stress the possible benefits in terms of engineering. In the following, I would like to highlight what we (as physicists) are interested in and have already extracted from active systems in nature ranging from large to small scales. Even these systems are very diverse, they all share the same property: an interaction at a local scale (either physical, chemical or social interactions) gives rise to a global emergent behavior.

1.1.1 Natural/biotic active matter

Large scale active systems

One of the most famous examples of active matter is a flock of birds (Fig. 1.1a). Depending on bird species, the size of a flock is ranging from less than ten to hundreds, to few thousands of birds. There is a wealth of literature regarding to birds collective behavior. Here, I would like to mention only a selection of the literature based on large flocks (more than 500 birds) which motion is spontaneous. This is because, as a physicist, we are mostly interested in intrinsic behavior (not the social response like

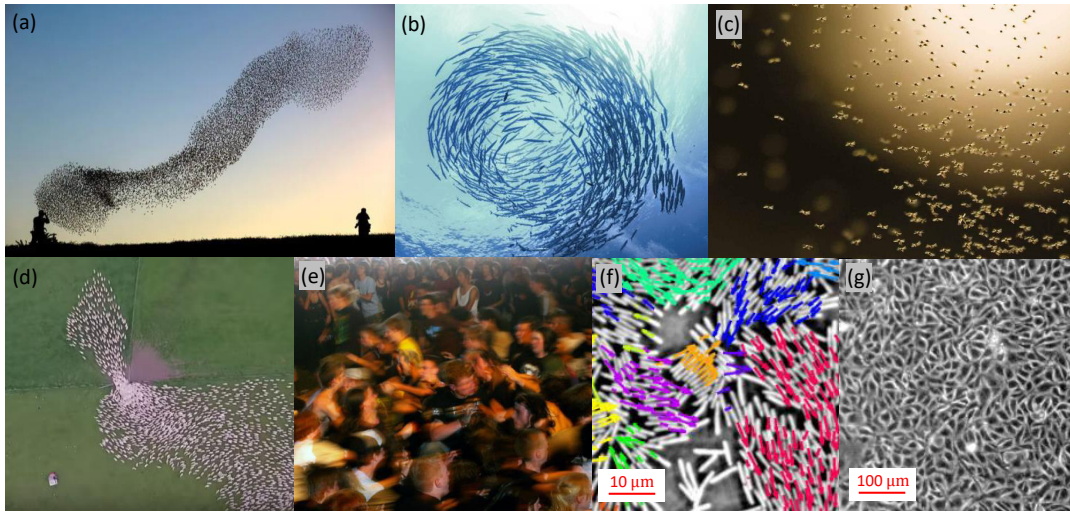


FIGURE 1.1: Several active matters in nature. (a) A flock of birds. Image by Amir Cohen/Reuters. (b) A school of fish. Retrieved from <https://daily.jstor.org/how-do-fish-schools-work/>. (c) A swarm of insects. Image by Peter Chadwick. (d) A sheep herd through a bottleneck. Retrieved from <https://www.youtube.com/watch?v=tDQw21ntR64>. (e) A group of people in a metal rock concert doing mosh pit. Retrieved from Ref. [29]. (f) *Bacillus subtilis* bacteria in a colony. Modified from Ref. [30]. (g) Madin-Darby canine kidney cells in a colony. Modified from Ref. [31].

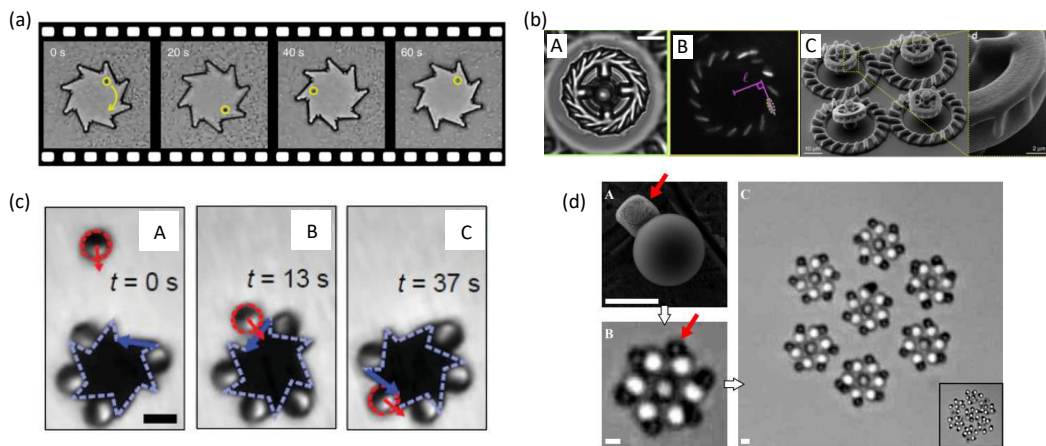


FIGURE 1.2: (a) Micro ratchet of diameter $48 \mu\text{m}$ powered by *E. coli* cells. Retrieved from Ref. [32]. (b) A: Top view of the 3D micromotor. The scale bar is $20 \mu\text{m}$. B: The same view but in fluorescence light. The *E. coli* cells are visible in white ellipsoids. C: 3D model of the micromotor. Modified from Ref. [33]. (c) The microgear powered by Janus particles. The scale bar is $5 \mu\text{m}$. Modified from Ref. [34]. (d) A: An abiotic phototactic microswimmer. B: A self-spinning microgear composed of seven swimmers. C: An assembly of seven microgears. (inset) The organization is destroyed when light switches off. The scale bars are $1 \mu\text{m}$. Retrieved from Ref. [35].

anti-predator behavior or leaderships) far from the boundary. The very first quantitative observation by Potts [36] suggested that a motion of a single bird, which is called an initiator, can influence the motion of the whole flock and this influence travels through the flock with a wave-like form. Later on, with a lot of improvement in data acquisition techniques and 3D tracking, Cavagna et al. were able to reconstruct the 3D trajectory of each individual bird of starling flocks in Rome [4, 5]. The most remarkable finding from this set of data is that birds interaction distance is not the Euclidean distance, but rather a topological distance, i.e., a bird interacts with its 6-7 nearest neighbors [37]. They also suggested that collective response in the flock is scale-free with the flock size [38]. Further analysis of bird trajectories revealed that the response from an initiator travels through the flock with a linear dispersion relation [6]. From this finding, the researchers developed a new model by considering a flock of birds as a flying ferromagnetic system [1]. This is one example of linking our current knowledge in physics to describe collective behavior in nature.

Other groups of animals that are also popular for physicists to study their collective behavior are fish (Fig. 1.1b) and insects (Fig. 1.1c). Both systems exhibit a sharp transition from an unpolarized to a polarized group upon varying density (oceanic fish school [39], fish school in laboratory [40] and marching insects [41]). This transition reminisces to the behavior of the Vicsek model [2]. In the case of a swarm of flying insects that has no alignment between members such as midges, the observation has revealed their near-criticality and scale-free behavior [42]. This means that if swarm size has changed, midges seem to regulate their motion to keep the swarm in the low-density disordered side of the transition (the same transition as in Vicsek model).

What do a flock of birds, a school of fish and a swarm of insects have in common is a low local density around each moving unit, i.e., a neighbor is unlikely to be closer than 1 body length [37, 42, 43]. This is because within a highly correlated moving group, a collision is a fatal event and thus must be avoided. By contrast for a group of mammals, it is sometimes acceptable to have physical contact between members (if individual speed is not too high), and this allows a higher local density. Even though most mammals are able to recognize other individual members and this may cause leadership or hierarchical structure in a group, biological evidence has shown that in many cases the role of leadership has little influence on group motion [13]. There are reviews on collective motion in vertebrates that have already discussed the role of leadership [13, 44]. In the following, however, I would focus solely on no leadership situation.

Sheep is a good subject to study in crowded conditions because it is non-aggressive by nature (a sheep often allows other sheep to stay in contact). Studying a flow of sheep through a bottleneck is also used to mimic a panicking crowd (Fig. 1.1d). The flow can be analyzed in the framework of granular physics and statistical mechanics [45]. A similar study has been done in a smaller animal such as mice [46].

Speaking of a compact system, a huddle of emperor penguins is also a good example. In the harsh condition in Antarctica, they form dense packs ($\sim 10^3$ individuals) in order to conserve internal body heat [47]. Considering a group of penguins as a matter, the study reported a first-order phase transition from huddling to no huddling behavior as the characteristic temperature increases [48] (see Fig. 1.3). A large-scale study of the dynamics of penguin huddles also reported small density waves propagate through the group [49] and later on a model of spherical penguin in a huddle was developed to explore this density wave [50].

In a recent study, Bain and Bartolo [51] have shown that a human crowd can also

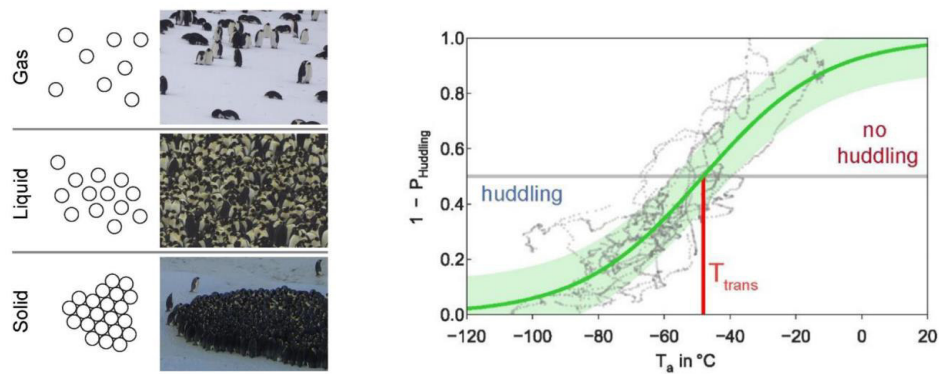


FIGURE 1.3: (left) A comparison of different states of matter to Emperor penguin colonies. (right) The phase transition from huddling to no huddling behavior as the temperature increases. Retrieved from Ref. [48].

display density wave propagation. They have investigated marathon runners channeled to the starting line (10^3 runners) and then established a new hydrodynamic theory of polarized crowds. How about disordered/unpolarized dense crowd? While it is not common for wild animals to exhibit such behavior at high density, unsurprisingly, we (humans) sometimes do it for fun! The very obvious scenario is a crowd in a metal rock concert. Traditionally, there are several collective movements that audiences usually perform during a concert. Bouncing with the others with unpreferred direction, which is a so-called *mosh pit*, is one of the popular movements (Fig. 1.1e). Impressively, Silverberg et al. [29] have shown that the individual speed distribution during the mosh pit movement, which is disordered, is well-fitted by the Maxwell-Boltzmann distribution.

Active matter at low Reynolds number

At the microscale, there is a wealth of biotic active matter. What makes them different from macroscale systems is that the inertia is totally negligible at small length scale [52]. A quantity to determine this limit is known as Reynolds number, which is the ratio of inertial forces to viscous forces. A microorganism moving in a liquid medium has a Reynold number of the order of 10^{-4} or 10^{-5} , while this number is about 10^4 or 10^6 for a bird flying in the air. At such low Reynolds number limit, life is tougher than at larger scale because of the scallop theorem³. A review from Elgeti et al. [53] has included swimming mechanics and models of different types of microswimmers. They also review the collective motion of colonies of bacteria/microorganisms. A similar review from a biological point of view is also available in Ref. [54]. Here, I would like to mention only selected works studying crowded conditions.

Cells in living tissues are also active matter even though they are very different from the previous examples. They are not swimmers, but rather crawling on a substrate and experience adhesion among themselves. This thus makes them a unique interesting active system [53, 55]. Due to their plasticity, they are a specific example of collective behavior of self-propelled deformable object [56]. Cells

³It is impossible to move at low Reynolds number using reciprocal movement.

collective motion/migration has been investigated in different cell types such as endothelial [57], epithelial [18] (wound-healing), and cancer cells [58]. As a function of cell density, tissue cells displays a kinetic phase transition from a disordered state into an ordered state [59]. This transition is often observed in other active systems. Furthermore, several studies at high cell density have revealed features similar to physical dense systems such as jamming transition [60], a glass-like transition [31] and a dynamical slowdown [61].

Unicellular organisms can also form dense crowds. The very first report of the non-trivial hydrodynamic phenomena in concentrated aerobic bacteria population is *bio-convection* [62]. The pattern is similar to thermal convection and it was explored using tools from hydrodynamics and nonlinear dynamics. Collective motion of highly concentrated cells of *Bacillus subtilis* is analogous to the molecular alignment of nematic liquid crystals [63]. Also, it is found large fluctuations in local instantaneous density: the denser the system, the larger are the fluctuations [30]. A very recent review on bacterial swarming from the statistical physics point of view can be found in Ref. [64].

1.1.2 Physical description of active matter

The above examples of active matter are full of emergent phenomena. They are a new challenging playground for physicists to build a new toolset for out-of-equilibrium physics. Starting from the original flocking models of Vicsek et al. [2], and Toner and Tu [65], the theory of active matter has been actively growing until now. Most active matters are swimmers, i.e., they move in a medium of either gas or liquid. In addition, some systems are on a surface, where the friction force takes place. Depending on whether the system conserves the momentum or not, active matter can be described by either ‘wet’ or ‘dry’ point of view [14]. For instance, if we consider liquid around a microswimmer, the hydrodynamics flow field around the swimmer can be described by a dipole and classified into pushers or pullers [53, 66] (see Fig. 1.4) and the interactions between the swimmers depend on their class. Nevertheless, in many studies, the influence of the environment is not considered for the sake of simplicity. In the following, I will discuss the main three models of dry active particle that physicists have used to study active matter.

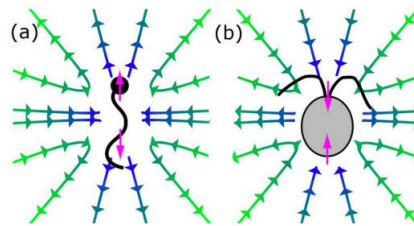


FIGURE 1.4: Hydrodynamics flow field around a dipole microswimmer, (a) pusher and (b) puller. Retrieved from Ref. [53].

Physical models of a single active particle

1. **Run-and-tumble particle (RTP):** A particle movement is a sequence of ‘run’ (propelling of constant speed in a straight line) and ‘tumble’ (stop and reorient) phases [67, 68]. This kind of motion is found in some bacteria such as *E. coli* [69] and *Chlamydomonas* [70].

2. **Active Brownian particle (ABP):** A particle self-propels with a fixed speed and continuously reorients itself according to rotational diffusion [71, 72]. This motion was first observed in protozoa [73]. It is also found in non-tumbling *E. coli* mutants and other non-tumbling microorganisms. ABP is a popular model for artificial active colloids, which will be presented shortly in Subsection 1.1.3. The 2D dynamics of a self-propelled particle is governed by the overdamped Langevin equations [74],

$$\dot{\mathbf{r}} = \zeta^{-1} [-\nabla U + \mathbf{F}_{\text{active}}] + \sqrt{2D_T} \boldsymbol{\zeta}, \quad (1.1)$$

$$\dot{\theta} = \sqrt{2D_R} \zeta_R, \quad (1.2)$$

where \mathbf{r} and θ are position and orientation of the particle, respectively. ζ is a drag coefficient. D_T and D_R are the translational and rotational diffusion coefficient, respectively. U is an external potential (can be the interaction in many-particles system). $\mathbf{F}_{\text{active}}(\theta) = f \hat{\mathbf{n}}(\theta)$ is a self-propulsion force of magnitude f and direction $\hat{\mathbf{n}} = (\cos \theta, \sin \theta)$. $\boldsymbol{\zeta}$ and ζ_R are white noise of force and torque which satisfy $\langle \boldsymbol{\zeta}(\mathbf{r}, t), \boldsymbol{\zeta}(\mathbf{r}', t') \rangle = \delta(\mathbf{r} - \mathbf{r}') \delta(t - t')$, where $\langle \dots \rangle$ refers to an average over the distribution and δ is Dirac delta function. In another notation, ABP model can be described by probability density function as well [75].

3. **Active Ornstein-Uhlenbeck particle (AOUP):** AOUP model [76, 77] is an approximation of the ABP model. Particle motion is governed by the following equation of motion,

$$\dot{\mathbf{r}} = \zeta^{-1} [-\nabla U + \mathbf{F}_{\text{active}}], \quad (1.3)$$

$$\tau_p \dot{\mathbf{F}}_{\text{active}} = -\mathbf{F}_{\text{active}} + \sqrt{2D_a} \boldsymbol{\zeta}(t). \quad (1.4)$$

Instead of a fixed amplitude active force like in the ABP model, the active force obeys the Ornstein-Uhlenbeck process where τ_p is a persistence time and D_a is an effective diffusion coefficient, which can be related with single-particle effective temperature. This treatment provides a simpler analytic expression and has thus attracted more theoretical attention [78, 79, 80].

Assembly of active particles at intermediate density.

When there is more than one active particle, the interaction between them is a crucial ingredient of the model. The first model of the dry flock was proposed by Vicsek et al. [2]. A motion of particle i in the flock is governed by

$$r_i(t + \Delta t) = r_i(t) + v_i(t) \Delta t, \quad (1.5)$$

$$\theta_i(t + \Delta t) = \langle \theta \rangle_{r_c} + \zeta_i(t), \quad (1.6)$$

where r_i is position and v_i is velocity with a fixed amplitude of an orientation θ_i . $\langle \theta \rangle_{r_c}$ refers to the average direction among neighbours which have a distance less than r_c from it. $\zeta_i(t)$ is a uniform noise of interval $[-\alpha/2, \alpha/2]$, where α is noise parameter. Local alignment is the only interaction in this model. Despite its simplicity, the model exhibits a phase transition from disordered self-propelled particles to an ordered flock upon varying particle density and α . This was the first model that can connect self-propelled particles to statistical physics. The continuum version of the Vicsek model was developed by Toner and Tu [65, 81] which leads to a hydrodynamic theory of flocking.

There are also many active systems that do not have an alignment interaction such as a swarm of insects and bacteria. In the latter case, it was observed a phase separation at high enough density and self-propulsion [82, 83, 84]. To capture this phenomenon, Tailleur and Cates [85] used a coarse-grained description of active particles. By considering a probability of finding one active particle in space (derived from either RTP or ABP), they have shown that the phase separation is due to a decrease of self-propulsion speed as the local density increases and thus the homogeneous phase becomes linearly unstable. Later on, this phenomenon was called Motility Induced Phase Separation (MIPS) [86]. While the first derivation of MIPS is a bottom-up approach, recently there is a top-down approach known as a *scalar active matter* [87]. By describing active matter in terms of field theory, this approach successfully derives MIPS as well.

1.1.3 Abiotic active particles

In parallel to the computational modeling, another approach to model active matter is from experiments with abiotic active particles. Artificial swimmers or walkers allow more systematic studies than living ones because we can tune their propulsion mechanisms, interactions, and environment. They allow us to create different features of collective motion that do not exist (or are not yet discovered) in natural active systems. Many artificial active systems have been developed experimentally so far (reviews can be found from Refs. [88, 89, 90, 91, 92]). To make a non-living particle become self-propelled, we have to break a symmetry at a local scale. There are many ways to achieve it and here I will summarize them into six self-propulsion mechanisms (Fig. 1.5).

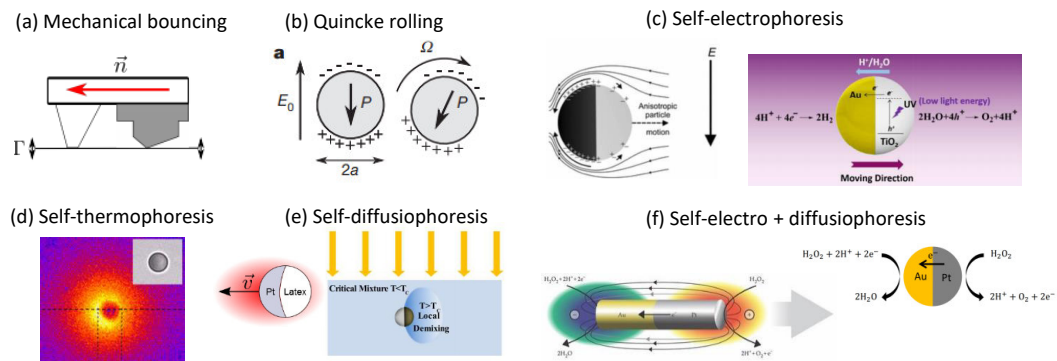


FIGURE 1.5: Sketches of different abiotic active walkers/swimmers. (a) A self-propelled polar disk. Modified from Ref. [93]. (b) A self-propelled colloidal roller with Quincke rotation. Modified from Ref. [94]. (c) Left: A Half-metallic Janus particle in an AC electric field. Retrieved from Ref. [95]. Right: TiO_2 -Au Janus particle in water powered by UV light. Retrieved from Ref. [96]. (d) Temperature map around a half-metal Janus microspheres under laser radiation. Retrieved from Ref. [97]. (e) Left: A latex-platinum Janus particle in a hydrogen peroxide solution. Right: A half-metal Janus microspheres in a critical mixture. Modified from Ref. [98]. (f) A Bimetallic rod and sphere in a hydrogen peroxide solution. The left figure is retrieved from Ref. [92].

- Mechanical bouncing:** Millimeter-scale objects on a vibrating plate can self-propel if their mechanical response to vibration is anisotropic. This is what Deseigne et al. [93, 99] have achieved with disks supported by two legs made

of different materials (see Fig. 1.5a). In this way, each disk displays a net motion with an orientation independent from the other disks. However, collisions lead to alignment. The authors have explored collective dynamics upon varying the vibration amplitude. The system displays a highly ordered phase at high enough density and this reminisces of the observation of Vicsek model.

2. **Quincke rolling:** Self-propulsion can also be obtained when a spherical object spontaneously rolls on a surface. Such a situation was obtained by Bricard et al. [94] using an effect called Quincke rotation [100]. Their system is micron-sized dielectric spheres immersed in a conducting fluid. Upon applying a uniform electric field, each microsphere acquires a dipole moment opposed to the electric field that makes it rotate in a random direction. Since the particles have sedimented to the bottom surface, this rotation makes them self-propel on this surface (see Fig. 1.5b). The Quincke rotation is found to overcome the Brownian translational and rotational diffusion. Their interactions make the rollers align. In a periodic racetrack, the microspheres exhibit a flocking band. Again, this collective behavior is found to be similar to the Vicsek model. In different confinement, the system self-organize into vortex [101] similar to a fish school.
3. **Self-electrophoresis:** Asymmetrical flow around a particle is also a possible origin of self-propulsion. The flow can be driven by induced charge electroosmosis (ICEO) [102], which occurs at the conductive surface of the particle in electrolyte liquid. Due to the momentum conservation, the particle moves towards the opposite direction of the flow and such motion is known as induced charge electrophoresis (ICEP) [103]. One example of such mechanism is a system of half-metallic Janus particles under an AC electric field by Gangwal et al. [95], and Nishiguchi and Sano [104] (see Fig. 1.5c left). In both studies, the particles settle to the bottom and the electric field is applied perpendicular to the bottom plane. The particles self-propel on the plane and their reorientation is subjected to rotational Brownian motion. An extension of this system is demonstrated by Han et al. [105] using a rotational magnetic field to guide particle orientation which results in circular orbits. Alternatively, Dong et al. [96] demonstrated light induced self-electrophoresis of TiO_2 -Au microspheres in pure water upon UV radiation (see Fig. 1.5c right).
4. **Self-thermophoresis:** Colloidal particles can also move in a self-generated thermal gradient. This so called self-thermophoresis has been implemented by Jiang et al. [97]. They used half-metal Janus microspheres (immersed in water or dilute surfactant solution) under radiation of a defocused laser beam. Absorption of the light on the metal side induces a local temperature gradient around the particle. The gradient leads to thermophoresis and thus self-propulsion (see Fig. 1.5d).
5. **Self-diffusiophoresis:** A concentration gradient also makes self-propulsion possible. An asymmetric particle can produce a local concentration gradient, which is known as self-diffusiophoresis, by different engineering approaches. For example, Howse et al. [106] used latex-platinum microspheres in a solution of hydrogen peroxide (H_2O_2). The platinum end is a catalyst for the decomposition of H_2O_2 and this leads to local chemical gradient around the particles. The particles undergo a persistent random motion, which is the result from self-propulsion and Brownian rotational diffusion. Another system was proposed by Refs. [107, 108]. They used polymer microspheres with protruding

photoactive hematite cube. These particles immersed in H_2O_2 solution and the self-propulsion is made possible by photocatalytic decomposition of H_2O_2 at the hematite end triggered by blue light. Also, Volpe et al. [109] and Buttinoni et al. [98] used half-metal Janus microspheres in a critical mixture. With homogeneously illuminated light, self-propulsion occurs from local asymmetric demixing at the metal cap (see Fig. 1.5e).

6. **Self-electrophoresis + self-diffusiophoresis:** If two sides of particles are both metallic, they can exchange electrons between both sides and this leads to self-electrophoresis, which occurs together with self-diffusiophoresis. This concept was first introduced by Paxton et al. [110] using gold-platinum nanorods immersed in a H_2O_2 solution. Later on, bimetallic microspheres were developed in our team by Theurkauff et al. [10] and Ginot et al. [8]. Gold-platinum Janus microspheres are found to be more effective than a half-metallic sphere. This is a great benefit to investigate their collective behavior at high density without the overreaction of H_2O_2 decomposition, which is always a problem in many H_2O_2 -fuel swimmers as it produces O_2 bubbles easily. The surface reaction of a gold-platinum Janus rod/sphere in H_2O_2 solution is illustrated in Fig. 1.5f.

Despite the fact that this field of study has just emerged at the beginning of the 21st century, it has grown up very fast and is presently flourishing. At this point, one might ask why most of the abiotic active systems are micron-sized colloidal particles (5 out of 6 example mechanisms)? To answer this question, we have to trace back to the (passive) colloidal science, which has a longer history as it has been used as a model for statistical physics since the 18th-19th century. In the following section, I will present why colloids are suitable for this role. I will also introduce sedimentation experiments with passive and active colloids as those last ones formed the basis of the work developed during my thesis.

1.2 Colloidal particles and how they make statistical physics visible

Statistical physics is a powerful approach linking microscopic behavior to macroscopic properties of a material. It deals with the behavior of atoms or molecules, which have an energy scale of thermal energy. Although it was successfully used to describe bulk thermodynamic properties, there had been no direct evidence of the molecular microscopic behavior as we cannot ‘see’ them. Until 1909, Jean Perrin performed a sedimentation experiment [111] that demonstrated the first realization of colloids as big atoms [112]. Even though their sizes are not comparable with atoms/molecules, colloidal particles (typical size of a nanometer to micrometer scale) are found to be affected by thermal energy as well. The great benefit is that this size is large enough to be observed with a microscope.

1.2.1 Perrin’s sedimentation experiment of passive colloids

Perrin [111] performed the first sedimentation experiment of passive colloids under the gravitational field. At a stationary state, the top part of colloidal suspension displays an exponential density profile as the barometric distribution, i.e.,

$$\phi(z) \sim \exp[-mgz/k_{\text{B}}T_0], \quad (1.7)$$

where $\phi(z)$ is the colloids density function of altitude z , m is the buoyant mass of a particle, g is the gravitational acceleration, k_B is the Boltzmann's constant and T_0 is the Brownian temperature. The competition between gravity and diffusive motion of the colloidal particles, that leads to this exponential distribution, is called sedimentation-diffusion equilibrium. From Eq. 1.7, one can define the sedimentation length (alternatively, gravitational length) $\ell_g = k_B T_0 / mg$. A particle gains $k_B T_0$ in potential energy every ℓ_g against gravity. Perrin's experiments helped proving experimentally the statistical physics. In addition, it allowed a precise determination of Avogadro number.

Thanks to the development of computational techniques and equipment, experimental study of colloidal science has progressed a lot from counting tens of thousands of particles by hand (what Perrin did). Light scattering techniques allow to probe the structure and dynamics of colloidal suspensions. For example Piazza et al. [113] derived the equation of state of colloidal suspensions from density profiles obtained by light scattering. Fast cameras mounted on microscopes enabled scientists to access individual particle position via particle tracking, which was first established by Crocker and Grier [114]. More on particle tracking will be discussed in Section 3.1.

1.2.2 Sedimentation of active colloids

As mentioned before, active matter is a new path to out-of-equilibrium physics. With the same spirit as Perrin's experiment, Palacci et al. [7] investigated the sedimentation of active colloids using latex-platinum Janus particles powered by H_2O_2 . These colloids are self-propelled via self-diffusiophoresis and they exhibit higher propulsion speed with H_2O_2 concentration. Upon increasing H_2O_2 concentration, the sedimentation length is found to increase as well. In another H_2O_2 -fuel swimmer, Ginot et al. [8] performed an in-plane 2D sedimentation experiment with gold-platinum Janus particles (see Fig. 1.6). They related the exponential density profile (in the dilute limit) of the active sediment to the one of an ideal gas with an activity-dependent effective temperature T_{eff} , which had been presented analytically and numerically by Tailleur and Cates [115]. All of these investigations reveal that active colloids in the dilute limit behave like 'hot' colloids with effective temperature instead of the Brownian temperature.

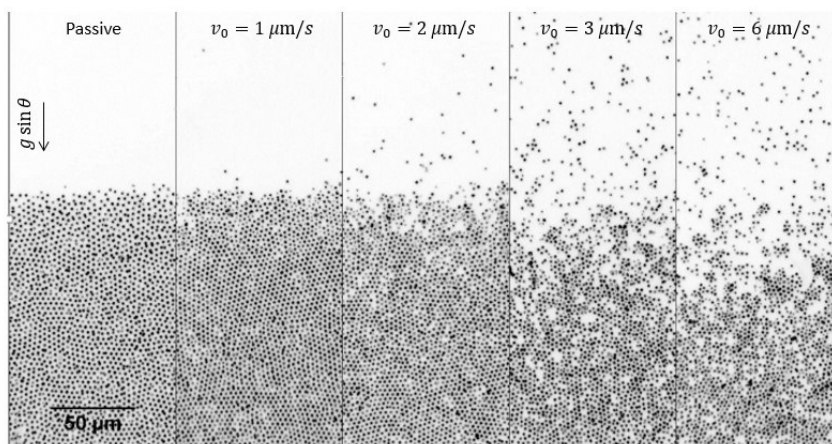


FIGURE 1.6: A snapshot from the in-plane sedimentation experiment of monolayer gold-platinum Janus particles. The hydrogen peroxide concentration increases from the left (passive) to the right. Image by Isaac Theurkauff.

The sedimentation experiment of active colloids shows a successful mapping from equilibrium to non-equilibrium physics at the low-density limit. There is still more space to explore at high density, in which particle-particle interaction plays an important role. How does a passive dense system respond to self-propulsion and does the mapping to equilibrium physics still holds? In the following, we will highlight experimental works on active dense systems.

1.3 Active dense systems in experiments

In the last decade, experimental studies on active matter in dense assemblies were limited to cells and tissues. Some non-trivial dynamics and many analogies with glass transition (will be presented shortly in Section 1.4) were observed [31, 61] (see Fig. 1.7a). However, in biological systems, cell density always changes during an experiment according to cell proliferation and death. Besides, there might be chemical signaling between cells. Therefore, they are not a perfect candidate for comparison with physical systems. Experimental investigations in a dense artificial active system have just emerged after I started my PhD in 2016. Here, I would like to discuss these very recent studies: what the specific point of each system is and what they have delivered.

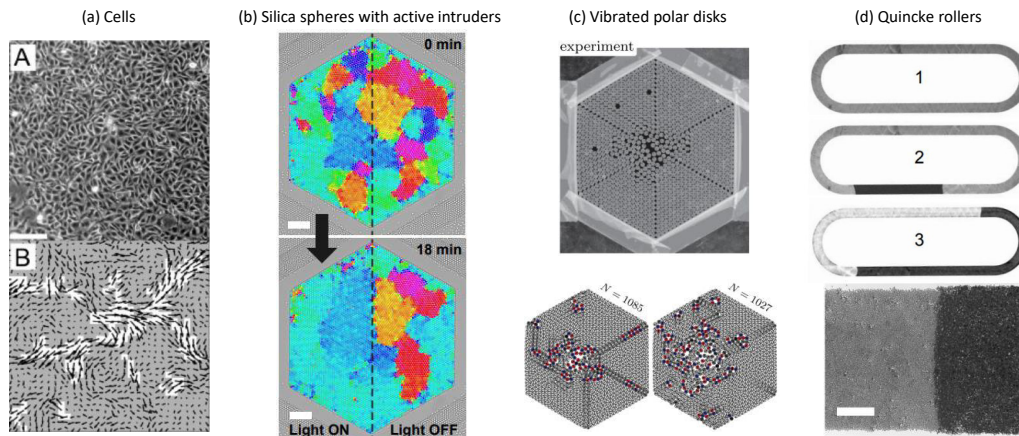


FIGURE 1.7: Highlight experimental work on active dense systems. (a) Glass-like cells dynamics. Retrieved from Ref. [31]. (b) Polycrystalline monolayer of silica spheres with a small fraction of light-activated active intruders. Scale bars: 50 μm . Retrieved from Ref. [116]. (c) Flowing 2D crystal of vibrated polar disks with alignment interaction. Modified from Ref. [117]. (d) A flock of Quincke rollers in a racetrack of density 0.38, 0.58 and 0.65, respectively. Below is a snapshot showing coexistence between a polar liquid and an amorphous active solid. Scale bar: 2 mm. Modified from Ref. [118].

A presence of a small fraction of active particles in a monolayer of passive particles shows faster rearrangement. Ramanarivo et al. [116] have demonstrated this using a monolayer of silica colloids initially organized in several small hexatic domains with different orientations (polycrystalline phase). Due to the thermal fluctuation, the system eventually organizes into a single orientation phase (single crystal). With the presence of small active intruders (light-activated particles [107]), the organization is dramatically accelerated. These intruders self-propel inside the system and readjust the boundaries of different orientations. This activity annealing takes place much faster than the thermal fluctuation alone (see Fig. 1.7b).

For a fully active system, Briand et al. [117] investigated a monodisperse assembly of vibrated polar disks [93, 99]. In their study, the polar disks are confined in a hexagonal arena (see Fig. 1.7c upper panel) and the passive counterpart of the system (isotropic disks) form perfectly hexatic arrangement. A frustration is induced by removing a few particles randomly. A loose and less ordered zone develops as more particles are removed (see Fig. 1.7c lower panel). Finally, the assembly of the polar disks spontaneously displays a macroscopic collective rotation while remaining in the crystalline structure, which they call *rheocrystal*.

In a microscopic system of Quincke rollers [94], Geyer et al. [118] have recently investigated the rollers propelling in a periodic racetrack at high density. These rollers have alignment interaction and thus promote the Vicsek flocking bands (polar liquid bands coexist with an isotropic gas) at low density. At higher densities but still not very dense, the systems exhibits a homogeneous polar liquid [119]. A traveling band of jammed solid, that they refer to an *active solid*, starts to emerge beyond a critical density. In this band, particle motion is more arrested and the collective motion is suppressed. The band propagates through the racetrack by continuously melting in the tail and solidifying in the front (see Fig. 1.7d). This is analogous to the propagation of a traffic jam. They also show that the active solidification is a first-order transition from the polar liquid.

None of the above studies has investigated a fully active dense system under significant thermal motion. Indeed, this is a key originality of my PhD. Before investigating how activity affects a dense system, let us address a classical picture we have for the passive counterpart.

1.4 Passive dense system with thermal agitation

At a high density, colloids are often used for a picture of the liquid-solid phase transition. Fig. 1.8 is a schematic representation of what occurs to a (molecular) liquid as temperature decreases (retrieved from Ref. [120]). As the liquid is cooled down, the molecules lose their kinetic energy, which results in slower motion. In an equilibrium pathway, liquid molecules organize in an ordered structure and thus a liquid becomes a *crystal* at a certain temperature, T_m (melting point). However, in some conditions, the crystallization is avoided and a liquid phase still exists below T_m . This state is called a *supercooled liquid*. If we further cooled down the supercooled liquid, the system relaxation time dramatically grows by several orders of magnitude, until the point where the relaxation time exceeds our experimental time (or our patience). We call the system in this state a *glass* and its corresponding transition point is called *glass transition temperature* T_g .

This phase diagram is also true if we compress the system instead of cooling it. One of the most important models is hard-sphere particles. Fig. 1.9 illustrates an equivalent phase diagram to Fig. 1.8 using colloidal particles density as a control parameter. Pusey and Mejen [121] were the first who experimented with hard sphere-like colloidal particles and demonstrated the phase diagram. By varying a concentration of stabilized PMMA particles in a refractive index-matched solvent, they could show the phase behavior from fluid, coexistence (fluid+crystal), crystal and glass (see Fig. 1.10).

To make the system choose the non-equilibrium cooling path, crystallization must be avoided. For colloidal systems, this can be done by mixing two sizes of particles or use a polydisperse (broad distribution of sizes) sample [122, 123]. For molecular glass formers, crystallization is prevented by fast quenching or mixing

of species that do not easily crystallize together. In the following, I will review the general features of both cooling paths: equilibrium path of crystallization and non-equilibrium path of supercooled liquid to glass. We will mention either temperature T or particle density ϕ as a control parameter depending on the example that we are talking about (either molecular or colloidal system).

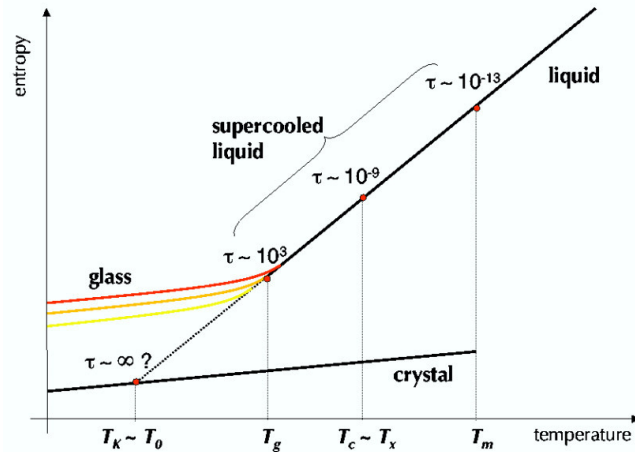


FIGURE 1.8: Schematic plot of entropy versus temperature ranging from liquid to glass or crystal. In the equilibrium pathway, a liquid becomes a crystal via the first-order phase transition at melting temperature T_m . In the nonequilibrium situation, a liquid remains below T_m and this state is called a supercooled liquid. A supercooled liquid turns to glass at T_g , a glass transition point, when the relaxation time exceeds experimental time. The diagram is retrieved from Ref. [120].

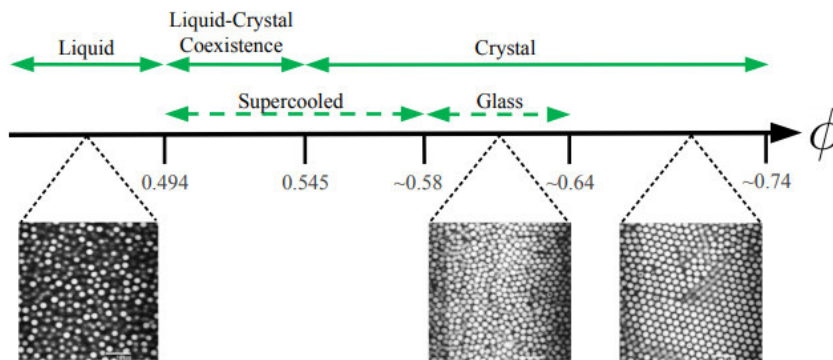


FIGURE 1.9: Phase diagram of colloidal hard spheres as a function of volume fraction ϕ . The equilibrium path, which is the case of monodisperse particles, is indicated by solid arrows. The non-equilibrium path, which requires polydispersity, is displayed by dashed arrows. The diagram is retrieved from Ref. [124].

1.4.1 Equilibrium path: crystalline, hexatic and polycrystalline phases

The phase transition of hard spheres from liquid to crystalline is non-trivial (long debate since the 1950s until 2010s) and depends on spatial dimensions. In 3D, it has been observed in simulations [126, 127] and experiments [121] of colloidal hard spheres that the melting is first-order. Nevertheless, it is more complicated for a 2D system. Mermin and Wagner [128] stated that a 2D system at finite temperature cannot form a crystal due to the thermal fluctuation, which was at odds with



FIGURE 1.10: Phase behavior of colloidal hard spheres. Suspension of PMMA particles in a range of densities (increasing from left to right). The suspensions were shone by white light and they exhibited different diffraction patterns in the next few days indicating the crystallization and glass formation at different densities. The image is modified from Ref. [125] (original figure from Ref. [121]).

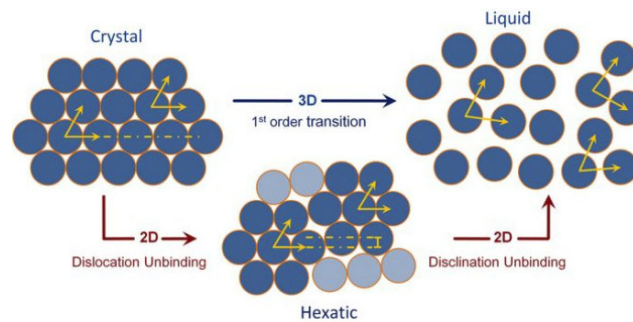


FIGURE 1.11: A schematic drawing showing the melting scenario in 3D and 2D. Retrieved from Ref. [137].

Alder and Wainwright [129] who had reported liquid-solid transition in a hard disks system. It was a long debate [130] on whether the 2D melting is one step via a first-order transition [131] or two steps composed of crystal-hexatic and hexatic-liquid transitions, which are both continuous. The latter scenario is widely known as the Kosterlitz-Thouless-Halperin-Nelson-Young (KTHNY) scenario [132, 133, 134]. The debate was ended by Bernard and Krauth [135]. In numerical simulation, they revealed that the 2D melting is two steps with a continuous liquid-hexatic transition and a first-order hexatic-crystal transition. Later on, this simulation evidence was supported by the experiment of a monolayer of colloidal hard spheres from Thorneywork et al. [136] using an in-plane sedimentation experiment of colloidal hard spheres.

Fig. 1.11 illustrates the summarized phase transition scenario in both 2D and 3D. In a crystal, the microscopic structure is a periodic lattice and thus the atoms/molecules are well-localized [138]. The system positional and bond orientational orders are both long-range (Fig. 1.11, yellow horizontal lines and arrows, respectively). In 2D, there is an intermediate phase between the crystal and the liquid called the *hexatic* phase. The long-range translational order is lost during this transition and only remains the long-range bond orientational order. Finally, the second transition to

liquid destroys the long range orientational correlation.

A system with defects would not form a single crystal, but rather a *polycrystalline* state which consists of several crystalline subdomains called grains. Besides, the defects are accumulated at the grain boundaries [139]. Unlike the hexatic phase where the bond orientation continuously changes in space, a polycrystalline contains well-defined grain boundaries between two grains of different orientations (for example, see Fig. 1.7b upper panel).

1.4.2 Nonequilibrium path: from supercooled to glass

The glass transition

In the nonequilibrium cooling path, the liquid is *supercooled* below melting temperature T_m . At this state, if we further cool the liquid, the relaxation time τ (or viscosity η) increases dramatically upon a slight drop in temperature T (or slightly increase in density for a colloidal system). Until a temperature such that the system cannot equilibrate within a reasonable time, it arrests in an amorphous solid state called a *glass*. The transition between the supercooled liquid to a glass is called the *glass transition*, which occurs at a glass transition temperature T_g (or a glass transition density ϕ_g for a colloidal glass). Fig. 1.12 shows the significant growth of viscosity upon decreasing temperature in different glass formers. This plot is known as Angell plot. The dependence of viscosity on temperature is characterized by fragility: a higher fragility, a steeper dependency. The temperature is scaled by T_g , which is system-dependent and conventionally defined as the temperature that gives a viscosity of about 10^{13} Pa s [140]. To have an idea of how slow glass formers can be compared to human patience, let us consider the world's longest-running experiment of the pitch drop [141]. The experiment was set in 1927 by pouring warmed pitch into a sealed stem glass funnel. Three years later, the sealed end was cut to allow the pitch to flow. The first pitch drop was observed eight years later after the cut. In 1984, from the six pitch drops during over 50 years, the viscosity of pitch could be estimated to be $10^6 - 10^8$ Pa s. The experiment is still going on until now, and there has been a total of nine drops so far.

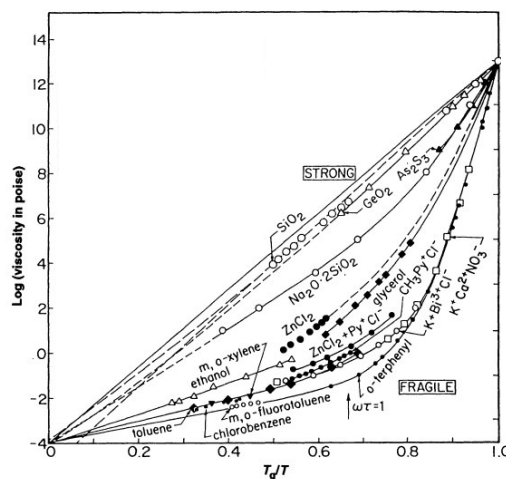


FIGURE 1.12: Angell plot: Logarithm of viscosity function of inversed temperature in different substances. Modified from Ref. [142].

Relaxation time

One can understand the slowing down of system dynamics by considering the energy landscape [143, 144, 145]. Fig. 1.13 is a schematic illustration of an energy landscape. The global minimum point is a crystal, which is the equilibrium situation. In a liquid state, the system has enough free energy to explore the whole phase space (by rearranging). In other words, the system is *ergodic*. Cooling down the system makes it more difficult to hop around different basins. As long as it can explore the phase space, the system is still ergodic and can be understood as a supercooled phase. Below a certain temperature, the system does not have enough free energy to pass the energy barrier, it is thus stuck in one basin. This is the point where $T < T_g$ and it results in a *non-ergodic* glass state.

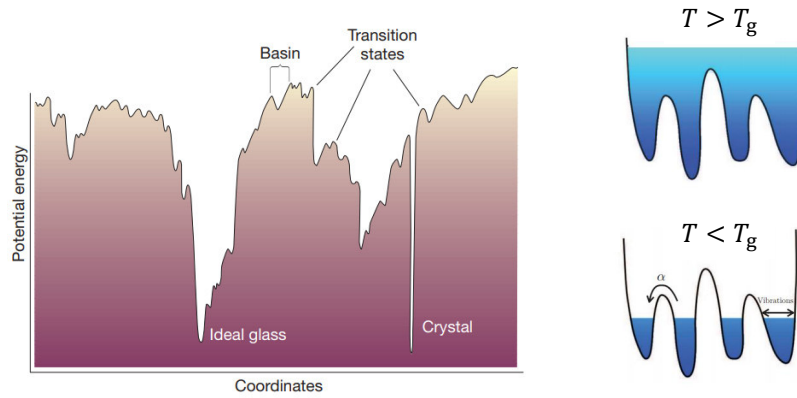


FIGURE 1.13: (Left) Schematic illustration of an energy landscape showing the true minimum state of crystal and the low energy point where the glass is trapped. Retrieved from Ref. [144]. (Right) Schematic illustration of (above) the liquid state where the system has enough energy to explore the energy landscape and (below) the glass state where the system is trapped in basins and required additional energy to jump to explore other states. Retrieved and modified from Ref. [145].

The *relaxation time* τ is the time needed to jump over a barrier of fixed height ΔE function of temperature, and it is expressed by an Arrhenius expression:

$$\tau \sim \exp[\Delta E/k_B T_0]. \quad (1.8)$$

An Arrhenius temperature dependence of the relaxation time corresponds to a straight line in the Angell's plot. However, many systems display a steeper dependence of the relaxation time (or viscosity) than Arrhenius. It means that those systems have a temperature-dependent energy barrier. We can interpret from the Angell's plot that the closer T to T_g , the larger $\Delta E(T)$ to cross. For these non-Arrhenius systems, the relaxation time is rather fitted with the Vogel-Tamman-Fulcher (VTF) form [146, 147, 148]:

$$\tau \sim \exp[A/(T - T_g)], \quad (1.9)$$

where A is a constant and T_g is a glass transition temperature. Equivalently, in a colloidal system, the relaxation time τ and density ϕ also follow the VTF relaxation. For hard sphere colloids, τ is found to diverge at ϕ_g [149]. However, for soft sphere colloids, one can observe a saturation of τ at $\phi > \phi_g$ [150] (see Fig. 1.14).

There are still a lot of unanswered questions on the glass transition scenario. The glass transition point (T_g or ϕ_g) is not well-defined and appears to be a broad range. Apart from that, looking at structure changing from supercooled to glass, we

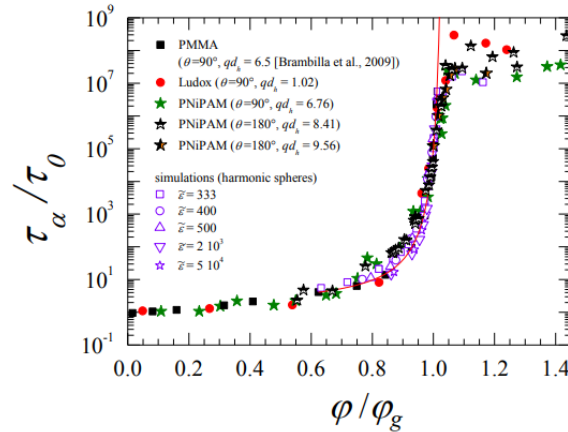


FIGURE 1.14: Rescaled relaxation time versus volume fraction of soft particles (both experiments and simulations) and PMMA hard spheres. The red solid line corresponds to the Vogel-Tamman-Fulcher form. Retrieved from Ref. [150].

cannot notice any particular change at the glass transition. ‘What happens at the glass transition?’ is still an open question although our theoretical understanding has tremendously progressed in the last decade. One promising approach is to probe the glass transition via rheology.

Rheological investigation near the glass transition

When approaching the glass transition, apart from the dramatically increase of relaxation, one can also notice a change in rheological response which is displayed by a *flow curve*: the dependence of the shear stress σ on the shear rate $\dot{\gamma}$. Petekidis et al. [151] have measured the flow curves of a suspension of PMMA hard spheres at various densities across the glass transition ϕ_g (see Fig. 1.15a). For $\phi \leq 0.4$, the flow curves exhibit a linear trend indicating the Newtonian regime such that $\sigma = \eta \dot{\gamma}$, where η is a constant viscosity. As ϕ approaches to $\phi_g \approx 0.58$, the system becomes more and more non-Newtonian as the limit of σ when $\dot{\gamma} \rightarrow 0$ is nonzero. This gives a clue of the emergence of solid mechanical behavior when the glass transition is crossed. In most glassy systems, the flow curve in the glass regime fits well with the Herschel-Bulkley model [152, 153]: $\sigma = \sigma_y + K \dot{\gamma}^n$ for $\sigma \geq \sigma_y$, where σ_y is the yield stress, K and n are model parameters. This fit indicates both the yield stress and shear-thinning regimes.

1.5 How self-propulsion influences dense systems?

Previously, we have seen that dense passive (thermal) systems have been extensively studied especially in the framework of glass transition, which is still a challenging phenomenon. From this point, we will combine the field of active matter with glassy physics by making each particle in the dense system become self-propelled. The main question is “how would the self-propulsion affect the system relaxation on both sides of the glass transition?”. Before my PhD, these questions had been investigated only by few numerical works. In this section, I will briefly review what had been learned so far. I will also review progresses that occurred during my PhD. Therefore, some of the following works are relatively new and the field of study has not yet settled.

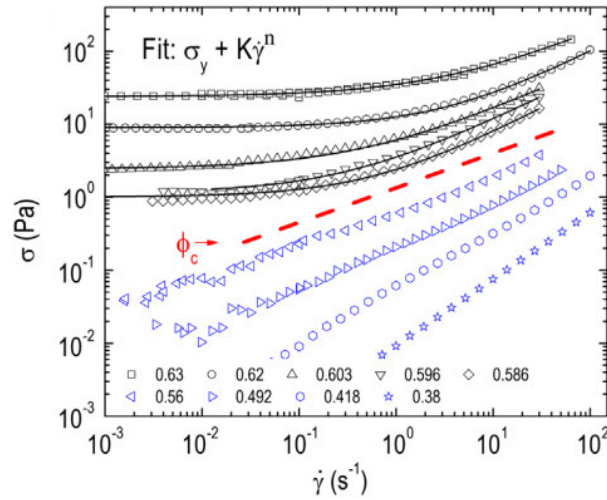


FIGURE 1.15: Flow curves of PMMA hard spheres colloids at various densities. The yield stress emerges above ϕ_g . The solid line is the fit with the Herschel-Bulkley model. Retrieved and modified from Ref. [153] (original from Ref. [151]).

1.5.1 Simulation works

As mentioned in Subsection 1.1.2, there are three main models for active particles. Since we are more interested in the role of self-propulsion in molecular dynamics at high density, I will only discuss the ABP and AOUP models without an alignment interaction. The ABP model was first used at the early stage. Bialké et al. [154] studied the 2D crystallization of repulsive active Brownian particles and showed that the freezing density significantly shifts towards higher values as the self-propulsion force increases. Later on, Digregorio et al. [155] investigated the full activity-density phase diagram of ABP models shown in Fig. 1.16a. They could recover the two-step melting scenario at zero activity. They also successfully identified the MIPS area (grey region) at high enough activity expanding a wide range of density. At finite activity and high density, the phase diagram shows the transition from liquid (white area) to active hexatic (blue area) and then to active solid phases (orange area). Similarly to Bialké et al. [154], the transitions shift to higher densities as the activity increases.

For the non-equilibrium path, Fily et al. [156] explored the density-temperature phase diagram using ABP model with soft repulsive potential. Instead of using monodisperse particles like Ref. [154, 155], they use polydisperse particles to avoid the crystallization. Fig. 1.16b is their resulting phase diagram. They identified the phase separation regime and the glass phase, which appears at high density but low self-propulsion speed. Nevertheless, the glassy dynamics and the change in the structure was not studied in detail. The approach to the glass transition was studied by Ni et al. [157]. They reported a shift of the glass transition towards higher densities as the self-propulsion force f or the Brownian reorientation time $\tau_R = 1/D_R$ increases.

A related topic is the study of the glass transition that occurs in athermal (no Brownian motion) active particles and its comparison with the thermal passive case. Berthier and Kurchan [158] have shown theoretically that athermal active suspension can undergo a dynamic arrest at high density, which is qualitatively analogous to the equilibrium glass transition. With a Monte Carlo simulation of self-propelled

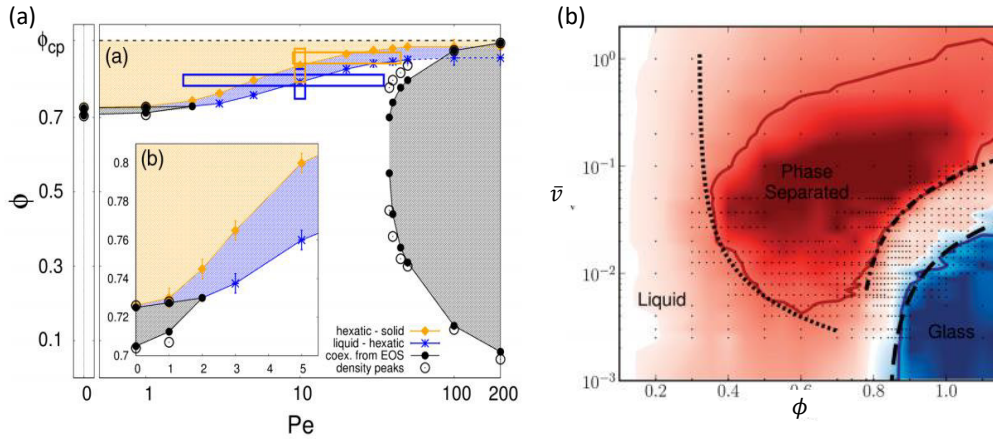


FIGURE 1.16: (a) Phase diagram of self-propelled hard disks showing liquid (white), liquid-hexatic coexistence phase (grey), active hexatic (blue) and active solid (orange) phases. Retrieved from Ref. [155]. (b) Phase diagram of polydisperse self-propelled particles showing the liquid, phase-separated and glass phases. Retrieved from Ref. [156].

hard disks whose self-propulsion is tuned by a persistence time τ_p [84], Berthier [159] showed that the glass transition is shifted toward higher densities when τ_p increases, which is in agreement with the ABP model by Ni et al. [157]. However, various athermal models have shown different outcomes. With the athermal AOUP simulation of the Kob-Anderson (KA) binary mixture [122], where particle motion is governed by an effective temperature T_{eff} and a persistence time τ_p , Szamel et al. [80] surprisingly found a non-monotonic response to an increase of τ_p at a finite T_{eff} : the relaxation first speeds up and then slows down. Later on, the same authors have shown that the nonmonotonicity disappears when the relaxation time is rescaled by high-temperature behavior [160] and it results in slower relaxation as τ_p increases. This is because the fragility (departure from Arrhenius behavior) increases with increasing τ_p . Finally, this group of authors has shown that activity can both promote or delay glassy dynamics depending on the initial state point. Using the AOUP model with a short-range repulsive potential [161], they have demonstrated that the glass transition line moves in a non-trivial way [162] as presented in Fig. 1.17. At low T_{eff} , increasing τ_p would shift ϕ_g towards higher density (activity delays glassy dynamics), while the trend is opposite at high T_{eff} . This shows that "activity" is not uniquely defined and one has to be careful about the respective role of T_{eff} and τ_p . Nevertheless, in all cases, the phenomenology in the active glass state is reported as the same as the equilibrium glass [160, 162]. In addition, a recent theoretical work from Nandi et al. [163] has shown that the microscopic details of the numerical model of active particles can yield completely different results.

Table. 1.1 summarizes predictions of glass transition density upon increasing activity. Due to the diversity of model particle and activity, it is thus a perfect time to carry out experiments on a real system to constrain numerical models and theories, and this is therefore the objective of my PhD.

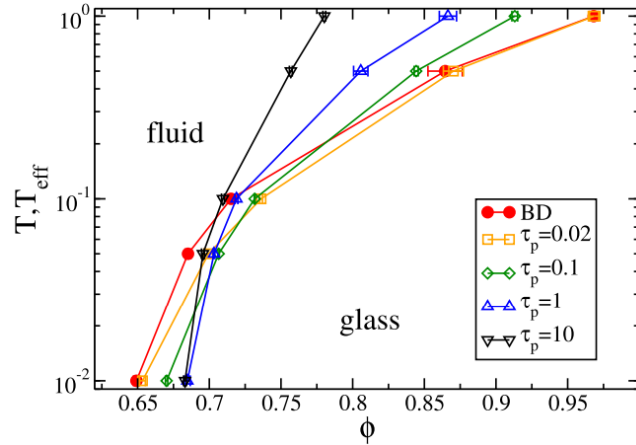


FIGURE 1.17: Fluid-glass phase diagram showing the evolution of the glass transition line upon τ_p . Retrieved from Ref. [162].

	Role of activity
Ni et al. [157] (ABP)	$\phi_g(\tau_p) \nearrow$ or $\phi_g(f) \nearrow$
Berthier [159] (Athermal MC)	$\phi_g(\tau_p) \nearrow$
Berthier et al. [162] (AOUP-WCA)	$\phi_g(\tau_p) \nearrow$ or $\phi_g(\tau_p) \searrow$ depending on T_{eff}
Nandi et al. [163] (theory)	depending on microscopic detail of model activity.

TABLE 1.1: Table summarizing the simulations on dense active systems focusing on the liquid-glass transition. MC = Monte Carlo simulation, WCA = Weeks–Chandler–Andersen potential [161].

1.6 Objectives

The field of active matter has emerged in the last decades and grown up very fast. Inspired by natural active matter, the artificial active system has been a new playground for physicists to probe and build new tools for out-of-equilibrium systems. A few years ago, a successful mapping from equilibrium statistical physics to the sedimentation of self-propelled colloids has been shown. This mapping reveals that active colloids at low density behave like ‘hot’ colloids with activity-dependent effective temperature. Nevertheless, we do not know if this mapping is valid at high densities, for which various numerical models have yielded different outcomes. Therefore, it is the perfect time to start the investigation of dense active systems by experiments. The aims of my PhD would be:

1. to perform experiments on active colloids at high density.
2. to investigate the system spontaneous dynamics upon tuning the activity level.
3. to analyze the result in a framework of glassy physics and compare it to the equilibrium counterpart.
4. to consider the system of crowded active colloids as a new kind of material in order to study it via a microrheology approach.

1.7 Thesis outline

This thesis is divided into seven chapters including the present introduction chapter. In Chapter 2, I will introduce experimental materials and methods. I will describe the active colloids that we used and how we prepared them. This chapter also contains the characterization of particle motion at the low-density regime. This chapter will end with possible alternative active colloids, which could be interesting for further works.

Chapter 3 presents the analysis tools that I have used and developed during my PhD. Dealing with a high-density regime, algorithms that were used by the previous PhD student and the original tracking package both caused a memory overload issue. I have developed scripts to deal with big data for particle tracking and analysis. The technical detail of the analysis tools provided in this chapter will be useful for the next three chapters. From time to time, I will have to recall the analysis tools introduced in this chapter.

Chapter 4 is the key point of the thesis, the experimental investigation of dense assemblies of active colloids. I will start the chapter by introducing our experimental setup to create a dense assembly and what to be concerned with. Then, I will focus on the dense part of the sediment and present our first observation on a non-monotonic response with activity level. The next parts of the chapter are dedicated to our careful characterization and analysis of such non-trivial behavior. The characterization starts with the measurement of the effective temperature and density. Then, we investigate the system relaxation as a function of density using another set of experiments to identify the density at which the non-monotonic behavior takes place. After that, we will discuss the relaxation dynamics at different activity levels using a new correlation length, that we defined from the particle orientation displacement. The chapter ends with our proposed analytic model explaining the origin of the non-monotonic behavior.

Chapter 5 will be a step towards microrheology. In this chapter, I describe two different experimental approaches and the corresponding results, as well as the development of a new home-made setup that would enable a third approach. The first approach consists in oscillatory microrheology in which we put a probe particle inside the colloidal sediment and control its motion using optical tweezers. I will discuss our setup and analysis within a framework of small amplitude oscillatory shear. The second approach is gravity-induced constant force microrheology. We investigated the creep motion of a probe pulled by gravity through the sediment. I will present an analysis of the observation on the probe trajectory followed by a supporting explanation from colloidal trajectories. Then, I will discuss our extended statistical analysis of the particle network. The final part of the chapter is a perspective towards a home-made magnetic microrheometer. I will present my contribution in the development of this setup.

Chapter 6 describes the simulation approach I have developed. This is an additional work with respect to the experimental core of my PhD. I will first present a simulation model of active Brownian particles and relevant simulation techniques. After that, I will discuss my simulation results ordered by density: dilute limit (individual motion), intermediate densities approaching the glass transition and then above the glass transition, where we investigate the aging dynamics of the system with a quenching simulation.

In Chapter 7, which is the last one, I will conclude all of my PhD work and also provide some perspectives for future studies.

Chapter 2

Experimental configuration and characterization in a dilute regime

In this chapter, I will describe the active colloids and the general experimental setup I used during my PhD with the characterization of our active colloids in a dilute regime. I will discuss how we investigated the particle motion, in both passive and active cases, and how we quantified the activity level. After that, I will present the preliminary results of our attempt to make an alternative Janus particle. The content of this chapter is a bit technical and full of detailed information, which could be interesting for those who want to reproduce the experiments.

2.1 Active Colloids

Before my PhD, there have been active colloids studies in our group. Starting with the latex-platinum Janus microspheres that self-propel in H_2O_2 solution [106], our lab had performed the first sedimentation experiment on such active colloids [7]. This study shows that in dilute limit, active systems can be mapped onto passive systems through an effective temperature. However, these latex-platinum particles are not suitable to study collective behavior at a high particle density. This is because they require high H_2O_2 concentration to move and this lead to overproduction of O_2 when there are too many latex-platinum particles in the system. Due to this excess O_2 bubbles nucleate, the particle motion is ruined dramatically. Therefore, it was necessary to find a new active system to investigate high density dynamics.

2.1.1 Gold-platinum Janus particle

Inspired by gold-platinum rod-like swimmers [110], the previous PhD students in the group had successfully developed gold-platinum Janus microspheres which are found to be much more efficient than the latex core Janus particle¹. Besides, these new active particles are heavy. When they are immersed in water, they settle down to the bottom of an experimental chamber. They do not leave the surface even when they are activated (if the activity is not too high²), instead, they perform a 2D persistent random motion. From these reasons, the gold-platinum Janus particles are very suitable to study collective behavior in 2D. For example, at area fraction between 5% – 10%, dynamic clustering emerges [10, 11]. Furthermore, studying suspensions of such active colloids is a way to probe the nonequilibrium equation of state, which

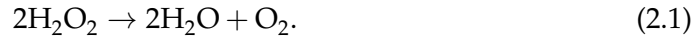
¹From our gold-platinum Janus particles, we obtained the propulsion velocity $\sim 2.5 \mu\text{m s}^{-1}$ at H_2O_2 concentration of $\sim 10^{-2}\%$, while the latex core Janus particles of Ref. [106] need about 5% concentration to achieve the same propulsion velocity.

²We observed their 3D motion at high H_2O_2 concentration as the same level as when the O_2 bubbles emerge.

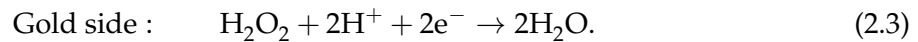
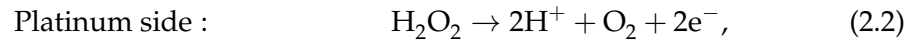
is found to be equivalent to an equilibrium system with effective adhesion [8]. These active particles are perfectly fitted to study the behavior of active systems in the dense regime, which is the focus of my PhD.

Propulsion mechanism

Since Paxton et al. [110] had introduced the gold-platinum rod-like swimmers, there have been many discussions on their propulsion mechanisms until now. Although all of the arguments share the same net decomposition of H_2O_2 ,



the key explanations of the propulsion force differ. In the original paper [110], Paxton et al. proposed that the driving force originates from the interfacial tension gradient according to the O_2 produced at the platinum end. Their model can predict nicely the propulsion speed, but not the moving direction (experimentally, they observed platinum end forwards). Later on, an electrokinetic mechanism was also taken into account which leads to the statement of asymmetric decomposition on platinum and gold surfaces [164, 165],



This description can successfully predict the moving direction of the bimetallic rod-like swimmers [166]. The bimetallic rod is considered as a galvanic cell where the platinum side is an anode (oxidation) and the gold side is a cathode (reduction). With this model, the movement of protons (H^+) from platinum to gold occurs in the electrical double layer around the surface of the rod (while the electrons moves inside the conductive rod). Such movement leads to an electroosmotic flow in the same direction as the proton migration, which results in the net motion of the rod towards platinum side [167]. In short, the propulsion mechanism of such bimetallic particles is governed by self-electrophoresis.

For platinum-coated Janus spheres, the propulsion mechanism is also governed by the same concept as in the bimetallic rod. In the case of an insulating core (e.g. polystyrene), the ionic flow can occur between the equator and pole of the platinum hemisphere cap [168]. In our case of a gold particle half-coated with platinum, electrons can move through the conductive core so that the surface chemical reactions take place on both sides (see Fig. 2.1) which induces the ionic flow around the sphere. As a result, the particle self-propels due to the self-electrophoresis and the self-diffusiophoresis.

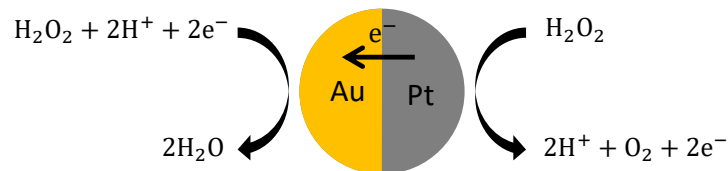


FIGURE 2.1: Schematic representation of the chemical surface reactions of a gold-platinum Janus particle in a solution of H_2O_2 . In our system, we see that the particle self-propels with the gold side forward.

Nevertheless, the description of the propulsion mechanism is found to be much more complex than only the surface reaction and the self-electrophoresis. The theoretical study of the self-propulsion in water shows that when the bulk reaction is taken into account, the prediction of the propulsion speed is significantly influenced [169]. Actually, an other recent study suggests to take into account the momentum from the reaction as well [170]. Moreover, the geometry and the surface properties of the particle also greatly influences the propulsion direction [171, 172]. Until now the underlying mechanism is not yet fully understood in the community.

2.1.2 Making of the gold-platinum Janus particle

The making of our gold-platinum particle starts from a pure gold particle as a core. Then, a thin layer of platinum is deposited on top of the gold particles and creates a hemisphere of platinum on one side, while the bottom part remains uncovered that is an exposed gold surface. In this section, we describe our synthesis procedure step-by-step and discuss some important points.

Gold particles

The first thing to be considered is the particle size. Since we want to observe the particles with an optical microscope, particles smaller than $1\ \mu\text{m}$ give a poor resolution and lead to errors on locating particle positions, especially when particles are close together [114]. Conversely, if the size is too large, the particles would not be affected by thermal agitation, which is the main ingredient in glassy dynamics of a dense system. Continuing from the work of the previous PhD student, Félix Ginot, we use gold microcarriers from Bio-Rad (ref. #1652264, see Fig. 2.2a) which have a diameter of $1.6\ \mu\text{m}$ and 10% of polydispersity (estimated by a scanning electron microscope, SEM). These gold particles are very suitable to make Janus particles when considering the size and polydispersity aspects.

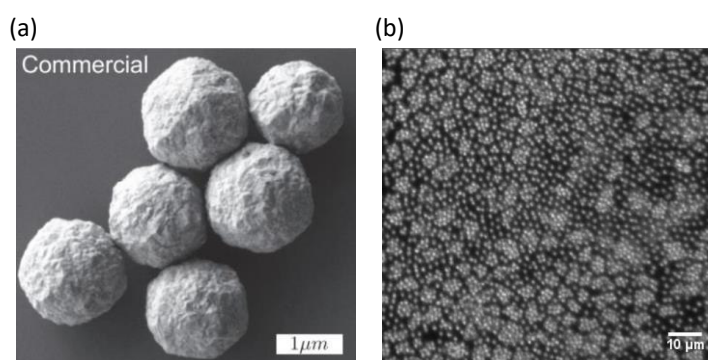


FIGURE 2.2: (a) The SEM image of the gold microcarriers from Bio-Rad (ref. #1652264) that we use to make Janus particles. Image by Félix Ginot and Rémy Fulcrand. (b) Optical image of the gold microcarriers from Bio-Rad before the filtration for the monomers. The sample is full of aggregates.

The only but important problem with the gold microcarriers from Bio-Rad is that the commercial products contains many aggregated clusters. Fig. 2.2b shows how these particles look under an optical microscope. There are many aggregated particles that are physically attached. Of course, we want only individual particles. The previous PhD student, Félix Ginot, had already proposed a selection procedure using the concept of sedimentation, which I also used during my PhD work. This

procedure is very simple and effective, however, it requires a lot of time (about one week) to have a sufficient amount of the individual particles. In my second year, I have found an alternative selection procedure from Ref. [173]. (In their work, they use the gold-platinum Janus particles in an engineering purpose. They have shown that these self-propelled Janus particles can be used to repair the electrical conductivity of a tiny electronic circuit.) Herein, the gold particle is capped by octadecanethiol. This procedure is much faster and it gives a significantly higher amount of products. Nevertheless, we are aware that the additional octadecanethiol should change surface properties of the gold particle, and thus affects the self-propulsion mechanisms and particle-particle interaction. To be able to compare with the results from my first year without any doubt, we continue using the first selection procedure of the simple sedimentation. We hope that after a characterization and then a comparison between the two procedures, the second procedure should shorten the selection time, approximately from one week to two days, and indeed will speed up the future work. In the following, I will describe both selection procedures and discuss their positive and negative points separately.

The first procedure, as mentioned above, is the sedimentation sorting. First we put about 5 mg of gold particles in 3 ml of isopropanol (C_3H_8O) contained in a flat bottom glass tube. We try to split the aggregates as much as we can by sonicating up to 3 min and then we wait for 1 min to let most of the big aggregates fall to the bottom. Then, we suck 1 ml of the upper part of the solution and put it in a new tube that already contains 3 ml of isopropanol. In this new tube, there are still many clusters, but only the smaller ones (clusters that are composed of 10 particles maximum). For the finer sorting, we sonicate the new tube for about 10 s (just to mix the solution) and then let the particle settle before collecting again the upper part. This time, we want to collect the individual gold particles. We thus estimate the waiting time and the amount of the solution to be collected from the sedimentation speed v_{sedim} obtained from Stokes' law,

$$v_{\text{sedim}} = \frac{\Delta\rho g \sigma^2}{18\eta}, \quad (2.4)$$

where $\Delta\rho = 19 \times 10^3 \text{ kg m}^{-3}$ is the density difference between gold and isopropanol, $g = 9.8 \text{ m s}^{-2}$ is the gravitational acceleration, $\eta = 2 \times 10^{-3} \text{ Pa s}$ is the viscosity of isopropanol at 25°C and $\sigma = 1.6 \mu\text{m}$ is the particle diameter. With this estimation, the sedimentation speed of an individual gold particle is $v_{\text{sedim}} \approx 13 \mu\text{m s}^{-1}$. Therefore, it should fall of 0.4 cm in 5 min. Comparing to a doublet which falls approximately 2 cm in 5 min, we decide to collect the upper solution of 1 cm after 5 min of waiting. This is equivalent to 1 ml. In practice, however, we still find some small aggregates (less than 5 particles) even when we wait up to 10 min. We guess that the hydrodynamic suction is strong enough to get the particles from the deeper part. We, therefore, have to suck the solution very gently to minimize this effect. We collect the upper solution in a new tube and add 1 ml of isopropanol in the previous tube to maintain the total volume. We have to repeat the fine sorting process more than 40 times to get a sufficient amount of gold particles. The final result is very satisfying, but as mentioned, the process is very time-consuming. Moreover, we lose most of the particles in the form of aggregates from this procedure.

In the alternative procedure that is used in Ref. [173], the aggregates are separated and the individual gold particles are capped by octadecanethiol (ODT, $C_{18}H_{38}S$). ODT is a hydrocarbon chain that has a thiol group (-SH) at one end. This end has a strong attraction to metal surface including gold and thus results in self-assembly of

a monolayer around a gold particle with the hydrocarbon tail pointing away. Here we immerse the gold particles (after they are sonicated for 30 min to brake the aggregates) in 0.5 mM ODT in absolute ethanol for 30 min. After that, we remove the supernatant and washed four times with distilled water. After each wash, we sonicate the solution for 30 min and let the particles settle for at least 30 min. The compared results between the control batch (without ODT) and the batch that has been immersed in ODT is shown in Fig. 2.3. Strikingly, there is no more large aggregates and most of the particles are individual. With only a little bit of filtration (e.g. sedimentation sorting), this batch is indeed ready for use. This procedure can be done within one day and it has much higher amount of products than the previous procedure. We have already tried making Janus particles from these gold particles and found that they become self-propel upon adding H_2O_2 . Their persistent random motion is qualitatively similar to the one from the first sorting procedure. However, we are not sure of how the additional of ODT on the gold surface will affect the propulsion mechanisms at the molecular scale. In order to be able to compare our results with Ginot's and to ensure consistency throughout my PhD, all results presented hereafter have been obtained from particles filtered through the first procedure. With a further characterization of the particle motion and interaction, we hope that we can save a lot of time for the filtration process in the future work.

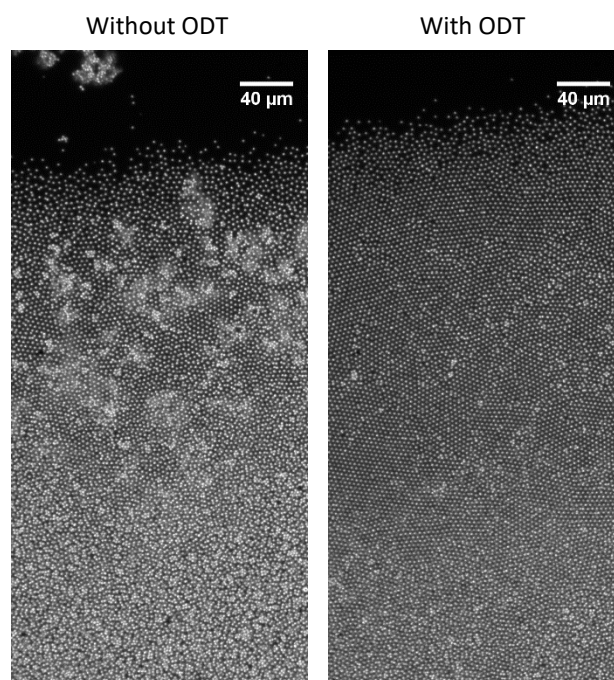


FIGURE 2.3: The result of the capping protocol using in Ref. [173]. (left) A control batch without the additional of ODT. (right) The batch that has been immersed in 0.5 mM ODT.

Platinum deposition and detachment of the Janus particles

At this step, the gold particles are now immersed in isopropanol. To prepare them for the platinum deposition, we need to deposit them onto a glass slide. This is simply done by tilting a 52 mm \times 75 mm glass slide (about 20°) and slowly injecting 200 μ l of dilute gold particles in isopropanol solution on the upper part of the glass slide. The goal of this step is to spread the colloids all over the glass slide (see Fig. 2.4

step 1). This step is crucial because if the colloids are too dense and too close to each other, they will be linked together after the platinum deposition and this will be a defect of the sample.

To make the platinum half, we coat a thin layer (20 nm) of platinum on the glass slide using the electron beam evaporation technique. The deposition rate is suggested to be as slow as possible (in our case, it is between 0.1 to 0.3 \AA s^{-1}) for the platinum layer to hold strongly on the gold surface. The platinum deposition was done by Nicolas Terrier (Institut des nanotechnologies de Lyon) and Rémy Fulcrand (liquides et interfaces, iLM), and it corresponds to step 2 in Fig. 2.4. With this deposition technique, the platinum ions approach the glass slide vertically and should cover only the top hemisphere of the gold particle. This is unlike the sputter deposition, which is the other popular deposition technique, where the platinum ions can go in any direction and possibly cover the lower hemisphere as well.

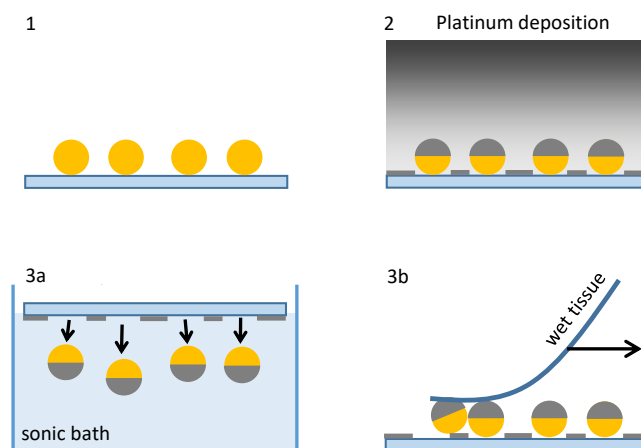


FIGURE 2.4: Schematic representation the making of our gold-platinum Janus particle. Step 1: Deposition of the gold particles on a glass slide. Step 2: Platinum deposition on the glass slide to create 20 nm platinum layer on the top. Step 3a: Detachment of the gold-platinum Janus particle using sonication. Step 3b: Detachment using the capillary force from a wet tissue.

The next step is to detach the Janus particles from the glass slide. There are two alternative ways in this step. The first way is the detachment by using sonication (step 3a Fig. 2.4), which has been used by the previous PhD students. At the beginning of my PhD, I also used this method to detach the Janus particles. It has to be done very carefully because the sonication can also detach platinum scales. We show in Fig. 2.5a,b the very unfortunate situation where a lot of platinum scales have fallen into the sample. It is extremely difficult to get rid of them to obtain an acceptable sample quality. We guess that it is because the sonication is too long or too strong. Despite our efforts on verifying these parameters on different batches, we could not conclude what the right condition for the detachment via sonication is.

Later on, I came across another detachment method from a discussion with other PhD students from another group. First, we soak one end of fine tissue with milliQ water and then wipe it gently back and forth on the glass slide without pushing any force on it (step 3b Fig. 2.4). The Janus particles are pulled by a capillary force and come with the wet tissue. Then, we collect the particles by dipping the wet end into a beaker of milliQ water and shake the tissue strongly. The particles should detach

from the tissue and suspend in water. After letting them settle down, we can collect them from the bottom of the beaker. Fig. 2.5c is the resulting Janus particles from the detachment by the wet tissue. The platinum scale is no more bothering us. There might be few small pieces of tissue in the sample, which is a lot easier to remove when comparing to the platinum scale.

After the detachment, the final step is to filter out any defects as much as possible. The defects can be in any form such as platinum scales, tissue, glass shed, small clusters of particles and any contamination from the air. We put the Janus particles in an experimental chamber (will be described in Section 2.2) and create in-plane sedimentation (by tilting the microscope) to separate objects of different sizes and use a micro-pipette tip to remove the defects directly from the spot observed via a microscope. After the long and tedious purification process, the final result is shown in Fig. 2.5d. This is the ready stage for the experiment.

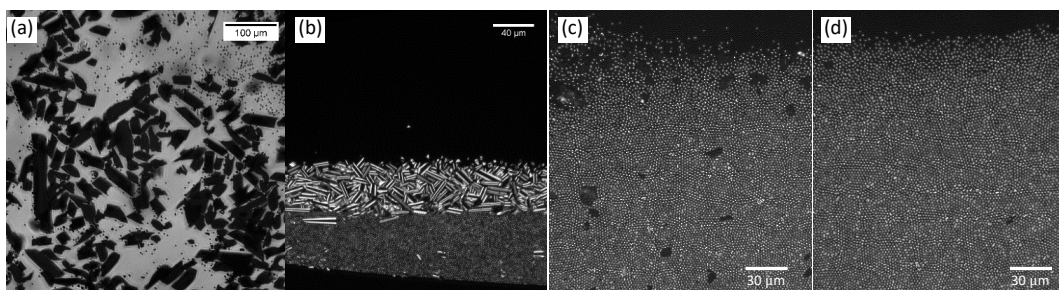


FIGURE 2.5: (a,b) Unfortunate situations of many platinum scales were also detached and mixed with the Janus particle. Observe with (a) transmitted light and (b) dark-field microscopy. (c) The resulting Janus particles from the detachment via the wet tissue method. (d) The Janus particles after the final filtration. At this stage, they are ready for the experiment.

2.2 Experimental setup

Our experimental setup is shown in Fig. 2.6. We put the Janus particles in a 96-well plate (a) and observe their 2D motions at the bottom via a camera connected to the monitor (b). The motorized stage controlled by a joystick (c) allows us to move the observation field without touching the plate. For the lighting mode, we use external dark-field microscopy: A custom-made LEDs ring is set below the sample and it is controlled separately via a DC power supply (d). We create in-plane sedimentation by tilting the microscope that is sitting on a metal plate supported by three screws (e). In this section, we describe more what to be concerned on each component.

(a) Experimental chamber

Here we use a 96-well plate from Falcon (Ref #353219) as an experimental chamber. After we disperse the Janus particles into the well already filled with $\sim 300 \mu\text{l}$ milliQ water (from the total volume of $370 \mu\text{l}$), the particles settle down and form a monolayer at the bottom. We thus observe their 2D motions through the flat and transparent bottom of the well. The main concerning point regarding the choice of an experimental chamber is the friction and adhesion between the particles and the bottom surface. We have tried with several substrates (glass and polymer brush coated on a glass surface) and they cannot be used because the particles get stuck

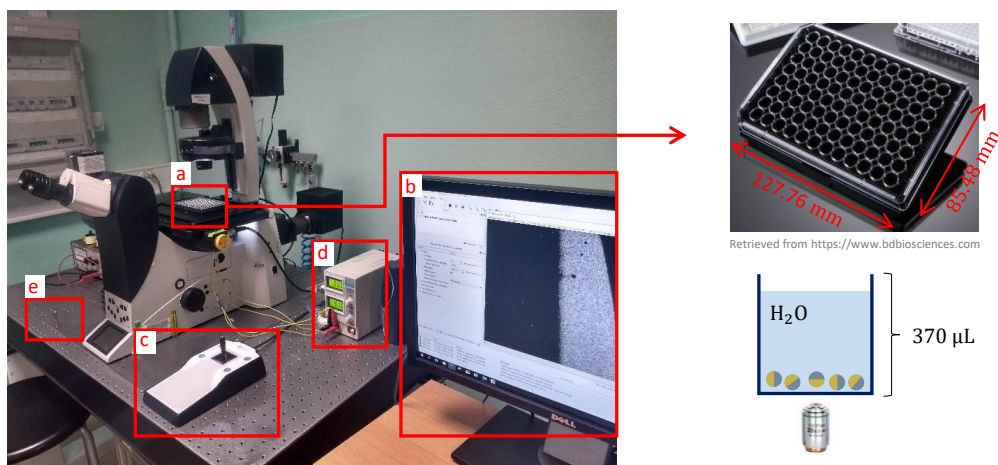


FIGURE 2.6: The experimental setup: (a) the 96-well plate as an experimental chamber, (b) monitor linking to the camera, (c) joystick to control the motorized stage, (d) DC power supply for the custom made dark field microscopy, and (e) an iron plate and screws to tilt the set-up. The lower left figure is a sketch illustrating the particle suspension in the experimental chamber.

on those surfaces. Since gold in water is negatively charged, we believe that a negatively charged substrate should create a repulsion between particles and the surface, and thus reduce the friction. We do not know exactly what has been the surface treatment of the commercial well plate. Anyway, we believe that it is strongly negatively charged because the particles move nicely on this surface.

Before the activation, the particles are in pure milliQ water. We activate them by adding H_2O_2 into the well. We note that due to the large volume of the solvent above the monolayer, we find that the effects of the activity are stable in time over several hours. In particular, the purely diffusive motion could be recovered only several days after the last H_2O_2 introduction. That is why we always wash several times our particles with milliQ water before starting a series of experiments and always increase step by step H_2O_2 concentration from that clean state.

(b) Imaging and data acquisition

We use an inverted microscope (Leica DMI 4000B) equipped by 20x plan fluorar objective and combined with 1.0x and 1.6x magnification lens. The microscope is connected with a Basler camera (acA2040-90um) that has an array of 2048×2048 pixels. Experimental images and videos are acquired using *pylon* software. The observation area is $559 \mu\text{m} \times 559 \mu\text{m}$ for the 1.0x magnification lens and $350 \mu\text{m} \times 350 \mu\text{m}$ for the 1.6x lens. If the particles are closely packed, we can observe up to $\sim 2.7 \times 10^4$ particles with the 1.6x lens.

(c) Motorized stage

The sample is mounted on a motorized XY translation stage (SCAN IM 130x85) that we can control manually via a joystick or we can also program for systematic observations at different positions. To minimize in-plane acceleration, we limit the moving speed at 0.02 mm s^{-1} and use S-curve acceleration.

(d) Lightning condition: dark-field microscopy

There are three built-in lightning modes in our microscope: transmitted, reflected and fluorescence mode (the latter mode was never used in our experiments). Our Janus particles appear to be black with white background in transmitted mode (see Fig. 2.7 left). This mode gives high contrast between the particles and background, however, it is indeed not good for locating the center of each particle. Since our Janus particles are opaque, we would prefer a lightning mode where the light comes from below. However, the reflection mode gives us a poorly contrast image (see Fig. 2.7 middle), which leads to high uncertainties on particle tracking.

Thanks to Félix Ginot and Gilles Simon who designed an external LEDs ring for dark-field microscopy in this setup. The resulting image has a great contrast of a black background with the particles as bright spots (see Fig. 2.7 right). Unless stated otherwise, we always use this external dark-field microscopy for my entire PhD work. One thing to be concerned of is that the LEDs ring always heats up the sample and thus leads to drift by thermal convection. To deal with this issue, we must turn on the LEDs for at least 4 hours to let the system reaches thermal equilibrium state before running an experiment.

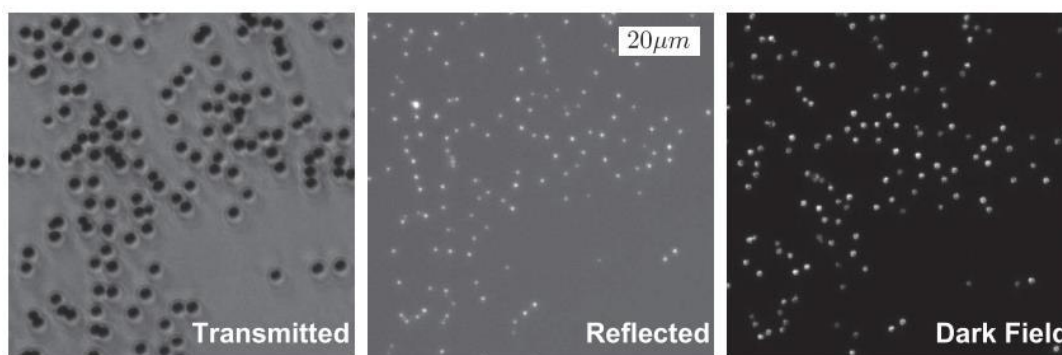


FIGURE 2.7: Optical microscope images from different lightning modes. Images by Félix Ginot.

(e) Angle control

To gather all the colloids together on one side of the chamber, we create in-plane sedimentation. To do so, we place an iron plate underneath the microscope itself standing on three screws positioned like an isosceles triangle (the top is on one side and the base is on the opposite side of the iron plate). This allows us to tilt the microscope with a control angle by adjusting the screws. Note that we always want to have a monolayer of the Janus particle assembly. If the tilt angle is too high, the particles will form a multilayer sediment. Using the transmitted lightning mode, we can check whether or not the sediment forms only a monolayer (see Fig. 2.8). By adjusting and checking again and again, we should find a good tilt angle, which depends on the amount of particles in the well. Typically, the tilt angle is about 0.1° .

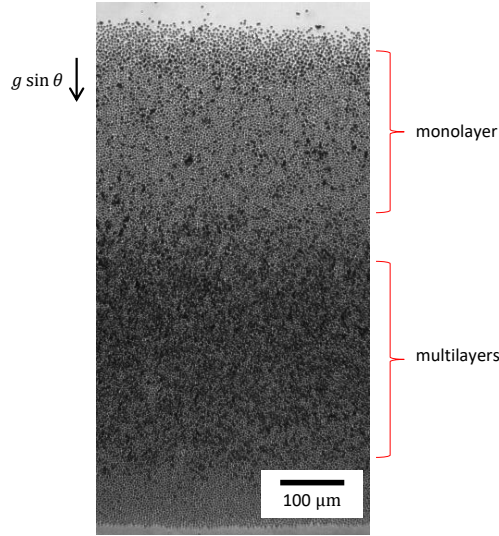


FIGURE 2.8: Sediment of the particles in transmitted lightning mode. Here, the tilt angle θ is too high and thus the lower part of the sediment forms multilayers.

An other thing we have to be concerned of in the experimental setup is a drift motion, which is a collective movement of the particles in a non-stationary state. For example, changing the tilt angle will cause the sediment to flow towards a new lowest position. To minimize the drift, we have to carefully set up the configuration in advance (typically, one day before) and make sure that the system is in the stationary state before starting the experiment.

2.3 Characterization in the dilute regime

In this section, we characterize individual particle motion in the dilute regime, where we have about 300 particles in $559 \mu\text{m} \times 559 \mu\text{m}$ observation area (area density $\phi \sim 0.003$). Note that we do not need the in-plane sedimentation to create such a dilute regime, we thus keep the tilt angle $\theta = 0^\circ$ to avoid the drift.

Starting from the passive case ($[\text{H}_2\text{O}_2] = 0\%$), we increase the H_2O_2 concentration logarithmically until the bubbles appear in the system. These bubbles come from the splitting of H_2O_2 into protons and O_2 on the platinum side of the Janus particles. At high H_2O_2 concentration, the rate of O_2 production is also high. That O_2 cannot diffuse away fast enough and bubbles nucleate and explode. This explosion, of course, will interfere with the particle motion, the real physics that we are interested in. Therefore, our experimental limit is the H_2O_2 concentration before the bubbles appear in our system. The set of experiments that we are going to discuss in this section has reached 0.13% H_2O_2 concentration as the maximum.

In the dilute regime, we record an image sequence at the frequency 20 Hz for 200 s. From these images, we detect particle positions and reconstruct 2D particle trajectories using *trackpy* package [174] (will be described in Section 3.1). In Fig. 2.9 we show the particle trajectories comparing between the passive and the highly active case. At the same time interval $\Delta t = 5$ s, the passive particles (Fig. 2.9a) remain close to their initial position, while the active particles (Fig. 2.9b) exhibits clearly larger displacement. The active particles are not only self-propelled forward, they also change their moving direction due to rotational diffusion.

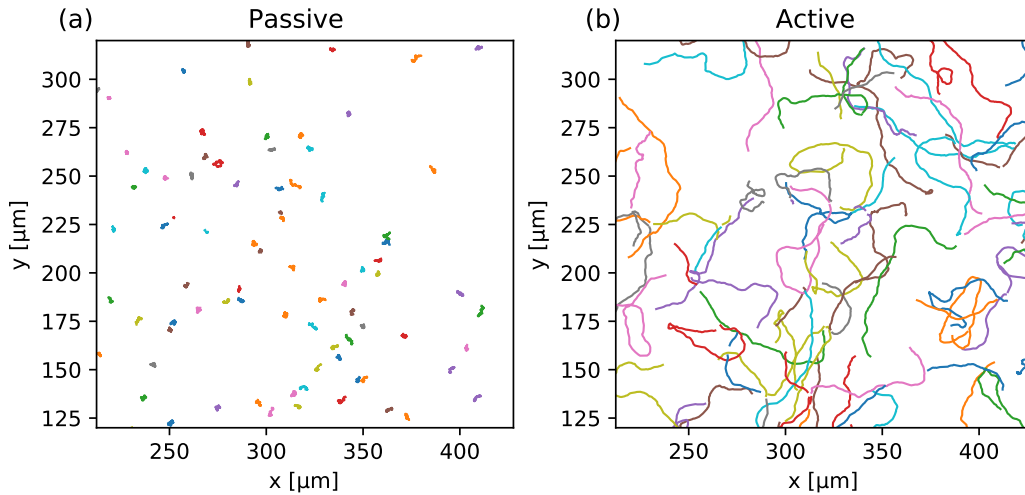


FIGURE 2.9: Particle trajectories during the time interval $\Delta t = 5$ s comparing between (a) the passive case, $[\text{H}_2\text{O}_2] = 0\%$, and (b) the active case $[\text{H}_2\text{O}_2] = 0.13\%$.

2.3.1 Van Hove function

We first look at a probability distribution of finding a particle i that has displaced by \mathbf{r} given a lag time Δt . This is actually a self part of van Hove distribution function [175], which is defined as

$$G_s(\mathbf{r}, \Delta t) = \langle \delta(\mathbf{r} - |\mathbf{r}_i(t) - \mathbf{r}_i(\Delta t)|) \rangle_i, \quad (2.5)$$

where $\langle \dots \rangle$ is an ensemble average among the particles and $\delta(\cdot)$ is the Dirac delta function. It is known that $G_s(\mathbf{r}, \Delta t)$ of Brownian hard sphere particles have a Gaussian-shape distribution. Here, we show the van Hove function of our Janus particle in the passive case in Fig. 2.10. This is simply a histogram of particle displacement in either x or y direction at a given Δt . The 2D van Hove function (left panel) has symmetric shape around the origin (0,0). At $\Delta t = 1.0$ s, the distribution concentrates closely to the origin and it distributes within the particle diameter $\sigma = 1.6 \mu\text{m}$. At longer lag time $\Delta = 9.0$ s, $G_s(\mathbf{r}, \Delta t)$ expands further. We can look at the dependence of Δt by looking at the distribution in 1D (right panel). Of course, $G_s(\mathbf{r}, \Delta t)$ becomes wider with Δt and always keeps in a Gaussian shape.

Next, let us consider the activity-dependence of $G_s(\mathbf{r}, \Delta t)$ obtained from our active Janus particles as shown in Fig. 2.11. At the same lag time $\Delta t = 0.3$ s for all activity levels, the van Hove function grows wider with H_2O_2 concentration. This shows that at the same Δt , the Janus particles at higher H_2O_2 concentration can displace further from the original position. However, unlike the passive case, $G_s(\mathbf{r}, \Delta t)$ deviates from the Gaussian shape. Especially at concentrations above $2.7 \times 10^{-2}\%$, $G_s(\mathbf{r}, \Delta t)$ has a flat top at the center and a decay at both ends. This deviation shows that the displacement mechanism of active particles is no longer diffusion alone.

Now we look at the 2D distribution of the highest activity at various Δt in Fig. 2.12. Strikingly at short Δt , the distribution has an annulus shape centered at the origin. This corresponds to a short-time ballistic motion. Particles displace from their original position (dark spot at the origin) and appear further than the particle diameter (bright ring). Because a particle orientation is random, it is likely to find the particles in any direction at a certain distance from the origin. At intermediate lag times,

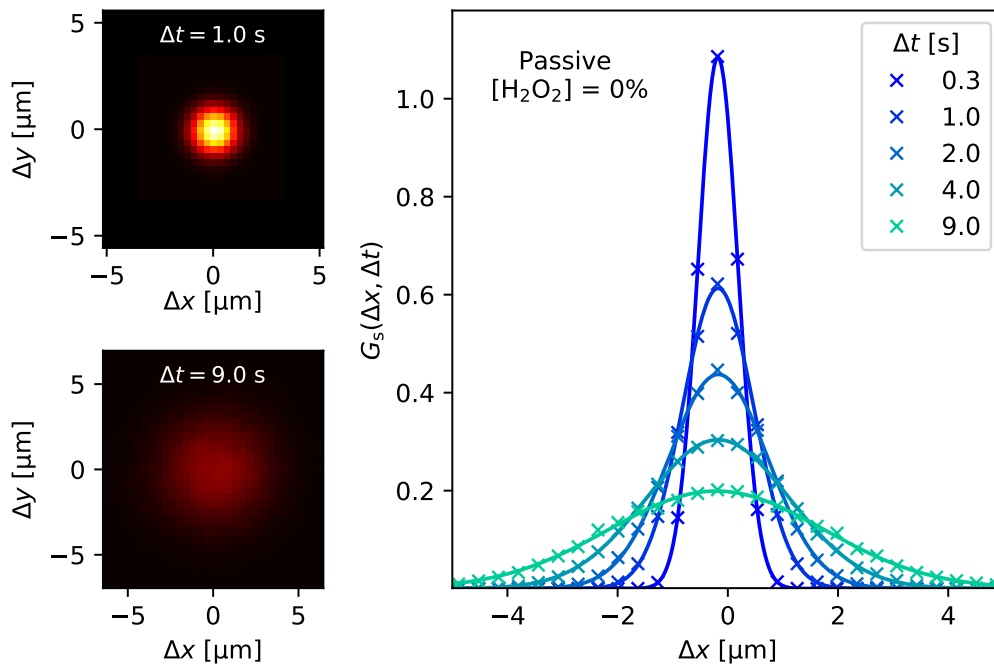


FIGURE 2.10: 2D (left) and 1D (right) van Hove distribution function, $G_s(\mathbf{r}, \Delta t)$, of the passive particles at different lag time Δt . The solid line is the Gaussian fit to the data.

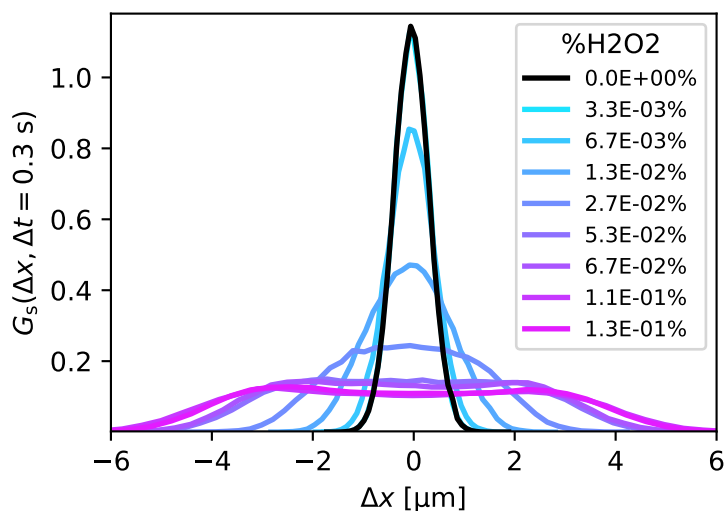


FIGURE 2.11: The 1D van Hove distribution function, $G_s(\Delta x, \Delta t)$, at the fixed lag time $\Delta t = 0.3$ s and various H₂O₂ concentrations increasing from black (without H₂O₂), to cyan to magenta, see respective insets.

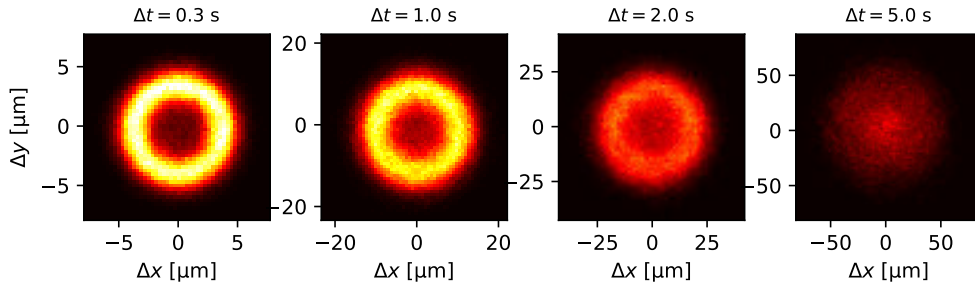


FIGURE 2.12: 2D van Hove distribution function, $G_s(r, \Delta t)$, of the active Janus particles at 0.13% H_2O_2 concentration and various lag time Δt . The color scale is the same for all four panels.

$\Delta t = 1.0\text{ s}$ and 2.0 s , the distribution is wider and still has the annulus shape, however, with the less and less contrast between the dark center and the bright rim. Finally at $\Delta t = 5.0\text{ s}$, the annulus has completely disappeared as the center spot become brighter than the rim. This reminds us of the 2D Gaussian distribution in the passive case in Fig. 2.10.

Recall from Fig. 2.11, we obtained the flat-top 1D distribution at high activity levels, not the two-peak distribution which reflects the annulus-shaped. It is because we have not considered the particle displacement in the other directions when calculating the histogram. For example, if the particle moves towards y direction, the binning of Δx will count for $\Delta x = 0$ and the 1D distribution of Δx will indeed nonzero at the center. Therefore, to show the complete information of the particle displacement, we should take the displacement in the other directions into account as well. To do so, we take a cross-section of the 2D distribution in Fig. 2.12 at $\Delta y = 0$ as shown in Fig. 2.13.

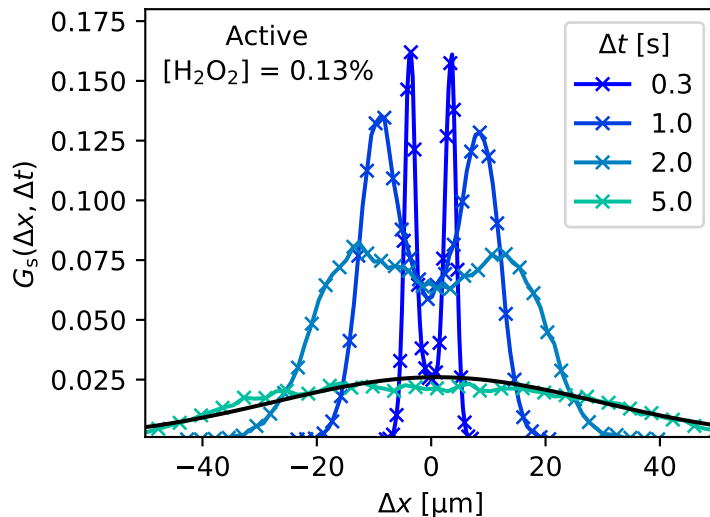


FIGURE 2.13: The 1D van Hove distribution function, $G_s(\Delta x, \Delta t)$, of the active Janus particles at $1.3 \times 10^{-1}\%$ H_2O_2 concentration and various lag time Δt . The distribution is obtained from the cross-section at $\Delta y = 0$ of Fig. 2.12. The black solid line at $\Delta t = 5.0\text{ s}$ is the Gaussian fit to the data.

The cross-section of 2D van Hove distribution can capture the short-time moving-forward motion. At a longer timescale, the two-peaks distribution starts to merge into one peak. The center of the distribution gets higher and then eventually becomes the highest point at $\Delta t = 5.0$ s. We notice that the long-time distribution is getting closer to the Gaussian distribution (black solid line) suggesting that there is a crossover from ballistic to diffusive motion at long Δt . To probe the transition between two regimes, we thus look at the mean square displacement of the particles at various Δt .

2.3.2 Mean square displacement and effective diffusion

The mean square displacement (MSD) is a common tool to investigate system dynamics at all time scales. For each particle i , we measure its square displacement between a lag time Δt and then take an average among all the particles, i.e.,

$$\langle (\Delta r)^2 \rangle = \left\langle \frac{1}{N} \sum_{i=1}^N (r_i(t_0) - r_i(t_0 + \Delta t))^2 \right\rangle_{t_0}, \quad (2.6)$$

where N is the total number of particles, $r_i(t_0)$ is a position of particle i at the time t_0 . For a Brownian particle, the MSD increases linearly with Δt and the constant of proportionality is the Brownian (thermal) diffusion coefficient D_0 , i.e.,

$$\langle (\Delta r)^2 \rangle = 2dD_0\Delta t, \quad (2.7)$$

where d is the translation degree of freedom of the system, in which our case $d = 2$.

In Fig. 2.14, we compute the MSD of our dilute experiment on active colloids. Indeed, the MSD of the passive case (black curve) increases linearly with Δt and has the slope equal to one in log-log scale, which means that the particle motion is purely diffusive ($\langle (\Delta r)^2 \rangle \sim \Delta t$). In the presence of H_2O_2 (cyan to magenta curves), the MSD displays ballistic motion (slope = 2) at short time scale such that

$$\langle (\Delta r)^2 \rangle \sim v_0^2(\Delta t)^2, \quad (2.8)$$

where v_0 is the propulsion velocity. We can see the evolution of the MSD curves with H_2O_2 concentrations: higher concentration, higher propulsion velocity. The slope of the MSD decreases to one at long Δt , showing long-timescale diffusive motion. We note that to avoid the finite size effect, we have verified that most of the trajectories remain in the observation area throughout the acquisition. The maximum lag time at which we calculate the MSD is 20 s. The fastest particle of $v_0 \sim 15 \mu\text{m s}^{-1}$ would displace $\sim 300 \mu\text{m}$ maximum (without reorientation), while the box size is $559 \mu\text{m}$.

The diffusive motion at long timescales comes from the fact that the particles are always subject to the rotational Brownian diffusion, which is characterized by the rotational time τ_R , even when translational Brownian motion of the particle is overcome by the ballistic motion. This is indeed a *persistent random motion* and it has already been discussed in Refs. [7, 106]. They have shown that the full analytic expression of the MSD (particle rotation in 3D but projected into 2D) is the following,

$$\langle (\Delta r)^2 \rangle = 4D_0\Delta t + \frac{1}{3}v_{3D}^2\tau_R^2 \left[\frac{2\Delta t}{\tau_R} + \exp\left(\frac{-2\Delta t}{\tau_R}\right) - 1 \right], \quad (2.9)$$

where v_{3D} is the particle velocity taken into account the 3D reorientation. Note that we can only measure the propulsion velocity projected in 2D, v_0 , and both velocities

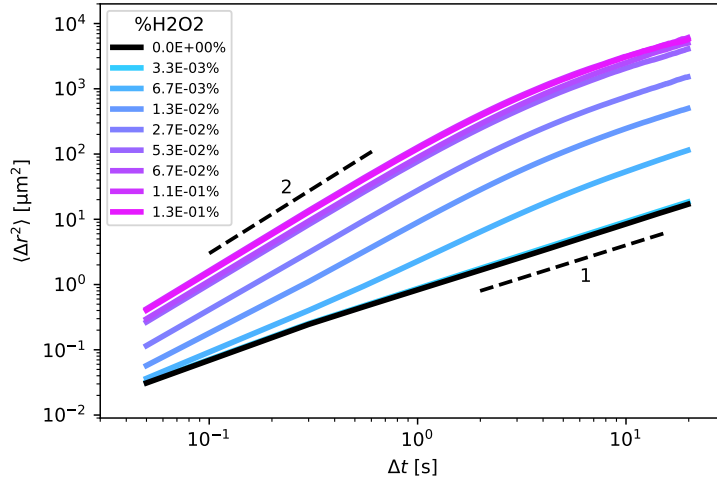


FIGURE 2.14: Mean square displacement (MSD) of the active colloids in the dilute regime at various H_2O_2 concentrations increasing from black (without H_2O_2), to cyan to magenta, see respective insets. Dashed lines indicate slopes 1 (diffusive motion) and 2 (ballistic motion).

are related such that $v_0^2 = \frac{2}{3}v_{3D}^2$. If we take the limit $\Delta t \rightarrow 0$ of Eq. 2.9, we obtain Eq. 2.7 showing that the particle exhibits purely Brownian motion at very short lag time. If $\Delta t \ll \tau_R$, we obtain

$$\langle (\Delta r)^2 \rangle = 4D_0\Delta t + \frac{2}{3}v_{3D}^2(\Delta t)^2 = 4D_0\Delta t + v_0^2(\Delta t)^2, \quad (2.10)$$

which corresponds to Eq. 2.8 if $\Delta t \gg 4D_0/v_0^2$, the time scale of the ballistic motion. This time scale is about 0.2 s for $v_0 = 2 \mu\text{m s}^{-1}$. This is why the ballistic regime is difficult to observe at too low H_2O_2 concentration.

If $\Delta t \gg \tau_R$, Eq. 2.9 becomes,

$$\langle (\Delta r)^2 \rangle = 4(D_0 + \frac{1}{4}v_0^2\tau_R)\Delta t \equiv 4D_{\text{eff}}\Delta t, \quad (2.11)$$

with the effective (activity-dependent) diffusion coefficient defined as,

$$D_{\text{eff}} = D_0 + \frac{1}{4}v_0^2\tau_R. \quad (2.12)$$

At such long timescales, the particle performs a persistent Brownian motion characterized by D_{eff} .

From the MSD curves in Fig. 2.14, we could not obtain the purely Brownian motion at the very short-timescale. However, we can see that the transition time between the ballistic and the effective diffusion regime is practically independent on H_2O_2 concentration and approximately about 6 s (estimated from the MSD curves).

From the MSD curves, we can extract D_{eff} of this persistent random motion by fitting the long-time scale MSD with Eq. 2.11 (see Fig. 2.15a). From the fitting of the passive case, we obtain the Brownian diffusion coefficient $D_0 = 0.2 \mu\text{m}^2 \text{s}^{-1}$, which is in a good agreement to the value obtained from the Stoke-Einstein relation. In Fig. 2.15b we show that D_{eff} increases monotonically with the H_2O_2 concentration. The saturation at high concentration is possibly the reaction rate limit.

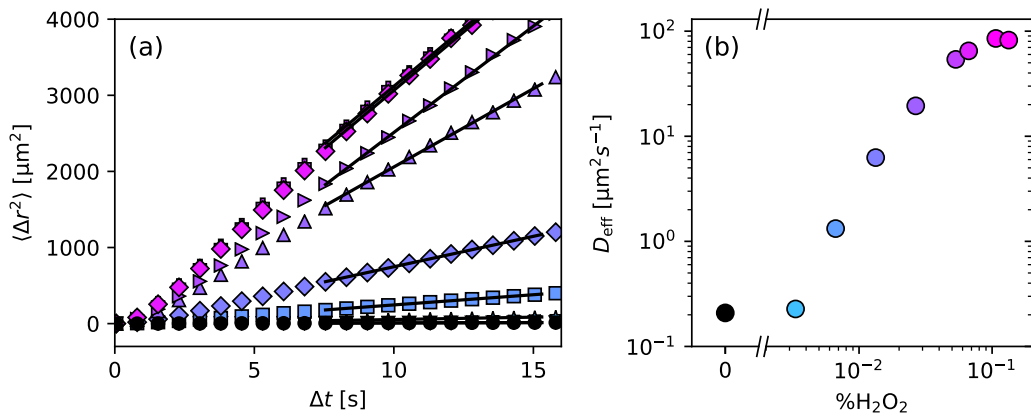


FIGURE 2.15: (a) Mean square displacement, MSD, of the active colloids in the dilute regime at various H_2O_2 concentrations with the same color code as in Fig. 2.14. The black solid lines is the linear fit to obtain effective diffusion coefficient (D_{eff}). (b) Corresponding D_{eff} versus H_2O_2 concentration, extracted from the long-time MSD in (a).

2.3.3 Propulsion velocity

Measurement of the propulsion velocity v_0 of a particle under persistent Brownian motion is not straightforward. From Eq. 2.10 we can see that the displacement of a Brownian particle subjected to a propulsion force is composed of two terms: diffusive and self-propulsion contributions, i.e.,

$$\Delta r = 2\sqrt{D_0\Delta t} + v_0\Delta t. \quad (2.13)$$

Therefore, the instantaneous velocity calculated from the displacement does not correspond directly to v_0 . There is also the diffusion term, $2\sqrt{D_0/\Delta t}$, which always causes the overestimation of the propulsion velocity.

One way to filter out the Brownian contribution is to smooth the particle trajectory. We thus apply a Gaussian filter of various smoothing sizes and determine the best value by comparing the raw trajectory with the smoothed one. If the smoothing size is too small, we would not get rid of the diffusion term. On the contrary, if it is too large, the trajectory would be modified too much.

One more thing to take into account is that the definition of v_0 is only valid in the dilute limit, which means that the particle moves freely without interacting with each other. Even if our experiment is performed in the very dilute phase ($\phi \sim 0.003$), it is still possible that the particles can collide to the others, especially at high activity levels. This can cause an error in the velocity measurement. We, therefore, ignore a part of a trajectory when the particle is closer than 2.5σ to any other.

After smoothing and filtering the trajectory, we calculate v_0 from the average instantaneous velocity among all particles at all initial time t_0 ,

$$v_0 = \frac{1}{\Delta t} \sqrt{\langle (r_i(t_0 + \Delta t) - r_i(t_0))^2 \rangle_{i,t_0}}, \quad (2.14)$$

where we choose $\Delta t = 0.5$ s, the regime of the ballistic motion. Despite all our efforts, we still obtain nonzero velocity in the passive case: $v_0 \sim 1.6 \mu\text{m s}^{-1}$ to $2.4 \mu\text{m s}^{-1}$ depending on the selected smoothing size. This means that our procedure is not yet perfect as the resulting velocity is sensitive to the choice of the smoothing parameter.

The above method was generally used by the previous PhD students. Here, we come up with another way to obtain v_0 from the MSD. Again recalling from Eq. 2.10, we know that the first term is the MSD of the passive particles, which is independent from activity level. We first perform a linear fit to the MSD of the passive case and then we subtract the fitting result from the MSD of the active cases. At this point, there should be no more Brownian contribution in the MSD and the only term left is $v_0^2 \Delta t^2$. Finally, we obtain v_0 by directly fitting the subtracted MSD at the short-timescale.

Checking the propulsion velocity of the passive case, we obtain $v_0 = 0.09 \pm 0.04 \mu\text{m s}^{-1}$, which is almost zero and thus more reliable than the first measurement. Besides, this measurement of v_0 is not depending on the choice of parameters. Note that for all H_2O_2 concentrations, we always obtain a propulsion velocity $2 \mu\text{m s}^{-1}$ less than the first procedure. We guess that it is because there is still a drift of $2 \mu\text{m s}^{-1}$ left from the drift subtraction algorithm (see Section 3.1). This is why we still obtain a nonzero propulsion velocity in the passive case from the measurement of instantaneous velocity. The subtraction of the MSD by the passive MSD can clear out this remaining drift. The resulting v_0 obtained from the MSD versus H_2O_2 concentration is shown in Fig. 2.16. It indeed increases monotonically with the H_2O_2 concentration and seems to saturate from $5.3 \times 10^{-2}\%$ concentration, consistently to D_{eff} in Fig. 2.15.

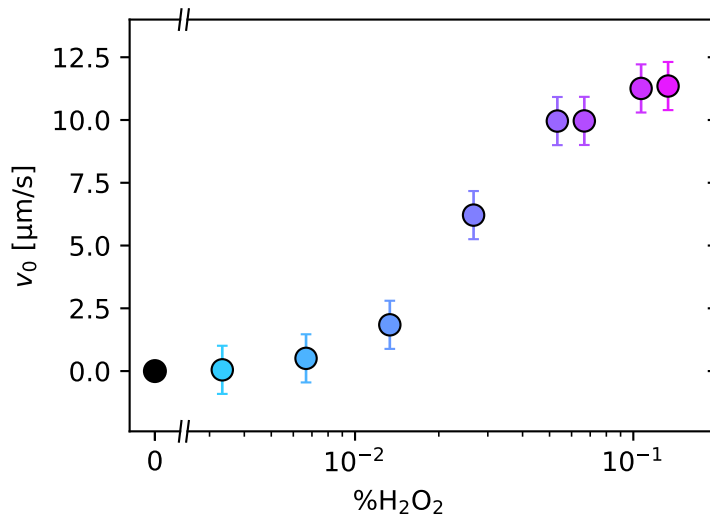


FIGURE 2.16: The propulsion velocity v_0 at various H_2O_2 concentrations.

Until this point, we have measured two quantities that can be used to characterize activity level in the dilute limit, D_{eff} and v_0 . Both quantities are measured at different time scale. D_{eff} is obtained from the long-timescale, while v_0 comes from the short-time measurement. Another quantity for the activity characterization is the rotational diffusion time τ_R . As mentioned above, it is the transition time from the ballistic motion to the long-term diffusive motion. Unfortunately, we cannot measure τ_R directly from the experiment because we cannot access to the particle orientation. One way to obtain τ_R is from the velocity-velocity correlation function [7, 106],

$$\langle \mathbf{v}_i(t) \cdot \mathbf{v}_i(t + \Delta t) \rangle = v_0^2 e^{-2\Delta t / \tau_R}. \quad (2.15)$$

However, due to the translational Brownian contribution, the correlation function of the instantaneous $v_i(t)$ gives us a noisy result.

Eq. 2.12 suggests that we can obtain τ_R from D_{eff} and v_0 . We thus plot D_{eff} versus v_0^2 in Fig. 2.17, which shows a linear relationship confirming that τ_R is independent from H_2O_2 concentration. From the linear fit, we obtain $\tau_R = 5.3 \pm 0.2$ s. This value is a bit more than the Stokes expectation:

$$\tau_R = \frac{\pi\eta\sigma^3}{k_B T} \approx 3.1 \pm 1.3 \text{ s}, \quad (2.16)$$

where the uncertainty comes from the polydispersity of the particle. However, the value obtained from Eq. 2.16 is very sensitive to particle diameter. If instead of the colloid diameter σ , we take twice the hydrodynamics radius estimated from the Brownian diffusion coefficient $D_0 = 0.2 \mu\text{m}^2 \text{s}^{-1}$,

$$R_H = \frac{k_B T}{6\pi\eta D_0} \approx 0.94 \mu\text{m}, \quad (2.17)$$

we thus obtain $\tau_R \approx 5.1$ s, which is in good agreement with our measurement.

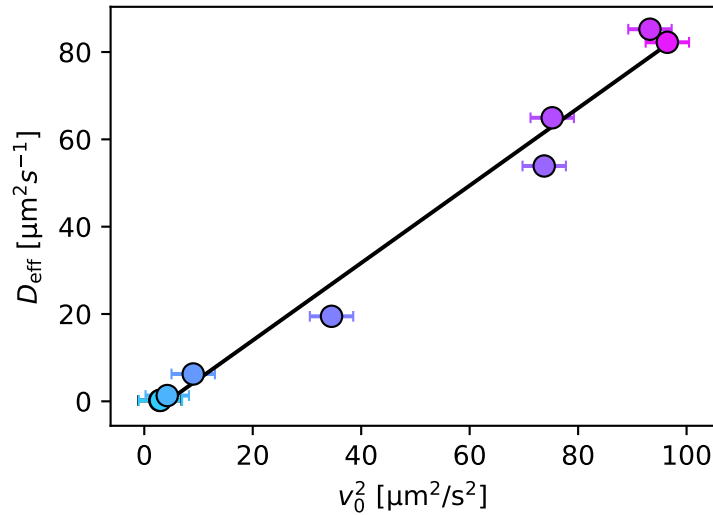


FIGURE 2.17: Verification of Eq. 2.12, $D_{\text{eff}} = D_0 + \frac{1}{4}v_0^2\tau_R$. D_{eff} and v_0 are obtained separately from the long-time MSD and the short-time MSD, respectively. The black solid line is the fitting curve and we obtain $\tau_R = 5.3 \pm 0.2$ s

2.4 Alternative gold particles for making active colloids

Our Janus particles made of gold micro-carriers from BioRad are working perfectly. They have a higher propulsion efficiency than latex or silica core Janus swimmers and they suit very well to our goal of observing 2D motion. However, their disadvantages are the long sorting procedure (as mentioned in Subsection 2.1.2) and very limited sizes available (Bio-Rad only provides spherical particles of 0.6, 1.0 and 1.6 μm diameters). The latter disadvantage prevents us from investigating the dependence of particle sizes and shapes or introducing well-controlled bidispersity to

prevent crystallisation. To overcome this limit, we look for an alternative way to make Janus particles.

In parallel to the main objective of my PhD, we have collaborated with Franck Bertorelle (Optique Non Linéaire et Interfaces, iLM) to make new gold particles. We have two main trials: (1) synthesis of micron-size pure gold particles and (2) coat gold nanoparticles on latex particles. While the synthesis of gold particles at nano-size is common, synthesising of micron-size gold particles is way more challenging. The concept is to first synthesise gold nanoparticles and then let them aggregate to form larger spherical particles [176]. Unfortunately, we have not yet obtained an acceptable outcome from this synthesis. The resulting gold particles are always too polydisperse and full of clusters. However, we have obtained a promising result from the second trial, coating latex particles with gold nanoparticles (AuNP).

2.4.1 Latex(AuNP)-platinum Janus particle

The synthesis starts from base latex particles as a core. It is important to use a particle that contains amine group on its surface because the AuNP primarily attaches to the amine group. Here we use amino microspheres of $6\ \mu\text{m}$ diameter from Polybead (ref. #19118-2). Afterward, AuNP is grown from the primary seeds and then cover the whole surface (see Fig. 2.18a and b).

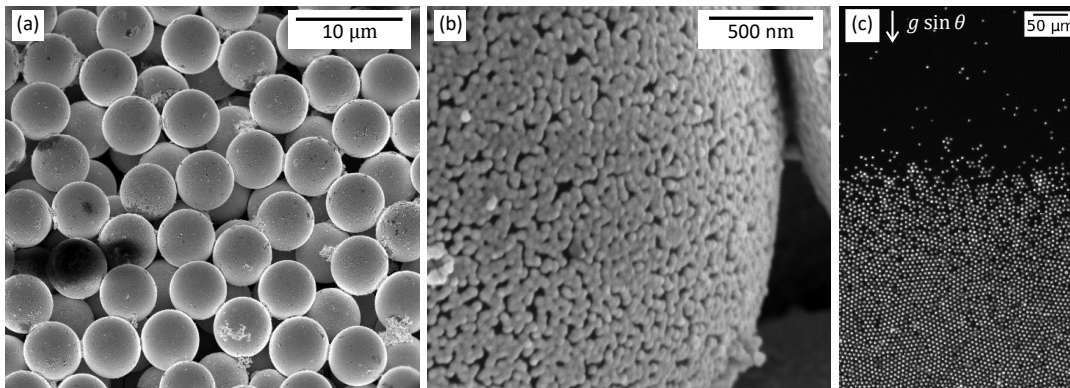


FIGURE 2.18: Amino microspheres coated by AuNP. (a) SEM image of several microspheres. The black stain on the left comes from an electronic charge effect due to the imperfect coating. It is an area where the non-conductive polystyrene surface is not covered by AuNP. (b) SEM image of a detail of a microsphere surface. The covering gold particles size is about 50 nm. (c) An optical image of sediment of Latex(AuNP)-platinum Janus particles immersed in $2 \times 10^{-2}\%$ H_2O_2 concentration after 2 h waiting time.

We apply the same procedure of the platinum deposition as in Subsection 2.1.2 to make Janus particles. We show the MSD of this particle in the dilute regime in Fig. 2.19. Obviously, the active particles shows only the ballistic regime. Using Eq. 2.16 to estimate its rotational time, we obtain $\tau_R \approx 165\ \text{s}$. This means that the particles move forward for about 2 mm before the rotational diffusion makes them change direction. This persistent length is much larger than our observation field. This is why we cannot capture the long-term diffusion motion from this active particle.

The maximum H_2O_2 concentration that we can reach is $2 \times 10^{-2}\%$. This is not because of nucleating O_2 bubbles, but because the motion of the particles becomes 3D. This upper threshold is much lower than our usual Janus particle which is $1.3 \times 10^{-1}\%$, however, the new Janus particle can move faster with $v_0 = 15\ \mu\text{m}\ \text{s}^{-1}$. In

addition, we remark that these colloids have much higher efficiency when compared to the normal latex-platinum Janus particle ($\sim 3 \mu\text{m s}^{-1}$ at 10% of H_2O_2) [7, 106].

When we activate the assembly of the particles, they easily move out of the plane. A few hours afterward, the particles again form monolayer sediment at the bottom and still self-propel on the surface (see Fig. 2.18c). Aiming to perform a 2D activity variation experiment on such sediment will be impossible since the particles move out of the plane every time the new H_2O_2 is added (even the total concentration is very low $\sim 6 \times 10^{-3}\%$).

I stressed again that I did not use these alternative Janus particles in the experiments I will describe in the next chapters. Anyway, this alternative way to obtain gold-platinum Janus particles could be further developed. For example, using smaller latex particles to reduce τ_R or making a thicker gold layer to gain more weight. It will indeed provide us more variety of choices of active particles.

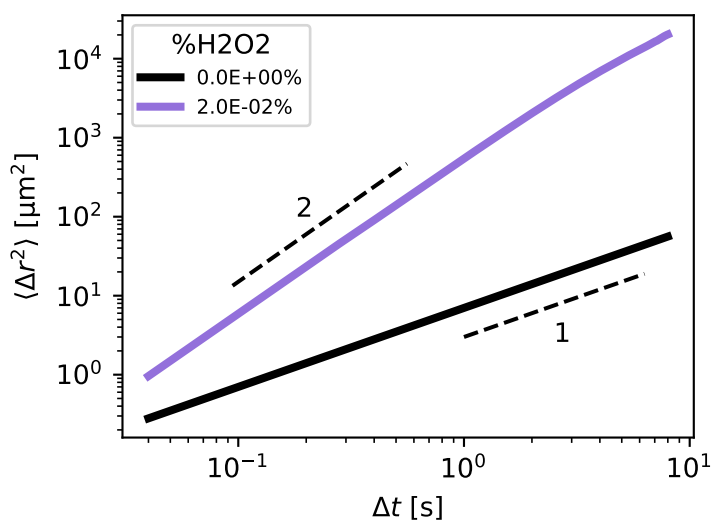


FIGURE 2.19: Mean square displacement, MSD, of the Latex(AuNP)-platinum active colloids in the dilute regime comparing between passive and active cases. Dashed lines indicate slopes 1 (diffusive motion) and 2 (ballistic motion).

Key concepts of the chapter:

1. We discussed the synthesis of the Au-Pt Janus particles:
 - (a) We proposed a new sorting procedure using ODT to obtain individual particles from the sample full of aggregates. This can significantly shorten the synthesis time from the previous sedimentation sorting.
 - (b) We replaced the detachment of the Janus particles using sonication by the wet tissue method, which greatly improved the sample cleanness and the purification time.
2. We characterized the particle dynamics in the dilute regime $\phi \sim 0.003\%$:
 - (a) Van Hove function,
 - (b) Mean square displacement, MSD, obtaining effective diffusion coefficient, D_{eff} ,
 - (c) Measurement of the propulsion velocity, v_0 ,
 - (d) Confirm reorientation time is independent of activity and obtain Brownian rotational time, τ_R , from D_{eff} and v_0 .
3. We developed an alternative way to obtain gold microparticles using latex coated by AuNP.

Chapter 3

Analysis tools for the dense regime

The raw data obtained from the experiments is in the form of an image sequence. To obtain quantitative data, we track particle positions frame by frame and reconstruct particle trajectories for further analysis. In this chapter, we identify our particle tracking procedure and the analysis tools that will be mentioned throughout the thesis. We will only discuss the passive system in order to test our tools and to compare the results with standard glassy physics. All the scripts are written in *python* programming language via Anaconda distribution [177], heavily using *numpy* [178], *scipy* [179], *pandas* [180], *trackpy* [174] and *NetworkX* [181]. The data visualization is using *Matplotlib* [182]. In addition to standard packages, we have developed scripts and modules to analyze specifically our experimental data. We note that the observation area is only a small fraction of the whole sample and particles can go out or come in this area during the experiment. We run both tracking and analysis algorithms on our local workstation (8-cores at 3.2 GHz, 12GB ram, 4+12TB of HDDs).

3.1 Particle tracking in a dilute regime

From the experiments, we obtain 2000-8000 images of 2048×2048 pixels (which costs 8-32GB) for each experimental condition. To convert images to quantitative information, we start from the particle detection and the trajectory reconstruction algorithms provided by *trackpy* package [174], which is a python package implementation of the widely-used Crocker & Grier algorithm [114]. Although this package is standard, tracking in a very dense situation needs further extension to prevent a memory issue. We will discuss this extension in Section 3.2. Here, we first present the general procedure of particle tracking in a rather dilute regime. We focus on the understanding of the algorithm in order to be able to optimize its parameters. The particle tracking procedure can be divided into four steps: detecting particles, reconstructing trajectories, filtering spurious trajectories and then subtracting the drift.

Step 1: Detecting particles

We first read a grey-scale experimental image as a 2048×2048 array, where each element $I(x, y)$ is the intensity ranging from black to white (0 to 256) of the corresponding pixel. The main idea of this detection algorithm is to detect local maxima within an area of particle apparent diameter, w . Unless stated otherwise, all distances in this section are in units of pixels. However, we must be aware that a raw experimental image usually contains imperfections such as long-wavelength background variation (comes from non-uniform sensitivity of camera's pixels and illumination) and purely random noise (digitization noise in the CCD camera), and these can lead to tracking errors. The purely random noise has typically 1-pixel correlation length and it can be suppressed by a Gaussian smoothing. The background variation is

removed by a boxcar average of an image with the filter size is equal to w . This is because the typical length scale of the background variation is much larger than particle size. These two steps are actually a bandpass filtration, which is already included in the particle detection function of *trackpy*. At this point, the resulting matrix is close to an "ideal" image $I_{\text{ideal}}(x, y)$ with almost no imperfection.

The next task is to detect particles in a form of blob-like objects. Particle positions in pixel (x, y) can be obtained as local maxima of $I_{\text{ideal}}(x, y)$. Each local maximum must be separated from the others by a separation parameter s that is equal to $w + 1$ by default. To find the local maximum, gray-scale dilation operation is applied to $I_{\text{ideal}}(x, y)$ with the dilation distance equal to s . Local maxima are therefore where the dilated image and $I_{\text{ideal}}(x, y)$ are equal. Therefore, if two local maxima are closer than s , the one with lower intensity will be discarded. In case of doublets and small aggregates, by tuning w and s , we can decide whether to track all individual particles or discard a whole aggregate (by firstly track it just as one particle and then remove it in later steps). In a dilute regime, we are interested in the individual motion of particles. Therefore, we always discard all the aggregates. We also note that local maxima that are closer to the edge than w are discarded from the tracking. Fig. 3.1a shows the result from this primary detection.

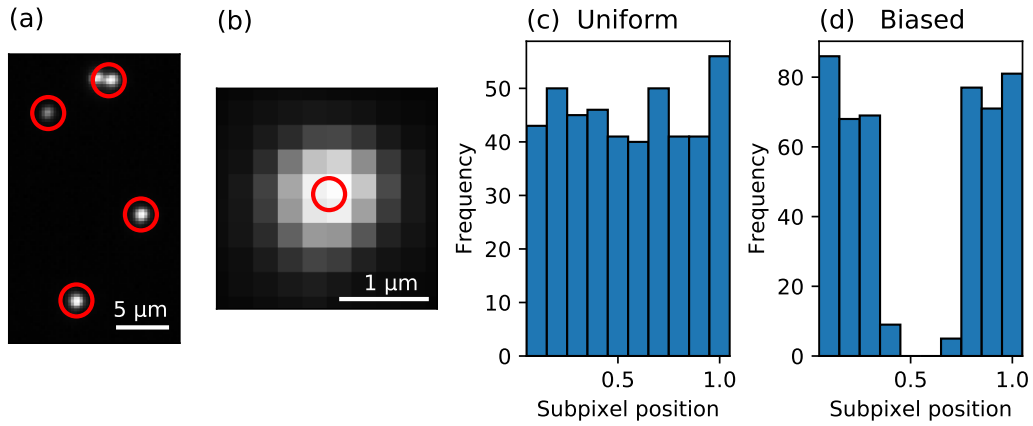


FIGURE 3.1: (a) Primary particle detection. Particles appear in white in a dark background. The red circles are centered at detected particle position. (b) Sub-pixel accuracy of the particle detection. The detected particle position is at the center of the red circle. (c) An acceptable uniform distribution reflecting a good choice of tracking parameters: particle size and smoothing size. (d) A biased sub-pixel position showing a non-uniform distribution.

The primary detection provides particle positions accuracy of one pixel. In fact, the detection function can provide sub-pixel accuracy. To do so, neighborhood of each local maximum (x, y) is defined as any pixels $(x \pm i, y \pm j)$ such that $i^2 + j^2 \leq R^2$, where $R = (w - 1)/2$. The offset is calculated iteratively by considering the brightness-weighted average centroid of the neighborhood as follows,

$$\begin{pmatrix} \epsilon_x \\ \epsilon_y \end{pmatrix} = \frac{1}{m_0} \sum_{i^2+j^2 \leq R^2} \begin{pmatrix} i \\ j \end{pmatrix} I_{\text{ideal}}(x + i, y + j), \quad (3.1)$$

where $m_0 = \sum_{i^2+j^2 \leq R^2} I_{\text{ideal}}(x + i, y + j)$ is the integrated brightness of the neighborhood pixels, which is referred in the tracking algorithm as *mass*. Initially, the center of the neighborhood is set to be the local maximum (x, y) . If the average in Eq. 3.1

yields an offset such that $|\epsilon_{x,y}| - R > 0.6$ in any directions, the center of the neighborhood will shift by one pixel in the direction of the offset $((x, y) \rightarrow (x', y'))$ and the iteration will continue until the condition $|\epsilon_{x,y}| - R < 0.6$ is satisfied. The final particle position is $(x_0, y_0) = (x' + \epsilon_x - R, y' + \epsilon_y - R)$ (see Fig. 3.1b). Besides, from the defined neighborhood pixels, other useful particle properties can be obtained such as *eccentricity* and *size* (from the radius of gyration of its Gaussian-like profile). These properties are very helpful in the filtering step when we want to discard any artifacts.

A crucial parameter for the particle detection is R . To check whether we have chosen a good value or not, one possible way is to monitor the sub-pixel bias. Ideally, the decimal part of both x_0 and y_0 should be evenly distributed (Fig. 3.1c). Choosing R too small, x_0 or/and y_0 tends to locate near the edge of a pixel resulting distribution that has a dip in the middle (Fig. 3.1d).

Step 2: Reconstructing trajectories

The next task is to link particle positions between consecutive frames and reconstruct their trajectories. The main idea is to match particles in frame t to corresponding particles in the next frame and then assign them an index. Crocker and Grier [114] have proposed an algorithm for the matching motivated by the dynamics of noninteracting Brownian particles. The probability distribution for N particles diffusing a distance Δr between lag time Δt is,

$$P(\{\Delta r_i\}|\Delta t) = \left(\frac{1}{4\pi D_0 \Delta t}\right)^N \exp\left(-\sum_{i=1}^N \frac{(\Delta r_i)^2}{4D_0 \Delta t}\right). \quad (3.2)$$

Maximizing this likelihood is equivalent to minimizing $\sum_{i=1}^N (\Delta r_i)^2$. Evaluating this sum requires $O(N!)$ computations. Luckily, the complexity can be greatly reduced by defining the maximum displacement, $(\Delta r)_{\max}$. This $(\Delta r)_{\max}$ must be larger than particle displacement between two consecutive frames and smaller than particle separation distance. This last condition ensured that there would be only one particle inside a disk of radius $(\Delta r)_{\max}$ around the original position of the previous frame. The algorithm thus recognizes the particle in one frame and the particle in the next frame as the same particle.

We note that it is very important to ensure that the data acquisition rate is fast enough to always have the particle displacement between two consecutive frames smaller than the separation so that $(\Delta r)_{\max}$ can be defined. Since we are working with self-propelled particles, the choice of $(\Delta r)_{\max}$ must be consistent with other parameters such as acquisition rate and particle velocity. For example, in the dilute regime we choose $(\Delta r)_{\max} \sim 1 \mu\text{m}$ while the particle separation is at least $1.6 \mu\text{m}$. At the acquisition rate of 20 Hz , we would lose particles that move faster than $20 \mu\text{m s}^{-1}$, and we have checked that we have never reached such high velocities in our experiments.

Even if we tune the tracking parameter very finely, there are always a few lost particles from one time step that reappear in the next few frames. By default, the algorithm would detect the reappearing particle as a new one. To resume the trajectory, the linking algorithm can be set to have memory. Missing particles that reappear nearby their last known locations will be remembered to keep the same index. However, the duration of the memory should not be longer than a maximum duration that would see particle displacement greater than $(\Delta r)_{\max}$. In that case, a

nearby particle could come close enough to replace the missing particle. This would lead to false indexing.

Step 3: Filtering spurious trajectories

Once the linking is completed, we still have to filter out spurious trajectories which come from the sample impurities and the false detection. Firstly, we add a simple condition: only keep trajectories that last for at least 30 frames (1.5 s at the acquisition rate 20 Hz). Secondly, we filter trajectories by their appearance. We can use the parameters from the particle detection (*mass*, *size* and *eccentricity*) to determine the sample impurities such as doublets, smaller aggregations and any alien particles.

Apart from the impurities, there are few particles that get stuck on the surface. These stuck particles are due to surface degradation of the experimental well. We notice that the longer we use the well, the more particles are stuck. We always try minimizing the stuck particles by performing the experiment with a fresh new well (within one week after the first usage). Nevertheless, few stuck particles in the dilute regime could have an influence on the statistics. We implemented a new function to discard them by looking for particles that have never displaced further than $2w$ from their original position in the first frame.

Step 4: Subtracting the drift

The raw trajectory right after the reconstruction is illustrated in Fig. 3.2a. All particles move toward the upper-right, which corresponds to a drift of velocity about $0.3 \mu\text{m s}^{-1}$. We have mentioned in Section 2.2 how we try to minimize the drift at the experimental stage. Even though the drift is never perfectly removed experimentally, we can continue reducing it from the trajectories using the drift subtraction algorithm (also from *trackpy*). To do so, the drift motion is calculated from the cumulative sum of the average particle displacement along the time t , $\sum_{t=0}^t \langle \Delta r_i(t) \rangle_i$. Then, it is subtracted from the trajectories, i.e.,

$$r_i^{\text{final}}(t) = r_i(t) - \sum_{t=0}^t \langle \Delta r_i(t) \rangle_i. \quad (3.3)$$

We show the final trajectories in Fig. 3.2b. There is no more global motion of the particles. In addition, the stuck particles on the left area of Fig. 3.2a are also removed. The resulting trajectory is now ready for analysis like what we have already discussed in Section 2.3.

3.2 Particle tracking in a dense regime

In a dense regime, particle tracking is more tricky than in the dilute case. When particles are closely packed, a deep knowledge is required for tuning tracking parameters. Besides, the amount of data is much larger because we track a lot of particles in one frame: from a few hundred particles in the dilute regime to $\sim 10^4$ particles per frame in the dense regime. In this section, we present two main points to be concerned with when changing from tracking in a dilute to a dense regime: tuning parameters and data management.

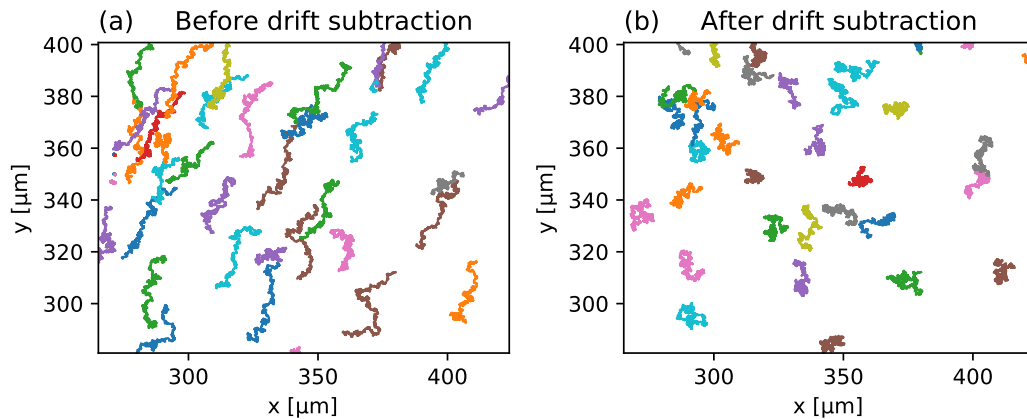


FIGURE 3.2: The reconstructed trajectories of passive particle in a dilute regime over $\Delta t = 100$ s: (a) before and (b) after filtering out stuck particles and drift subtraction.

3.2.1 Tracking parameters

To detect particles when they are closely packed, we have to tune carefully tracking parameters. The aim is to detect all particles, however, there are always some particles that are lost from the tracking. For example, when a particle appears to be a bit darker than its neighbors (whether it shows the platinum side or it diffuses slightly upwards). We thus have to minimize the lost particles by digging into the detection function of *trackpy*. We can decrease the minimum threshold or the percentile value of local maxima. We also suggest that using a separation s that is slightly smaller than the apparent diameter w prevents us from losing the particles (reduce from 10% to 2% lost particles). With an adjustment of s and w , we can decide how to deal with unavoidable sample impurities such as doublets and small aggregates. Depending on the type of analysis we want to carry out, we can either discard a whole aggregate (by tracking only the brightest spot, see Fig. 3.3a, and remove it in the next filtering step) or track all particles in an aggregate (see Fig. 3.3b). Generally, if we focus on particle dynamics (like in Chapter 4), we discard all aggregates, so that they are not taken into the statistics. For microrheology (in Chapter 5), we keep every single aggregated particle because we are more interested in morphology.

3.2.2 Data streaming with hierarchical data format (HDF)

By default of the *trackpy* package, the datatype of a resulting file (both position and trajectory files) is a comma separated values (CSV) text file. To process this type of data, we have to import the whole file in memory at once. It is fine in the dilute and intermediate regime where the number of particles is not large (typically less than 4000 particles). However, when we extend our study to the dense phase, the number of interesting particles is of the order of 10^4 . The position matrix of all particles of all frames can exceed 1 GB. It is thus impractical to import the whole data in memory for linking the trajectories and further analysis. We therefore took this obstacle as an opportunity to learn data streaming, which is very useful to handle such big data.

The *trackpy* package has already provided an advanced feature on data streaming using the hierarchical data format version 5 (HDF5), which is a multidimensional array of data. HDF5 is structured like a dictionary. We can specify a *group* to store a *dataset* (actual data) within one HDF5 file. The great benefit of HDF5 is data slicing,

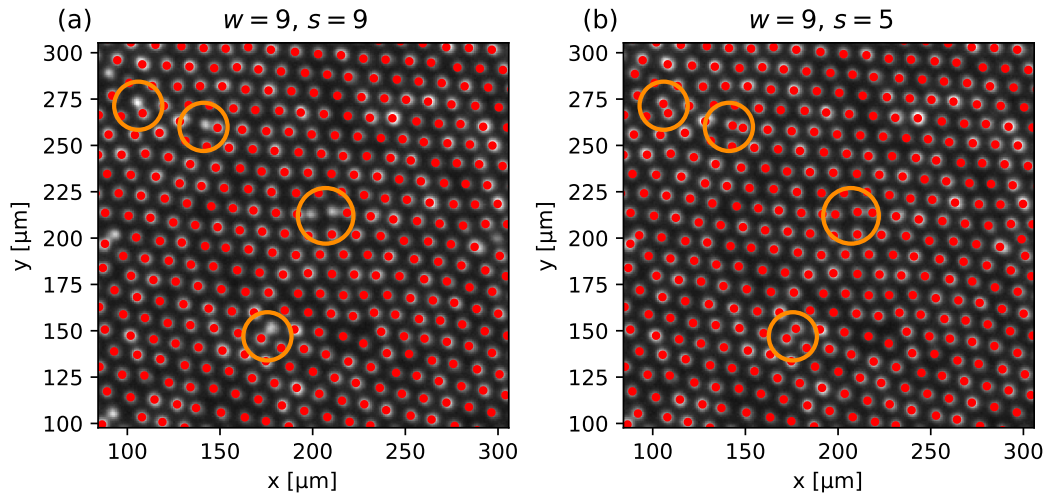


FIGURE 3.3: Demonstration of particle tracking in the dense regime. Particles appear in white in a dark background. The tracked particles are represented by red dots. The particle apparent diameter w is 9 px in both images, and the separation distance s are (a) 9 px and (b) 5 px. The orange circles emphasize the differences between two values of s .

which means we can extract only a part of a dataset into memory for processing. Also, we can write partially a dataset into a HDF5 file as many times as we want. This powerful attribute allows us to read and write an unlimited data size during the processing.

In our usage, the resulting position and trajectory matrix are stored frame by frame in a HDF5 file and we are able to write or retrieve frames one by one. This is already implemented in the original *trackpy*. However, the filtering spurious trajectories and the drift subtraction algorithm for a framewise data are still missing from the original package. We have thus developed our python scripts to perform these tasks and also for further analysis. For example, the simplest way to visualize the data is plotting particle trajectories. The original plot function of *trackpy* can only read a CSV file format. In Fig. 3.4, we show particle trajectories (in the dense regime) processed from the HDF5 data. We have also developed the script supporting HDF5 data format for classical analysis such as MSD and radial-pair correlation function $g(r)$, and specific tools for dense systems such as static/dynamic structure factor $S(q)/S_4(q, \Delta t)$, hexatic order parameter ψ_6 , overlap function $F(\Delta t)$ and network analysis. The rest of this chapter is a brief description of the analysis tools for our experimental result in a dense regime.

3.3 Structure investigation

Structure is an important property to determine a state of the system. The classical tool to investigate the structure in real space is radial-pair correlation function $g(r)$. Another tool to see a long-range correlation in structure is static structure factor $S(q)$, which is defined in a reciprocal space. For the last tool to determine a local order in the system, we use hexatic order parameter ψ_6 .

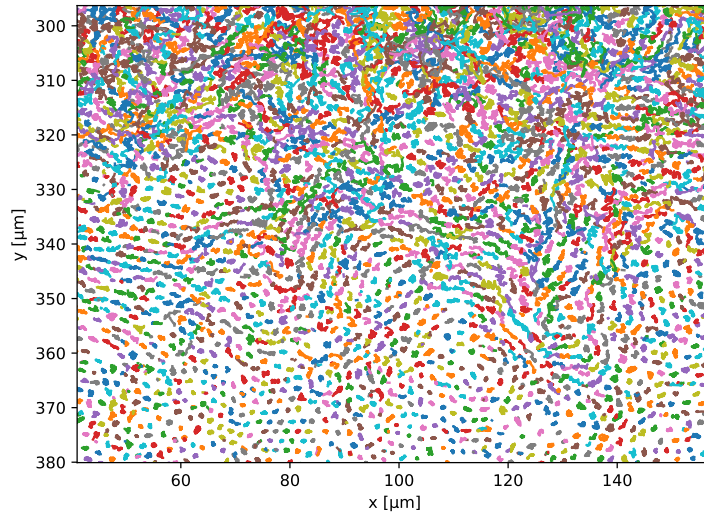


FIGURE 3.4: The reconstructed trajectories of active particles in a middle part of the sediment over $\Delta t = 15.2$ s. The gravitational gradient is along y direction downwards.

3.3.1 Radial-pair correlation function, $g(r)$

Radial-pair correlation function $g(r)$ is related to the probability of finding other particles at a given distance from a particle of interest. The shape of $g(r)$ can roughly tell us whether our system is in a gas, liquid or solid phase. In the dilute fluid (gas) phase of a hard sphere system, there is no internal structure and all distances are equally possible except below the particle diameter σ_0 . The $g(r)$ is zero for $r < \sigma_0$ and equal to one for $r > \sigma_0$. By contrast, for a solid phase in which particles are located only at several possible distances, $g(r)$ shows peaks at those distances and valleys at distances where particles are rarely located.

$g(r)$ is also linked to pair potential $u(r)$ between particles. At low density limit, they are directly linked via $\lim_{\phi \rightarrow 0} g(r) = \exp(-u(r)/k_B T_0)$ [183]. This relation no longer holds at higher densities due to many-body interactions. However, Ref. [184] has recently proposed a novel iterative method to obtain $u(r)$ from $g(r)$ which works for any density. Therefore, knowing the shape and peak value of $g(r)$ provides us not only a system internal structure, but also the pair potential of a particle.

The definition of $g(r)$ is in the following [185]:

$$g(r) = \frac{1}{\rho N} \frac{1}{2\pi r dr} \sum_i^N \sum_{j \neq i}^N \delta(r_{ij}), \quad (3.4)$$

where ρ is the number density, N is the number of particles in the area of interest, dr is the bin size, r_{ij} is the distance between particle i and particle j , and δ is a rectangular impulse function such that

$$\delta(r_{ij}) = \begin{cases} 1, & \text{if } r < r_{ij} < r + dr \\ 0, & \text{otherwise.} \end{cases} \quad (3.5)$$

To calculate $g(r)$ from the particle trajectories, we first have to specify a cutoff distance (we use $\sim 7\sigma_0$). For each particle, we search for its nearest neighbors (will be

described in Subsection 3.5.1) within the specified cutoff distance. Then, we bin the neighboring distance and normalize each bin by a corresponding area, which is a circumference of a circle of radius r . Finally, we apply the same algorithm for every particle and every frame to obtain the average $g(r)$ at the end.

Since we always deal with a finite experimental area, particles near the edges must be handled very carefully. There are two possible solutions to deal with the edges: (1) Only consider particles that are further from the edges than the cutoff distance (see Fig. 3.5a), or (2) handle the particle near the edges by considering an arc of the ring, not the whole circumference, for the normalization (see Fig. 3.5b). The second solution should give the most accurate result with high statistics, but with a cost of computation. However, if we have a wide enough experimental area comparing to the cutoff distance, the first solution would provide almost the same accuracy with much lighter computation. We note that typically for amorphous solid, $g(r)$ is suited to see short-range structure. Therefore, choosing a too large cutoff would give useless information at long-range distance with unnecessary computation and increased margins, so poorer statistics.

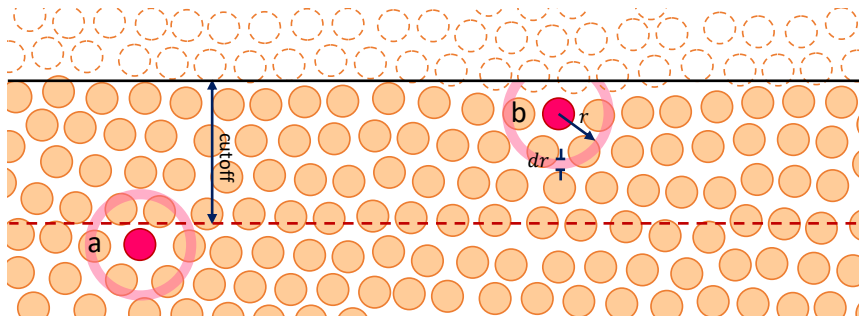


FIGURE 3.5: Schematic view of our experimental field of view. The solid black line is the edges of the observation field. The tracked particles are presented in filled circles. The dashed circles are particles outside the observation field and they are not picked up by the tracking algorithm. There are two possible ways to handle the boundary: (a) Only consider particles that are further from the edge than the cutoff distance. The normalization area is thus a full ring (the pink ring). (b) If a particle is closer to the edge than the cutoff distance, the normalization area is the arc of the ring that is inside the observation area.

We show a typical example of $g(r)$ of our system in the dense phase in Fig. 3.6. The smallest peak on the left corresponds to the doublets or small aggregates. Even if we subtract most of them during the tracking process, few of them are still present. However, they have little influence on the ensemble average among particle positions. The highest peak corresponds to neighbors in the first shell. We can obtain inter-particle distance from the position of the highest peak, which we find that it is always slightly larger than the physical diameter $\sigma_{\text{phys}} = 1.6 \pm 0.2 \mu\text{m}$. This is due to the electrostatic repulsion between our Janus particles in water. We thus use the position of the highest peak of $g(r)$ to define an effective diameter σ_0 . Depending on the experimental conditions such as batch of colloids or tilt angle, we obtain σ_0 between $2.0 \mu\text{m}$ to $2.3 \mu\text{m}$.

The next two smaller peaks at $r \sim \sqrt{3}\sigma_0$ and $2\sigma_0$ correspond to neighbors in the second shell. There are two distances with almost the same height which is typical in 2D hexatic arrangement. We can also notice the third shell neighbors from the next two peaks. The visibility of these small peaks show internal structure of the system. If we compare the $g(r)$ between two samples, we can thus say which one is less structured by considering the appearance of these peaks.

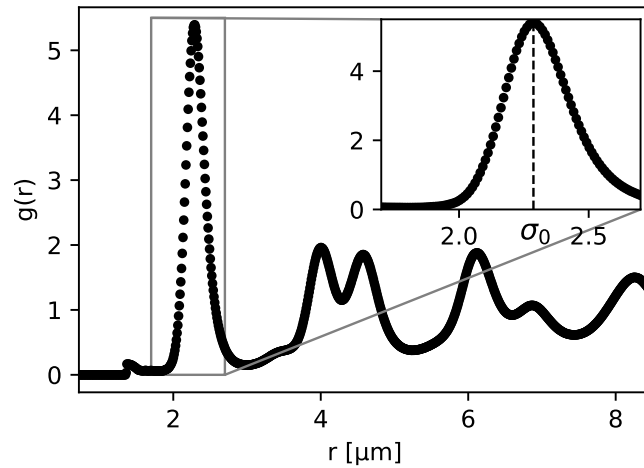


FIGURE 3.6: Typical example of the pair correlation function $g(r)$ of our dense passive system at the bottom part of the sediment. The reference effective diameter σ_0 is taken from the first-peak position.

3.3.2 Static structure factor, $S(q)$

While $g(r)$ is very well suited to investigate short-range order, another useful tool to see the long-range structure is the static structure factor $S(q)$. Light, neutron and X-ray scattering experiments are often used to probe material structure. The resulting intensity pattern, showing structure in reciprocal space, is related to $S(q)$.

In our experiments, we obtain particle positions from particle tracking. Therefore, we can compute $S(q)$ from the following mathematical expression [185],

$$S(q) = \frac{1}{N} \left\langle \sum_{i,j} e^{-i\mathbf{q} \cdot (\mathbf{r}_i - \mathbf{r}_j)} \right\rangle. \quad (3.6)$$

In practice, rather than computing directly Eq. 3.6, we obtain $S(q)$ from a digital (fast) Fourier transform of a binary image $I(x, y)$ corresponding to particle position in real space, \mathbf{r}_i :

$$I(x, y) = \begin{cases} 1, & \text{if } (x, y) = \mathbf{r}_i \\ 0, & \text{otherwise} \end{cases} \quad (3.7)$$

The reason why we use the binary image instead of the real experimental image is that we have to separate the form factor from the structure factor. To illustrate this, we show in Fig. 3.7a a raw experimental image in the dense phase and its corresponding zoom-in binary image in Fig. 3.7b. However, our image is not periodic and particles closer than $2w$ from any edge are not detected. Therefore, before applying the fast-Fourier transform, the image must be cropped (to remove $\sim 2w$ from the edges) and multiplied by a Hanning window. We use the *ImageStructureFactor* class from Ref. [186] for the fast-Fourier transform and radial average of the transformed image (see Fig. 3.7c) to obtain $S(q)$.

The resulting $S(q)$ from time average is shown in Fig. 3.8. The highest peak locates at $q = 1/\sigma_0$ corresponds to the first shell of neighbors. At small q , $S(q)$ is flat indicating no long-range spatial correlation in the system.

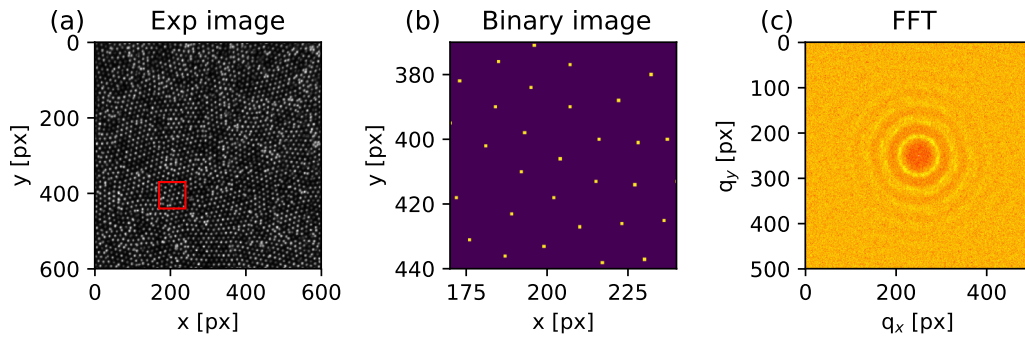


FIGURE 3.7: Illustration of a step-by-step procedure to obtain $S(q)$ from the experimental images. (a) A raw experimental image. (b) A binary image corresponds to a small area (red square) in (a). (c) Fast-Fourier transform of a corresponding binary image of (a). $S(q)$ is obtained from a radial average of (c).

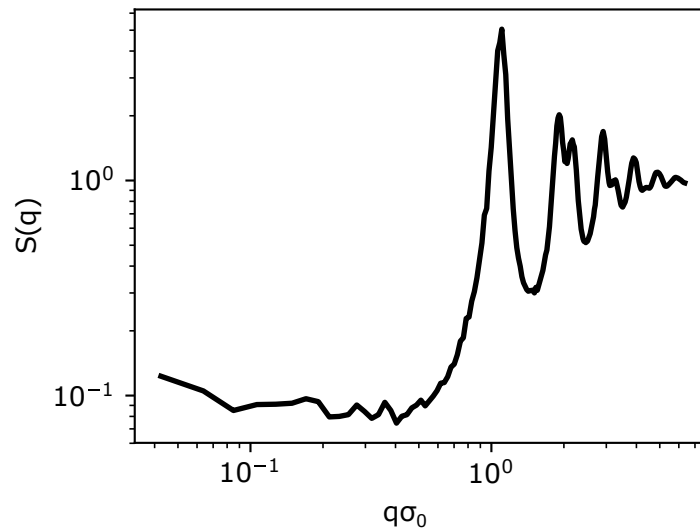


FIGURE 3.8: Static structure factor $S(q)$ of the passive system at the bottom part of the sediment.

3.3.3 Hexatic order parameter, ψ_6

Both $g(r)$ and $S(q)$ analyse the structure using an average over particles. They provide us the mean-field information of the monolayer hexatic arrangement in the dense phase. Since our system always contains some impurities in the form of doublets and small aggregates, the particle arrangement is never perfectly crystalline. To investigate local structure around individual particle and see how ordered/disordered phase distribute in the system, we use the hexatic order parameter $\psi_{6,i}$ which quantifies the six-fold symmetry of 6-nearest neighbors of each particle i , i.e.,

$$\psi_{6,i} = \frac{1}{6} \sum_{j \in N_i} \exp(6i\theta_{ij}), \quad (3.8)$$

where N_i is the set of the 6-nearest neighbors of particle i . θ_{ij} is the angle between the x -axis and the vector connecting particles i and j .

One can compute $\psi_{6,i}$ directly from Eq. 3.8. It first requires to obtain θ_{ij} from an arctangent, and then evaluate the exponential term from sines and cosines. This computation is heavy when dealing with a large number of particles. However, there is a trick to perform this task with less computation. Following from Ref. [187], the exponential term of power of 6 can be rewritten as

$$e^{6i\theta_{ij}} = (\cos \theta_{ij} + i \sin \theta_{ij})^6. \quad (3.9)$$

Hence, the real and imaginary components are given by

$$\begin{aligned} \Re(e^{6i\theta_{ij}}) &= \cos^6 \theta_{ij} - 15 \cos^5 \theta_{ij} \sin^2 \theta_{ij} + 15 \cos \theta_{ij} \sin^4 \theta_{ij} - \sin^6 \theta_{ij}, \\ \Im(e^{6i\theta_{ij}}) &= 6 \cos^5 \theta_{ij} \sin \theta_{ij} - 20 \cos^3 \theta_{ij} \sin^3 \theta_{ij} + 6 \cos \theta_{ij} \sin^5 \theta_{ij}. \end{aligned} \quad (3.10)$$

Here the $\cos \theta_{ij}$ and $\sin \theta_{ij}$ can be calculated easily from particles separation vector \mathbf{r}_{ij} and its components Δx_{ij} and Δy_{ij} , i.e.,

$$\begin{aligned} \cos \theta_{ij} &= \Delta x_{ij} / |\mathbf{r}_{ij}|, \\ \sin \theta_{ij} &= \Delta y_{ij} / |\mathbf{r}_{ij}|. \end{aligned} \quad (3.11)$$

With this powerful trick, we can compute $\psi_{6,i}$ of all particles in one frame at once. We first search for particles 6-nearest neighbors (will be described in Subsection 3.5.1) and collect the neighborhood in a $(N, 7)$ array. It is an array of all particles index in the first column and their corresponding nearest neighbors in the 2nd (the nearest) to 7th (6th nearest neighbor) columns. The rest of the algorithm is just simple matrix operations. We compute \mathbf{r}_{ij} and obtain $\cos \theta_{ij}$ and $\sin \theta_{ij}$ from Eq. 3.11. Then we obtain the real and imaginary components from Eq. 3.10 and divide by 6. After discarding particles near the edges (distance from the edges less than $2\sigma_0$), we collect the resulting $\psi_{6,i}$ of all particles in complex form because it contains the information of both modulus and phase of $\psi_{6,i}$. We display maps of modulus and orientation of $\psi_{6,i}$ in the passive case as illustrated in Fig. 3.9.

The modulus of $\psi_{6,i}$ quantifies how close to the hexatic arrangement the neighborhood of particle i is. If the modulus is close to 1, it means that the 6-nearest neighbors of particle i locate like a hexagon around it. This indicates a highly local order around particle i . The further $|\psi_{6,i}|$ is from one, the more distorted from the hexagon shape. Fig. 3.9a shows that in our dense phase, the structure of the system is a mixture of highly ordered phase (purple-dark blue particles) and low ordered phase (orange-yellow particles). In this case, we can infer that our system is in the glass phase.

To see the bond orientational order in the high $|\psi_{6,i}|$ phases, we consider the projection of the phase of $\psi_{6,i}$ [135, 155]. This phase is in the range $[-\pi, \pi]$ and it corresponds to the lattice orientation $[0, \pi/3]$. We show in Fig. 3.10 the relation between these two ranges. To convert the phase to the orientation, we use the projection of the phase towards y direction (upward). To illustrate this we show in Fig. 3.9b a resulting projection map evidencing clear boundaries between small domains of different orientations. Besides, inside each high $|\psi_{6,i}|$ domain, there is no long-range orientation order. This evidence supports that our present example is indeed glassy. Furthermore, we can use the bond orientation to differentiate between purely crystalline, hexatic and polycrystalline phase in a sample that is highly ordered.

While $\psi_{6,i}$ maps are well suited to see the spatial distribution of high/low order domains, they only represent one snapshot of the system. To get an idea on the distribution of $\psi_{6,i}$ in one system we can compute the PDF of the modulus of $\psi_{6,i}$ among

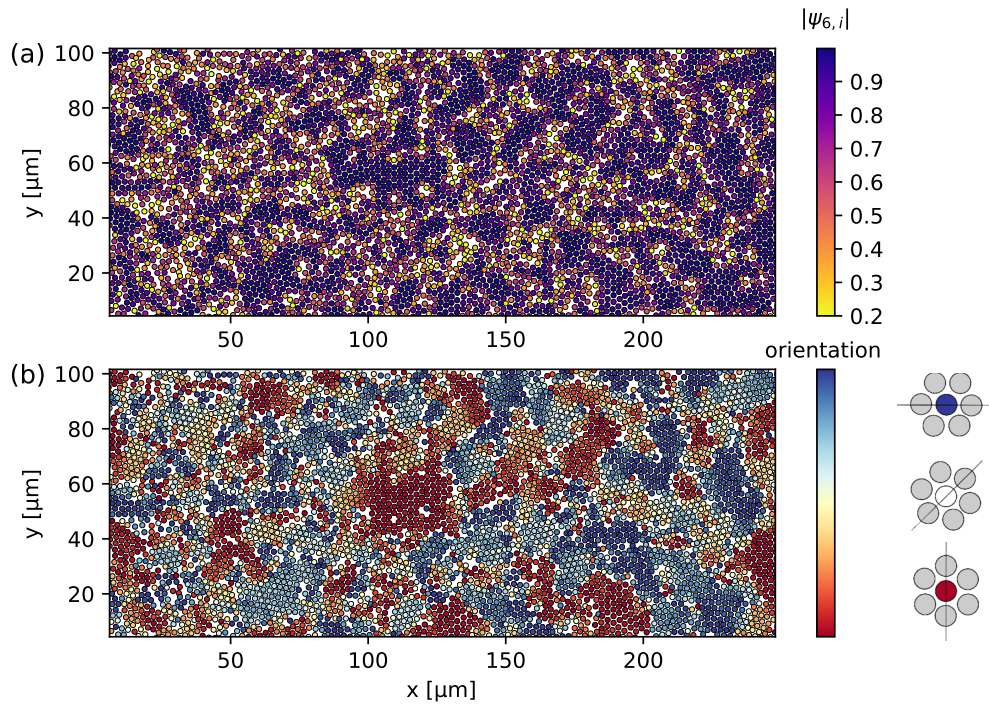


FIGURE 3.9: Maps of hexatic structure parameter $\psi_{6,i}$ of the passive system at $\phi = 0.75 \pm 0.03$: (a) modulus and (b) orientation. The white areas are from sample impurities and tracking errors.

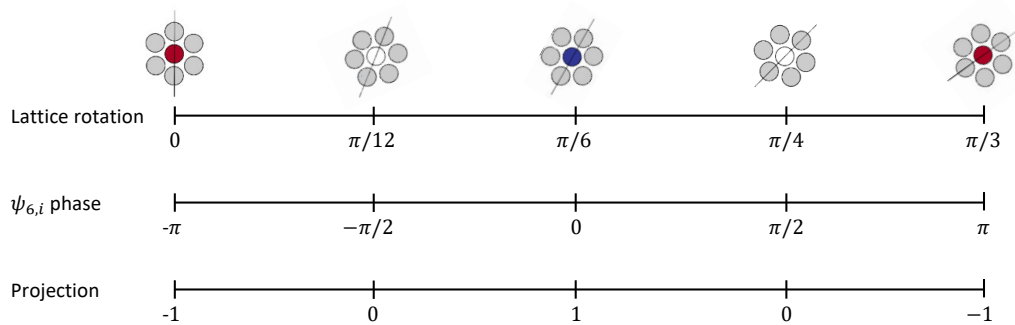


FIGURE 3.10: Schematic chart showing the conversion between lattice rotation, $\psi_{6,i}$ phase and the projection of the phase.

all particles in every frame. We show a typical example of such distribution in our dense phase in Fig. 3.11. The highest peak on the left corresponds to highly ordered particles. We do not have a clear origin of the two lower peaks at $|\psi_{6,i}| \sim 0.33$ and $|\psi_{6,i}| \sim 0.65$. We guess that they relate to the sample defects and our definition of neighbors. From the PDF, it looks like the majority of the particles are highly ordered. Actually, we calculate that in this particular sample there are 47% of the particles that have $|\psi_{6,i}| > 0.8$, which from now on we call crystalline particles.

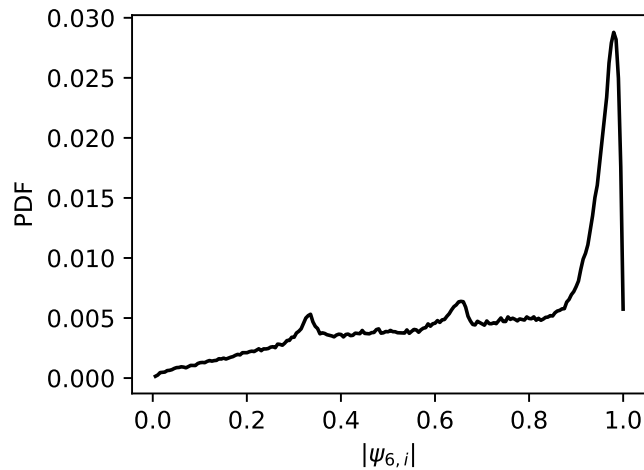


FIGURE 3.11: Example of the PDF of the modulus of the hexatic order parameter $|\psi_{6,i}|$ of the passive case at the bottom part of the sediment.

3.4 Dynamical analysis

In the following, we will briefly describe analysis tools we use to capture the system dynamics. The most classical tool would be the mean square displacement, MSD. Another tool that is widely used in glass community is the overlap function $F(\Delta t)$, from which we can define the relaxation time τ . The last one is the four-point correlation structural factor $S_4(q, \Delta t)$ that is used to investigate the dynamics heterogeneity, which is normally observed near the glass transition. These quantities are computed by comparing the dynamics of the same particles between two frames (cross-frame analysis) and then by averaging over all particles. The result is displayed as a function of lag time Δt . For the sake of statistics, we also average the result among different initial time t_0 for each given Δt . The smaller Δt , the better statistics. We thus always restrict the largest t_0 at one-third of the total acquisition time.

3.4.1 Mean square displacement, MSD

We have already mentioned the mean square displacement (MSD) in Subsection 2.3.2 when we investigated the particle motion in the dilute regime. Now, we are going to discuss it in more detail focusing on the dense regime. The calculation of the MSD is the same definition as provided before in Eq. 2.6, i.e.,

$$\langle (\Delta r)^2 \rangle = \left\langle \frac{1}{N} \sum_{i=1}^N (r_i(t_0) - r_i(t_0 + \Delta t))^2 \right\rangle_{t_0}.$$

For the dilute case, the algorithm calculating MSD is straightforward. Particle trajectories are grouped by particles index and the individual displacement at a given Δt is then calculated. However, in the dense phase, we cannot import the whole trajectory into memory at once. We, therefore, import only two frames separated by Δt at once and match particles index between both frames before calculating their displacement. Furthermore, since we are looking at the dynamics at a long-timescale, calculating every consecutive Δt is not efficient. Instead, we vary Δt logarithmically, which can save a lot of calculating time.

We show in Fig. 3.12 a typical MSD in our passive system at the bottom of the sediment ($\phi \sim 0.75$). The MSD exhibits typical glassy dynamics: an increase at a short-time scale before reaching a plateau and then a second increase at long-time scale. This plateau indicates a caged motion, in which a particle is trapped in a cage formed by its neighbors. We can extract a cage size from the plateau height. The error bars are obtained from the standard deviation among individual particles and different initial time t_0 .

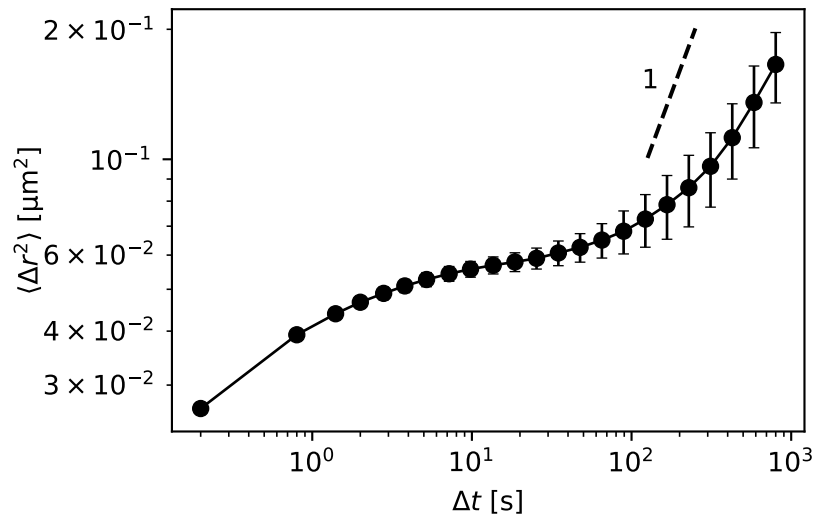


FIGURE 3.12: The mean square displacement MSD of the passive system at the bottom part of the sediment ($\phi \sim 0.75$). The dashed line indicates the slope one, which refers to diffusive motion.

3.4.2 Overlap function, $F(\Delta t)$

Another dynamic quantity that has been used widely in the glass community is the overlap function $F(\Delta t)$ [188], which tells us the ratio of particles that have not moved within a given lag time Δt .

To calculate the overlap function, we first define a microscopic overlap function $w_i(t_0, \Delta t) = \Theta(a - \|\vec{r}_i(t_0 + \Delta t) - \vec{r}_i(t_0)\|)$ where Θ is the Heaviside step function. $w_i(t_0, \Delta t)$ indicates whether particle i has moved further than $a = 0.3\sigma_0$ between times t_0 and $t_0 + \Delta t$. Next, we compute the average among different t_0 :

$$F(\Delta t) = \left\langle \frac{1}{N} \sum_{i=1}^N w_i(t_0, \Delta t) \right\rangle_{t_0}. \quad (3.12)$$

The computing algorithm of $F(\Delta t)$ is very similar to the one for the MSD. Instead of the mean square displacement, we just compute $\langle w_i(t_0, \Delta t) \rangle_i$ at the end of the t_0 loop. An example of a $F(\Delta t)$ is shown in Fig. 3.13. In this example, there is a two-step relaxation typical of glassy dynamics where the second relaxation corresponds to the exit from the plateau of the MSD in Fig. 3.12. We define the relaxation time τ when half of the particles has already moved, i.e., $F(\tau) = 0.5$.

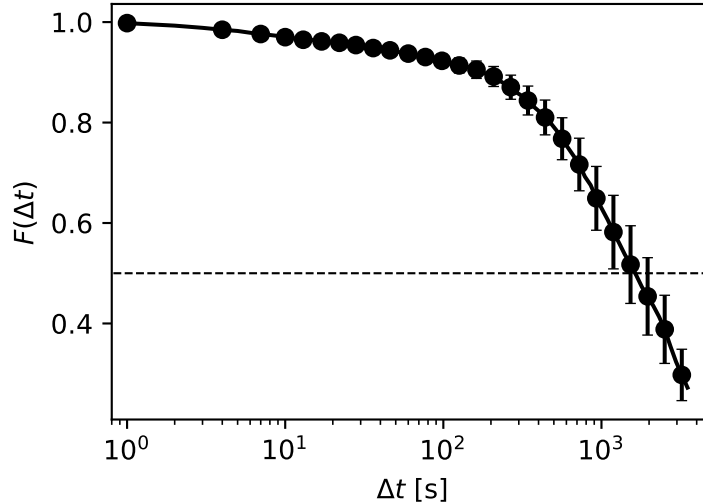


FIGURE 3.13: The overlap relaxation function $F(\Delta t)$ of the passive system corresponding to Fig. 3.12. The relaxation time τ is defined when $F(\Delta t)$ reach 0.5 (dashed line).

MSD and $F(\Delta t)$ provide the global information of the system dynamics, and we can quantify the physical relaxation parameters from them that are the cage size and the relaxation time τ . However, this is not enough to investigate an out-of-equilibrium dense system since it has been found that the motion of the particles exhibits spatio-temporal dynamics fluctuation. In the same system, the particles can be divided into "fast" and "slow" sub-domains, and these domains also evolve with time. This is known as "dynamic heterogeneity" [189]. To capture this emergent dynamic, many people use the following four-point structure factor. We will see that this quantity cannot be applied properly in our system, however for the sake of completeness, the next session defines it and shows its limits.

3.4.3 Four-point structure factor, $S_4(q, \Delta t)$

The four-point structure factor $S_4(q, \Delta t)$ [185, 188, 190] has been used to quantify spatial correlations between slow particles. $S_4(q, \Delta t)$ depends on both (reciprocal) space and time. For simplicity, we calculate $S_4(q, \Delta t)$ at a fixed interval time when $\Delta t = \tau$. First, we find the slow particles from the displacement between two frames separated by τ . Then, similarly to the static structure factor, we create a binary image but only of the slow particles. After that, we apply the fast-Fourier transform to the binary image and obtain the radial average.

In case we have a strong gravitational gradient in one direction, analyzing a wide area would average the effect of the density variation along the gradient. To work at a constant density, we divide the sediment into several thin slices perpendicular to

the density gradient and analyze each slice separately. We then obtain the $S_4(q, \Delta t)$ from a 1D image. The slicing will be described in detail in Chapter 4 and the dynamical analysis tools are the same for both 2D and 1D cases, except $S_4(q, \Delta t)$. From the binary image of slow particles of one slice, we do the coarse-graining of the size $2\sigma_0$ in x direction, which is the direction of the density gradient, for a better statistic. We subtract each line with its mean and multiply by Hanning window to have the edge goes to zero (same method as $S(q)$). At this point we have a stack of the coarse-grained slices elongate in y direction, $S(x, y, t_0, \tau)$. Finally we apply the fast-Fourier transform in y direction and do the averaging as follows,

$$S_4(q_y, \tau) = \left\langle \frac{1}{L_x} \sum_{x=0}^{L_x} \left(\frac{|\tilde{S}(x, q_y, t_0, \tau)|^2}{\sum_{q_y} |\tilde{S}(x, q_y, t_0, \tau)|^2 / L_y^2} \times \frac{N_s(x)}{N(x)} \right) \right\rangle_{t_0}, \quad (3.13)$$

where L_x is the length of the coarse-grained slice in x direction (same as L_y) and $N_s(x)/N(x)$ is the ratio of slow particles in x slice.

Fig. 3.14a shows the $S_4(q_y, \Delta t)$ of our passive system at various densities. The four-point structure factor at large q shows a similar shape as the static structure factor (Fig. 3.8). This means that the local structure of the slow domains is identical to the structure of the whole system. The more interesting point is at small q . The $S_4(q, \Delta t)$ increases as $q \rightarrow 0$ indicating a long-range spatial correlation of these slow domains, which is an evidence of dynamic heterogeneity, and it is more pronounced when increasing density.

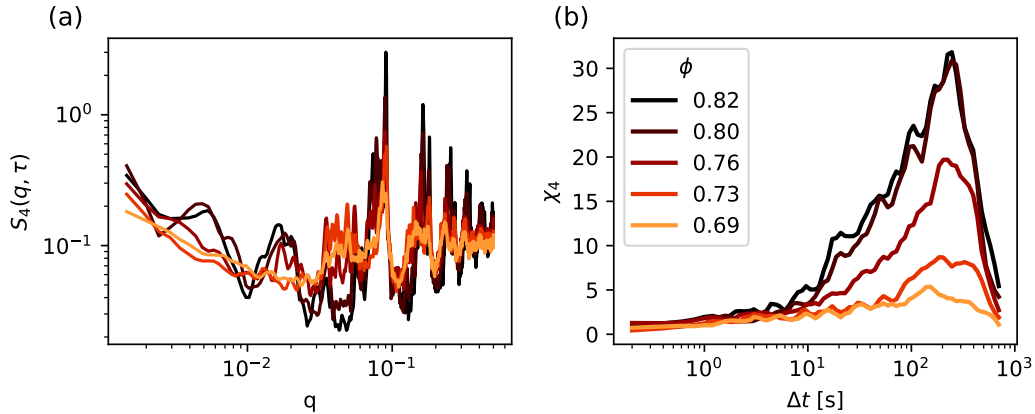


FIGURE 3.14: (a) The four-point structure factor $S_4(q, \tau)$ in the passive system obtained from different slices of the sediment with different densities. (b) The dynamic susceptibility, $\chi_4(\Delta t)$ as a function of lag time Δt .

There are two parameters to quantify the heterogeneity of dynamics: the dynamic susceptibility, $\chi_4(\Delta t)$, and the dynamic correlation length $\xi_4(\Delta t)$, and they are related to $S_4(q, \Delta t)$ at small q via the Ornstein-Zernicke form,

$$S_4(q, \Delta t) = \frac{\chi_4(\Delta t)}{1 + q^2 \xi_4(\Delta t)^2}. \quad (3.14)$$

One can obtain the dynamic susceptibility via $\chi_4(\Delta t) = \lim_{q \rightarrow 0} S_4(q, \Delta t)$. However, in practice we cannot use this relation and Eq. 3.14 to obtain directly χ_4 and ξ_4 , respectively, because we are limited by the observation window which prevent us to access long enough length scale. As can be seen from our example in Fig. 3.14a, the

fit of $S_4(q, \tau)$ by Eq. 3.14 is impossible here because we see no plateau. We therefore follow Refs. [188, 190, 191] to define χ_4 in an open system (like ours) as

$$\chi_4(\Delta t) = \frac{1}{N} (\langle N_s^2(\Delta t) \rangle - \langle N_s(\Delta t) \rangle^2), \quad (3.15)$$

where N_s is the number of slow particles in the system, and N is total number of the particles. We note that Eq. 3.15 is just an estimation and is true only in thermodynamic limit. The time for $\chi_4(\Delta t)$ to reach its maximum, t_4^{\max} , is found to be related with τ [192]. Moreover, it has been shown that the increase of $\chi_4(\Delta t)$ relates to an increase of $\zeta_4(\Delta t)$ [193] and they both increase when the system approaches the glass transition [194, 195].

In Fig. 3.14b we show an example in our experimental system (corresponding to the dense passive case) $\chi_4(\Delta t)$ obtained from Eq. 3.15. $\chi_4(\Delta t)$ is higher at high densities indicating a higher degree of dynamic heterogeneity. The maximum points stay at the same position reflecting that the relaxation time does not depend on the density. We will show later in Chapter 4 that the system considered in this example has already crossed the glass transition density. This is why $\chi_4(\Delta t)$ does not shift towards higher Δt when the density is increased like in Refs. [194, 195].

Since our experiments are always dealing with a confine observation area, obtaining a quantity that involves long-range correlation (like $\chi_4(\Delta t)$ and $\zeta_4(\Delta)$) is tricky as the uncertainty is very high. We, therefore, have to find another way to estimate a dynamic correlation length using network analysis.

3.5 Network analysis

In this section, the assembly of the colloids is considered as a network. The particles and their neighborhood are represented by *nodes* and *edges*, respectively. With the network analysis, we can visualize changes in the structure during the system relaxation, and we can infer the relaxation mechanisms of the system (Chapter 4). It is also an essential tool for a further study on the rheology of active colloids (Chapter 5).

3.5.1 Defining neighbors

When we view our system as a network, a crucial point is how we determine the connection between particles, i.e., whether particle j is a neighbor of particle i or not. There are several criteria to define the neighborhood. The simplest definition is using a fixed Euclidean distance between two particles. However, since we are working on different densities and the interparticle distance varies a lot, using a fixed distance threshold would be difficult to interpret the resulting behavior in our system. We thus prefer to use a criterion that is independent of the system density. In the following, we describe the two neighbor definitions that we use throughout our study and discuss in which situation we choose to use one definition rather than another one.

6-nearest neighbors (6-NNs)

Looping on all particle pairs to identify the nearest neighbours of each particle would be inefficient. Instead, we use the k-neighbors lookup algorithm, which is already implemented in *cKDTree* function. The algorithm is based on Ref. [196], from the

scipy.spatial module [179]. A k -d tree [197] is a data structure in a form of binary search tree (BST) but with coordinates as sorting values. In 2D ($k = 2$), a left branch always corresponds to points that are either on the left or below points in a right branch (see Fig. 3.15). Once the data are organized in this way, searching nearest neighbors is significantly faster than the brute force search (this is true only at low dimensions). This is because an entire part of subtrees can be ignored once it has been verified that a query point is closer to a point in other branches. For example in Fig. 3.15, if one wants to find the nearest neighbors of the point G, we can completely eliminate the points B, D, and E which are on the left side of the point A (left branch). In practice, the searching time is in order of $O(2^d + \log N)$ (while the brute force search gives $O(N)$).

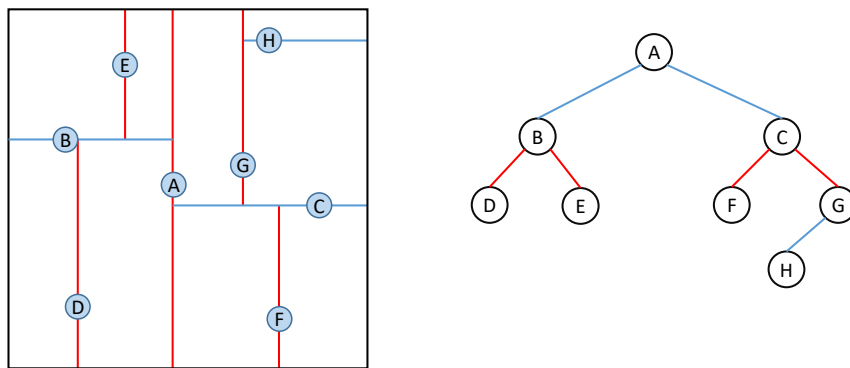


FIGURE 3.15: A schematic diagram showing how a set of 2D coordinates is organized in a 2-d tree structure. First, the group of points are divided into left and right comparing to the center point A (determined from the median of the horizontal direction). The next branches are for the median in the vertical direction from both sides of A: B for the left box and C for the right box. The division process keeps repeating by switching back and forth between horizontal (red lines) and vertical division (blue lines). The resulting 2-d tree is shown on the right side.

Voronoi neighbors

For a given set of coordinates, the Voronoi cell around each coordinate consists in all points of space that are closer to the considered coordinate than to any other coordinate of the set. Fig. 3.16 is an example of a Voronoi diagram constructed from the particle coordinates of our experiment. We can understand Voronoi cells as a result from a bisection of the Delaunay triangulation (orange lines). Voronoi vertices are intersection points of the bisectors and they are connected via Voronoi ridge lines (green lines). Therefore, particles i and j are neighbors if both of them share the same Voronoi ridge line. To search for Voronoi neighbors, we use *scipy.spatial.Voronoi* function which uses the Qhull library [198] for the computations.

The choice of neighbors definition is arbitrary. Anyway, there are some circumstances where one is better than the other. In a 2D dense homogeneous sample most particles have 6 neighbors in contact (hexagonal arrangement), whether the phase is ordered or disordered [199], we see that it is better to use the 6-nearest neighbors definition rather than the Voronoi neighbors definition. One advantage is that the definition of ψ_6 is more stable than with a varying number of neighbors. Also,

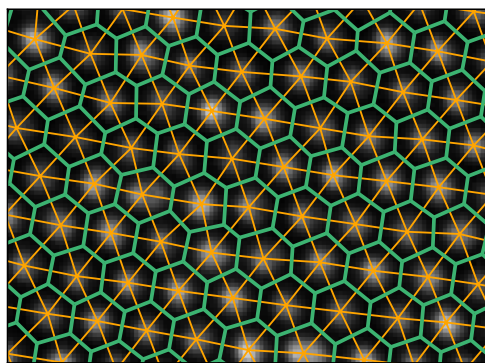


FIGURE 3.16: The illustration of Voronoi (green lines) and Delaunay (orange lines) diagram for the particle coordinates in the dense phase.

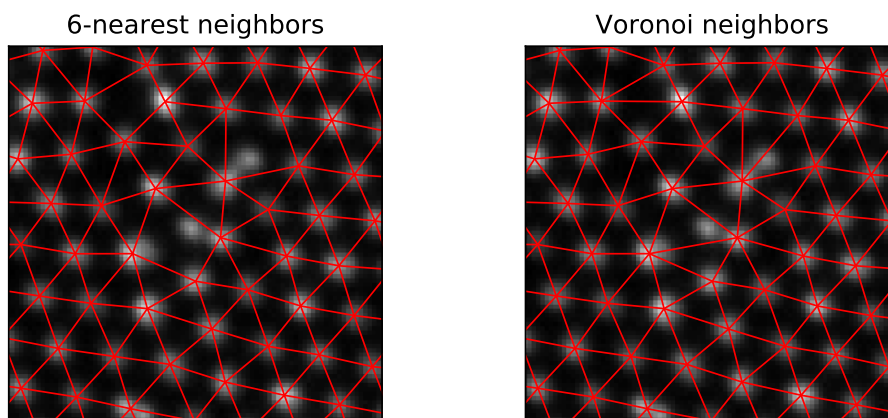


FIGURE 3.17: A comparison between 6-nearest neighbors and Voronoi neighbors at the same part of the sample. Red lines are bonds between neighbors. The bonds are defined by two-way relation: particle i is a neighbor of particle j if and only if particle j is a neighbor of particle i .

the *cKDTree* algorithm automatically provides a rank from the 1st to the n th nearest neighbors. For example, we can compute an average distance to the 1st nearest neighbors and compare with a cage size obtained from the MSD. In addition, Fig. 3.17 shows that the 6-NNs definition can deal with the defects better than the Voronoi. On the other hand, in the rheology experiment, the 6-NNs fails because a particle close to an intruder would need to reach to its second shell to find 6 neighbors, while the Voronoi (with a constraint of neighboring distance) provides a more accurate neighborhood.

3.5.2 Defining graph and connected components

Once the neighborhood is properly defined, we use *NetworkX* package [181] to construct the graph of particle network where particles are nodes and neighborhood are edges. The edge is defined only if two particles are neighbors of each other and it must be shorter than $1.5\sigma_0$. This package is also helpful to handle with graphs. We can define a subgraph that contains several clusters of any particular type of particles. For example in Fig. 3.18, we identify a subgraph of slow particles and obtain its

connected components as clusters of slow particles¹. We can measure a characteristic size of slow domains $\zeta(\Delta t)$ by averaging a spatial expansion of each cluster. We can also apply the same measurement for clusters of orientational correlated particles and obtain an orientation correlation length $\ell(\Delta t)$ (will be described in Chapter 4).

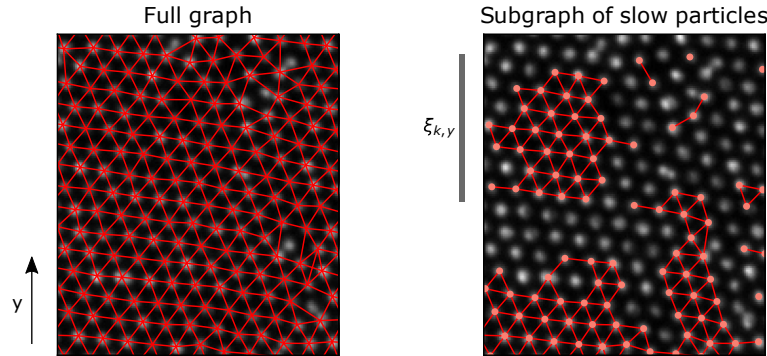


FIGURE 3.18: Identifying clusters of slow particles using connected components. The neighborhood (defined by 6-NNs) is displayed as the red lines between particles. The slow particles are represented with the light orange dots on the right plot. The characteristic size in y direction of the slow domain k , $\zeta_{k,y}$, is measured from the spatial extension (in y axis) of the cluster.

3.5.3 Broken bonds and bonds life time

During the relaxation, particles sometimes change their neighbors either from an individual cage jump via cooperative relaxation [200, 201, 202] or collective rearrangement of different domains. (This will be described further in Subsection 4.6.5.) We describe a bond between two neighboring particles that was present at t_0 but no longer exist at $t_0 + \Delta t$ as a broken bond.

To define the broken bonds in the particle network, we first construct two graphs at time t_0 and $t_0 + \Delta t$. We name them 'graphA' and 'graphB', respectively. Once we have created the full graphs, we take subgraph of particles that exist in both frames: subgraphA and subgraphB. This is to avoid the effect of lost particles. After that, we take the intersection of the two subgraphs (refers to edges that exist in both frames) and then subtract the intersection from the subgraphA. The resulting graph is, therefore, a broken bonds map. In addition by switching the order of the two frames, we can obtain a map of new born bonds instead of broken bonds.

The broken bonds map can compare only two frames separated by Δt . To investigate the bonds correlation in time, we can measure the ratio of bonds that have not broken at different Δt . Fig. 3.19 shows an example of the bonds correlation of the passive dense regime. During the experimental time, the bonds correlation scarcely drops (only about 0.5%). The very few broken bonds reflects the cooperative relaxation, which is a typical relaxation mechanism in a dense passive system. We discuss the difference between the passive and active dense system regarding the bonds correlation and broken bonds map in Chapter 4. The network analysis is also useful in the microrheological study of the system. We can visualize which parts of the sediment are deformed according to the displacement of an intruder and make a comparison of the deformation between the passive and active cases (more detail in Chapter 5).

¹Here defined as particles that have displaced less than the median

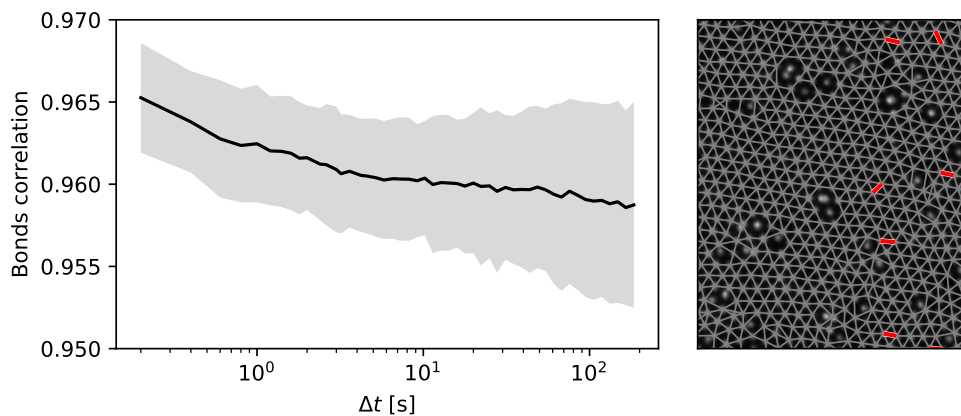


FIGURE 3.19: (right) Example of bonds correlation of the bottom part of passive sediment. Uncertainties are shown by transparent area around the curve. (left) Broken bonds map during $\Delta t = \tau = 300$ s. The grey bonds are bonds defined from t_0 excluding lost particles at $t_0 + \Delta t$ (subgraphA). The broken bonds are represented by the red lines.

Key concepts of the chapter:

1. We discussed the particle tracking using *trackpy* package [174]
 - (a) The criteria of tracking parameters: detecting features and linking trajectories.
 - (b) Filtering spurious trajectories and subtracting the drift.
2. We switched to the HDF5 file because the memory issue when dealing with the dense phase.
3. We developed our python scripts to process the HDF5 file format and analyze the particle trajectories.
 - (a) Structure analysis: $g(r)$, $S(q)$ and ψ_6 .
 - (b) Dynamical analysis: MSD, $F(\Delta t)$, $S_4(q, \Delta t)$ and $\chi_4(\Delta t)$.
 - (c) Network analysis: Broken bonds and bonds life time.

Chapter 4

Experimental Investigation on Dense Assemblies of Active Colloids

In Chapter 2, we have discussed the individual dynamics of our active colloids and have shown that the dynamics are enhanced by the increase of H_2O_2 concentration. Now, we are going to investigate the system at high-density. What we know from a passive suspension is that the relaxation dynamics slows down by orders of magnitude upon compression. The point of ergodicity breaking is the glass transition, that is the packing fraction above which the system cannot be equilibrated within a reasonable time. The influence of activity on the glass transition has already been investigated numerically. Some studies reported a shift towards higher densities [157, 159], and some suggested that the glass transition moves in a nontrivial way depending on the current state of the system [162]. In any case, they found that the qualitative phenomenology of glassiness remained unchanged [160, 162].

In this chapter, we will present our experimental investigation, not only on the glass transition but also on the dynamics beyond the glass transition. Unlike the above-cited numerical works, which approach the glass transition from the ergodic supercooled state, we will extend the investigation beyond to the non-ergodic glass and to non-ergodic polycrystal. We will start by presenting our experimental configuration to create a dense assembly of our colloids, and the experimental procedure. Then, we will discuss the system response when focusing on the densest part of the assembly, at which we found the non-monotonic response with the H_2O_2 concentration. We then present the activity characterization in such a dense phase and how we identify the non-monotonic behavior condition. After that, we discuss the relaxation mechanism from our experimental evidence. Finally, we end this chapter with our simple model to explain on the origin of the non-monotonic behavior.

4.1 Experimental configuration and characterization

4.1.1 Creating the dense phase

To gather the colloids that are diffusing all over the bottom surface of the experimental well, we need to confine them in one place. This can be done by in-plane sedimentation. We tilt the whole setup (microscope and the 96-well plate) with a small angle $\theta \approx 0.1^\circ$ to confine the colloids on one side of the well (see Fig. 4.1a). The angle is really important because it controls the confinement in the system and we have to keep the same angle for each set of experiments. We also have to avoid the sediment to form multilayer if this angle is too high.

In Fig. 4.1b, we show the total image of the sediment. The in-plane sedimentation allows us to observe different densities by moving the observation window along the direction of the tilt. To study the dynamics in the dense regime, we fix the observation window near the bottom part of the sediment but still far from the wall of the well to avoid any boundary effects. The zoom-in dense regime is shown in Fig. 4.1c. For the characterization of activity levels (will be discussed in Subsection 4.3.1), we move the window to the top part of the sediment. The movement is done with a motorized XY translation stage (SCAN IM 130x85), which can be programmed to move systematically between the dense phase and the top part. We set the speed of the move to be $20 \mu\text{m/s}$ and use a S-curve acceleration profile to avoid drifting motion.

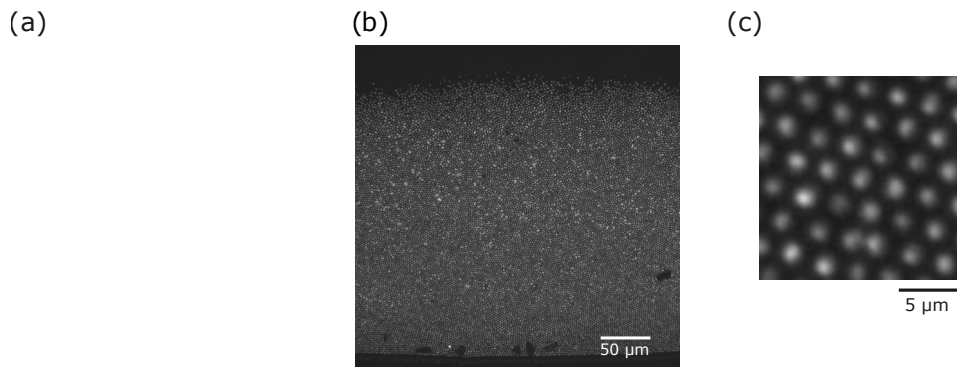


FIGURE 4.1: (a) Experiment configuration to obtain the dense regime. The whole setup is tilted with the angle $\theta \approx 0.1^\circ$ in order to confine the particles on one side of the experimental chamber. (b) Total image of the sediment. The rectangle represents the observation area of the dense regime. (c) Zoom-in image of the dense regime.

4.1.2 Minimizing the drift

This is one of the experimental difficulties. Drift is a global motion of the sediment due to a global gradient such as gravity and flow of the fluid. It overcomes particle motions that we want to investigate, both Brownian motion (passive colloids) and the persistent random motion (active colloids). If the drift is small and homogeneous, we can remove it from the particle tracking process (described in Section 3.1). However, large drift and non-homogeneous drift are difficult to handle. We thus try to minimize the drift as much as possible from the experimental state.

To do so, we have to let the colloids settle in the most stable state before performing the experiment. After adjusting the tilt angle, we leave the sample on the microscope stage overnight. On the next day before and during the experiment, we have to avoid any movement of the stage. However, even if we are very careful on the above adjustment, we still observe some drift especially in the top part of the sediment. We guess it comes from convection flow because the sample is always heated by the LEDs external dark-field, i.e., from 25°C before turning on the LEDs to 33°C at the end of the experiment. We thus also turn on the LEDs overnight (or at least 4 hours before starting the experiment) in order to reach a thermal equilibrium.

4.1.3 Introducing H₂O₂ and data acquisition

To vary the activity levels in a wide range, we increase the H₂O₂ concentration logarithmically starting from 0% (passive case). The limit of the experiment is set by the highest H₂O₂ concentration that we can reach without having any bubbles, which are the product of H₂O₂ splitting on the platinum side of the colloids. Also, to avoid the drift, opening and closing the cover while adding H₂O₂ has to be done very carefully not to change the position and orientation of the experimental well.

Data is acquired 30 minutes after adding new H₂O₂. This is to let the system reach a stationary state before the acquisition. Data is in a form of grayscale image sequence. Unless stated otherwise, in the dense phase we acquire data at 5 Hz for 30 minutes because we are interested in long-timescale motion. In the top part of the profile, we record at 20 Hz for 3 minutes because the particles displacement is faster than in the dense phase. We might lose some fast particles from the tracking if we use too low frame rate.

4.1.4 Effective diameter and density definition

In Fig. 4.1c, one might notice that the particles do not physically touch each other even though they are confined by gravity. This is because particles are stabilized by electrostatic forces. To define area density in our system, the physical diameter is not a good choice since the colloids separate further than $\sigma_{\text{phys}} = 1.6 \mu\text{m}$. To do so, we consider our colloids as *soft colloids* with an effective diameter σ_{eff} , which we measure from position of the first (highest) peak of the radial-pair correlation function $g(r)$ (specified in Subsection 3.3.1). We take σ_{eff} of the passive case to define a reference effective diameter for other activity levels, $\sigma_0 \equiv \sigma_{\text{eff}}^{\text{passive}}$. Depending on the experimental conditions such as a batch of colloids or the tilt angle, we obtain σ_0 between $2.0 \mu\text{m}$ to $2.3 \mu\text{m}$. Thus, our area density is defined as $\phi = \pi R_0^2 \rho$, where ρ is a number density and $R_0 = \sigma_0/2$.

4.1.5 Hexatic order parameter, $\psi_{6,i}$

Dealing in such a dense phase, we often receive a question of whether our system is glass or crystalline. We note again that our Janus particles are 10% polydisperse and always contain doublets and triplets. Depending on the filtration process, the structure order can vary from one batch to the others. We quantify the degree of local order by the hexatic order parameter $\psi_{6,i}$ (specified in Subsection 3.3.3). The more $|\psi_{6,i}|$ differs from one, the more the structure departs from the hexagonal shape. In the present sample that we are going to discuss, there are 47% of the particles that have $|\psi_{6,i}| > 0.8$, which from now on we refer to them as *crystalline* particles. We also check a spatial map of $|\psi_{6,i}|$ from one snapshot in Fig. 4.2. The crystalline domains are small and sparsely distributed in space. For all the above reasons, we are confident that our present sample is not fully crystalline.

What we have mentioned in this section is the experimental configuration and characterization tools. In the following, we will investigate how the self-propulsion influences the dense sediment. We will show a first observation of the non-trivial response of the dense phase to the activity of the particles. After that, we will use another set of experiments with deeper analysis to explain this non-trivial behavior and also to show that our results are reproducible.

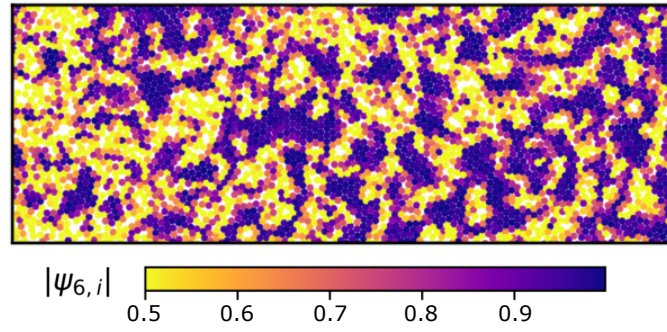


FIGURE 4.2: Map of $|\psi_{6,i}|$ of one snapshot in the passive system. Direction of the in-plane gravity is downward.

4.2 My first observation of the non-monotonic behavior

We first focus on the deepest part of the sediment using mean square displacement, MSD (introduced in Subsection 3.4.1), to characterise the system dynamics. Before adding any H_2O_2 , the MSD curve of the dense passive sediment shows a glassy behavior (see Fig. 4.3a, black curve). The presence of the plateau at the intermediate time-scale ($0.5 < \Delta t / \tau_R < 20$) means that particles are trapped inside a cage formed by their neighbors. Before the plateau, the increase of the MSD at short time-scale ($\Delta t / \tau_R < 0.5$) reflects the particle motion inside the cage. If we could reach a higher-speed acquisition rate, we should retrieve the diffusive motion inside the cage. At long-time scale ($\Delta t / \tau_R > 20$), the particles eventually manage to diffuse away from their cage as shown in the second increase of the MSD after the plateau. These are key features of glassy behavior, which typically occurs in any (passive) dense systems with thermal fluctuation.

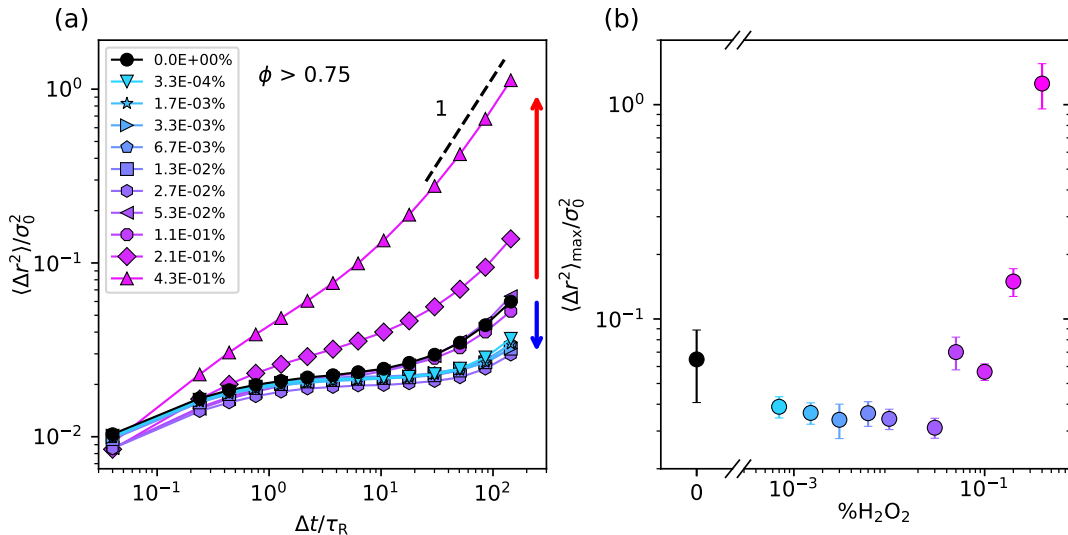


FIGURE 4.3: (a) Mean square displacement (MSD) of the dense assemblies of active colloids at various activity levels. Starting from the passive (black), the very first nonzero activities (light blue to purple) show the reduction of mobility. As the activity continues increasing, the opposite trend is observed. The system mobility increases with activity (pink curves). (b) Values of the MSD at the longest lag time of various activity levels.

What we are interested in is the influence of self-propulsion on the glassy dynamics. We thus vary the H_2O_2 concentration while keeping the same observation area. What we expected at the beginning was an increase of mobility with the H_2O_2 concentration: higher activity, higher mobility. Surprisingly, we found that this is not always the case. At the low H_2O_2 concentrations, the MSD curves (blue curves) fall below the MSD of the passive case. This indicates that (slightly) active particles are more confined than the passive situation. Moreover, it can be noticed that they also stay inside the cage longer as shown from the extended plateau. As we continue increasing the concentration of H_2O_2 , we found the opposite trend. At high enough concentration, the MSD goes up until it has the same level as the passive case (purple curves), and then finally exceeds the passive case (magenta and pink curves). This shows the increase of mobility with H_2O_2 concentration, which we have expected in the first place. We can also see that the plateau is shorter and less obvious. Finally, the glassy behavior is suppressed at the highest H_2O_2 concentration as indicated by the disappearance of the plateau.

For the moment, we call this non-monotonic behavior the ‘back and forth’ behavior. The ‘back’ (or ‘forth’) behavior refers to the regime where the system mobility is lower (or higher) than the passive case. We illustrate again the system mobility quantified by MSD at the maximum lag time in Fig. 4.3b. It obviously shows the non-monotonic evolution with the H_2O_2 concentration. At the concentration lower than $\approx 0.04\%$ the system mobility ($\langle \Delta r^2 \rangle_{\max} / \sigma_0^2$) drops from 6.5×10^{-2} in the passive case to $\approx 3.3 \times 10^{-2}$. The dynamic is back to the same level as the passive one at $\approx 0.10\%$, and then it becomes higher at the two highest concentrations. The latter situation (the ‘forth’ regime) is quite straightforward as we inject more energy and the system mobility is higher. The most interesting part would be the ‘back’ regime, which is unexpected. We have investigated this behavior with some classical tools in glassy physics ($g(r)$, $S(q)$ and $S_4(q, t)$ see Appendix 1 Fig. 4.25, 4.26 and 4.27), but none of them shows the non-monotonic response.

In the rest of this chapter, we will focus on the characterization and explanation of this non-trivial behavior. In the following section, we first check whether the activity level, which is characterized from the density profile, behaves monotonically with the H_2O_2 concentration or not.

4.3 Sedimentation of active colloids

4.3.1 Characterization of activity levels: Effective temperature

There are several ways to characterize activity level in self-propelled particles. For example, we have shown in Section 2.3 for the dilute limit that we can measure the propulsion speed v_0 and the effective diffusion coefficient D_{eff} . However, in the dense experiments, we cannot access to particle free individual motion. We thus have to use another way which works for sediment of particles.

In Fig. 4.4, we show the sedimented particles in the passive and in the active cases. What can be noticed here is that the particles go further in the direction opposite to gravity in the presence of activity. We can relate the density profile of the sediment to a temperature by using the same spirit as the historical experiment of Jean Perrin [111]. In the sedimentation of passive colloids of mass m in a gravitational field, the competition between particle diffusion and gravity g results in the sedimentation diffusion equilibrium: the density profile $\phi(x)$ of the sediment shows

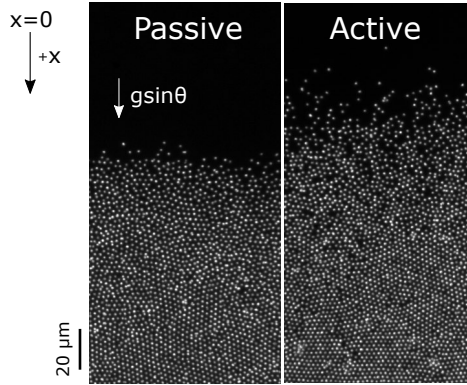


FIGURE 4.4: The sedimentation profile comparing the passive (left) and active (right) cases. With the activity, the colloids are able to move against the direction of gravity. We define x in the same direction as $g \sin \theta$ and has the origin above the sediment where $\phi(x = 0) \rightarrow 0$.

an exponential form at low enough density,

$$\phi(x) \sim \exp[mgx/k_B T_0] \quad (4.1)$$

where x is pointing to the same direction as g and has the origin above the sediment where $\phi(x = 0) \rightarrow 0$. k_B is the Boltzmann constant and T_0 is Brownian temperature. From Eq. 4.1, one can define the sedimentation length as $\ell_g = k_B T_0 / mg$. In the case of active colloids, it has been shown in Ref. [8] that active colloids in the dilute limit behave as if they are ‘hot’ with an *effective temperature* T_{eff} while the bulk temperature T_0 does not change with activity. In other words, the active colloids have longer sedimentation length than the passive one. We thus apply this concept to our tilted setup by replacing g by $g \sin \theta$ and T_0 by T_{eff} .

Recall that we acquire data at two fixed locations: one close to the bottom (dense regime, see Fig. 4.1b) and one at the profile (dilute regime). This is to remain in the very same experimental condition between the dense phase and the activity characterization in the dilute phase. Fig. 4.5a shows the density profile at different H_2O_2 concentrations (same concentration as in Fig. 4.3). It can be seen that the density profile is steeper in the passive case and then becomes broader with the increase of H_2O_2 concentration.

We focus on the dilute limit $\phi \ll 0.1$ and show the fit of $\log \phi$ for each H_2O_2 concentration in the inset. According to Eq. 4.1, the fit yields the value of ℓ_g . We obtain $\ell_g \sim 2 \mu\text{m}$ in the passive case and $\ell_g \sim 20 \mu\text{m}$ in the highest activity levels. Accordingly, the Brownian/effective temperature can be obtained from $T_{0,\text{eff}} = mg \sin \theta \ell_g / k_B$. We can compare the Brownian temperature T_0 measured from the density profile in the passive case¹ with the thermal bath temperature measured directly from a thermometer. Both values are approximately 300 K, while our highest activity level gives $T_{\text{eff}} \approx 5000 \text{ K}$. To get rid of the uncertainties on m and θ , we present the activity level in terms of T_{eff}/T_0 . Fig. 4.5b shows a monotonic increase of T_{eff}/T_0 with the H_2O_2 concentration. At this point, we are thus confident that the activity level increases monotonically with the addition of H_2O_2 .

¹with the determination of the tilt angle and the internal angle of the well $\theta_{\text{internal}} \approx 5.1 \times 10^{-3} \text{ rad}$.

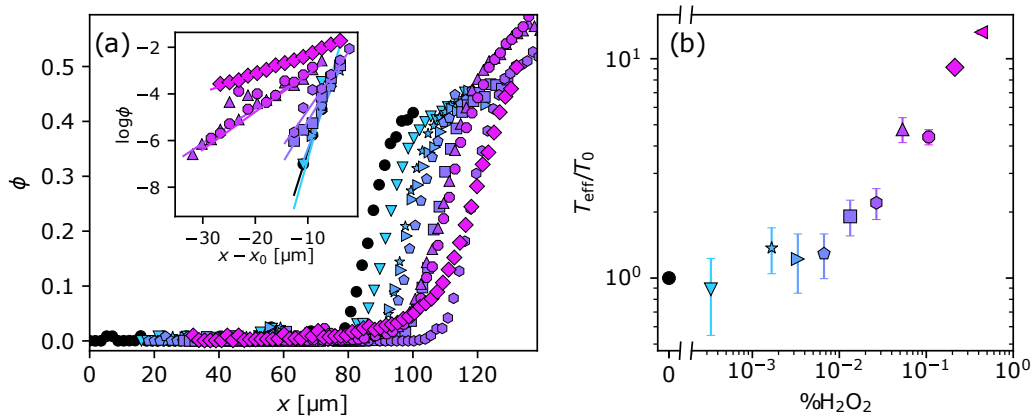


FIGURE 4.5: (a) Density profile $\phi(x)$ of various activity levels. x is the direction along $g \sin \theta$. (inset) $\log \phi$ in the dilute regime as a function of the distance $x - x_0$, where x_0 is the position where the profiles have the maximum slope. The solid lines is the fitting function $\phi(x) = \phi_0 \exp(-\lambda x)$, where $\lambda = mg \sin \theta / k_B T_{\text{eff}}$. (b) T_{eff}/T_0 versus H_2O_2 concentrations, where T_{eff} is the effective temperature obtained from the fitting and T_0 is the Brownian temperature.

4.3.2 Compaction

Another thing to be noticed in Fig. 4.5a is the shift of the profile towards the right, the direction of gravity, with the increase of H_2O_2 concentration. This is a hint showing that the sediment gets more compact. The average density ϕ in the dense part (see Fig. 4.6) shows a rise of about 15% from the passive case to the highest activity level. Additionally, the experimental images (inset) show that the inter-particle distance becomes smaller. This compaction can be seen from the radial-pair correlation function $g(r)$ as well (see Appendix 1 Fig. 4.25).

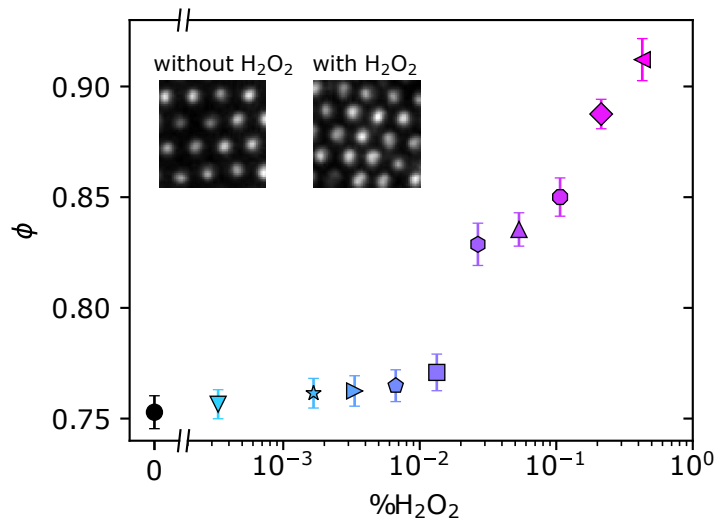


FIGURE 4.6: Area density ϕ at various H_2O_2 concentrations. ϕ is obtained from $\phi = \pi R_0^2 \rho$, where R_0 is the effective radius of the passive dense assembly and ρ is a number of particle per unit area. The insets show the direct observation of the compaction upon adding H_2O_2 .

We can think of two possible origins of the compaction: (1) the presence of H_2O_2 that changes the particle interaction potential and (2) the self-propulsion that helps particles to force against the electrostatic repulsion between them. The latter origin regards to effective attraction has been observed and characterized in the same system at the top part of the sediment [8]. We try to decouple those two origins by measuring the average density of the sediment of pure gold colloids upon increasing H_2O_2 concentration. There is absolutely no self-propulsion in this case, however, we still observe compaction of 4% showing that the presence of H_2O_2 changes the interparticle interaction. This change could even be stronger in the presence of Janus gold-platinum particles.

One could suspect that the ‘back’ behavior could be only a result of this compaction effect and has minor effect from the self-propulsion. Also, density is an important parameter to describe the state of the system. In the next section, we will show how we carefully control for density changes and how we characterize the density-dependent behavior.

4.4 Density control experiment

In the first set of experiments, we obtained the data from only two fixed places: the top part and the lowest part of the sediment. We thus performed another set of experiments in order to acquire the data of the whole sediment including the intermediate density regimes and then divided the sediment into slices perpendicular to the gravity. If thin enough, a slice can be considered at fixed density. Therefore, even if the compaction occurs when we add H_2O_2 , we can match slices from one activity to the others that have the same density. At the end, we will show that with the controlled density, we still obtain the non-monotonic behavior. Moreover, with this density controlled experiments, we can define the condition of this non-trivial behavior.

4.4.1 Slicing the profile

We divide the profile into thin slices in y -direction (see Fig. 4.7a). The slice width is chosen to have approximately 1000 ± 100 particles per slice. To define the slice position, first, we apply the particle tracking to the whole sediment. Then, we sort the x position of all particles in one frame. The maximum x corresponds to the lowest position in the sediment. We set the position of the lowest slice nearby the wall of the experimental chamber. Then, we define the top edge by using the x position of the next 1000th particle from the sorted x . This is also the first edge of the next slice. We keep repeating the process until we have less than 1000 particles left in the final slice, that we do not take it into account for our analysis because the statistics is low and the slice area is poorly defined. Once we have the slice positions, we assign particles into a slice corresponding to their x position and apply this to every frame. Lastly, we subtract the drift in each slice independently with others following the method described in Section 3.1.

In Fig. 4.7b, we show the time average densities ϕ in each slice as a function of the slice positions x . Except for the top slice, ϕ increases linearly with x until $x \approx 150 \mu\text{m}$ and then it saturates for about $40 \mu\text{m}$ before decreasing at $x > 180 \mu\text{m}$. The shape of $\phi(x)$ indicates that the bottom of the well is not perfectly flat and slightly rises before the wall. We, therefore, limit our analysis to $x < 180 \mu\text{m}$. In addition, to fill up the density gap between two slices, we can slice again the same experimental

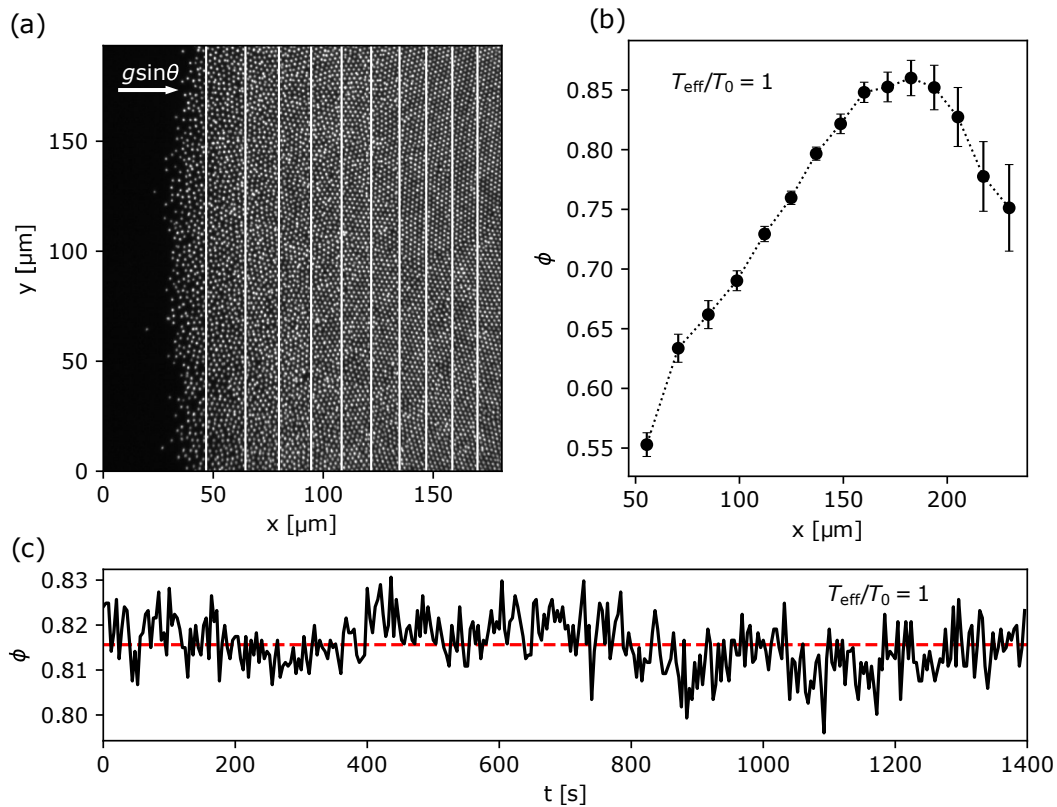


FIGURE 4.7: (a) Profile of the colloidal sediment ranging from dilute regime, to intermediate regime, up to dense regime. The profile is divided into small slices (white lines) in a perpendicular direction to the in-plane gravity in order to keep the constant density in each slice. We choose 1000 particles per slice except for the most dilute slice. (b) Area density ϕ of each slice as a function of slice position. Errors come from the time averaging. The non-monotonicity is due to the curvature of the bottom of the well near the wall. In the analysis, we always neglect the last four slices. (c) The fluctuation of ϕ during the experimental time for the slice with average density of $\phi = 0.82$.

video by shifting slice position. The new lowest position is thus the middle of the first non-shifted slice.

We are confident that the density is uniform in the direction perpendicular to gravity because the colloids are confined by the in-plane gravity. Recall that in the passive case, the sedimentation length of our colloids is $2 \mu\text{m}$, which is smaller than the width of the slices ($> 11 \mu\text{m}$). The density fluctuation in time of one slice is shown in Fig. 4.7c. This comes from particles entering and leaving the slice, and also from the tracking errors. From that, we estimate the error on the density around ± 0.02 .

4.4.2 Density-dependent dynamics of the passive sediment

From the slices, we can compute dynamic quantities as a function of the density by changing the slice altitude x . In the following, we are going to investigate only the passive case and compare our result with the general knowledge of glass transition. For instance, we show the MSD computed in y direction (the direction along the slice) in Fig. 4.8a. In the dense slices $\phi > 0.69$, the MSD clearly shows the glassy

behavior. The plateau height decreases with increasing density indicating smaller cage size. It is worth noting that the plateau escape time, when we recover diffusive motion (slope = 1), does not have a strong dependency on ϕ . The plateau is less visible at $\phi = 0.66$ and $\phi = 0.63$, and finally disappears at $\phi = 0.55$.

Another dynamic quantity that has been used widely in the glass community is the overlap function $F(\Delta t)$ (introduced in Subsection 3.4.2), which tells us the ratio of particles that have not moved within a given lag time Δt . Fig. 4.8b shows $F(\Delta t)$ at various densities corresponding to the MSD in Fig. 4.8a. At the lowest density, $F(\Delta t)$ relaxes with a single exponential step indicating nonglassy behavior. At higher densities, we observe a two-step relaxation typical of glassy dynamics.

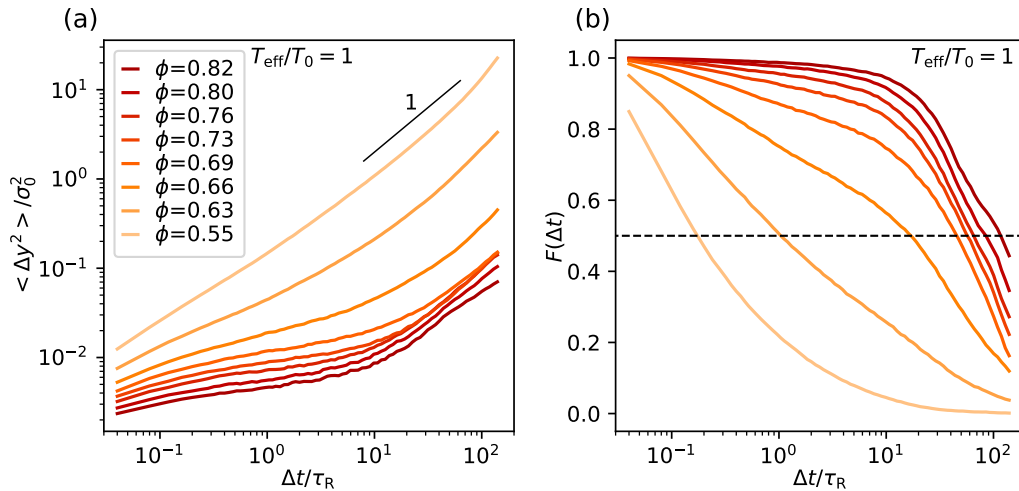


FIGURE 4.8: (a) Mean square displacement in y direction and (b) overlap relaxation function $F(\Delta t)$ of the passive sediment at various densities. The relaxation time is defined when $F(\Delta t)$ reaches 0.5 (dashed line).

The reason we switch to $F(\Delta t)$ is that we can define a relaxation time τ of the system from it. Here we define τ when half of the particles have already relaxed, i.e., $F(\tau) = 0.5$. We plot the relaxation time dependence with ϕ in Fig. 4.9. τ rises steeply with ϕ until $\phi_g \approx 0.67$, which we define here as the operational glass transition density, and then depends weakly on ϕ afterwards. Below ϕ_g , the density dependence of τ is well-fitted with the Vogel-Tamman-Fulcher (VTF) dependence [146, 147, 148],

$$\tau = \tilde{\tau} \exp \left[\frac{A}{(\phi^*/\phi) - 1} \right], \quad (4.2)$$

where $\tilde{\tau}$ is the relaxation in the dilute phase, A is an arbitrary constant approximately 0.19 for our data, and ϕ^* is the ideal glass transition density. We obtain $\phi^* = 0.69$ from the fit. For $\phi > \phi_g$, in other steep potential systems, we are familiar with the divergence of τ near the glass transition [142]. Nevertheless, what we have obtained here is the saturation of τ beyond ϕ_g . This is actually consistent with systems of soft particles [150].

So far, this is what we have recovered from our system in the passive case, which can be described by the phenomenology of the physics of glass transition. In the following, we check the crystalline order in our system to know in which state we are before applying further analysis.

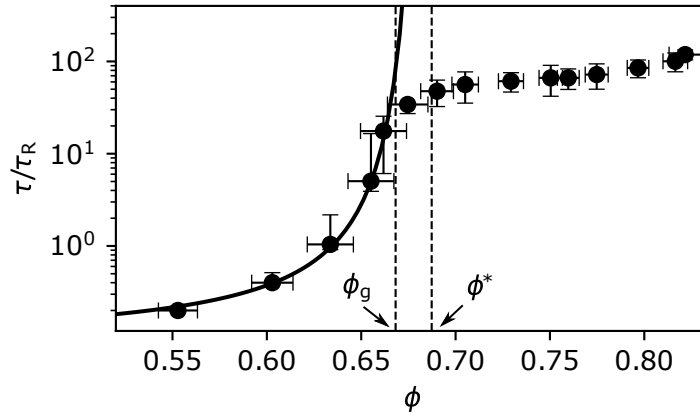


FIGURE 4.9: Density dependence of the relaxation time in the passive system. The horizontal error bars come from the time variation within a slice. For $\phi < 0.67$, the vertical error bars are from the interpolation of τ/τ_R according to the uncertainties of ϕ . For $\phi > 0.67$, the vertical error bars come from the uncertainties among different sampling initial time t_0 . The solid line is the VTF fit $\tau \propto \exp\left(\frac{A}{(\phi^*/\phi)-1}\right)$, where we obtained $A \approx 0.19$, and $\phi^* = 0.69$ is the ideal glass transition volume fraction.

4.4.3 Glass or crystalline?

To determine the crystalline order, as before, we compute the hexatic order parameter $\psi_{6,i}$ for each particle i . We first see how the order changes with density by computing $\psi_{6,i}$ for each slice as shown in Fig. 4.10. We can see that the order increases with density as there are more and more particles with high $|\psi_{6,i}|$ in the denser slices. This is because pressure from the top slices helps the packing of the lower slice.

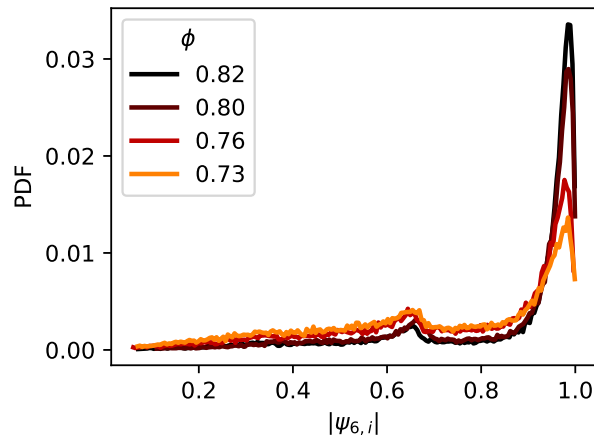


FIGURE 4.10: The PDF of the modulus of the hexatic order parameter $|\psi_{6,i}|$ of the passive system at different slices with different densities.

To determine whether the slice is crystalline or not, we compute the ratio of crystalline particles ($|\psi_{6,i}| > 0.8$), $N_{\text{crys}}/N_{\text{all}}$, in every slice and every activity level (see Fig. 4.11). High values of $N_{\text{crys}}/N_{\text{all}}$ at large ϕ confirms that the lowest part of the sediment is very ordered. Besides, for a given density, we can see that the crystalline order decreases with the activity level.

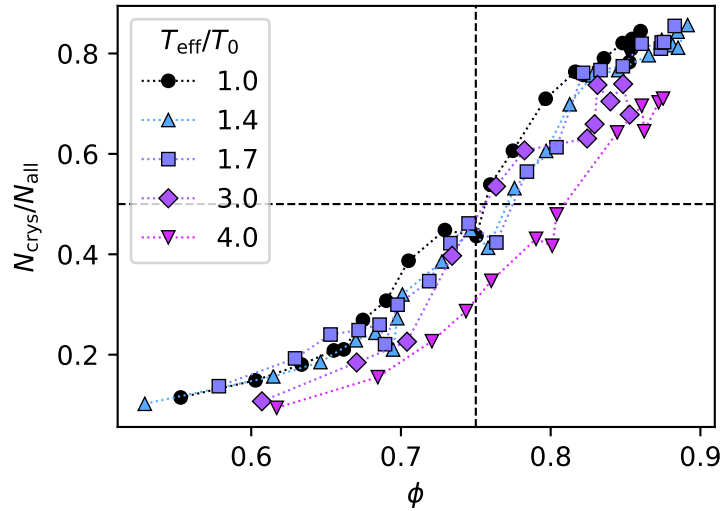


FIGURE 4.11: Density dependence of $N_{\text{crys}}/N_{\text{all}}$, a ratio of a number of crystalline particles to a total number of particles. The horizontal dashed line at $N_{\text{crys}}/N_{\text{all}} = 0.5$ is the threshold value where we limit our analysis in order to avoid the crystalline region. This corresponds to $\phi < 0.75$ (the vertical dashed line).

In the next section, we restrict our analysis to densities where $N_{\text{crys}}/N_{\text{all}} < 0.5$ for every activity level, which corresponds to $\phi < 0.75$. We also explicitly exclude the trajectories of crystalline particles from the analysis². Nevertheless, later on, we will show that the non-monotonic behavior still occurs even when the crystalline particles are taken into account. Moreover, in the densest part of the sedimentation ($\phi > 0.80 \pm 0.02$) where the particles are mostly crystalline, we still observe the non-monotonic behavior.

4.4.4 Activity-dependent dynamics at fixed densities

Previously, we discussed the density-dependent dynamics in the passive system. Now we are going to see the influence of activity levels at various fixed densities. To filter out the compaction issue described in Subsection 4.3.2, here we control the density among different H_2O_2 concentrations by matching slices that have approximately the same density. Fig. 4.12 shows the density-controlled overlap function $F(\Delta t)$ at various T_{eff}/T_0 . At $\phi = 0.62 \pm 0.02$ (see Fig. 4.12a), all activity levels have one-step relaxation showing nonglassy dynamics. As expected, the relaxation is faster at higher T_{eff}/T_0 . This monotonic behavior of the system dynamics with activity levels still holds at $\phi = 0.65 \pm 0.02$ (see Fig. 4.12b). Here at $T_{\text{eff}}/T_0 = 1$, $F(\Delta t)$ starts to show the two-steps relaxation. At higher activity levels, $T_{\text{eff}}/T_0 = 1.4$ and 1.7, the glassy dynamic is less visible and completely disappears at the two highest activities. This is the evidence that activity pushes glass transition to a higher density as already reported in simulation works [157, 159].

A stark difference is at $\phi = 0.72 \pm 0.02$ (see Fig. 4.12c) where we recover the non-monotonic behavior. For $T_{\text{eff}}/T_0 \leq 1.7$, $F(\Delta t)$ clearly shows the glassy behavior, while it is not anymore a clear two-step relaxation at $T_{\text{eff}}/T_0 = 3.0$ and the highest

²We note that we already checked that the neighbors of crystalline particles do not influence the system dynamics (see Appendix 2 Fig. 4.28).

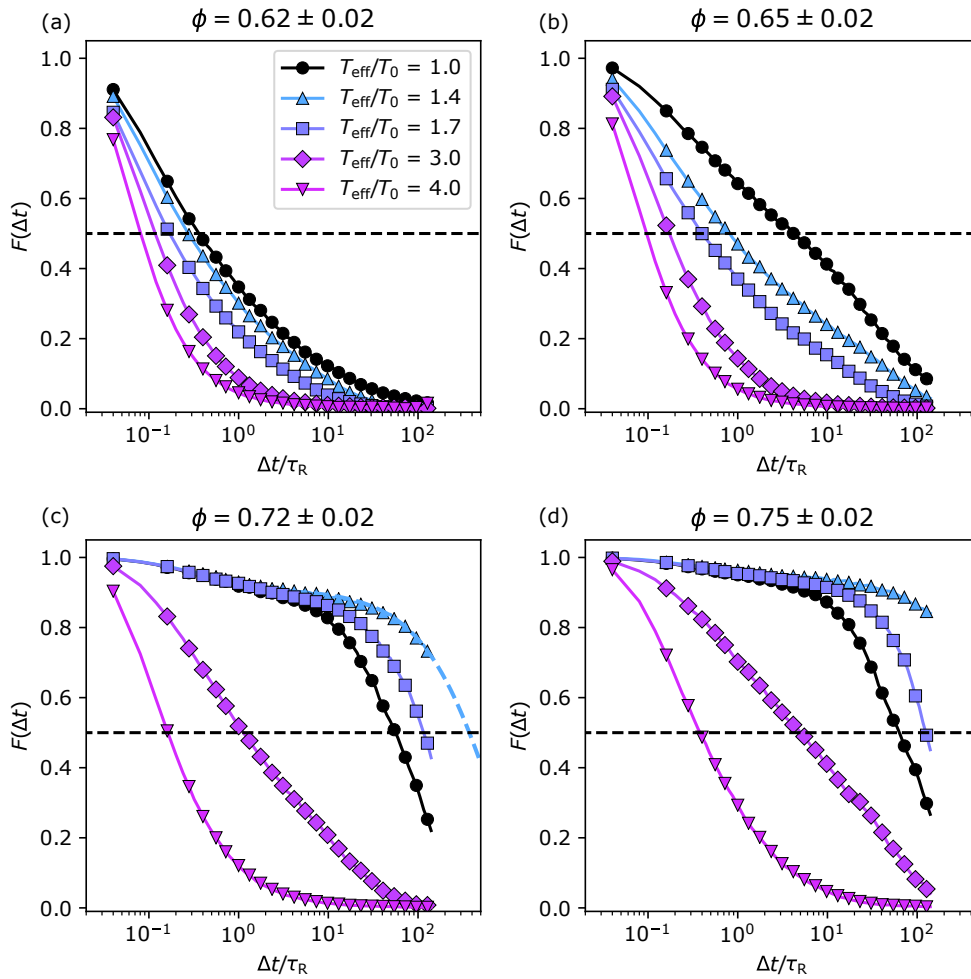


FIGURE 4.12: Overlap function $F(\Delta t)$ at various activity levels comparing among four fixed densities: (a) $\phi = 0.62 \pm 0.02$, (b) 0.65 ± 0.02 , (c) 0.72 ± 0.02 and (d) 0.75 ± 0.02 . The relaxation time τ is defined where $F(\Delta t)$ reaches 0.5 (black horizontal dashed line). The blue dashed line in (c) is the extrapolation of a stretched exponential fit to define τ in case $F(\Delta t)$ has not reached the threshold.

activity is obviously nonglassy. $F(\Delta t)$ of the first nonzero activity exits the plateau much later than in the passive case and it does not reach the threshold $F(\tau) = 0.5$ within our maximum lag time. We thus obtain the relaxation time τ by extrapolating $F(\Delta t)$ with a stretched exponential function and obtaining the value when the fitting function reaches 0.5. The dynamic is slightly faster in the next nonzero activity ($T_{\text{eff}}/T_0 = 1.7$), but still slower than in the passive one. This is obviously the ‘back’ behavior. The following ‘forth’ behavior is when $T_{\text{eff}}/T_0 \geq 3.0$. The relaxation is faster than in the passive and the system mobility gets higher with increasing activity levels. For a higher density $\phi = 0.75 \pm 0.02$ (see Fig. 4.12d), $F(\Delta t)$ exhibits the same behavior as in Fig. 4.12c, but with longer τ and more visible plateau for $T_{\text{eff}}/T_0 \leq 1.7$.

From here we are confident that the non-monotonic response originates directly from the particle self-propulsion, not from a pure effect of compaction. This is because we can still observe it even at a fixed density. Furthermore, from the density variation, we notice that there is a transition density between $\phi = 0.65 \pm 0.02$ and

0.72 ± 0.02 where the activity influences to the system mobility differently: monotonic and non-monotonic. Next, we are going to focus on this transition and try to identify the transition point.

4.5 Identify the non-monotonic behavior condition

In this section, we look the relaxation for all the densities and various activities. The goal is to construct a general liquid-glass phase diagram and to check if there is a mapping to the physics of glass transition from our active system or not. We will use these evidences to identify the condition of the non-monotonic behavior.

4.5.1 Liquid-glass phase diagram

Knowing the relaxation time from $F(\tau) = 0.5$ of various densities and activity levels, we can construct a liquid-glass phase diagram as shown in Fig. 4.13a. The glass transition line on the phase diagram is estimated from the fit of VTF relation, which will be discussed shortly, and ergodicity on each side of this line will be discussed in Subsection 4.5.3. We can see that before the glass transition, the relaxation time of the ergodic supercooled liquid decreases with the distance from the glass transition line. However, this trend does not hold in the non-ergodic glass phase. In the phase diagram, we draw two vertical lines corresponding to the two densities in Fig. 4.12b and c. We then follow both lines starting from $T_{\text{eff}}/T_0 = 1$ and illustrate the resulting τ in Fig. 4.13b. At $\phi = 0.65$ (blue line, triangles), the original passive system is an ergodic supercooled liquid. We observe a monotonic decrease of τ with increasing T_{eff} . By contrast, when starting from a passive state that is non-ergodic at $\phi = 0.72$ (red line, circles), we observe the non-monotonic behavior that translates the rise and fall of the saturation level of the relaxation time. τ increases at low levels of activity and then decreases after the crossing of the glass transition line to the ergodic phase as the activity increases further.

4.5.2 VTF relation

Now we look at the density-dependence of the relaxation time for different activity levels, and we summarize it in Fig. 4.14a. Recall that we have already discussed the density-dependence of relaxation time for the passive case in Subsection 4.4.2: the steep rise before ϕ_g and then the saturation beyond ϕ_g . As the activity level increases, the rise of τ follows the same dependence on ϕ , but shifted towards higher and higher densities. We observe that ϕ_g increases monotonically with activity, which is consistent with theoretical expectations for glassy systems with an additional active force at constant persistence time and increasing effective temperature [160, 162, 163].

In general, for passive soft particles, the saturation value for τ only depends on the relaxation time in the dilute limit [150]. By contrast, here we observe a non-monotonic dependence of the saturation value on T_{eff}/T_0 . In our lowest nonzero activity ($T_{\text{eff}}/T_0 = 1.4$, light blue triangles), the saturation is at least an order of magnitude above the saturated τ in the passive case. At our second activity ($T_{\text{eff}}/T_0 = 1.7$, violet squares), a saturated relaxation time is about twice longer than in the passive case, that is a decrease with respect to $T_{\text{eff}}/T_0 = 1.4$. Finally, for higher activities ($T_{\text{eff}}/T_0 = 3.0$, purple diamonds and 4.0, pink down triangles), the relaxation time never reaches values beyond the passive case and no saturation is observed within accessible densities.

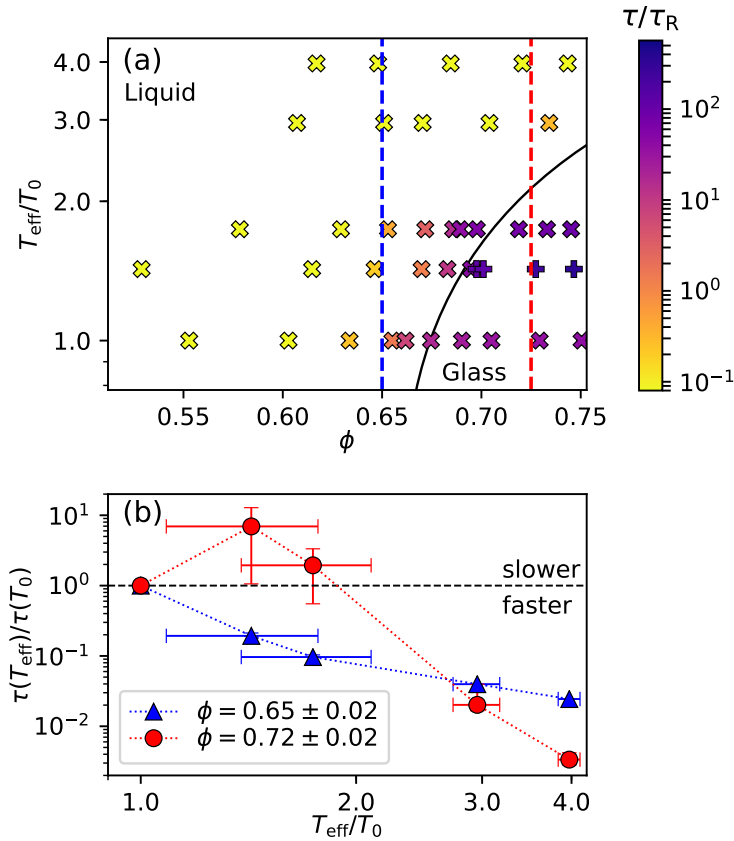


FIGURE 4.13: (a) Phase diagram showing the dependence on both density and activity of τ , obtained directly from $F(\tau) = 0.5$ (cross symbols), by extrapolation of $F(\Delta t)$ (plus symbols). The solid curve is a guide for the eye materializing the glass transition line. Two vertical dashed lines at $\phi = 0.65$ (blue) and $\phi = 0.72$ (red) correspond to the densities in (b). (b) Contrast of activity dependence of τ between both sides of glass transition. For $\phi = 0.72$ (red circles), the first three points are glassy, non-ergodic and we observe a non-monotonic dependence on activity, but not at $\phi = 0.65$ (blue triangles) where all points are ergodic. The horizontal dashed line shows τ in the passive case.

The increase of τ with density fits well with the VTF dependence (Eq. 4.2) not only for the passive case, but also for all nonzero activities. In Fig. 4.14b we normalize the relaxation time τ by $\tilde{\tau}$, the relaxation time in the dilute limit, and density ϕ by $\phi^*(T_{\text{eff}})$. This shows that all activities collapse into one master curve (red solid line) for the ergodic supercooled regime ($\phi < \phi_g(T_{\text{eff}})$). The collapse indicates that we can map the general feature of physics of glass transition below ϕ_g into our active system in the ergodic supercooled phase. However, this collapse does not hold beyond the glass transition. It suggests that $\tilde{\tau}(T_{\text{eff}})$ and an effective temperature T_{eff} is not enough to describe the effects of self-propulsion on the non-ergodic glass. Moreover, this saturation value follows the non-monotonic behavior: an order of magnitude jump between the passive case and the first nonzero activity, and then a decrease with increasing activity.

From all these evidences, we suggest that the non-monotonic behavior occurs at the crossover between ergodic and non-ergodic initial passive systems. In the following, we verify the ergodicity breaking in our system.

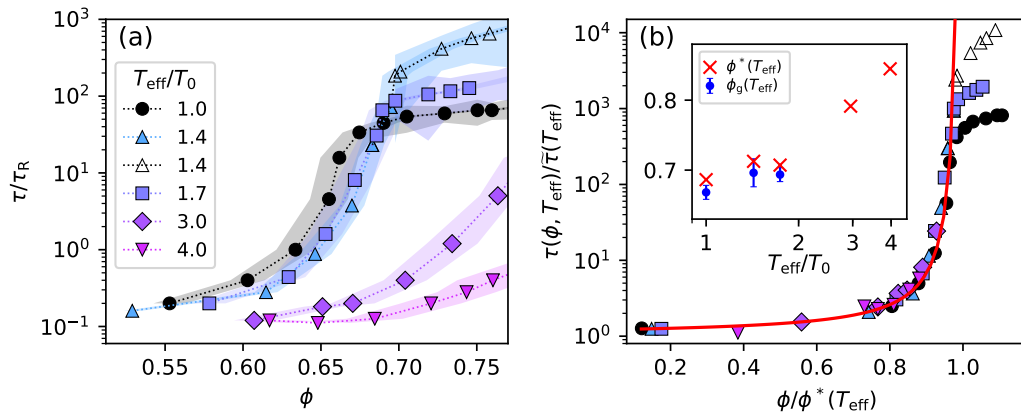


FIGURE 4.14: Density dependence of relaxation time τ at various activity levels. (a) For $T_{\text{eff}}/T_0 = 1.4$, τ is longer than the maximum lag time at densities higher than 0.70. Open triangles are obtained by extrapolation of $F(\Delta t)$. Transparent areas around curves show uncertainties that come mostly from the uncertainty of area density (± 0.02) below ϕ_g or the standard deviation of τ from different sampling above ϕ_g . (b) Collapse of density dependence of relaxation time on Eq. 4.2 (red curve). Beyond glass transition collapse is lost and saturation level follows a non-monotonic trend with activity. Inset: Ideal and operational glass transition volume fractions, ϕ^* and ϕ_g respectively, function of activity.

4.5.3 Ergodicity breaking

In an ergodic system, the relaxation should depend only on the lag time Δt , not on the reference time t_0 . By contrast, the relaxation of a non-ergodic system depends on the waiting time since system preparation. To confirm that we cross the ergodicity limit between $\phi = 0.65 \pm 0.02$ and $\phi = 0.72 \pm 0.02$, we investigate the waiting time dependence of $F(\Delta t)$ in the passive case. We select two waiting times separated by $140\tau_R$ and show the result in Fig. 4.15.

At $\phi = 0.65 \pm 0.02$ there is no significant difference between the two waiting times. We thus confirm that at this density the system is ergodic. It is where we found that the relaxation time responses monotonically to activity level. At $\phi = 0.72 \pm 0.02$ where we observe the non-monotonic behavior, $F(\Delta t)$ relaxes differently depending on the waiting time. The longer waiting time t_2 relaxes later than the shorter waiting time t_1 . We thus confirm that the system is non-ergodic at this density and we state again that the non-monotonic behavior appears when crossing the ergodic to the non-ergodic limit.

We note that the data acquisition in the active case is always performed at the same waiting time: $360\tau_R$ after new H_2O_2 was added to the system.

4.5.4 Particle motion before and after ergodicity breaking

Now we know that the ergodicity breaking is the condition of the non-monotonic behavior. The following question is what makes the system response differently. We therefore look at the ensemble dynamics of the system through MSD, which gives us informations on the change of cage size induced by the activity. In Fig. 4.16, we show MSD for different activity levels at two fixed densities, below and above $\phi_g(T_0) = 0.67$. At $\phi = 0.65 \pm 0.02 < \phi_g(T_0)$ (see Fig. 4.16a), the shape of the MSD evolves monotonically with T_{eff}/T_0 . The passive case displays a subdiffusive plateau, which

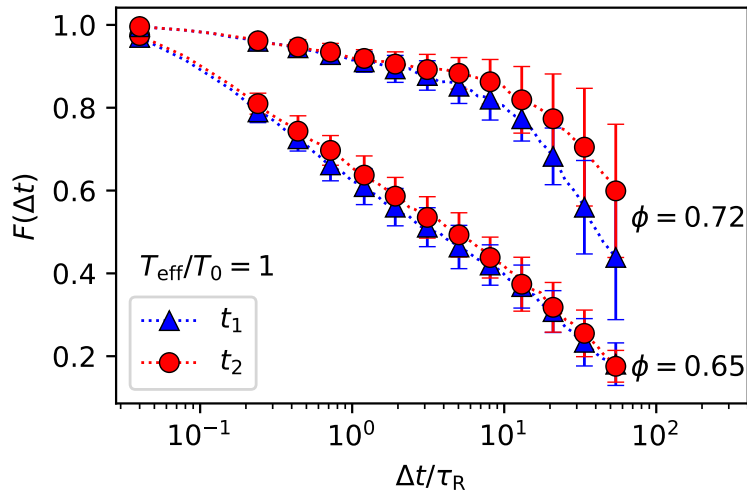


FIGURE 4.15: Relaxation function $F(\Delta t)$ of the passive case at different waiting times t_1 and t_2 such that $t_2 - t_1 = 140\tau_R$. The results are presented for ergodic ($\phi = 0.65 \pm 0.02$) and nonergodic state ($\phi = 0.72 \pm 0.02$). The time unit is divided by Brownian reorientation time $\tau_R = 5$ s.

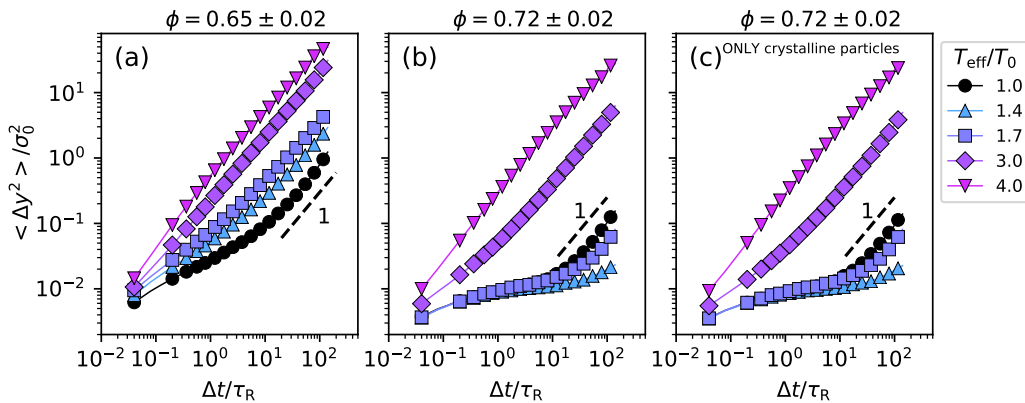


FIGURE 4.16: MSD along y direction at two fixed densities, in the ergodic (a) and nonergodic (b,c) phase, and various activity levels. (a) and (b) are the MSD excluding crystalline particles, whereas (c) shows the MSD of the crystalline particles. The dashed line has slope one to emphasize where the MSD exhibits diffusive motion.

level increases with activity until totally disappearing from the two highest activities. The increase in plateau height from the passive case to $T_{\text{eff}}/T_0 = 1.4$ and 1.7 indicates wider cages.

Beyond glass transition, at $\phi = 0.72 \pm 0.02$, the dynamics of the system shows a stark difference. The level of the plateau in Fig. 4.16b does not depend on the activity at low levels. However, the exit of the plateau does depend on activity in a non-monotonic way. For $T_{\text{eff}}/T_0 = 1.4$, the plateau is left later than in the passive case. For the next activity ($T_{\text{eff}}/T_0 = 1.7$), the MSD exit the plateau earlier, but still later than the passive case. The last two activities show no plateau.

The plateaus have the same level at low activities. It means that weak self-propulsion is not enough to enlarge the accessible area. It reveals that each particle faces steep energy barriers. Particles are already as close as they can be. Since

their interaction potential is steep at short distances, the extra energy afforded by $T_{\text{eff}}/T_0 < 2$ cannot push the particles significantly closer. By contrast in the supercooled regime, the particles are relatively further apart, feeling softer confinement. Therefore, even weak self-propulsion can push against these barriers and enlarge the accessible area, which is shown the increasing plateau level of MSD.

Actually, the ordering seems to barely affect what we have observed purely in noncrystalline particles. Comparing Fig. 4.16b and c, that show respectively the MSD of the noncrystalline and crystalline particles, we observe nearly identical dynamics. Besides, the spatial rearrangement of crystalline region are rather compact and stable in time (see Appendix 3 Fig. 4.29). Therefore, the non-monotonic phenomenology does not seem to be specific to glass. Instead, the relevant divide seems to be the breaking of ergodicity that affects both glass and crystal.

To sum up, low levels of self-propulsion enlarge the cage in the supercooled regime but not in glass regime, whether or not we take local crystallinity into account. The exit from the cage is actually delayed longer at low activities, a point that cannot be explained solely from spatially averaged dynamics.

Our next task is to trace the relaxation mechanisms from individual particle motion, however, the slices that we have analyzed so far are too narrow to see any spatial correlation. We thus need a wider slice of a constant density. Fortunately, despite the density gradient, one part of the sediment seems to have a constant density $\phi \approx 0.85$ on a wider range (see Fig. 4.7b). We shall benefit from this feature to define a new wider slice at such a high density. In the following section, we shall focus on the wide highly ordered slice, which we will characterize as polycrystalline, and we shall probe the relaxation mechanism in microscopic scale from this region.

4.6 Polycrystalline slice: probing the relaxation mechanism

4.6.1 Checking the structure order

From now on, we focus on a dense slice of $\phi = 0.85 \pm 0.03$ and with width $\approx 30\sigma_0$. At such high density, the system is highly ordered. Looking at the PDF of $|\psi_{6,i}|$ in Fig. 4.17, there is a slight drop of the $|\psi_{6,i}|$ peaks from the passive to the first two nonzero activities. The lost of ordering can be noticed only at high enough T_{eff}/T_0 . Here the percentage of crystalline particles drops from 80% in the passive case to 75% for $T_{\text{eff}}/T_0 = 3.0$ and to 68% for $T_{\text{eff}}/T_0 = 4.0$.

We show a map of $|\psi_{6,i}|$ of the passive case in Fig. 4.18a to see how the crystalline particles are localized. There are highly ordered domains except around defects. Following Refs. [135, 155] and as explained in Subsection 3.3.3, we consider the projection of the phase of $\psi_{6,i}$ as shown in Fig. 4.18b. We can thus clearly distinguish crystalline domains of consistent orientation separated by sharp grain boundaries where sample impurities concentrate (low $|\psi_{6,i}|$). This slice is indeed polycrystalline and not hexatic. Besides, the map of $\psi_{6,i}$ (both modulus and orientation) does not change from the passive case to the first two nonzero activities (see Appendix 3 Fig. 4.30).

4.6.2 Relaxation of the wide polycrystalline slice

We explore the microscopic details of the relaxation mechanism in a polycrystalline slice. Fig. 4.19 shows the overlap function, $F(\Delta t)$, in this slice at various activity levels. Both crystalline and noncrystalline particles are taken into account. $F(\Delta t)$

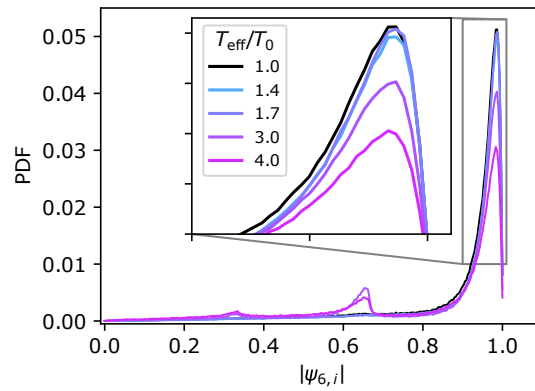


FIGURE 4.17: PDF of hexatic structure parameter ($\psi_{6,i}$) of the wide slice at $\phi = 0.85 \pm 0.03$ and different activity levels.

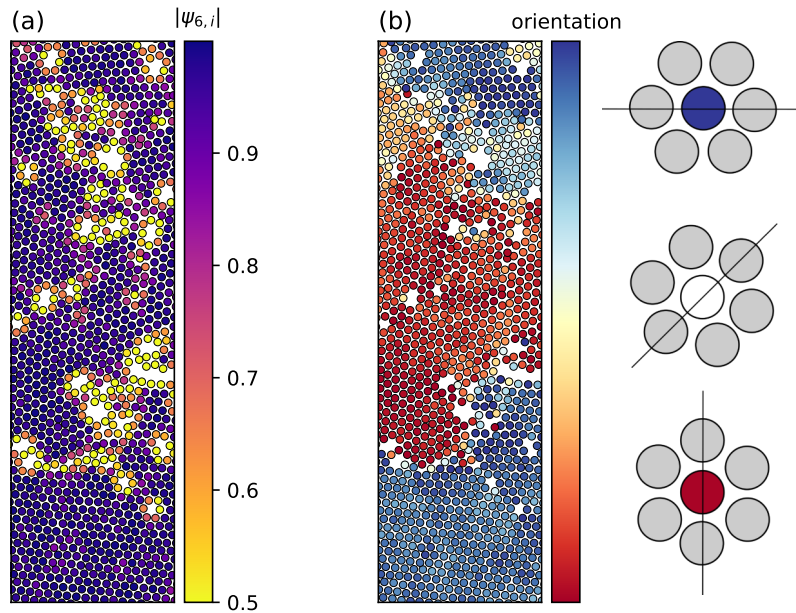


FIGURE 4.18: Maps of hexatic structure parameter $\psi_{6,i}$ of the passive system at $\phi = 0.85 \pm 0.03$: (a) modulus and (b) orientation. Sketches on the right shows which orientation corresponds to which color. The white areas are from sample artifacts and tracking errors. The particles position is exactly the same as in Fig. 4.20a,b for the passive system.

displays the same non-monotonic behavior as before. The plateau of $T_{\text{eff}}/T_0 = 1.4$ is longer than the one obtained for the passive case and does not show any sign of relaxation. For the next nonzero activity, the system starts to relax at the very end, but still later than the passive one (about two times longer). For $T_{\text{eff}}/T_0 = 3.0$ and 4.0, the plateau gets shorter with activity levels, and $F(\Delta t)$ relaxed faster than for the passive and low activities cases. Here we confirm that the non-monotonic behavior observed in the non-ergodic state is not specific to glass, but also exists for a highly ordered structure like polycrystalline.

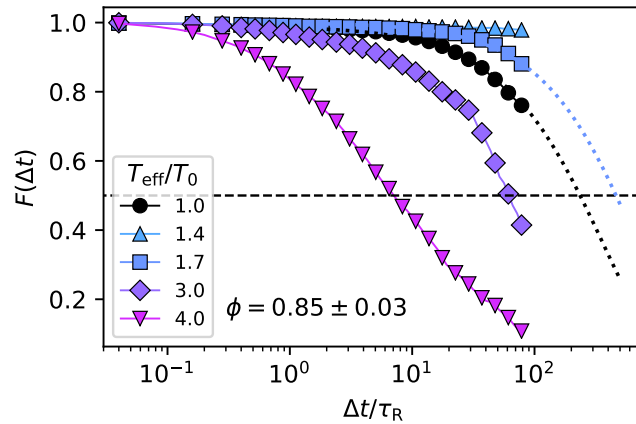


FIGURE 4.19: Overlap function $F(\Delta t)$ in a polycrystalline slice. The threshold where the relaxation time is defined is at $F = 0.5$ (dashed line). The dotted lines at $T_{\text{eff}}/T_0 = 1.0$ and 1.7 are the extrapolation of a stretched exponential fit of $F(\Delta t)$ to obtain τ . For $T_{\text{eff}}/T_0 = 1.4$, $F(\Delta t)$ has not exited the plateau and the extrapolation is not applicable.

We note that even in the wider polycrystalline slice, the standard four-point correlation $S_4(q, t)$ (please refer to Subsection 3.4.3) is difficult to obtain. The results are noisy and difficult to interpret (see Appendix 1 Fig. 4.27). In the following, we find an other way to define a correlation length.

4.6.3 Orientation of displacement

In order to probe how the system relaxes, we look into the orientation of particle displacement. To compute displacements \vec{u}_i , we focus on the time interval $\Delta t = 32\tau_R$, which corresponds to $F(\Delta t)$ exiting from the plateau in the passive system (see Fig. 4.19). Fig. 4.20a spatially maps the orientation of the displacements at different activity levels. To highlight large displacements, only the 50% faster particles are colored according to the orientation of their displacement, while the slower particles are displayed by empty circles. This representation highlights spatial correlations of the orientations. In the fast domains, particles tend to have almost the same direction as their neighbors, and this is true for all activities. Furthermore, the boundaries between the domains seem sharper at higher activities.

We are able to observe shear zones where two zones of opposite orientation slide past each other (3rd panel), and vortices where the particles rotate around a relatively immobile center (4th panel). The position, shape and size of these rearrangements bear little correlation with the crystalline grains and grain boundaries identified in Fig. 4.18.

A similar collective motion of ‘flowing crystal’ has been observed in Refs. [117, 203], which are experiments on granular material at high density. However, their active agent shows alignment interaction via collisions, whereas our active colloids do not align with each other. Even though we cannot access directly to particle orientation, we are confident that there is no alignment interaction in our system. When considering clusters of the same system of active particles at the intermediate density regime, Ref. [11] has shown that the orientation of colloids inside the clusters fits well with the random orientation model.

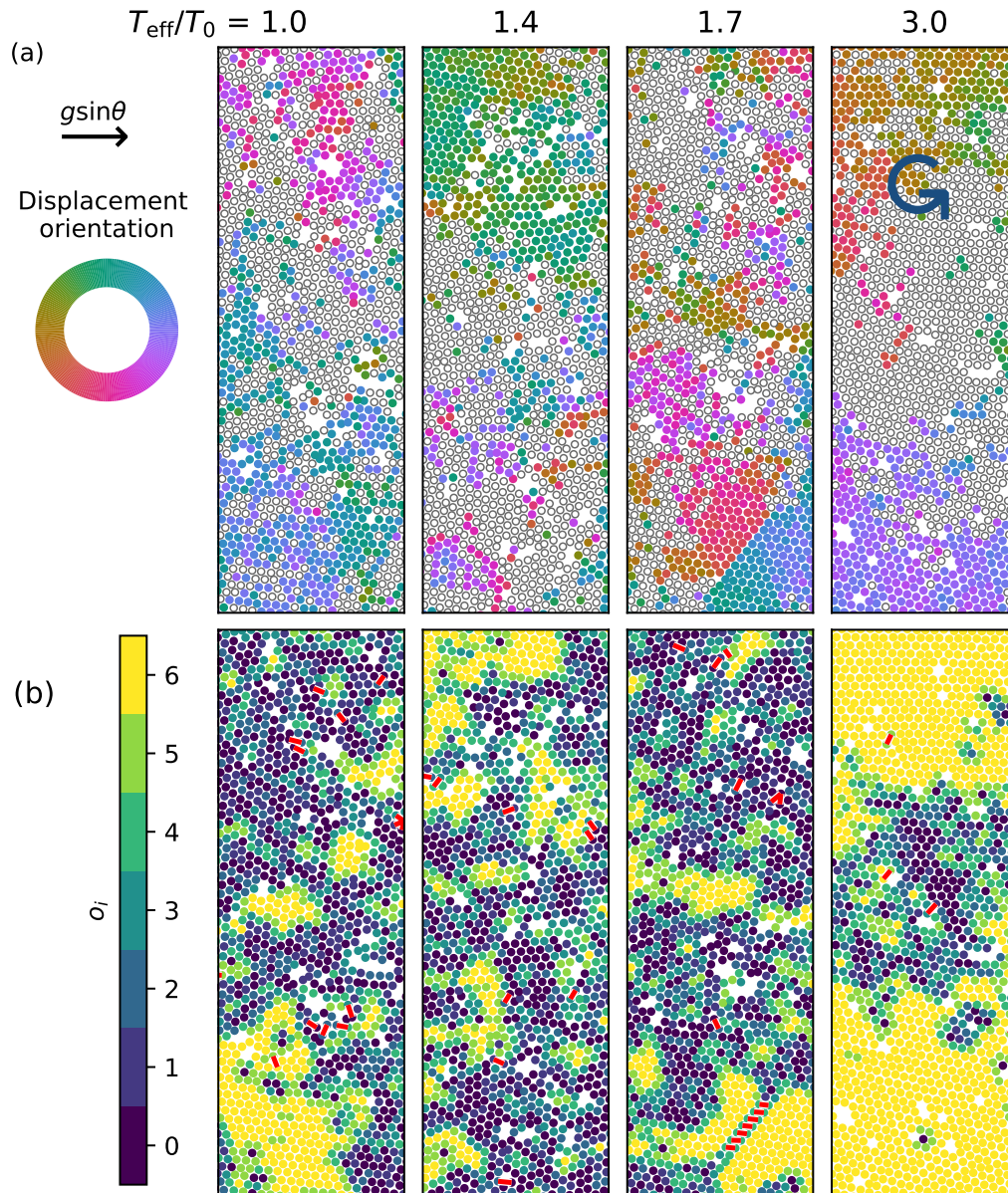


FIGURE 4.20: (a) Orientation of displacement between two frames such that $\Delta t = 32\tau_R$ at various T_{eff}/T_0 and fixed $\phi = 0.85 \pm 0.03$. Orientations are indicated by colors. The slowest half of particles are shown as empty circles. The circle arrow in the last panel highlights the vortex collective motion. The white areas are from sample artifacts and tracking errors. (b) Directional correlation map that displays for each particle i the number o_i of its six neighbors that have the same orientation of displacement as i . The red lines represent broken bonds during Δt .

4.6.4 Directional correlation map

Next, we characterize further the spatial correlation of orientation displacement. For each particle i , we count the number of its six-nearest neighbors j that have moved in the same direction after Δt :

$$o_i = \sum_j \Theta \left(\frac{\vec{u}_i \cdot \vec{u}_j}{|\vec{u}_i| |\vec{u}_j|} - 0.5 \right), \quad (4.3)$$

where Θ is the Heaviside step function. Fig. 4.20b shows the map of o_i for the same snapshot as in Fig. 4.20a. Although the value of the orientation is lost in this representation, we can clearly observe its spatial correlation. We observe that the fast domains in Fig. 4.20a roughly correspond to highly oriented domains in Fig. 4.20b. This hints toward relaxation processes where neighboring particles move together in the same direction. Such collective motions are characteristic of active matter. However, here oriented domains are present even in the passive case. This proves that the mechanisms (e.g., dislocation, defect, or grain boundary motion) that make directed motion emerge from microscopically isotropic motion are already present in the passive polycrystal. Again, no explicit alignment interactions are needed to induce collectively directed behavior.

4.6.5 Broken bonds

To characterize how collective relaxation modes affect the structure of the system, we look for changes in the neighboring network during the relaxation over Δt . As discussed in Subsection 3.5.3, we analyze the network and obtain broken bonds: bonds that have disappeared between time t and Δt . We recall briefly the definition of a broken bond: a bond between particle i and particle j at time t_0 is defined if (i) particle j is one of the 6-nearest neighbors of i and vice versa, (ii) the distance r_{ij} is shorter than $1.5\sigma_0$. A bond is broken between t_0 and $t_0 + \Delta t$ if (i) it belongs to the bond network at t_0 , (ii) it does not belong to the bond network at $t_0 + \Delta t$, (iii) both particles i and j are tracked at $t_0 + \Delta t$.

The broken bonds are presented by red lines in Fig. 4.20b. There are very few broken bonds during the relaxation except in shear zones (panel 3). It means that at high activity particles move in a correlated manner, such that relative positions between neighbors almost do not relax, despite fast relaxation of absolute positions.

We quantify bond correlation with time at various activity levels shown in Fig. 4.21. Bonds correlation is a ratio of bonds that have not broken between lag time Δt . Here in the passive and low activity cases, there is no obvious bonds relaxation throughout the experimental time, while $F(\Delta t)$ relaxes. This indicates that most particles keep their neighbors during the relaxation implying cooperative relaxation. On the contrary, the bond correlation starts to decay at high activity levels. Even though the correlation is still high, we can notice more relaxation than in the passive and low activity cases.

We then take a closer look at a lower density which allows the system to relax better than the polycrystalline slice. The bond correlation at $\phi = 0.72 \pm 0.02$ is shown in Fig. 4.22a. We notice that the bonds relax non-monotonically with T_{eff}/T_0 following the same trend as the non-monotonic behavior. At our longest lag time Δt , we can observe a slight decrease of the bond correlation in the passive and the first two nonzero activities, where the system is in a non-ergodic glass state. The illustration of the broken bonds in the passive case is shown in Fig. 4.22b. We can see that the broken bonds are sparse and not localized, which is consistent with the cooperative

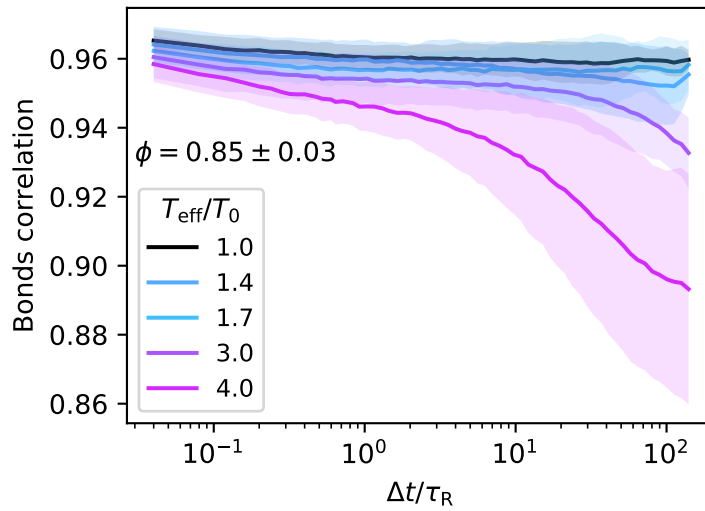


FIGURE 4.21: Bonds correlation at $\phi = 0.85 \pm 0.03$: a ratio of bonds that have not broken between lag time Δt . Uncertainties are shown by the transparent area around the curves.

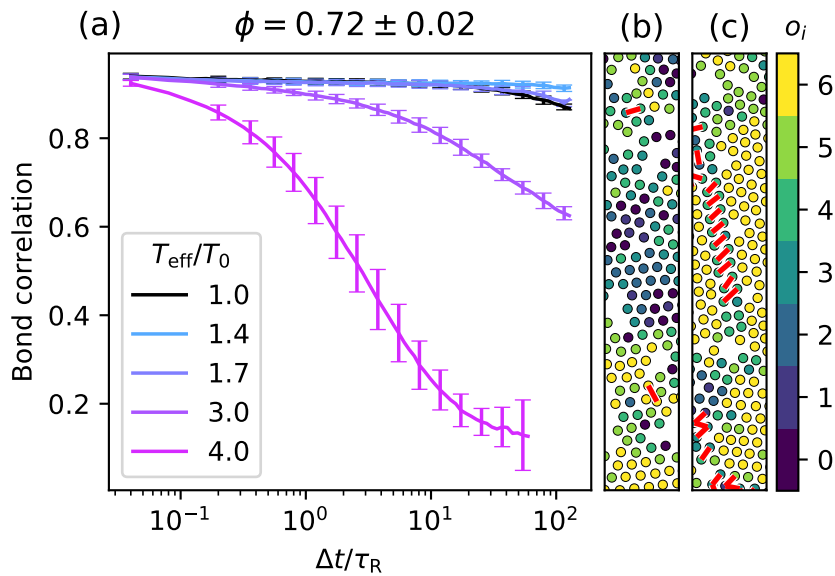


FIGURE 4.22: (a) Bond correlation with Δt at $\phi = 0.72 \pm 0.02$ and various activities. (b,c) Directional correlation maps, o_i , for $T_{\text{eff}}/T_0 = 1.0$ and 3.0 , respectively, at $\Delta t = 12\tau_R$. The red lines between two particles represent broken bonds during Δt . The white areas are from sample artifacts and tracking errors.

relaxation mechanism. At higher activities where the system has entered the liquid phase, the bonds relaxation is clearly seen. At $T_{\text{eff}}/T_0 = 3.0$ the system is still close to the glass transition. We are thus able to observe broken bonds at the boundary between two groups of particles travelling in opposite directions (see Fig. 4.22c). This is a clear sign of collective motion.

4.6.6 Defining characteristic length ℓ

From the directional orientation map in Fig. 4.20b we noticed qualitatively two things. Firstly, the system with faster relaxation in Fig. 4.20a seems to have higher orientational direction correlation. Secondly, the size of highly correlated domains displays the non-monotonic behavior just like the relaxation: decreasing when the system goes from the passive to $T_{\text{eff}}/T_0 = 1.4$ and then increasing with T_{eff}/T_0 . We see that the size of these highly correlated domains can be a characteristic length reflecting the system relaxation.

To measure the size of the highly correlated domains, we have to define a network of the correlated particles. As explained in Subsection 3.5.2, we take the subgraph of the correlated particles and split it in connected components, which will give us different clusters of correlated particles ($o_i \geq 4$). For each cluster k , we measure its radius of gyration in the y direction (perpendicular to $g \sin \theta$):

$$\ell_k = \frac{1}{N_k} \sqrt{\sum_{i \in k} y_i^2 - \left(\sum_{i \in k} y_i\right)^2 / N_k}, \quad (4.4)$$

where N_k is the number of particles in cluster k . The probability distribution function (PDF) of ℓ_k of all clusters at all time for various activities are displayed in Fig. 4.23a. For ($\ell_k/\sigma_0 < 5$), the distributions at all activities collapse. Compared to the distribution in the passive case, low activities are deprived of large oriented domains, whereas high activities have an excess probability of large oriented domains. Above $\ell_k \approx 10$ the distributions follow the non-monotonic behavior.

We define the characteristic length ℓ by a weighted average of ℓ_k on all clusters at all time:

$$\ell = \frac{\sum_{t_0} \sum_k N_k \ell_k}{\sum_{t_0} \sum_k N_k}. \quad (4.5)$$

As shown on Fig. 4.23b, ℓ displays a non-monotonic evolution with activity consistent with the ‘back and forth’ behavior: a drop of a factor 2 from the passive case to the lowest activity, and then a progressive increase at higher activities. This non-monotonic response is not captured by the size ζ of the slow domains (defined in the same way as ℓ , except that the 50% slower particles are considered instead of the particles where $o_i \geq 4$). ζ is almost constant, with a possible decreasing trend.

In Fig. 4.23c we show the correlation between the length ℓ and the relaxation time τ . The length ℓ evolves in reverse to what one would expect for a 4-point correlation length in glassy systems. Larger 4-point correlation implies longer relaxation in passive glassy systems [120], in active supercooled liquids [160], and in active crystals with alignment interactions [203]. Here, large ℓ corresponds to fast relaxation. Indeed, ℓ measures the size of domains with correlated orientation of displacement, associated with collective rearrangements, whereas 4-point correlation measures the size of cooperatively rearranging regions. A large domain moving collectively in the same direction enhances relaxation, whereas a large cooperative region size implies a larger energy barrier and thus longer relaxation. This hints to the existence of relaxation mechanisms specific to self-propelled particles that involves collective directed motion instead of cooperative rearrangements.

At this point, the speedup of the dynamics at high activities can be explained by the rise of collective motion. However, the delayed exit from the plateau at low activity levels occurs when collective motion is still negligible. Therefore, our results in the polycrystal point to a drop in efficiency of cooperative rearrangements between the passive case and our lowest activities.

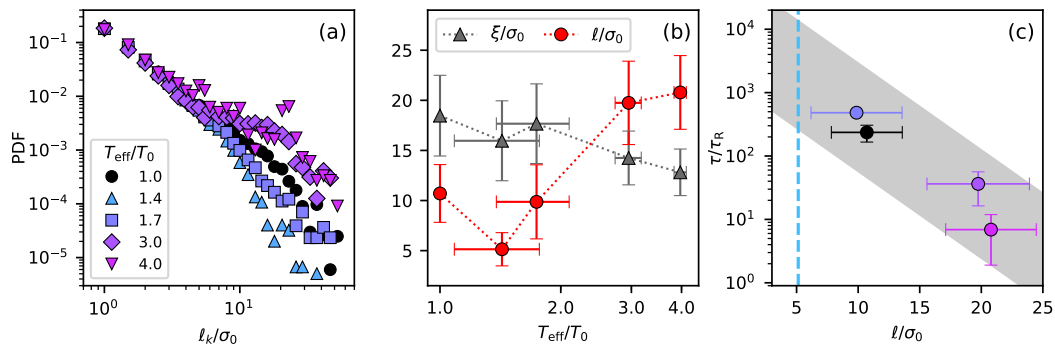


FIGURE 4.23: (a) Probability distribution function (PDF) of ℓ_k for each domain k at $\phi = 0.85 \pm 0.03$ and various T_{eff}/T_0 . (b) Average size of directional correlation domains ℓ (red) and slow domains ξ (gray) at various T_{eff}/T_0 . (c) The correlation between the relaxation τ measured from Fig. 4.19 and size of correlated domains ℓ . The measurement is done at various T_{eff}/T_0 color-coded as in (a). The vertical dashed line corresponds to $T_{\text{eff}}/T_0 = 1.4$ where the relaxation function $F(\Delta t)$ has not yet relaxed within our maximum lag time.

4.7 Simple model for the efficiency drop in cooperative rearrangements

So far, we have provided the experimental evidence showing that the weak self-propulsion weakens cooperative relaxation in the passive non-ergodic system. How does this happen? One can think about the motion of a particle inside a cage. For cooperative rearrangements to occur, an energy barrier of height E needs to be crossed. The relaxation time can be expressed in an Arrhenius form as $\tau = f^{-1} \exp(-E/k_B T_{\text{eff}})$. Here, we suppose that in the limit where T_{eff} is close to T_0 the extra energy provided by self-propulsion is not altering significantly the argument of the exponential. However, the attempt frequency f might be altered by the process of space exploration.

If we replace the many particles problem by the simpler problem of a single particle that explores a cage of size $a = 0.3\sigma_0$, f is then the frequency at which the test particle is coming close to the lowest barrier in the cage. For a Brownian particle, the exploration is governed by the translational diffusion motion. The time for a particle to displace by Δr is $t = (\Delta r)^2/4D_0$. Hence, the time that it takes to cross the cage is

$$\tau_{\text{cage}}^{\text{B}} = \frac{\zeta a^2}{4k_B T_0} \approx 0.1\tau_{\text{R}}, \quad (4.6)$$

where $\zeta = 6\pi\eta R_H$ is a drag coefficient. By contrast, in the case of a self-propelled particle without translational diffusion, the persistent random walk can be characterised by the magnitude of the self-propulsion force and the persistence time which is $0.5\tau_{\text{R}}$ [7, 106]. Since the cage size is shorter than the persistence length, the cage exploration time is thus the persistence time,

$$\tau_{\text{cage}}^{\text{P}} = 0.5\tau_{\text{R}}. \quad (4.7)$$

In other words, while a Brownian particle explores the cage isotropically, an athermal self-propelled particle moves through the cage and very soon hits the wall.

The self-propelled particle then has to wait for rotational diffusion to change its direction in order to move to other parts of the cage. Comparing the time scale between two exploration mechanisms, we obtain,

$$\frac{\tau_{\text{cage}}^{\text{P}}}{\tau_{\text{cage}}^{\text{B}}} = \frac{8}{3} \left(\frac{R_{\text{H}}}{a} \right)^2 \approx 5. \quad (4.8)$$

It means that the only physically important parameter is the ratio between hydrodynamic radius and interaction length. For a hard disks with $\sigma_0 = 2R_{\text{H}}$, we would expect $\tau_{\text{cage}}^{\text{P}}/\tau_{\text{cage}}^{\text{B}} \approx 7.4$. Conversely, athermal self-propelled particles should not be slower than Brownian particles if $\tau_{\text{cage}}^{\text{P}} < \tau_{\text{cage}}^{\text{B}}$, that is $\sigma_0 > 2.7(2R_{\text{H}})$, a very soft potential.

Eq. 4.8 suggests that for our system, an athermal self-propelled particle explores its cage 5 times slower than a Brownian particle. From our experimental result, the magnitude of the slowdown is larger than the factor of 5. We conjecture that the many-body nature of cooperative motion has to be taken into account to reach quantitative agreement. A reduction in attempt frequency at the single-particle scale may translate nonlinearly into a larger relaxation time at the level of the cooperative region. Furthermore, we have to take into account that the number of degrees of freedom per particle jumps from 2 in the Brownian case, to 3 in the self-propelled case where orientation become important. In other words, directional motion adds N degrees of orientational freedom that increase even more the complexity of the landscape and slows down relaxation.

With this explanation of the drop in efficiency of cooperative rearrangement when the particle motion becomes directional, we therefore name this phenomenon "Deadlock from the Emergence of Active Directionality (DEAD)". At this point, one might question *why* the slowdown is so sudden? To answer this question, we come up with a simple model using again the simplified situation: a single particle problem exploring a cage.

Propulsion-diffusion in a cage

Our particles are submitted to both translation Brownian motion and propulsion forces. The cage exploration limit is between the time when translational Brownian motion has left the ballistic regime and the propulsion direction is considered fixed (because the cage size is much smaller than the persistence length). In this range of time, a particle motion is a combination of translation diffusion with a constant drift v_{P} . This is analogous to the sediment-diffusion problem of Jean Perrin [111], replacing the weight by the propulsion force F_{P} .

In general, the Péclet number is defined as

$$\text{Pe} = \frac{\text{advection transport rate}}{\text{diffusive transport rate}}. \quad (4.9)$$

In our situation where the particle is propelling with a velocity v_{P} , the Péclet number over the cage of size $0.3\sigma_0$ is

$$\text{Pe} = \frac{v_{\text{P}}(0.3\sigma_0)}{D_0}. \quad (4.10)$$

Rather than considering the propulsion velocity, we consider the effective diffusion coefficient of active Brownian particles. From Refs. [7, 204], it has been shown as

$$D_{\text{eff}}(\phi \rightarrow 0) = D_0 + \frac{1}{6} v_{\text{P}}^2 \tau_{\text{R}}. \quad (4.11)$$

Hence,

$$\frac{D_{\text{eff}}}{D_0} - 1 = \frac{1}{6} \frac{\tau_{\text{R}}}{D_0} v_{\text{P}}^2, \quad (4.12)$$

$$v_{\text{P}}^2 = \frac{6D_0}{\tau_{\text{R}}} \left(\frac{D_{\text{eff}}}{D_0} - 1 \right). \quad (4.13)$$

Substituting Eq. 4.13 into Eq. 4.10 we obtain

$$\text{Pe} = 0.3\sigma_0 \left(\frac{6}{D_0 \tau_{\text{R}}} \right)^{1/2} \left(\frac{D_{\text{eff}}}{D_0} - 1 \right)^{1/2}. \quad (4.14)$$

Recall that $\tau_{\text{R}} = 8\pi\eta R_{\text{H}}^3/k_{\text{B}}T_0$ and $D_0 = k_{\text{B}}T_0/\zeta$, where $\zeta = 6\pi\eta R_{\text{H}}$. In addition, T_{eff} is defined from D_{eff} such that $k_{\text{B}}T_{\text{eff}} \equiv \zeta D_{\text{eff}}(\phi \rightarrow 0)$. Consequently, $D_{\text{eff}}/D_0 = T_{\text{eff}}/T_0$. Hence,

$$\text{Pe} = \frac{3}{\sqrt{2}} \frac{0.3\sigma_0}{R_{\text{H}}} \left(\frac{T_{\text{eff}}}{T_0} - 1 \right)^{1/2}. \quad (4.15)$$

Fig. 4.24 displays the relation between Péclet number and the effective temperature from Eq. 4.15. The propulsion force dominates the cage exploration when $\text{Pe} > 1$, which corresponds to the effective temperature

$$\frac{T_{\text{eff}}}{T_0} = 1 + \frac{2}{9} \left(\frac{R_{\text{H}}}{0.3\sigma_0} \right)^2 \approx 1.45. \quad (4.16)$$

This is the lowest activity we can achieve in the experiment. Therefore, the sudden jump from the passive to the first activity can be explained by the steeply rise of Pe at the very beginning where the cage exploration is already ruled by the physics of self-propelled particles.

For hard or slightly soft potentials, the non-monotonic behaviour should be observed as soon as the relevant Péclet number (effective temperature) range is explored. For example, we note that the simulations of glassy active Brownian hard spheres in 3D by Ni et al. [157] report their lowest Péclet number at 3 (within our definition that takes the size of the cage into account, 10 in their definition). In our experiments that is above where propulsion energy overcomes the drop in cooperative rearrangements.

Alternatively, the drop of the cage exploration efficiency can be explained using velocity-velocity correlation function. By comparing the inertial time τ_{v} and the rotational time τ_{R} , we can see that the cage exploration is ruled by the active Brownian particle model as soon as the activity is nonzero. We provided this explanation in the Appendix 4.

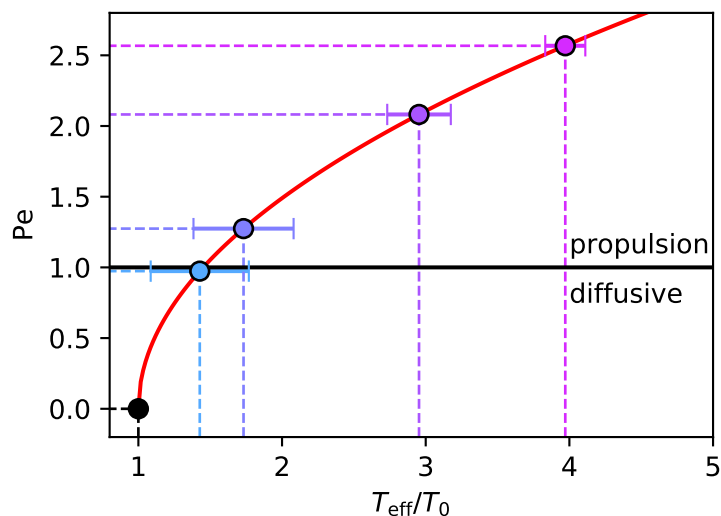


FIGURE 4.24: Péclet number versus T_{eff}/T_0 corresponds to Eq. 4.15 (red solid line). The horizontal solid line represents $Pe = 1$, the transition point whether the diffusive motion or self-propulsion motion dominates the cage exploration. The T_{eff}/T_0 measured experimentally from the sedimentation profile is shown by the circles.

4.8 Conclusions

We investigated experimentally of a sediment of active colloids, which provides us the full range of densities. We found that the glass transition density shifts towards higher values when the activity levels increases. This agrees with the previous numerical investigation [157, 159]. We also showed that the approach to glass transition from the supercooled phase fits well with the VTF relation upon scaling with activity-dependent glass transition and relaxation time in the very dilute limit. The most remarkable finding from this experiment is the failure of the mapping from the passive to active system when the ergodicity is broken. In this regime, we evidenced a non-monotonic response with the activity level. At low activity level, the system exhibits less dynamics than in the passive case, while it has more dynamics when the activity is high enough. Furthermore, we have shown that this phenomenology is not restricted to the amorphous glass, but is also observed in polycrystalline regions where grain boundaries are pinned. There, we were able to link the relaxation time to the size of collective motion. We thus evidenced that the non-monotonic behavior is linked to a drop in the efficiency of cooperative relaxation modes between passive and low-activity cases. We also developed a simple model to show that this drop of cooperative relaxation is due to a lower efficiency of the cage exploration when a Brownian particle becomes weakly self-propelled.

We published the work of this chapter in Klongvessa et al. [205, 206].

Key points of the chapter:

1. We performed experiments on a sediment of active colloids, which contains dilute phase, ergodic supercooled phase, non-ergodic glass phase and non-ergodic polycrystalline phase. We characterized the activity levels using **effective temperature** defined from the dilute phase of the sedimentation profile. This effective temperature is valid for all density regimes.
2. We found a **non-monotonic response** with the activity levels in the densest part of the sediment.
3. We characterized the system density and found a **compaction** upon increasing H_2O_2 concentration. To control for the compaction effect, we divided the sediment into thin slices with various densities. We then characterized slices with the same density for different activity levels. As a results, the non-monotonic behavior is still observed at high enough density.
4. By varying the density, we showed that the active supercooled regime is described well with the VTF relation. However, the **mapping** from the passive to active system fails when the ergodicity breaks.
5. We found that the non-ergodic polycrystals also have the non-monotonic response. With a wide polycrystal slice, we probed the relaxation mechanism and defined a new **correlation length** of directionally correlated domains. The correlation length has the same non-monotonic trend with the system relaxation: cooperative relaxation is observed in the passive system and low activity levels, and collective relaxation at high activity.
6. In terms of cage exploration, we proposed a simple **model** to explain the efficiency drop in the cooperative relation when the particles become active: a Brownian particle explores the cage isotropically with translational diffusion, while a weakly active particle is subjected to rotational diffusion. The active particle keeps colliding to the same direction until the diffusion makes it reorients to the other direction. This results in less efficient cage exploration compared to the passive case.
7. We named this phenomenon "Deadlock from the Emergence of Active Directionality (DEAD)"

Appendices

Appendix 1: Classical tools in glassy physics

Radial-pair correlation function $g(r)$

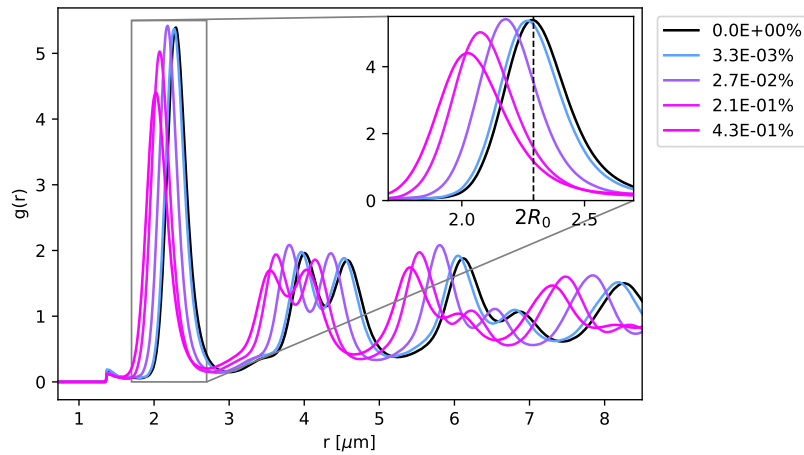


FIGURE 4.25: Radial-pair correlation function $g(r)$ computed from the bottom part of the sedimentation $\phi > 0.75$ at various H_2O_2 concentrations. Note that we omit some low concentration data.

Static structure factor $S(q)$

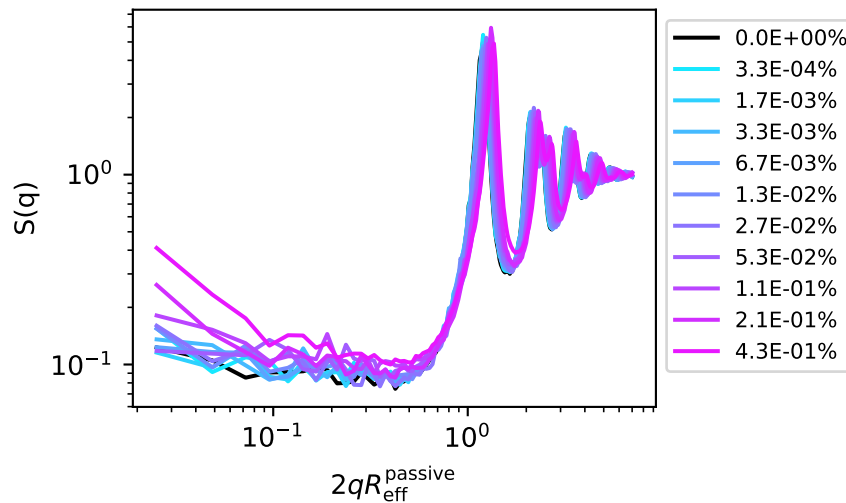


FIGURE 4.26: Static structure factor $S(q)$ computed from the bottom part of the sedimentation $\phi > 0.75$ at various H_2O_2 concentrations.

Four-point structure factor S_4 and dynamic susceptibility χ_4

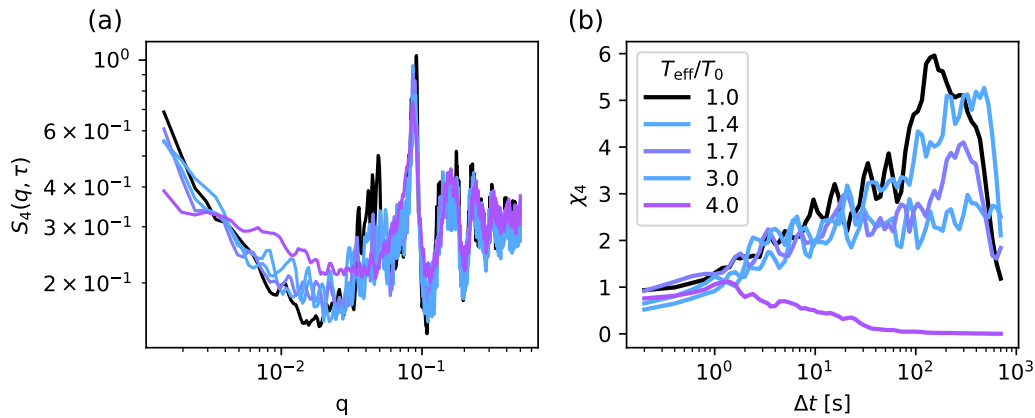


FIGURE 4.27: (a) Four-point structure factor $S_4(q, \tau)$ and (b) dynamic susceptibility χ_4 computed from the bottom part of the sedimentation $\phi > 0.75$ at different activity levels

Appendix 2: Comparing dynamics with and without crystalline particles

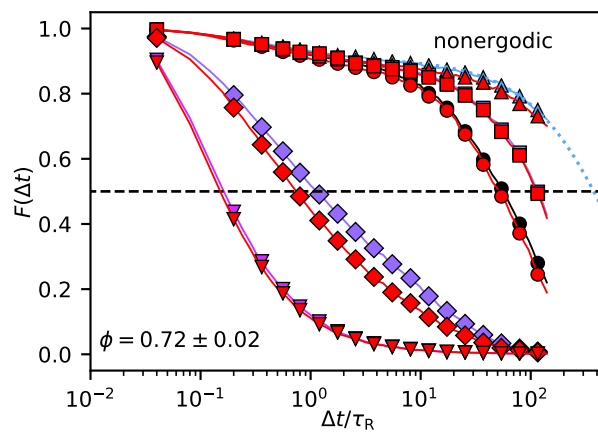


FIGURE 4.28: Same $F(\Delta t)$ plot as in Fig. 4.12c of the main text, with (in red) the neighbours of crystalline particles excluded from the calculation.

Appendix 3: Time evolution the crystalline particles map

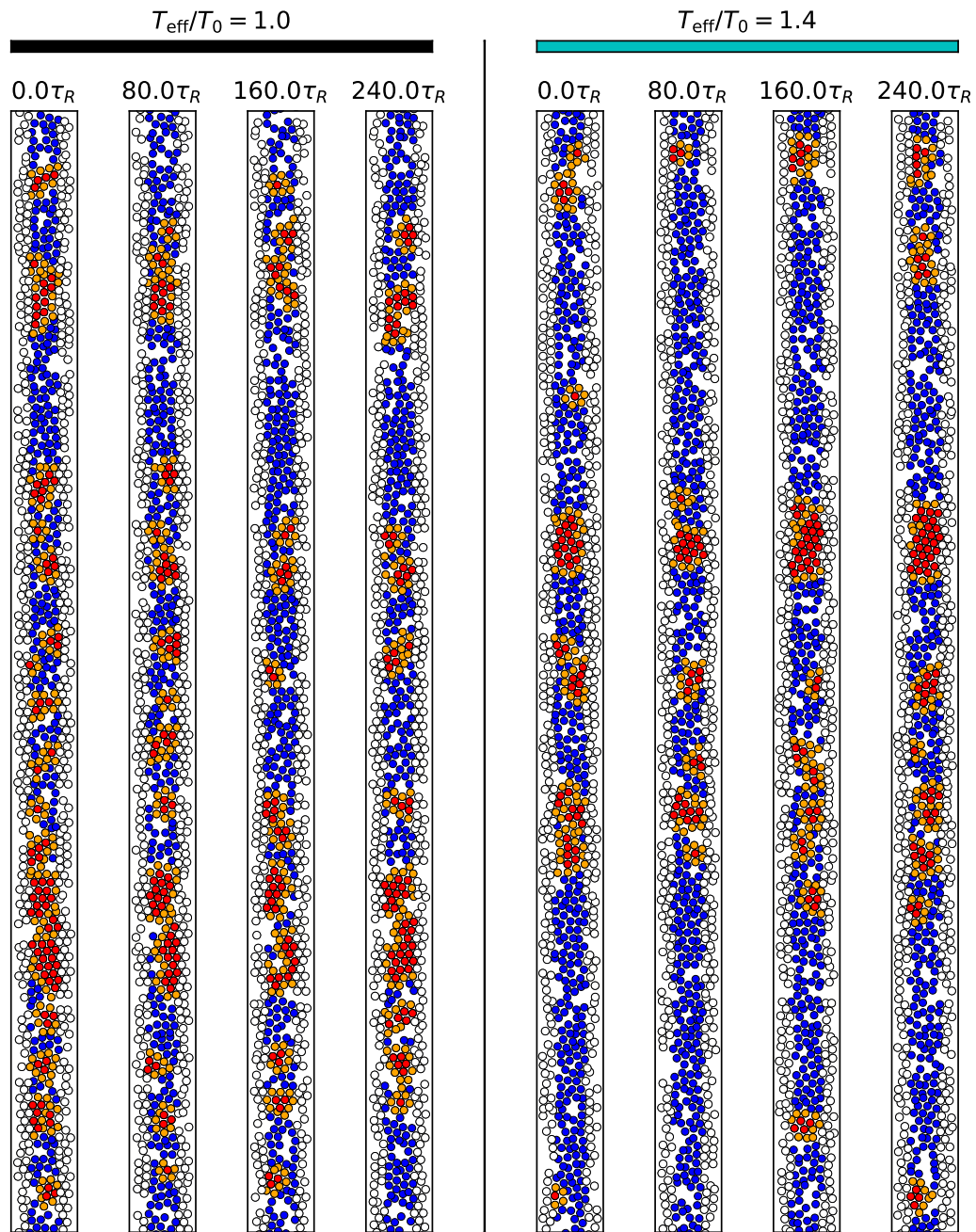


FIGURE 4.29: Snapshots at several times of a slice at $\phi = 0.72$ in passive (left) and the first nonzero active (right) cases. Particles are displayed with different colors: Crystalline particles (red), particles in direct contact with crystalline particles (orange), particles nearby the edges (white), and the remaining particles (blue).

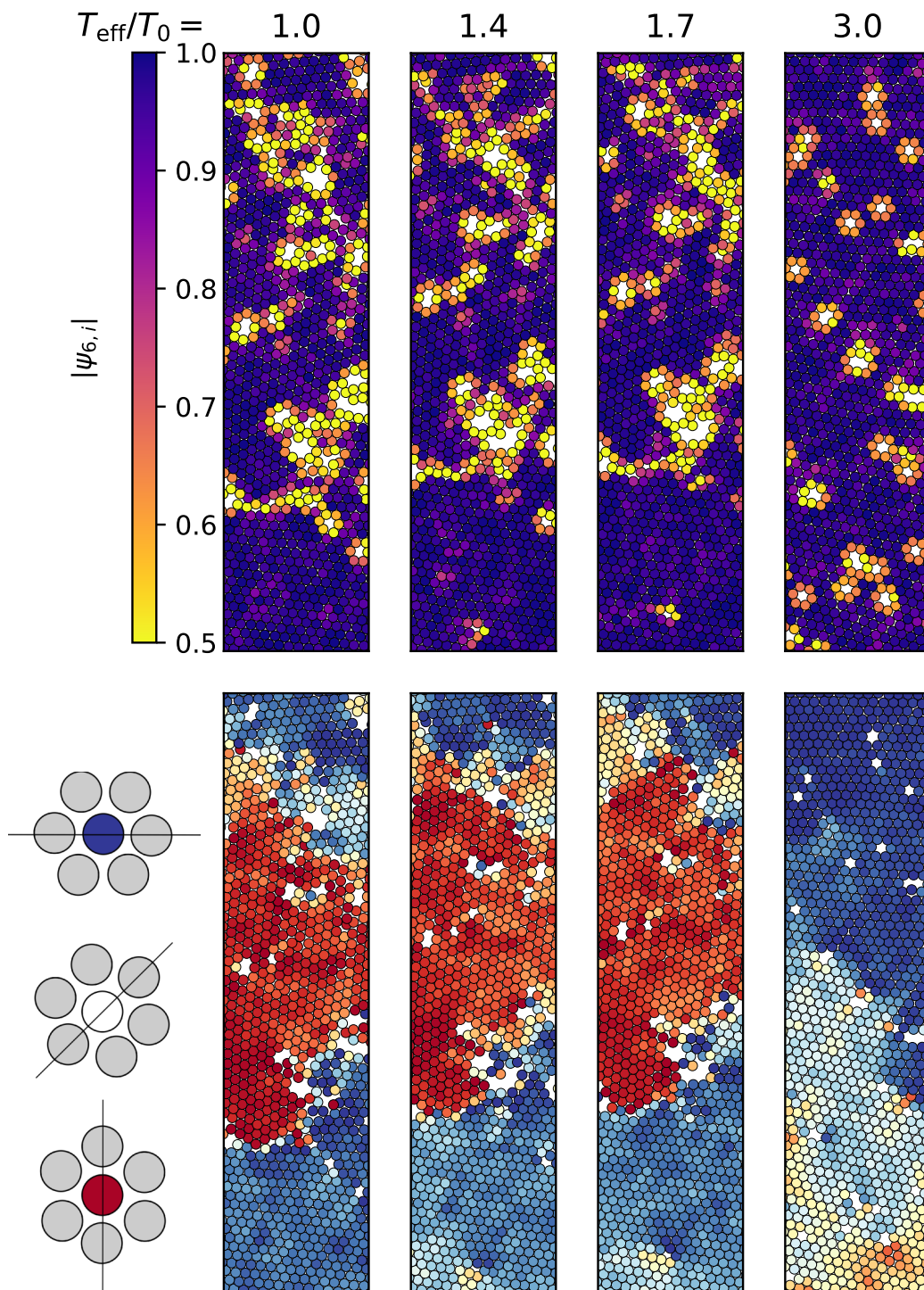
$\psi_{6,i}$ map

FIGURE 4.30: Maps of $\psi_{6,i}$ of different activity levels at $\phi = 0.85 \pm 0.03$: (a) modulus and (b) orientation. The white areas are from sample artifacts and tracking errors.

Appendix 4: Alternative explanation: Velocity-velocity correlation function

We consider the equation of motion for a Brownian particle of mass m with velocity \boldsymbol{v}_B ,

$$m\dot{\boldsymbol{v}}_B = F(t), \quad (4.17)$$

where $F(t)$ is the instantaneous force acting on the particle at time t . For a Brownian particle subject to Stokes drag with a coefficient ζ , $F(t)$ is composed of an inertial force $\zeta\boldsymbol{v}_B(t)$ and a random force $\boldsymbol{\zeta}(t)$ from surrounding fluid acting on the particle. Thus, Eq. 4.17 becomes

$$m\dot{\boldsymbol{v}}_B = -\zeta\boldsymbol{v}_B(t) + \boldsymbol{\zeta}(t). \quad (4.18)$$

This is a so-called Langevin equation of motion for a Brownian particle. We expect the random force $\boldsymbol{\zeta}(t)$ to have the following properties;

$$\langle \boldsymbol{\zeta}(t) \rangle = 0, \quad \langle \boldsymbol{\zeta}(t_1) \cdot \boldsymbol{\zeta}(t_2) \rangle = f\delta(t_1 - t_2). \quad (4.19)$$

If we neglect the random force $\boldsymbol{\zeta}(t)$, the general solution of Eq. 4.18 is

$$\boldsymbol{v}_B(t) = \boldsymbol{v}_B(0)e^{-t/\tau_v}, \quad (4.20)$$

with the inertial time $\tau_v = m/\zeta$. Hence the 2D velocity-velocity correlation function for a Brownian particle is

$$\langle \boldsymbol{v}_B \cdot \boldsymbol{v}_B \rangle = \langle v_B^2 \rangle e^{-t/\tau_v}. \quad (4.21)$$

The average velocity square $\langle v_B^2 \rangle$ can be obtained from the equipartition theorem for a 2-degree of freedoms system,

$$E_k = \frac{1}{2}m \langle v_B^2 \rangle = k_B T_0, \quad (4.22)$$

Therefore, Eq. 4.21 becomes

$$\langle \boldsymbol{v}_B \cdot \boldsymbol{v}_B \rangle = \frac{2k_B T_0}{m} e^{-t/\tau_v}. \quad (4.23)$$

In the case of an active particle with a propulsion velocity \boldsymbol{v}_P , the Active Brownian Particle (ABP) model [106, 7] expresses the 2D velocity-velocity correlation function as

$$\langle \boldsymbol{v}_P \cdot \boldsymbol{v}_P \rangle = \langle v_P^2 \rangle e^{-2t/\tau_R}, \quad (4.24)$$

with a Brownian rotational time τ_R . In the same way as in Eq. 4.21 and Eq. 4.22, $\langle v_P^2 \rangle$ can be obtained by replacing T_0 to an effective propulsion temperature T_P . Therefore, Eq. 4.24 becomes

$$\langle \boldsymbol{v}_P \cdot \boldsymbol{v}_P \rangle = \frac{2k_B T_P}{m} e^{-2t/\tau_R}. \quad (4.25)$$

The velocity of active Brownian particle composes of a propulsion velocity and a Brownian velocity,

$$\boldsymbol{v} = \boldsymbol{v}_P + \boldsymbol{v}_B. \quad (4.26)$$

The velocity-velocity correlation is given by

$$\langle \boldsymbol{v} \cdot \boldsymbol{v} \rangle = \langle \boldsymbol{v}_P \cdot \boldsymbol{v}_P \rangle + \langle \boldsymbol{v}_B \cdot \boldsymbol{v}_B \rangle + 2 \langle \boldsymbol{v}_P \cdot \boldsymbol{v}_B \rangle, \quad (4.27)$$

where the last term is zero because we expect no correlation between both velocities. Hence,

$$\langle \mathbf{v} \cdot \mathbf{v} \rangle = \frac{2k_B T_0}{m} \left[e^{-t/\tau_v} + \frac{T_P}{T_0} e^{-2t/\tau_R} \right]. \quad (4.28)$$

To find a relation between the effective propulsion velocity T_P and the effective temperature T_{eff} measured from the experiment, we look at the long-term diffusion coefficient of active Brownian particles. From Refs. [204, 7], it has been shown as

$$D_{\text{eff}}(\phi \rightarrow 0) = D_0 + \frac{1}{6} v_P^2 \tau_R, \quad (4.29)$$

where $D_0 = k_B T_0 / \zeta$ is the Brownian translational diffusion coefficient and $D_{\text{eff}} = k_B T_{\text{eff}} / \zeta$ is the effective diffusion coefficient. By substituting v_P from Eq. 4.25, we obtain

$$k_B T_{\text{eff}} = k_B T_0 + \frac{1}{3} k_B T_P \frac{\zeta}{m} \tau_R \quad (4.30)$$

$$T_{\text{eff}} = T_0 + \frac{1}{3} T_P \frac{\tau_R}{\tau_v} \quad (4.31)$$

$$\frac{T_P}{T_0} = 3 \frac{\tau_v}{\tau_R} \left(\frac{T_{\text{eff}}}{T_0} - 1 \right). \quad (4.32)$$

Finally, the Eq. 4.28 becomes

$$\langle \mathbf{v} \cdot \mathbf{v} \rangle = \frac{2k_B T_0}{m} \left[e^{-t/\tau_v} + 3 \frac{\tau_v}{\tau_R} \left(\frac{T_{\text{eff}}}{T_0} - 1 \right) e^{-2t/\tau_R} \right]. \quad (4.33)$$

From Eq. 4.33, it can be seen that the velocity-velocity correlation is composed of two terms. When $T_{\text{eff}}/T_0 = 1$ (passive case), the characteristic time is only governed by τ_v . As soon as $T_{\text{eff}}/T_0 > 1$, the characteristic time is a combination of τ_v and τ_R . However, in our system, the inertial time $\tau_v = \frac{2}{9} \frac{R_H^2}{v} \frac{\rho}{\rho_{\text{water}}} \approx 2 \mu\text{s}$ is negligible when compared with $\tau_R = 5 \text{ s}$. Therefore, as soon as the activity is nonzero, the cage exploration is ruled by the ABP model, which gives higher velocity-velocity correlation than the purely Brownian model in the time scale of cage exploration. This can also explain *why* the drop of relaxation from the passive case to the first nonzero activities is sudden.

Chapter 5

Microrheology of Active Colloids Sediment

In the previous chapters, we have focused on the behavior of active sediment without external perturbation. We have discovered the different responses when increasing activity at the onset of glass transition. The next question is how the active sediment reacts to an external perturbation? How the response will be different from the response of a passive suspension? These questions lead us to a study of rheology. By viewing the assembly of our active colloids as a new type of material, we can try to extract its rheological properties. We can also make a characterization to see where the colloidal sediment lies in between fluid and solid phases, and whether this position changes upon increasing activity level.

There have been other studies investigating rheological properties of active systems such as living cells [207, 208, 209] and active bacterial bath [210, 211]. Putting a passive probe particle inside a dilute bacterial suspension, it is found that the probe diffusion motion, which is related to the effective suspension viscosity, is enhanced compared to a solution without swimming bacteria. For a dilute suspension of active Brownian particles, a theoretical framework showed that the diffusion motion of the probe scales with effective temperature rather than bath temperature [212]. Apart from using thermal agitation, the same theoretical group applied an external force to pull the probe particle through the dilute suspension and they found a ‘swim-thinning’ behavior when the pulling force is weak enough [213].

Since we have carried out the very first experimental study on the dense assemblies of active colloids, we decided to investigate its rheology as well. This chapter is divided into four sections. In the first section, we introduce key concepts of rheology and microrheology. The remaining sections describe three works with different actuation approaches, in which the last one is being a prospective work. Please note that compared with the previous chapters, the experiments presented here are in a more preliminary stage.

5.1 Key concept of rheology and microrheology

Rheology is the study of flow and deformation of matter [214]. Typically, it applies to fluid-like (that flow) and solid-like (that deform elastically or plastically) materials. Since there is a broad spectrum between ideal fluid and ideal solid, rheological properties can be used to characterize a given material that sits somewhere in between.

In rheology, there are two quantities that are always mentioned: shear stress σ (a force acting over a unit area) and shear strain γ (deformation of a material). For an ideal fluid, the property to characterize the flow is viscosity η , which is the

coefficient of proportionality between σ and the rate of deformation $\dot{\gamma}$, which is often called shear rate, i.e.,

$$\sigma = \eta \dot{\gamma}. \quad (5.1)$$

For the case of an ideal solid, if the stress is smaller than a certain threshold (depending on a material), the relation between shear stress and strain is in a similar form as Hooke's law,

$$\sigma = G\gamma, \quad (5.2)$$

where G is called the elastic modulus. This relation with a constant G means that there is no time dependence in the deformation induced by the stress. If the stress is removed, the material immediately returns to its original shape.

Yield stress fluid

Many materials contain both fluid-like and solid-like properties. In some materials, if the applied stress is weak enough, the material shows an elastic response like an elastic solid. As soon as the stress reaches a certain threshold, the material flows like a viscous fluid. A material with such a property is known as yield stress fluid [215], and it is often modelled with the Herschel-Bulkley model [152]:

$$\sigma = \sigma_y + K\dot{\gamma}^n, \quad \sigma \geq \sigma_y, \quad (5.3)$$

where σ_y is the yield stress threshold, K and n are model parameters. Typical examples of yield stress fluid are toothpaste, foams, mayonnaise, etc. All of them remain in the same shape after we squeeze them out from their containers.

Viscoelastic material

Many materials contain rheological responses of both fluid (viscous) and solid (elastic) properties at the same time and they are known as viscoelastic materials. The relationship between stress and strain of such a material can be expressed as $\sigma = \sigma(\gamma, \dot{\gamma})$, which is a combination of the solid-like and fluid-like counterparts. Unlike a yield stress material in which the response depends on the applied stress alone, the response of a viscoelastic material also depends on the time scale of how the material is sheared. Many polymers [216] and biological tissues [217] are examples of viscoelastic materials, and they are greatly involved with our daily life.

There are several rheology tests to characterize a given material whether it is a solid, fluid, yield stress fluid, or a viscoelastic material. In the following, I would like to introduce two of them that we used in this thesis: oscillatory testing and creep testing.

Oscillatory test

One way to characterize materials is by using small amplitude oscillatory shear (SAOS). When applying sinusoidal stress of small amplitude to a viscoelastic material, the resulting strain is also sinusoidal with the same frequency but different phase δ . Actually, the other way around is also commonly used: applying sinusoidal strain $\gamma(\omega, t) = \gamma_0 \sin(\omega t)$ and then measuring the resulting stress $\sigma(\omega, t) = \sigma_0 \sin(\omega t + \delta)$. The ratio of the stress to the strain is called complex shear modulus $G^* = \sigma_0 / \gamma_0$. Hence, the resulting stress can be represented in the following form:

$$\sigma(\omega, t) = G'(\omega)\gamma_0 \sin(\omega t) + G''(\omega)\gamma_0 \cos(\omega t), \quad (5.4)$$

where $G'(\omega) = G^* \cos \delta$ and $G''(\omega) = G^* \sin \delta$ are called the storage modulus and the loss modulus, respectively, which are both frequency dependent. Alternatively, Eq. 5.4 can be expressed using a complex number notation as

$$\tilde{\sigma}(\omega, t) = (G'(\omega) + iG''(\omega))\tilde{\gamma}(\omega, t) = |G^*|e^{i\delta}\tilde{\gamma}(\omega, t). \quad (5.5)$$

in which we can see that $G'(\omega)$ is the real part of G^* , and $G''(\omega)$ is the imaginary part.

One can define the loss tangent $\tan \delta = G''/G'$ to express the phase angle. If a material is purely elastic, the loss tangent is equal to zero ($\delta = 0$). On the other hand, a purely viscous material will result in infinite loss tangent ($\delta = \pi/2$). The response of a viscoelastic material is therefore in between both cases ($0 < \delta < \pi/2$). We illustrate the relationship between stress and strain in oscillatory rheology of these three cases in Fig. 5.1a. We note that here we only discuss the small deformation (linear regime). For a large deformation, the response is non-sinusoidal as higher harmonics are no longer negligible (non-linear regime).

For yield stress materials in the linear regime, we could expect an elastic response as G' is much larger than G'' . If γ_0 is increased and has reached the nonlinear regime, G' is found to decrease and then eventually crosses G'' . Beyond this point, the material is more fluid-like [153].

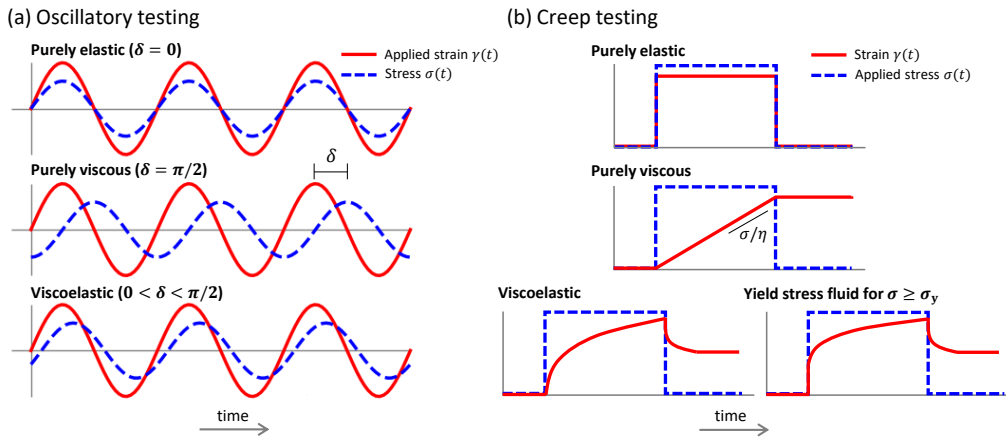


FIGURE 5.1: Strain $\gamma(t)$ and stress $\sigma(t)$ relationship in (a) oscillatory test of small amplitude, and (b) creep-recovery test. The response is shown comparing between purely elastic, purely viscous and viscoelastic materials.

Creep testing

Another way to characterize materials is by creep testing. The principle is to apply small constant shear stress to a sample and measure the resulting strain. In Fig. 5.1b, we show expected relation between the strain $\gamma(t)$ and the applied stress $\sigma(t)$ for different types of materials: elastic, viscous, viscoelastic and yield stress materials. According to Eq. 5.1 and Eq. 5.2, we should expect that a purely elastic material deforms immediately when the stress is applied and remains the same afterward, while a purely viscous material deforms with a constant rate σ/η . A viscoelastic material typically shows an initial elastic response (sharp rise of γ) followed by a delayed elastic response ($\dot{\gamma}$ decreases with time) before reaching a constant $\dot{\gamma}$. In the case of a yield stress fluid, if the applied stress is lower than the yield stress σ_y , the response is elastic. The creep test is also used to determine the yield stress point of

yield stress fluids by varying the stress level until the sample begins to flow. Once it flows, the strain sharply increases at the beginning, and then the shear rate decreases before reaching a constant value, similarly to a viscoelastic material [218]. Therefore, from the shape of the strain response, the elastic and viscous properties of a given material can be extracted.

When the stress is removed, different materials respond differently as well. An elastic material returns to its original shape immediately, whereas a purely viscous sample does not recover. A viscoelastic material first recovers elastically and then the recovery rate is slower and slower until it reaches the steady state, which is not the original shape. The full test from applying and then removing the stress is called the creep-recovery test.

A typical rheological measurement is done using a rheometer, which is a device that applies shear strain (or stress) to a sample and measures resultant stress (or strain). In Fig. 5.2, we illustrate rheology measurements using a rheometer. A sample is placed in between two parallel plates. One of them is movable in order to shear the sample either with a constant stress (for the creep test) or a sinusoidal motion (for the oscillatory test). Since the rheological properties of a material are depending on a time scale, it is often used to investigate frequency-dependence of G' and G'' . Different kinds of materials can be characterized by the frequency response of both moduli.

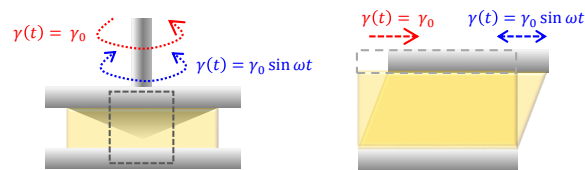


FIGURE 5.2: Schematic illustration of a rheometer. A sample is placed in between two parallel plates, in which one of them is movable. For the creep test, it rotates with a constant speed. For the oscillatory test, it moves with a sinusoidal motion.

Microrheology

Many viscoelastic materials require investigation at high frequency and small length scale, which are not accessible by conventional rheology (maximum frequency 10-50 Hz and typical length scale in mm). This leads to a new focus on rheology at a smaller scale known as microrheology. Most of microrheology approaches use micron-size particles to induce deformation and to probe material response from the inside. They can be divided into two main classes depending on the force acting on the probe particle: passive and active microrheology.

In passive microrheology, the probe motion results from thermal energy $k_B T_0$. Viscoelastic properties of a material can be extracted from the mean square displacement (MSD) of probe particles via the generalized Stokes-Einstein relation [219, 220]. In active microrheology, on the other hand, the probe particle is submitted to an external driving force (commonly use optical [221, 222], and magnetic [223, 224, 225] forces, see Fig. 5.3). The response of the system can be investigated through the displacement of the bead with the same principle as in bulk rheology.

There are four great benefits of microrheology compared to the conventional bulk rheology. (1) Wider frequency range towards higher limit (up to 10^3 Hz or

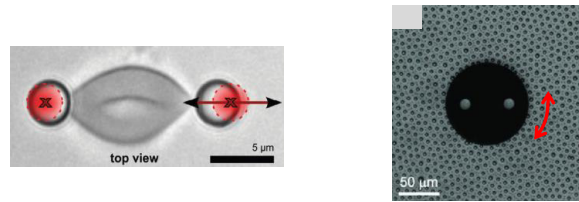


FIGURE 5.3: Two examples of microrheology. (Left) A red blood cell is bounded in between two optically trapped particles. One of the particles is oscillated to perform whole-cell rheology. The image is retrieved from Ref. [226]. (Right) A micro-rotor in a colloidal monolayer. The rotor is oscillated due to an external magnetic field. The image is modified from Ref. [224].

higher [227]). (2) The length scale for the investigation is in the order of the probe size ($\sim \mu\text{m}$). This is well-suited to study spatially heterogeneous samples because the investigation is performed locally, unlike the bulk rheology. (3) It requires a much smaller amount of sample. While a typical rheometer requires few ml of a sample, an order of μl is sufficient for microrheology. This is very useful in the case of a limited sample amount available such as cells or biomaterials. (4) It is applicable to non-conventional 2D geometries such as Langmuir monolayers [228], surfactant interfaces [225] and also our colloidal monolayer.

The rest of this chapter will present our microrheological investigation in active colloidal sediment. In the next section, we apply small amplitude oscillatory shear (SAOS) to our system using optical tweezers. The goal is to extract G' and G'' of the sediment of different activity levels. The third section is an actuation by gravity. We drop an intruder and let it creep through the colloidal sediment and observe different motion of the intruders when the activity is added. Analysing the motion of the intruder and the colloids helps us understanding the origin of the difference. We go further in the analysis using relative position of the colloids and evidence a Stokes flow. The last section is a perspective towards a magnetic actuation that we are trying to implement in our lab. This last section is a bit technical and mostly a description of the developing setup, which is the initiation for a future work that would be further developed after my PhD.

5.2 Actuation by optical tweezers: Periodic motion of a tracer

This part of my PhD was done in the institute of industrial science, the University of Tokyo, with financial support from the PICS-CNRS budget of Mathieu Leocmach. I had spent one and a half months in the soft matter research group of Prof. Hajime Tanaka. The experiment was conducted in collaboration with Isaac Theurkauff and with some technical help from Nicolas Bruot. At that time, they were post-doctoral researchers in the group.

In this section, I will first introduce some key concepts of optical tweezers that were used in the experiment and then present the experimental configuration. Finally, I will discuss the result of the SAOS.

5.2.1 Optical tweezers and its application to microrheology

Optical tweezers consist of a highly focused laser that can trap and control an object in focus. It is an effective tool to manipulate a micron-sized object [229]. Its precision is in the order of nanometer and millisecond, which results in subpiconewton applied forces [222]. The principle of the optical tweezers is illustrated in Fig. 5.4a. When the laser beam passes through an object, the scattering light results in a reaction force to the object (due to momentum conservation). Because the incident light has a Gaussian intensity profile, the reaction force always pulls the object to the focal point of the laser beam.

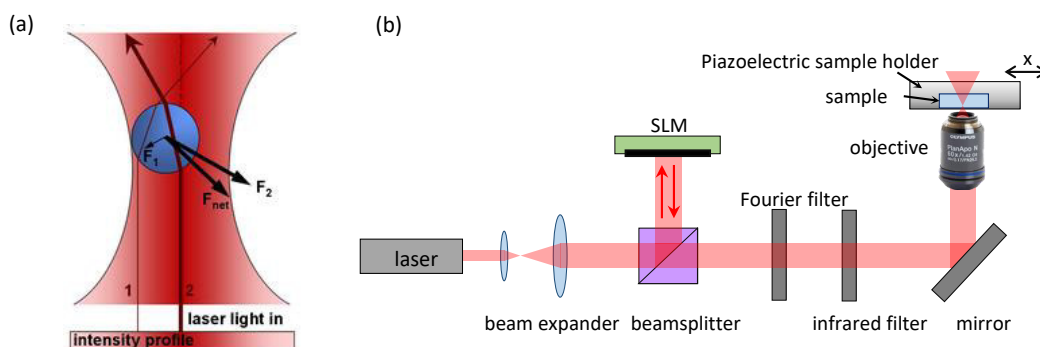


FIGURE 5.4: (a) A schematic drawing illustrating the principle behind optical tweezers. The incident laser beam, which has a Gaussian profile, goes through an object as displayed in light rays 1 and 2 (red arrows). Forces F_1 and F_2 are associated to the light rays 1 and 2. The net force F_{net} is thus always pulling the object to the center. The image is retrieved from <http://ufls-iitk.vlabs.ac.in/optical.php>. (b) A schematic diagram of the optical tweezers used in our experiment. A spatial light modulator (SLM) creates a hologram of the optical trap. We can design the hologram using a software (HOTkit, Arrayx). In this experiment, we always use a single spot optical trap.

Optical tweezers have been widely used as an active microrheology technique [230]. Using a trapped particle as a probe and then control the trap motion, which is identical to control the force applied on the probe particle. The most basic movement is an oscillation with a small amplitude at various frequency [231, 232], which is analogous to conventional bulk rheology in the linear regime. To extend to the nonlinear regime, the trap is moved with a constant speed with a larger displacement [232, 233].

5.2.2 Our experimental setup

The group of Prof. Tanaka already had optical tweezers installed by Isaac Theurkuaff and Nicolas Bruot for their research. Before I went there, we had sent some gold particles and experimental plates to Isaac for preliminary testing the setup and preparing a piezoelectric sample holder in advance. I brought with me the Janus colloids, a custom-made dark-field LEDs ring and sample plates to complete the setup. Please note that this subsection contains mostly technical details of the experimental setup, and I will also mention issues we had and how we dealt with them.

Optical tweezers setup

The setup of the optical tweezers in Prof. Tanaka's group is shown in Fig. 5.4b. The laser beam comes from a 1064 nm-wavelength fiber laser (IPG, YLR-10-LP, 10 W) and it is split via a 50:50 beamsplitter cube. Half of the beam is reflected on a spatial light modulator (SLM, 512x512, Boulder Nonlinear Systems), which creates a hologram of the optical trap designed via a software (HOTkit, Arryx). We note that we always use a single spot optical trap in our experiment. After the beam goes back to the beamsplitter, it passes a Fourier and infrared filter, respectively, before reaching the microscope. The beam reflects inside the microscope on a dichroic mirror (950 nm shortpass, Semrock FF01-950/SP) and finally enters an objective. The focal point of the laser is thus the focal point of the objective.

Microscope setup and our sample

The experimental setup is illustrated in Fig. 5.5a. We used the same 96-well plate as introduced in Section 2.2. The plate was cut into 5 cm × 5 cm to be fitted to a two-axis piezoelectric sample holder. The motion of the holder is controlled by a function generator. The laser beam for the optical trap is sent through a 60x Olympus UPlanSApo 1.20 NA water immersion objective mounted on an Olympus IX81 microscope. Below the sample holder, we installed a custom-made dark-field LED ring, which I brought from Lyon.

The main object of this experiment (and this thesis) is of course the active Janus particles. In the beginning, we planned to optimize the time by preparing the Janus particles in Lyon and bringing them with me to Tokyo. This is also because we did not know exactly the conditions in Tokyo (such as equipment and accessibility to a clean room) to make a new fresh batch of Janus colloids there. Unfortunately, the (first) problem we had is that after the travel, the Janus colloids were stuck on the surface of the glass container. After we managed to retrieve some of them, they showed very poor propulsion efficiency. At this point, we decided to make a new batch of Janus colloids using sorted gold particles that I had also brought from Lyon as a backup plan. The platinum deposition was done by sputtering technique with the thickness 35 nm in Takeda cleanroom of the University of Tokyo. We acknowledge the help from Antony Genot and Eric Lebrasseur, and we are also very grateful for the additional expense from Prof. Tanaka's group.

The new Janus particles were dispersed in the well filled with deionized water. To confine them and create a dense phase, again, we used a small tilt angle. However, this was impossible to tilt the whole setup because the microscope is equipped with the optical tweezers. We, therefore, tilted the experimental plate inside the piezoelectric holder. The tilt angle is less than 0.5° (measured by changing the focus between two points). At this small angle, we can still obtain a good focus of about 95% of 225 μm × 225 μm observation area. Before starting the experiment, we always let the colloids settle overnight to make sure that they were in a stationary position.

Probe particle

We spent some time trying several types of probe particles. This is because we observed an unexpected interaction between some probe particles and the Janus colloids when we added H₂O₂ to activate the colloids. Some probes showed a repulsive effect, and some showed an attractive effect. We also noticed that the effect is enhanced when the probe was trapped by the laser. The probe that we finally chose to

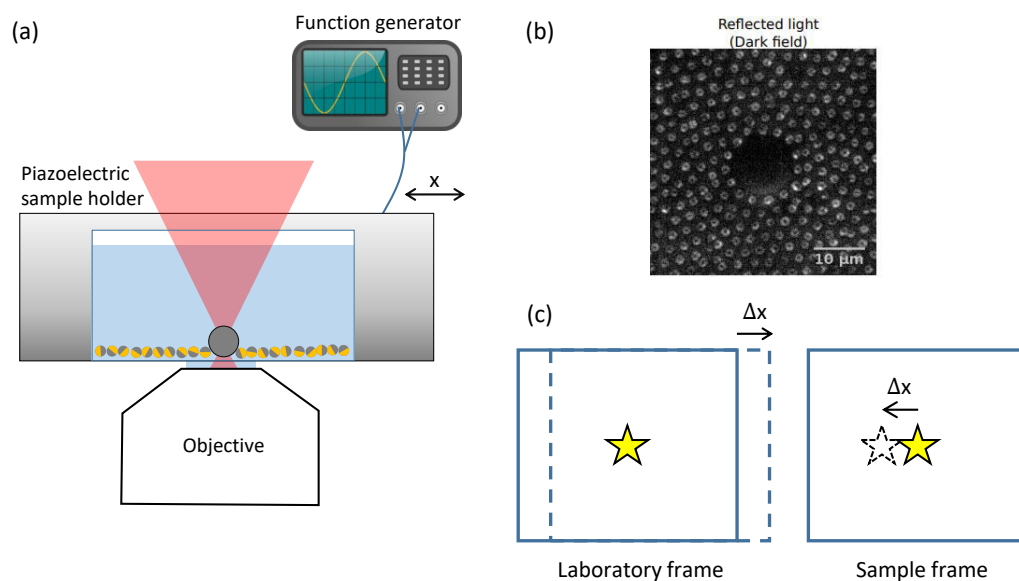


FIGURE 5.5: (a) Schematic experimental setup. The sample is held by a two-axis piezoelectric holder, which is connected with a function generator in order to control the movement. The optical trap is fixed with the objective and thus results in relative motion to the monolayer Janus particles. (b) An experimental image with the dark-field light mode. The trapped bead of at the center and is surrounded by the Janus particles. (c) A schematic drawing illustrating movement of the optical trap (yellow star) respect to the sample frame (blue frame). On the left, the sample is moved while the trap is held fixed, which is the situation in the laboratory frame. On the right, the resulting motion in the sample frame.

minimize this effect (Sigmund Lindner glass beads #5210-07) appeared to have only a weak attractive effect when the laser was on. However, estimated by eyes, this effect was independent of H_2O_2 concentration and we saw no difference between the passive and active cases. We introduced $1\ \mu\text{l}$ of a very dilute solution of the probe particles into the well with the Janus colloids. It is important to verify the right concentration of the probe particles before. This can be done by checking the amount of the probe in a bare well. The goal is to have not too many probes falling into the colloidal sediment. After we introduced the probe solution, we turned on the laser and tried to trap one probe particle. Once we successfully trapped it, we dragged it into the Janus colloids sediment. Fig. 5.5b shows the resulting image of the probe particle (apparent diameter $17\ \mu\text{m}$) surrounded by the Janus colloids in dark-field lighting.

There was another serious problem when we dealt with the optical trap. We have found some strange effects when the laser lost the probe particle (for example, when we dragged the trap too fast) and focus inside the colloidal sediment. If we were lucky, the laser only blew the colloids upwards around the focal point. We just had to move the trap and fetch the probe to continue our experiment. However, sometimes the laser created a sudden effect like a small explosion of air bubbles and left some colloids stuck on the bottom surface. This is indeed the worse situation because we lost some precious Janus colloids and we had to restart all over again. After several such failures, we had learned that this effect was less probable at lower laser power. We therefore always stayed at the minimum laser power of $0.1\ \text{W}$. Such a weak trap is also good to be able to detect the perturbation on the probe from the Janus colloids.

We did the characterization for the trap stiffness k from the probe particle in the static trap with no colloids around. k is extracted from the fit of the probe position x over 30 min with a Gaussian distribution $\exp(-(xk/k_B T_0)^2)$. As a result, we obtained $k \approx 6 \times 10^{-7} \text{ N m}^{-1}$.

Actuation

For the microrheology measurements, the piezoelectric sample holder moves the well plate in a sinusoidal way along the direction x , which is perpendicular to the direction of in-plane gravity, while the optical trap is held fixed with respect to the laboratory frame. Of course, in the sample frame, the trap is the one moving. Fig. 5.5c illustrates the relative situations between the laboratory frame (moving sample) and the sample frame (moving probe). We imposed an oscillation of amplitude $5 \mu\text{m}$ with a period of 2 s. Images were acquired at 25 Hz.

The stress felt by the sample is proportional to the force the optical trap exerts on the probe, itself proportional to the relative displacement of the probe with respect to the trap, that is directly obtained by particle tracking of the probe $\sigma \propto \Delta x_{\text{probe}}$.

The strain of the sample is proportional to the displacement of the probe relative to the sample, $\gamma \propto \Delta x_{\text{probe}} - \Delta x_{\text{sample}}$. We obtain Δx_{sample} by tracking particles far away from the probe, assuming that they were not affected by the motion of the probe.

Two examples of the observed oscillations are shown in Fig. 5.6, respectively with a stress mostly in quarter of phase with the strain (indicating mostly viscous response) and a stress mostly in phase with the strain (indicating mostly elastic response). Both measurements were done in the same passive sediment but at different places. In the following, we will name these experiments ‘fluid experiment’ and ‘solid experiment’, respectively. For both experiments the stress and strain signals are sinusoidal with negligible higher harmonics. We are thus in the linear regime.

We can obtain the complex modulus G^* using Eq. 5.5 together with the prefactor $k/6\pi R_{\text{probe}}$ [222], where k is the trap stiffness and $R_{\text{probe}} = 8.5 \mu\text{m}$ is the probe apparent radius.

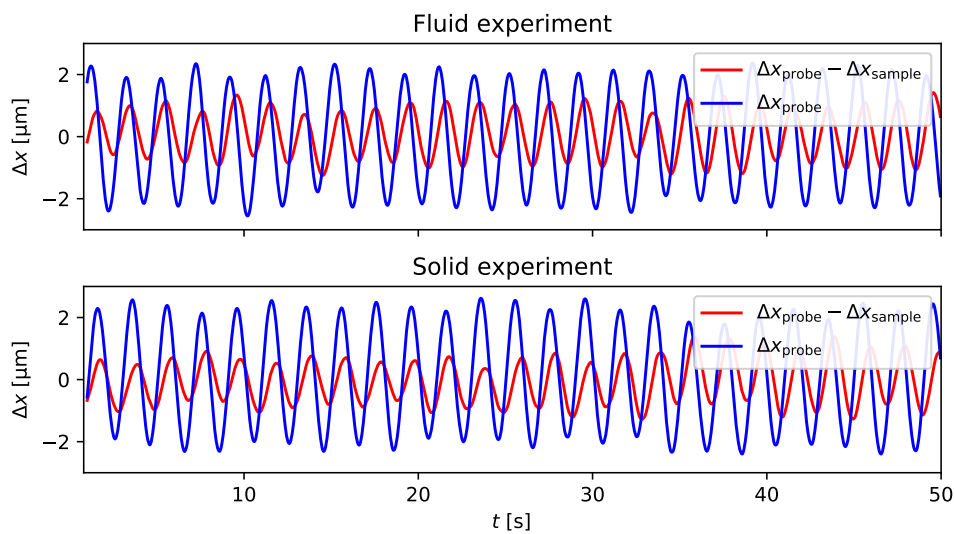


FIGURE 5.6: Relation of strain $\gamma \propto \Delta x_{\text{probe}} - \Delta x_{\text{sample}}$ (in red) and stress $\sigma \propto \Delta x_{\text{probe}}$ (in blue) of ‘fluid experiment’ and ‘solid experiment’ in the passive sediment. Both measurements were done in the same sediment but at different places.

5.2.3 Result

Starting from the passive fluid (respectively solid) situation, we increase the concentration of H_2O_2 . At each step, we characterize the activity levels (T_{eff}/T_0) on the density profile far from the probe, and we perform a SAOS measurement. Resulting storage and loss modulus, G' and G'' respectively, are plotted function of T_{eff}/T_0 for both experiments in Fig. 5.7.

When starting from the passive fluid (fluid experiment), the increase in activity seems to cause an increase in G' and a decrease in G'' , although the response remains fluid like ($G'' > G'$). However, we should keep in mind that the local density of the colloids around the probe particles is increasing with H_2O_2 concentration as well (as mentioned in Subsection 4.3.2). Indeed, we measure an increase in packing fraction around the probe from 0.86 to 0.90. That is why we cannot conclude that active forces are necessarily the cause of this stiffening. When starting from the passive solid (solid experiment), the increase in activity also seems to cause an increase in G'' and a decrease in G' . Here also we measure an increase in packing fraction from 0.85, to 0.87, to 0.91.

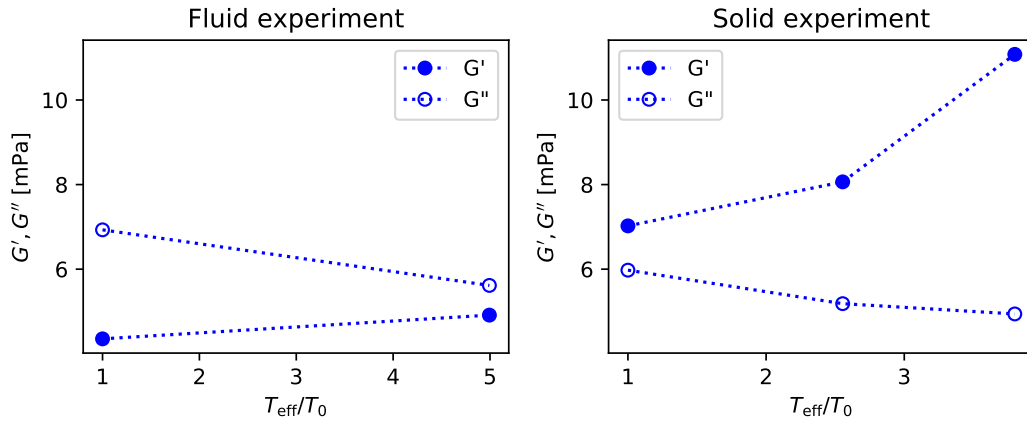


FIGURE 5.7: The resultant storage modulus G' and loss modulus G'' function with activity levels T_{eff}/T_0 for (left) fluid experiment and (right) solid experiment. The uncertainty is within the marker size.

To sum up for this part, we have developed a first microrheology experiment using optical tweezers. From our first observations, it seems possible that activity causes higher stiffness in both fluid and solid parts of a colloidal sediment. Nevertheless, this point still needs to be carefully verified because the local density around the probe particle was not held constant. Also with the light-induced attraction of the colloids to the probe, it seems that optical tweezers may not be the right tool to investigate microrheology in this system. It is indeed difficult to disentangle the different contributions. When I came back to Lyon, we decided to pursue a new path of microrheological investigation using another type of actuation forces described below.

5.3 Actuation by gravity: An intruder falls through the sediment

In our original experimental setup in Chapter 4, we always tilt the setup to confine the colloidal particles. Without any modification on the setup, we decided to perform active microrheology using gravity as an actuation force. In brief, we dropped a probe particle above the sediment and let it creep through the colloidal assembly like an intruder. This may sound simple, but actually, it is a challenging experiment with a high chance of failure.

The work in this section is a part of the internship of Selvamugesh Rajmohan, a 2nd-year master student I co-advised from March to July 2019. We have developed the experimental procedure together. Selvamugesh did mostly the experimental parts and preliminary analysis of the intruder motion. On my side, I analyzed further the intruder motion and particle trajectories, from which we extended to network analysis. After the end of his internship, my supervisors and I tried to extend the analysis by stepping from discrete to continuous description, thanks to a fruitful discussion with François Graner from Université Paris Diderot.

5.3.1 Experimental configuration and procedure

We used the in-plane sedimentation as described in Subsection 4.1.1 to confine our colloids, and followed the same procedure to avoid the drift as in Subsection 4.1.2. The main new feature of this experiment is an intruder. We want an intruder that is relatively large compared to our colloids and has no long-range interaction with the Janus colloids, both with and without H_2O_2 . Importantly, it must settle down to the bottom of the experimental well and be able to move on the bottom surface when the setup is tilted. After searching and trying different particles, we decided to use glass beads of Sigmund Lindner (#5210-07, 5-30 μm in diameter) as our intruder¹.

The first challenging point is to grab a few glass beads and drop them over the colloidal sediment. Note that we want to have only one glass bead per movie for our analysis. Also, some glass beads are not spherical, some contain dark spots inside and some of them are physically attached to one another. These kinds of glass beads would be a problem on the tracking and analysis. We thus need to see them before picking a good one.

In the 96-well plate, we prepare one well for the active colloids and another adjacent well for the glass beads diluted in deionized water. Using the motorized stage, we can switch our observation between both wells. First, we let the colloids settle overnight. On the day of the experiment, we add a dilute solution of the glass beads in one empty well, not the well with the colloids. The glass beads quickly settle to the bottom and then slide towards the minimum position according to the tilt angle. We notice that the motion of the glass beads on the surface is slipping without rotating. At this point, we can determine a good glass bead from its appearance and motion. We suck a few glass beads using a small pipette tip and drop them into the well of the colloids. Importantly, we must drop them on the side opposite to where the colloids are and let them slip towards the colloids. The distance between the place where we drop the glass beads and the sediment also helps us take away unwanted glass beads. Sometimes the glass bead stops moving before reaching the sediment (possibly from surface impurities). In this case, we may perturb it to make

¹This is the same type of probe particle that I previously used in Section 5.2. In the absence of optical trap, we did not detect any additional interaction in the presence of H_2O_2 .

it move again. We wait until one glass bead is close enough to the sediment and then start the data acquisition. We acquire at 5 Hz until the glass bead reaches a final position inside the sediment. This is how we perform the experiment at a single activity level.

Unconventional H_2O_2 variation

After many trials of an experiment starting from the passive case and then increasing systematically the activity level, we could never reach a high activity level due to several difficulties². We, therefore, decided to change the way we vary the activity level. Since we are more interested in a highly active case, we first started at a high concentration of H_2O_2 . After we managed to drop a glass bead and it has crept nicely through the sediment, we diluted the well by adding deionized water to have lower activity levels and then performed another experiment. When we finished the experiment, we removed solution from the well and added deionized water until we observed purely Brownian motion of the colloids, we left the sediment overnight and performed the passive experiment on the next day.

We successfully performed two active experiments in one day. At the end of the day, we diluted the experimental well to obtain passive sediment and let it rest overnight. On the next day, we did one passive experiment and then tried to add a little amount of activity. Unexpectedly, we noticed contamination by an alien particle (probably pollen). The colloids repelled from it and one part of the sediment was disturbed. After removing that alien particle, we had to let the colloids settle again overnight. We did one more passive experiment and then another experiment at low activity on the next day. Table 5.1 summarizes our experiments as described above together with the size of the glass beads σ_{GB} , sedimentation length of the colloids ℓ_g and the corresponding T_{eff}/T_0 measured with the same procedure as in Subsection 4.3.1. We think that the slight difference in ℓ_g between the two passive cases is due to the contamination.

Defining the reference position and time

Since each glass bead falls to a different place in the sediment, we need to define a reference altitude when comparing all the experiments of various activity levels. We pick the abscissa point where the density profile has the steepest slope as our reference position, $x = 0 \mu\text{m}$ (see Fig. 5.8). Consequently, the time when the glass bead passes this point is the reference time $t = 0 \text{ s}$. Fig. 5.9 shows the experimental images of the passive and active cases at the time $t = 0 \text{ s}$. With this definition, $t < 0 \text{ s}$ refers to time before the impact. Throughout this section, we shall stick to the same definition of the reference position and time.

² (1) To get the glass beads, we control the micropipette by hands using the monitor to help us locate the position. This step takes time to achieve. (2) After releasing the glass beads in the well with the colloids, the glass beads sometimes fall into the edge of the sediment, and we could not take this trial. (3) The glass beads sometimes stuck along the way because of surface impurity or too small tilt angle. (4) The more we open the sample cover (to get the glass bead), the higher chance of contamination. Some alien particles from the air can decrease experiment quality. Worse than that, some particles show long-range interaction with our colloids. We have seen that the colloids (even the passive colloids) move away from these particles. This indeed destroys the sediment and we have to re-do the experiment from the beginning after removing the contamination.

TABLE 5.1: This table summarizes the set of experiments that were performed at the same tilt angle and the same sediment of colloids. The white rows are for the experiments performed before the sediment was disturbed, and the grey rows later. For each experiment, we show the glass bead diameter σ_{GB} , sedimentation length of the colloids measured from the dilute part of the density profile ℓ_g and the corresponding T_{eff}/T_0 . Here we use the Brownian temperature T_0 separately among the two correlated sets of experiments, i.e., (1,3) and (2,4,5). The experiments are ordered by the sedimentation length ℓ_g .

Exp No.	Marker	Exp description	σ_{GB} [μm]	ℓ_g [μm]	T_{eff}/T_0
1	▲	Passive	$15.6 \pm 0.2 \mu\text{m}$	$1.6 \pm 0.2 \mu\text{m}$	1.0
2	●	Passive	$15.6 \pm 0.2 \mu\text{m}$	$1.8 \pm 0.1 \mu\text{m}$	1.0
3	▼	Lowest activity	$15.3 \pm 0.2 \mu\text{m}$	$2.4 \pm 0.2 \mu\text{m}$	1.5 ± 0.1
4	◆	Moderate activity	$16.1 \pm 0.2 \mu\text{m}$	$8.0 \pm 0.2 \mu\text{m}$	4.4 ± 0.2
5	■	Highest activity	$14.5 \pm 0.2 \mu\text{m}$	$11.7 \pm 0.4 \mu\text{m}$	6.5 ± 0.3

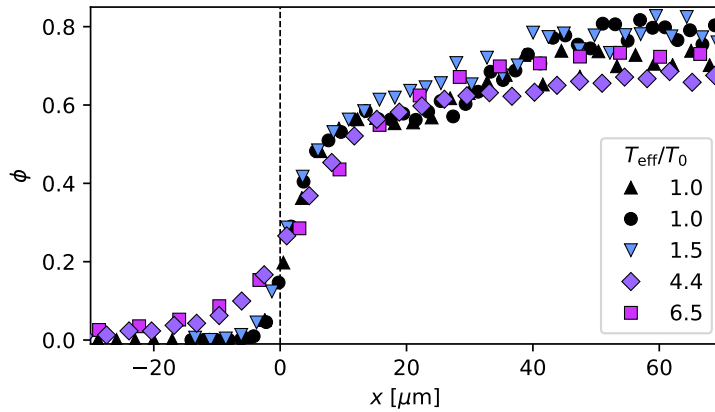


FIGURE 5.8: Density profile at various activity levels. The x value is shifted to have the point where the profile has the steepest slope at $x = 0$.

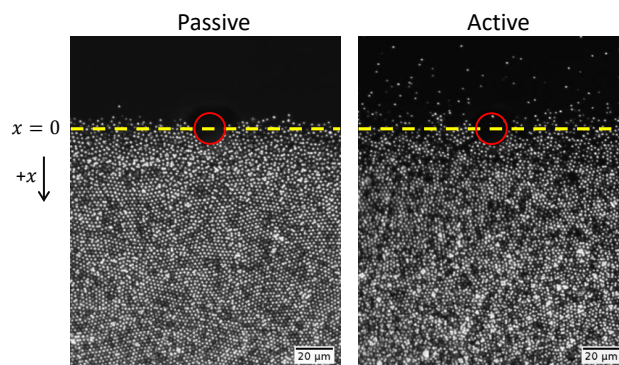


FIGURE 5.9: Two snapshots of the upper part of the profile comparing between passive and active cases. We define the starting time $t = 0$ s when the glass bead is at $x = 0$.

5.3.2 Qualitative observation

Fig. 5.10 shows snapshots of the passive (Exp. 2) and highly active (Exp. 5) experiments when the glass bead position x_{GB} has reached the same distance x . The first thing we notice is the recovery of the disturbed surface. In the passive sediment (left panel), we can notice the wake of the glass bead during the whole falling event. Estimated from the experimental image sequences, the surface has fully recovered at $t = 55$ s, just before the glass bead stops. On the other hand, for the active sediment, we barely notice the glass bead wake even at the early stage. The surface has recovered at $t = 30$ s, while the glass bead is still in the intermediate density. The faster recovery at a higher activity level might be simply explained by the effective diffusion D_{eff} of the active colloids. At low density, the active colloids diffuse with $D_{\text{eff}} > D_0$ are thus able to fill the wake of the glass bead faster than the passive colloids.

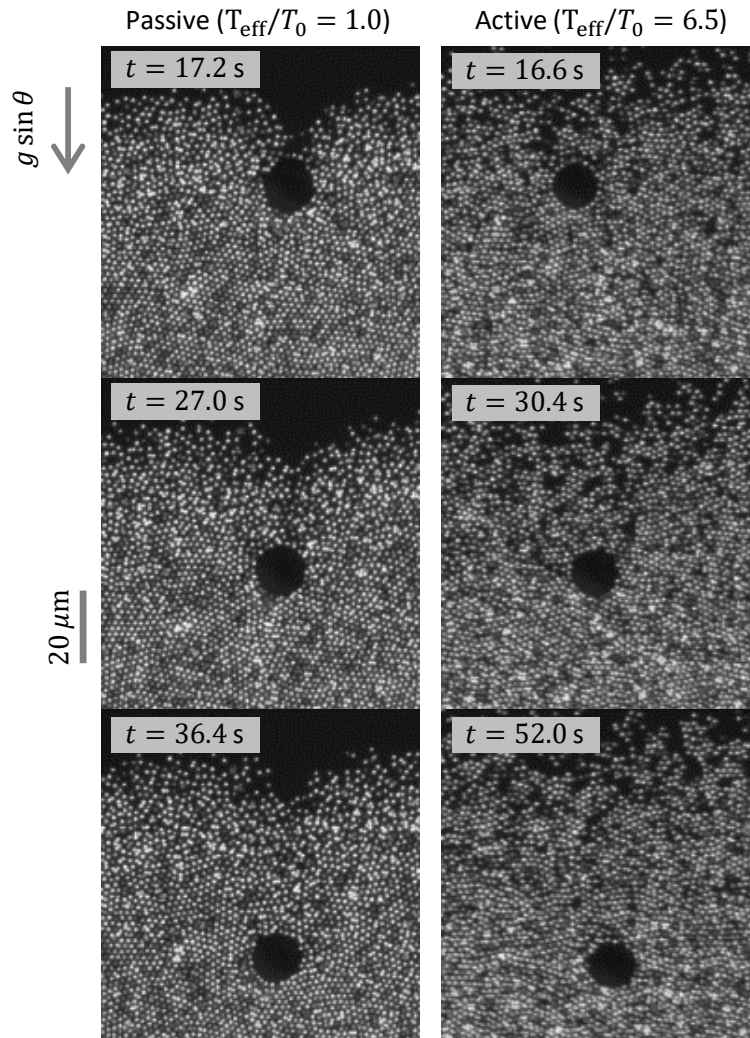


FIGURE 5.10: Snapshots of a creep motion of the glass bead into the sediment. The comparison between passive (Exp. 2) and active (Exp. 5) cases is made when the glass bead has the same distance: $x_{\text{GB}} = 30 \mu\text{m}$ (top), $x_{\text{GB}} = 50 \mu\text{m}$ (middle) and $x_{\text{GB}} = 70 \mu\text{m}$.

From the snapshots, we also notice the time it takes for the glass bead to creep through the sediment. To reach $x_{\text{GB}} = 30 \mu\text{m}$ (first row in Fig. 5.10), the glass bead in the active sediment takes slightly less time than in the passive sediment. After that, the trend reverses. The second row ($x_{\text{GB}} = 50 \mu\text{m}$) shows that the glass bead in the active sediment moves slower than in the passive sediment by just 3.4 s and has become dramatically slower in the last row ($x_{\text{GB}} = 70 \mu\text{m}$) with 15.6 s difference.

We are tempted to explain the movement in the first part by looking at the density profile in 5.8. Since the profile in the passive sediment is steeper than the active one, the glass bead in the passive sediment faces almost immediately high density regime after the impact, whereas in the active sediment, the glass bead is still in an intermediate regime. Therefore, at the beginning, the glass bead in the active sediment falls faster than in the passive case because it moves in a more dilute medium that opposes less resistance. Later on, both glass beads are in a dense regime of the sediment. This is where we start to see that the glass bead in the active sediment becomes much slower than the passive case. Our next task is to analyze the glass bead motion quantitatively in order to verify this observation and then compare among the five experiments that we have.

5.3.3 Glass bead trajectory

To obtain a glass bead trajectory, we can apply the same tracking procedure with *trackpy* as described in Section 3.1 by using the glass bead apparent diameter for the tracking parameter. When the glass bead is surrounded by the colloids, it appears as a dark circle on a bright background. We thus have to invert the image brightness before the tracking. Nevertheless, this tracking procedure fails at the early stage because the glass bead appearance is poorly defined when it is not yet inside the sediment. To complete the glass bead trajectory, we use the manual tracking plug-ins of ImageJ to track the glass bead position from the beginning. We also track manually a few points within the sediment to ensure consistency with the automatic tracking of *trackpy*. In Fig. 5.11, we show the resulting combined trajectories from both tracking procedures.

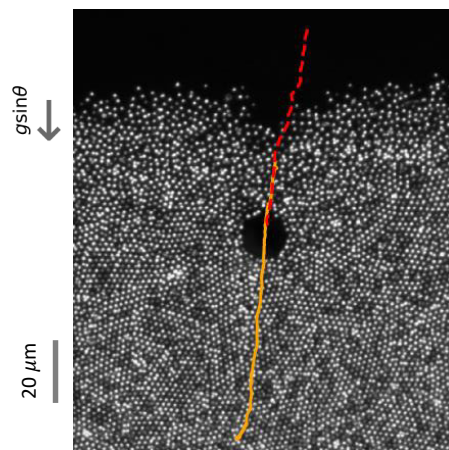


FIGURE 5.11: The trajectory of the falling glass bead into the sediment. The initial part of the trajectory is tracked by the manual tracking plug-ins of ImageJ (red dashed line). The orange line comes from automatic tracking using *trackpy*, possible only when the bead is surrounded by the bright colloids.

We show in Fig. 5.12a the glass bead position along x axis, x_{GB} , function of time t . Initially, all experiments are superimposed, but later they display different evolution, and x_{GB} saturates at different values in the final stage. There is no correlation with the glass bead size. This is due to the fact that the glass bead falls into different parts (different depths) of the sediment. We take a closer look to what happens just before and after the impact in Fig. 5.12b. We obtain the impact speed u and initial creep velocity v by fitting the data separately before and after the impact at $t = 0$, respectively (see Table. 5.2). Before the impact, the glass bead of Exp. 4 has a significantly higher velocity than the rest. This glass bead indeed is the largest one among our five experiments. However, since there is no difference between Exp. 5 and Exp. 1,2 in term of the impact velocity while the glass bead size is about 6% different, we suggest that the highest velocity in Exp. 4 comes from our perturbation to make the glass bead moves.

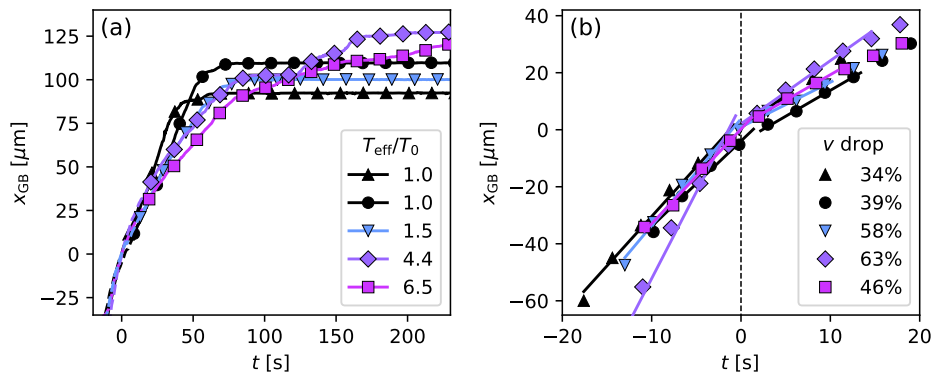


FIGURE 5.12: Glass bead position along x axis function of time, $x_{\text{GB}}(t)$. (a) A full-range of time: before the impact until the saturation. The dashed line at $x < 25 \mu\text{m}$ is obtained from the manual tracking. (b) The zoom-in of the time just before and after the impact. The solid lines are the linear fit obtained separately for $t < 0$ s and $t > 0$ s, to obtain impact velocity and absorbed velocity.

TABLE 5.2: Impact speed u and initial creep speed v of the glass bead in each experiment. The last column shows the percentage of speed loss after the impact.

Exp No.	Marker	T_{eff}/T_0	$\sigma_{\text{GB}} [\mu\text{m}]$	$u [\mu\text{m}/\text{s}]$	$v [\mu\text{m}/\text{s}]$	Velocity loss
1	▲	1.0	$15.6 \pm 0.2 \mu\text{m}$	3.5 ± 0.1	2.3 ± 0.01	$39 \pm 2\%$
2	●	1.0	$15.6 \pm 0.2 \mu\text{m}$	3.0 ± 0.1	1.8 ± 0.02	$34 \pm 1\%$
3	▼	1.5 ± 0.1	$15.3 \pm 0.2 \mu\text{m}$	3.7 ± 0.1	1.6 ± 0.02	$46 \pm 1\%$
4	◆	4.4 ± 0.2	$16.1 \pm 0.2 \mu\text{m}$	6.1 ± 0.1	2.2 ± 0.05	$63 \pm 1\%$
5	■	6.5 ± 0.3	$14.5 \pm 0.2 \mu\text{m}$	3.3 ± 0.1	1.8 ± 0.03	$58 \pm 1\%$

In terms of density, one should expect that the velocity loss would be higher for the passive sediment. This is because when thinking of the shape of the density profile, the passive sediment has a sharper profile than the active one. Therefore, the glass bead should feel a sharper transition when it hits the colloids, while in the active sediment, the glass bead should be able to maintain its velocity after the impact and this should give lower velocity loss than that of the passive. Actually, what we obtained is that the velocity loss is higher in the active sediment ($\sim 50\%$) than in the passive one ($\sim 40\%$). This contradiction hints that the effect of the activity on the glass bead motion is already significant at the intermediate density.

Back to Fig. 5.12a, the effect of activity on the glass bead motion is more obvious when considering the whole creep motion. In the passive sediment, x_{GB} seems to increase linearly with the time t until a sharp transition to the saturation at the end, whereas the glass bead in the active case shows a deceleration while creeping: the slope of x_{GB} with time is continuously decreasing from the beginning and approaches zero at the final position. We emphasize again this difference in the glass bead motion at various T_{eff}/T_0 in Fig. 5.13. Here we present the glass bead motion in terms of x_{GB}^* and t^* , the normalized position and time at the saturation point, respectively. With this representation, we see a clear activity dependence of the glass bead motion and it is monotonic with the activity level.

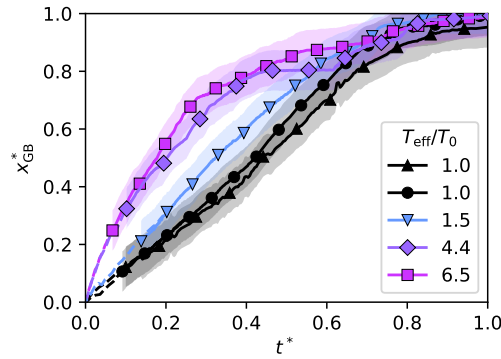


FIGURE 5.13: Normalized position and time such that $x_{\text{GB}}^* \equiv x_{\text{GB}}(t)/x_{\text{GB}}(t_{\text{saturate}})$ and $t^* \equiv t/t_{\text{saturate}}$, where t_{saturate} is the saturation time when the glass bead reaches the final position.

From the glass bead position, we can compute instantaneous velocity, $v(t)$, throughout the falling event. Fig. 5.14 shows $v(t)/v_0$ of different activity levels with time t , where v_0 is the instantaneous velocity at $x = 0$. This plot emphasizes the difference in the travel time between the passive and active cases. It can be seen that the glass bead in the passive sediment stops moving after $t \sim 80$ s while the one in the active sediment still slowly creeps through the sediment for about 2 minutes. Besides, it is striking to see that $v(t)$ in both passive cases show an acceleration from $t \sim 15$ s after entering into the sediment, while this does not occur in all active cases.

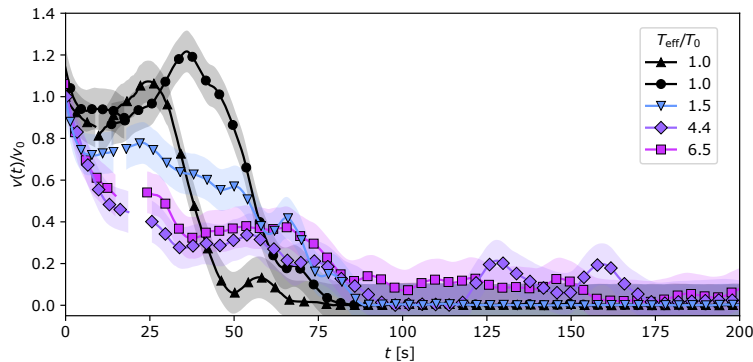


FIGURE 5.14: Instantaneous glass bead velocity $v(t)$ function of time. The instantaneous velocity is divided by v_0 , the instantaneous velocity at $x = 0$.

To investigate the acceleration and find out why it occurs only in the passive cases, we look at $v(t)$ function of distance x as shown in Fig. 5.15a (the density profile with the same x scale is provided in Fig. 5.15b to compare the effect of the density). We can see that before the impact, $v(t)$ decreases in all the cases due to the well geometry. After the impact, the glass beads in the two passive cases (the black curves) stop decelerating and maintain their velocity for about $30\ \mu\text{m}$ ($\sim 2\sigma_{\text{GB}}$). On the other hand, in the two highly active cases (the purple and magenta curves), the glass bead velocity continues to decrease and saturate before decrease again to zero at the end. At the low activity (the blue curve), the behavior is in between the two cases. The glass bead first continues to slow down for a short distance ($x \sim 10\ \mu\text{m}$) and then the velocity saturates before decreasing again to zero.

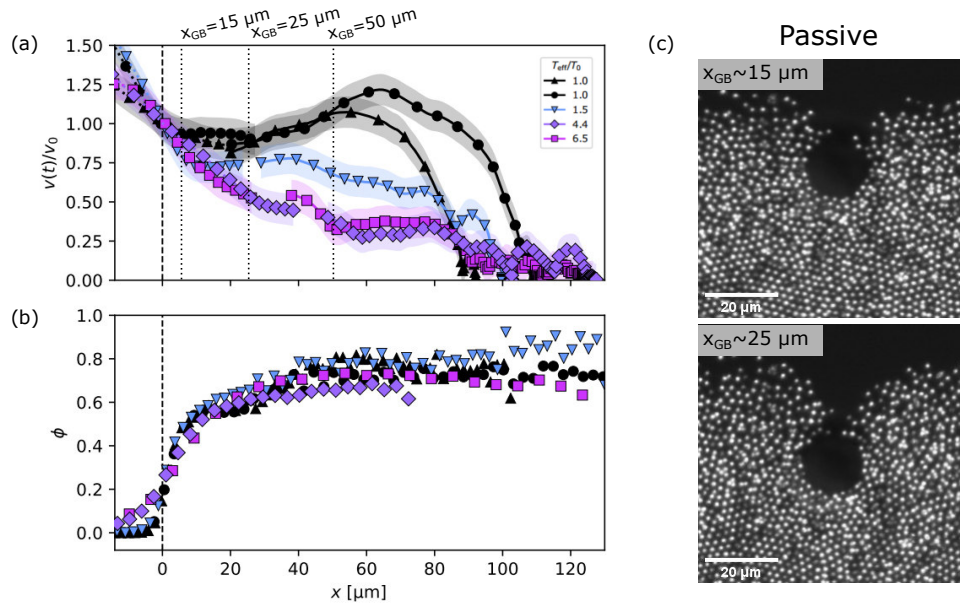


FIGURE 5.15: (a) Instantaneous glass bead velocity $v(t)$ function of distance x . The instantaneous velocity is divided by v_0 , the instantaneous velocity at $x = 0$. (b) The density profile comparing at the same distance x . (c) Snapshots before (top) and after (bottom) the colloids go behind the glass bead, which is the possible origin of the acceleration. The top snapshot at $x_{\text{GB}} \sim 15\ \mu\text{m}$ corresponds to the saturation phase of $v(t)/v_0$. The acceleration occurs at $x_{\text{GB}} \sim 25\ \mu\text{m}$, which corresponds to the bottom snapshots.

At this level of analysis, we could explain the acceleration in the passive case from the snapshots in Fig. 5.15c. The depth where the acceleration occurs ($x \sim 25\ \mu\text{m}$) corresponds to the time when some colloids come behind the glass bead ($t \sim 15\ \text{s}$). Once the passive colloids surround the glass bead, they push it from behind (in the direction of gravity) which results in the acceleration of the glass bead. We believe that the acceleration is not observed in the active sediment because the active colloids behind the glass bead does not always push the glass bead in the same direction. Instead, the glass bead in the active sediment displays an overdamped motion when the velocity approaches zero. We will come back to this point once we discuss the trajectory of the surrounding colloids.

In another representation, Fig. 5.16 shows the instantaneous velocity as a function of density (obtained from the density profile before the bead enters the sediment, not the exact local density around the glass bead since it is poorly defined). This plot emphasizes the difference of the glass bead motion for different activity

levels. From this plot, we state that there are different phases of the glass bead motion: deceleration phase, constant velocity phase, and acceleration phase. The deceleration phase happens at the beginning before the impact ($\phi < 0.3$). After the impact, the glass bead velocity in the passive sediment first shows the constant velocity phase for a long-range of density $0.35 < \phi < 0.60$ followed by the acceleration phase and then a sudden deceleration phase. For the glass bead in the low active sediment, it continues to decelerate for a short range of density and then maintains a constant velocity for $0.4 < \phi < 0.65$. There is a slight acceleration before a sudden deceleration similarly to the passive sediment. This scenario is totally different in the highly active sediment. We see that the glass bead continues to decelerate for a long-range of density after the impact. The constant velocity phase occurs at a relatively high density compared to the passive and low active sediment. Finally, the glass bead decelerates and then stops without showing the acceleration phase.

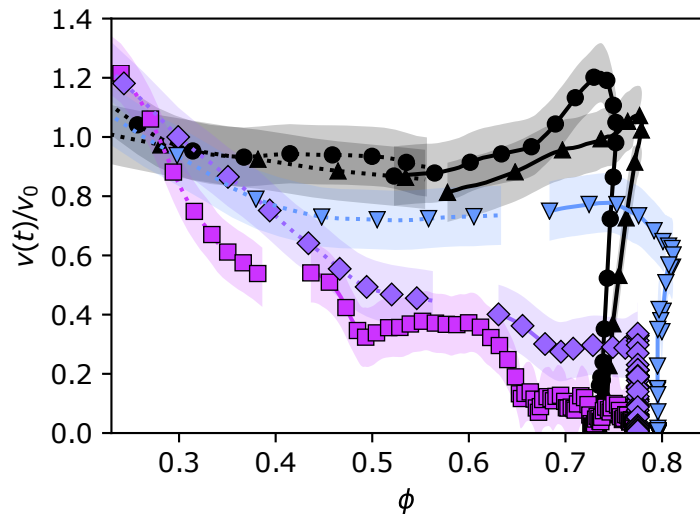


FIGURE 5.16: Instantaneous glass bead's velocity $v(t)$ function of density ϕ obtained from the density profile $\phi(x)$. The instantaneous velocity is divided by v_0 , the instantaneous velocity at $x = 0$.

To sum up of this part, we analyzed the glass bead motion and observed a stark difference between the passive and active sediment. It is also interesting to find that the effect of activity is robust since we can observe its effect at a low activity (Exp. 3). To explain the origin of the difference between the passive and active cases, we shall try to look at colloidal particle trajectories.

5.3.4 Colloidal particle trajectories

We performed particle tracking as described in Section 3.1 and Subsection 3.2.1. In Fig. 5.17 we show the trajectories of the colloids at the same position and time as the snapshots in Fig. 5.10. We compare the passive case (Exp. 2) and the highest active case (Exp. 5) with the time interval of $\Delta t = 4$ s for the trajectories.

It is obvious to notice the difference between both cases. The colloidal particles in the passive sediment show the dipole-like field around the glass bead throughout the motion. From the trajectories, we can estimate the size of the influenced region, which is about twice the glass bead diameter. For the active sediment, the influenced

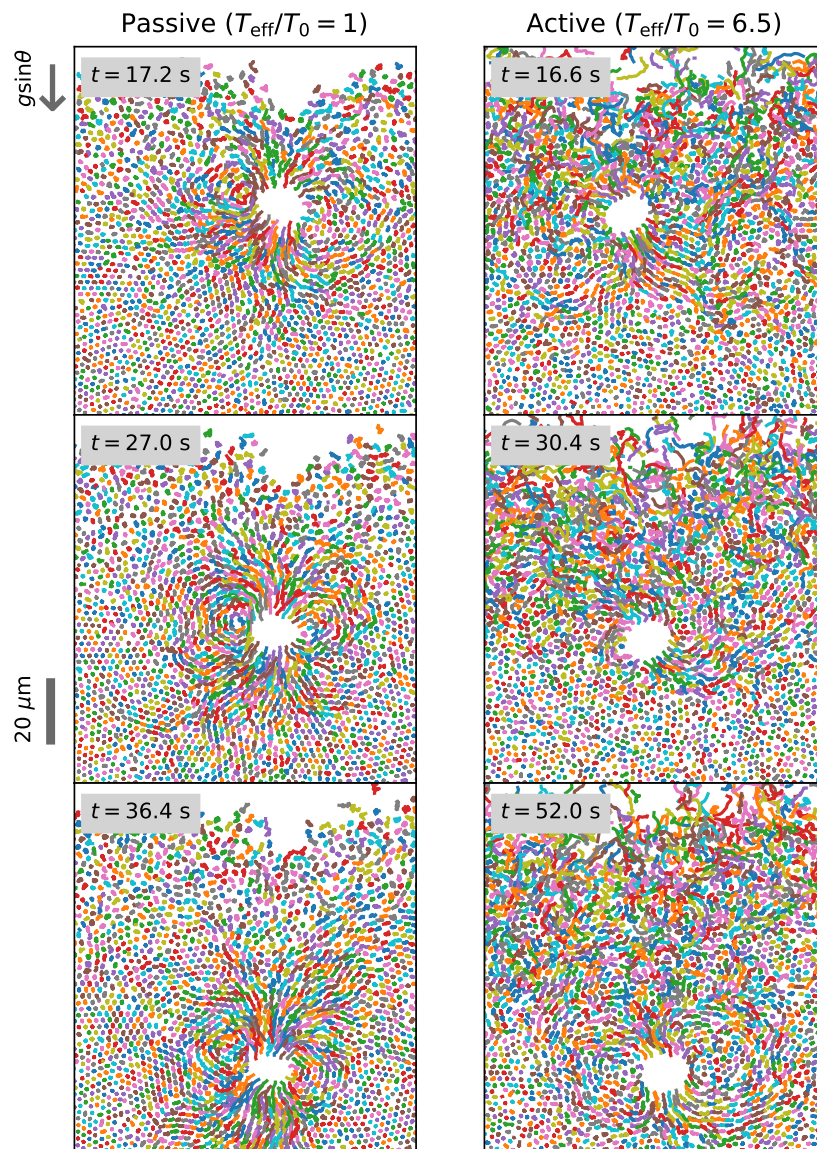


FIGURE 5.17: Trajectories of the colloidal particle during the creep motion of the glass bead comparing between the passive (Exp. 2) and the active (Exp. 5) cases. The time is chosen to be matched with the snapshots in Fig. 5.10: $x_{\text{GB}}(t) = 30 \mu\text{m}$ (top), $50 \mu\text{m}$ (middle) and $70 \mu\text{m}$ (bottom). The trajectories is shown of the time interval $\Delta t = 4 \text{ s}$.

region is poorly defined especially in the first row ($x_{GB} = 30 \mu\text{m}$) where the glass bead is still in a highly dynamic region. It is clear that the influenced region is much smaller than that of the passive case reflecting the higher resistance by the active colloids. In the last row of the active case ($x_{GB} = 70 \mu\text{m}$), it is possible to observe the flow field of the surrounding colloids. Unlike the passive sediment, the active colloids at the front tend to move laterally rather than being pushed forward by the glass bead.

Let us come back to the pending question at the end of Subsection 5.3.3: what is the origin of the difference in glass bead motion in the passive and active sediment? We argued that the passive colloids push the glass bead from above which results in the acceleration phase, but why does this not happen in the active sediment? One way to represent the push is to look at flux of the colloids around the bead. We computed the flux from the averaged displacement times number of colloids in a grid element of $1.7 \mu\text{m} \times 1.7 \mu\text{m}$ at a position respect to the glass bead. The displacement is computed between two consecutive frames of time difference 0.2 s. In Fig. 5.18, we present the flux time-averaged over the time interval such that the bead has sunk by its own diameter. The average is done in the reference frame of the falling bead. We add that the average is not only for the statistics, but also to get rid of the spontaneous motion of the colloids (either thermal agitation, self-propulsion, or both of them). We choose to compare Exp. 1 (passive) and Exp. 4 (active) because their respective glass beads have a similar size. To capture the different phases of the glass bead motion, we shall focus on two different glass bead positions: $x_{GB} = 15 \mu\text{m}$ (passive sediment: constant velocity phase, active sediment: deceleration phase) and $x_{GB} = 50 \mu\text{m}$ (passive sediment: acceleration phase, active sediment: constant velocity phase).

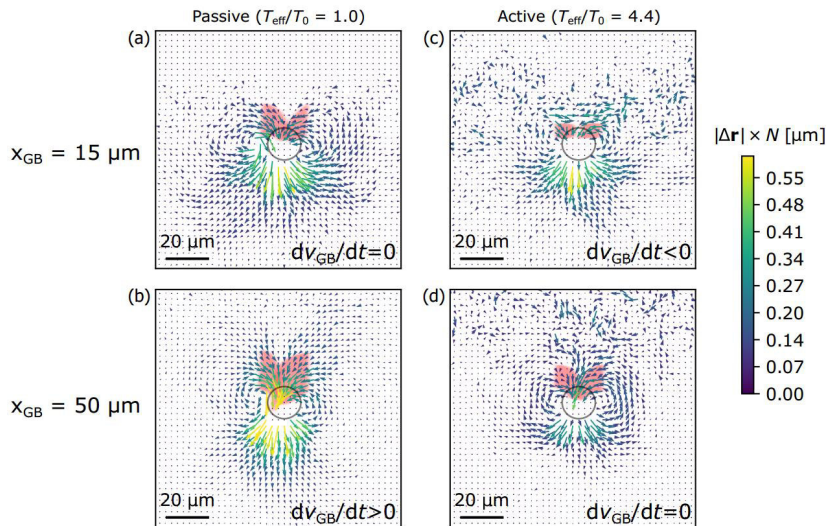


FIGURE 5.18: The averaged maps of displacement $|\Delta\mathbf{r}|$ times number of colloids N in a grid element representing flux of colloids around the glass bead (represented by the grey circle at the center). $|\Delta\mathbf{r}|$ is taken during the time difference $\Delta t = 0.2$ s (one frame difference) and it is averaged over the time interval such that the glass bead has moved by one diameter. The initial time of the average is the time that the glass bead was at (upper panel) $x_{GB} = 15 \mu\text{m}$ and (lower panel) $x_{GB} = 50 \mu\text{m}$. The maps compare the passive (left panel) and active (right panel) sediment. The pink region above the glass bead is to highlight the push in each state of the glass bead motion: (a,d) constant velocity, (b) acceleration, and (c) deceleration.

In the passive sediment, the glass bead at $x_{\text{GB}} = 15 \mu\text{m}$ is in the constant velocity phase. We can see in Fig. 5.18a that the flow field expands laterally with respect to the glass bead direction of motion and it has a dipole-like shape. While the glass bead is moving, the colloids at its front slide to the side and come back to push the bead from above. The push is enhanced when the bead goes deeper in the sediment because there are more and more colloids above the bead. This is shown in Fig. 5.18b ($x_{\text{GB}} = 50 \mu\text{m}$) as there are more flux going downward on top of the bead. At this state, the glass bead is accelerating and the flow field is elongated along the glass bead direction of motion. In the case of the active sediment, we can notice that the push is less than that of the passive case at the same depth. At $x_{\text{GB}} = 15 \mu\text{m}$, Fig. 5.18c shows that there is little downward movement of the active colloids above the bead. Instead, the flux is horizontal and it corresponds to the closure of the wake after the bead has passed through. This observation confirms that the closing of the wake is active and caused by the specific motion of self-propelled particles. The glass bead at this state is decelerating and the dipole-like flow is less visible. At a greater depth of $x_{\text{GB}} = 50 \mu\text{m}$, we can see more downward flux as shown in Fig. 5.18d. The bead at this depth corresponds to the constant velocity phase and the flow field looks similar to Fig. 5.18a, which is also in the constant velocity phase of the passive sediment.

Why the push is different in the passive and active sediments? We can answer this point by considering the movement of the colloids above the bead. Without the self-propulsion, the passive colloids are pulled downward by the gravity. If they are on top of the bead, they act as a pressure on the bead and results in a downward push. If the colloids are self-propelled, they can defy the gravity (as shown by the longer sedimentation length) and thus push less on the bead when comparing with the passive sediment at the same depth. Besides, from Fig. 5.16, we can see that this scenario is monotonic with the activity levels. The density at which the constant velocity phase occurs is higher when activity increases. Note that higher density means higher resistance from the colloids at the front. Therefore, even the push becomes significant, it is not enough to overcome the resistance at such a high density. This is why the acceleration phase is not visible in the active sediment.

The analysis of the colloid trajectories helps us understanding how activity influences the glass bead motion. Until now, we mostly focused on the colloids above the bead, which induce the push. In the following analysis, we shall try to see more precisely what the colloids are doing around the bead. We already have a clue of the dipole-like field from the trajectory plots in Fig. 5.17 and from the flux in Fig. 5.18. Now, we will probe colloids relative motion with their neighbors using the same analysis as in Subsection 4.6.5: network analysis and broken bonds.

5.3.5 Network analysis and broken bonds

We first define the neighboring network using the Voronoi neighbor definition with the upper limit edge length of $1.8\sigma_0$. With this choice of neighbors, edges between particles around the glass bead are handled accurately unlike the 6-nearest neighbor definition. Then, we compare the network between time t and $t + \Delta t$. Edges that appear in t , but disappear in $t + \Delta t$ are thus broken bonds. Conversely, newborn bonds are edges that do not exist in t , but appear in $t + \Delta t$. (For more detail on the network analysis, please refer to Section 3.5.)

In Fig. 5.19, we show the bond network at the time t when $x_{\text{GB}}(t) = 50 \mu\text{m}$ for one passive and one active sediment. Broken bonds and newborn bonds were computed

using the time interval Δt such that the glass bead has moved by one diameter. In the passive sediment, we see that most of the broken bonds (red links) are concentrated around the bead. Estimated by eyes, the typical size of the broken bonds area is about $60 \mu\text{m}$, which is about four times of the glass bead diameter. We can also see a few shear lines in the colloidal sediment either inside or outside the area of influence. They are lines of broken bonds crossing with newborn bonds (loss of neighbors in one direction and gain new one in the other direction). We noticed that the typical length of these shear lines is about 10 colloidal diameters.

When applying the same analysis to the active sediment, the broken bonds area is poorly defined. There are many broken bonds within the sediment even far away from the glass bead because of the high dynamics of the active colloids. To minimize this spontaneous rearrangement in the analysis, we need to reduce the time interval Δt . However, we will obtain less broken bonds if Δt is smaller. This is a drawback of the analysis of the broken bonds because the comparison is made between two frames separated by a large Δt . We thus need a new analysis tool to investigate such an influence in the active sediment.

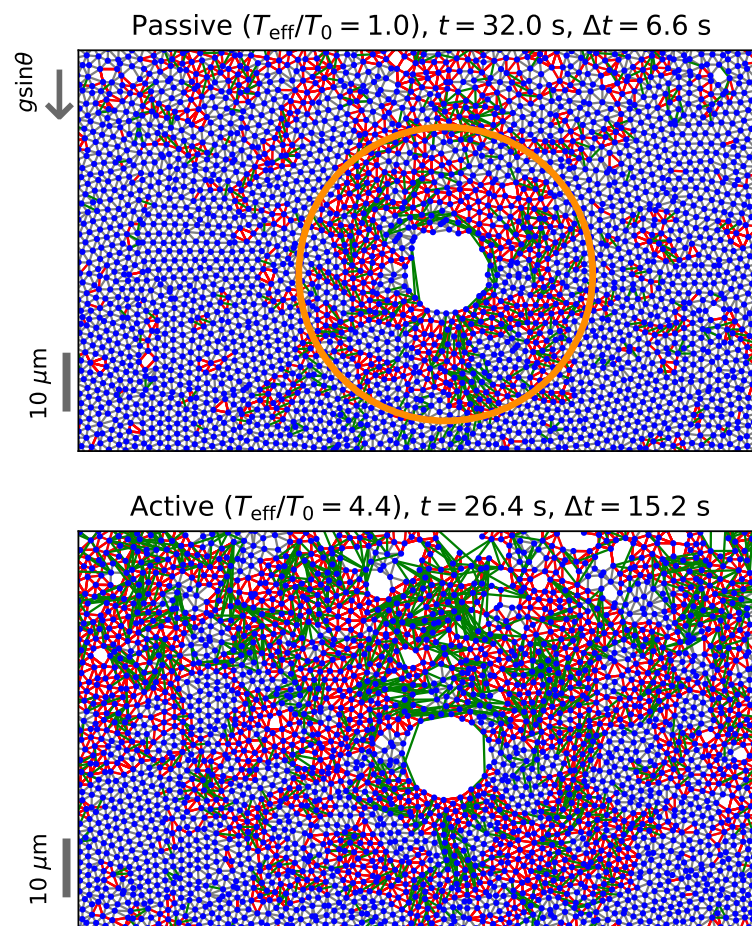


FIGURE 5.19: Bonds network showing the change of neighboring network during the time Δt , the interval time when the glass bead sinks by its diameter. Bonds are defined by Voronoi neighbors (grey lines). The broken bonds are bonds that appear in t , but no longer exist at $t + \Delta t$ (red lines). Conversely, newborn bonds do not exist in t but appear in $t + \Delta t$ (green lines). The orange circle in the top panel is the estimated area of influence by the glass bead motion. In this case, it is around $30 \mu\text{m}$ from the glass bead position.

5.3.6 Texture analysis: statistical tools to investigate bonds deformation

To get rid of the noisy broken bonds in the active sediment, we have to consider a time scale that is faster than the one of collective rearrangement of the colloids. Then, by averaging among series of frames, the background noise (the place that is further away from the glass bead) should be reduced. In the following we use an analysis framework developed by François Graner and Benjamin Dollet [234] that translates a discreet description of a system in terms of particle trajectories and links into a continuous description on a regular grid. In this framework we will be able to consider a time interval shorter than the time for collective rearrangements of the colloids. The continuous description will enable time averaging that will average out the background noise. We would like to acknowledge François Graner for a very fruitful discussion and insightful suggestions. Also, we would like to thank Benjamin Dollet for providing his implementation of this analysis in MATLAB code. The analysis in this part of the thesis used a python package implemented by Mathieu Leocmach.

Principle of the texture analysis

In this part, I would like to introduce the principle of the analysis and all the relevant quantities. The detailed information in this part is provided in Ref. [234]. This analysis starts from a set of coordinates of particles and a definition of link between them (e.g. Voronoi neighborhood). The link vector ℓ between two neighboring particle i and j which are at (x_i, y_i) and (x_j, y_j) , respectively:

$$\ell = \begin{pmatrix} x_2 - x_1 \\ y_2 - y_1 \end{pmatrix} \equiv \begin{pmatrix} X \\ Y \end{pmatrix}. \quad (5.6)$$

The outer product of the link vector with itself, $\ell \otimes \ell$, yields a link matrix \mathbf{m} ,

$$\mathbf{m} \equiv \ell \otimes \ell = \begin{pmatrix} X^2 & XY \\ YX & Y^2 \end{pmatrix}. \quad (5.7)$$

The ensemble average of \mathbf{m} among links in a given region of time and space is defined as a texture matrix \mathbf{M} [235],

$$\mathbf{M} = \langle \mathbf{m} \rangle = \begin{pmatrix} \langle X^2 \rangle & \langle XY \rangle \\ \langle YX \rangle & \langle Y^2 \rangle \end{pmatrix}. \quad (5.8)$$

This matrix \mathbf{M} represents an average state of the system. To trace average geometrical change of the texture with time, one can define a matrix \mathbf{B} as follows,

$$\mathbf{B} = \left\langle \frac{d\mathbf{m}}{dt} \right\rangle, \quad (5.9)$$

where \mathbf{B} is the ensemble average taken on links that exists in two consecutive frames. Therefore \mathbf{B} does not take into account link appearance or disappearance between successive time frames. Such topological changes of the link network can be described by the averaged texture of the appearing (respectively disappearing) links: $\langle \mathbf{m}_a \rangle$ (respectively $\langle \mathbf{m}_d \rangle$). The topological texture changes matrix \mathbf{T} is defined as,

$$\mathbf{T} = \dot{n}_a \langle \mathbf{m}_a \rangle - \dot{n}_d \langle \mathbf{m}_d \rangle, \quad (5.10)$$

where \dot{n}_a is the rate of link appearance per unit time per existing link, and the same for \dot{n}_d in case of link disappearance.

The goal of this analysis is to link discrete local deformation to continuous local deformation. Since the matrices \mathbf{B} and \mathbf{T} still contain discrete objects' length scale, it is better to define their continuous counterpart that have no more length scale. The continuous counterpart of the topological changes \mathbf{T} is defined as

$$\mathbf{P} = -\frac{1}{2} \frac{\mathbf{M}^{-1}\mathbf{T} + \mathbf{T}\mathbf{M}^{-1}}{2}, \quad (5.11)$$

which has the dimension of s^{-1} and is called the *statistical topological rearrangement rate*. For the continuous counter part of \mathbf{B} , which is called *statistical symmetrised velocity gradient* \mathbf{V} , is defined as

$$\mathbf{V} = \frac{\mathbf{M}^{-1}\mathbf{C} + \mathbf{C}^t\mathbf{M}^{-1}}{2}, \quad (5.12)$$

where $\mathbf{C} = \frac{N_c}{N_{\text{tot}}} \langle \ell \otimes \Delta\ell / \Delta t \rangle$, N_c is a number of links conserved between both frames and N_{tot} is an average number of links in both frames. We can see that the matrix $\mathbf{M}^{-1}\mathbf{C}$ is similar to \mathbf{B} since it vanishes if there is no deformation, i.e., the pattern move like a rigid body. If \mathbf{M} and \mathbf{C} commute, Eq. 5.12 can be written as $\mathbf{V} = \mathbf{B}\mathbf{M}^{-1}/2$.

Actually, \mathbf{V} is the symmetric part of $\mathbf{M}^{-1}\mathbf{C}$. The anti-symmetric part is written as

$$\mathbf{\Omega} = \frac{\mathbf{M}^{-1}\mathbf{C} - \mathbf{C}^t\mathbf{M}^{-1}}{2}, \quad (5.13)$$

which is called *statistical rotation rate* $\mathbf{\Omega}$. In 2D, $\mathbf{\Omega}$ can be reduced to a scalar.

Representation of matrices

In 2D, the matrices mentioned above can be represented by ellipses, which major and minor axis are oriented along the eigenvectors of the matrix. Positive eigenvalues are marked with solid lines (see Fig. 5.20). A matrix of two eigenvalues λ_1 and λ_2 is represented by a crossed ellipse if $\lambda_1 > \lambda_2 > 0$. For an isotropic matrix, in which $\lambda_1 = \lambda_2 > 0$, the crossed ellipse is replaced by a crossed circle. If one of the eigenvalues is negative but its absolute value is equal to the positive one, i.e., $\lambda_1 = -\lambda_2 > 0$, the circle is left only with one axis corresponding to the positive eigenvalues. If the value of both eigenvalues are not equal (and one of them is negative, $\lambda_2 < 0$), the matrix is represented by an ellipse with one visible axis. It looks like a coffee bean (major axis is visible), if $\lambda_1 > -\lambda_2$. On the contrary, if $\lambda_1 < -\lambda_2$, the ellipse looks like a capsule (minor axis is visible).

For the matrix \mathbf{P} (the statistical topological rearrangement), a positive eigenvalue refers to the direction of disappearing links. The coffee bean ellipse means that links in the major axis direction are breaking. The capsule ellipse indicates link appearing along the major axis direction. In a situation where a number of breaking links and appearing links are nearly the same, the ellipse then looks like a circle. In the case of the matrix \mathbf{V} (the statistical velocity gradient), a positive eigenvalue corresponds to link extension. If the strain is more in extension than in compression, \mathbf{V} is represented by the coffee bean, in which the major axis is the stretching direction. The capsule ellipse means that the compression is larger and the major axis corresponds to the compression direction. The circle appears when both compression and extension are equal.

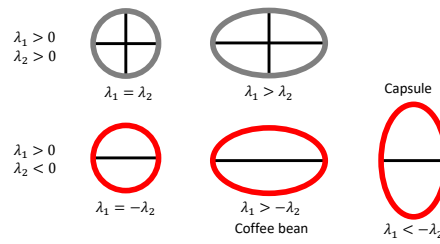


FIGURE 5.20: A representation of a matrix of eigenvalues λ_1 and λ_2 using a circle (if $\lambda_1 = \lambda_2$) and an ellipse (if $\lambda_1 > \lambda_2$), which elongates along the higher eigenvalues. A solid line represents positive eigenvalues. If both eigenvalues are positive, the matrix is represented by a crossed circle/ellipse. If one of the eigenvalues is positive and one is negative, the circle and the ellipse show one solid line, corresponding to the positive eigenvalues. If the ellipse elongates along the positive eigenvalues, it is recognized as a coffee bean shape. The capsule shape is for the ellipse that elongates along the negative eigenvalues. The figure is reproduced from Ref. [234].

Texture analysis in our experiment

To apply the texture analysis in our experiment, we first have to define a grid space. In order to perform time average, we set our grid in the frame of the bead. We choose a grid spacing of $1.7 \mu\text{m}$ and we have more than 100 links in every grid element during the averaging time interval such that the glass bead has moved by one diameter. The deformation of the neighboring network is taken between two consecutive frames ($\Delta t = 0.2 \text{ s}$). Each matrix is computed and then time averaged. Here, we chose the sequence from the time when the glass bead is at $x_{\text{CB}} = 50 \mu\text{m}$ until it has moved by one diameter. By averaging the map, we thus have enough statistics and also we can get rid of the spontaneous rearrangement far from the glass bead.

We show in Fig. 5.21 the matrices \mathbf{P} , \mathbf{V} , and $\mathbf{\Omega}$ from our experiment at different activity levels. The map of \mathbf{P} and \mathbf{V} reflect the topological and geometric changes, respectively. In the two passive cases, the coffee bean ellipse of \mathbf{P} in front of the bead indicates that the links have broken in the direction that is perpendicular to the glass bead direction. This corresponds to the coffee bean ellipse of \mathbf{V} which refers to the links extension in the same direction. Above the bead, \mathbf{P} displays a capsule shape indicating the link appearance in the horizontal direction. The direction of these newborn links is correlated with the compression direction, which can be seen by the capsule ellipse of \mathbf{V} . The pattern of \mathbf{P} and \mathbf{V} are the same for the active sediments, but less obvious when the activity increases. Remember that, at this depth, the glass bead moves slower with activity levels (see Fig. 5.15). As we took the network difference between $\Delta t = 0.2 \text{ s}$ in all cases, the slower glass bead thus results in less different pattern. However, such patterns of \mathbf{P} and \mathbf{V} are sufficient to investigate what is going on around the bead.

The other quantitative property that we can extract from this analysis is the statistical rotational rate $\mathbf{\Omega}$. An advantage of $\mathbf{\Omega}$ is that it consists in a single scalar value in a 2D system, which makes further analysis much simpler. In Fig. 5.21, we represent $\mathbf{\Omega}$ using a color map that indicates its direction and amplitude. Around the glass bead, the rotational rate is high and it is symmetric along the glass bead direction as expected. To probe θ -dependence and distance-dependence of $\mathbf{\Omega}$, we switch from a square grid to a polar grid centered on the bead position (see Fig. 5.22). With this representation, it is easier to obtain the value of $\mathbf{\Omega}$ as a function of angle and distance.

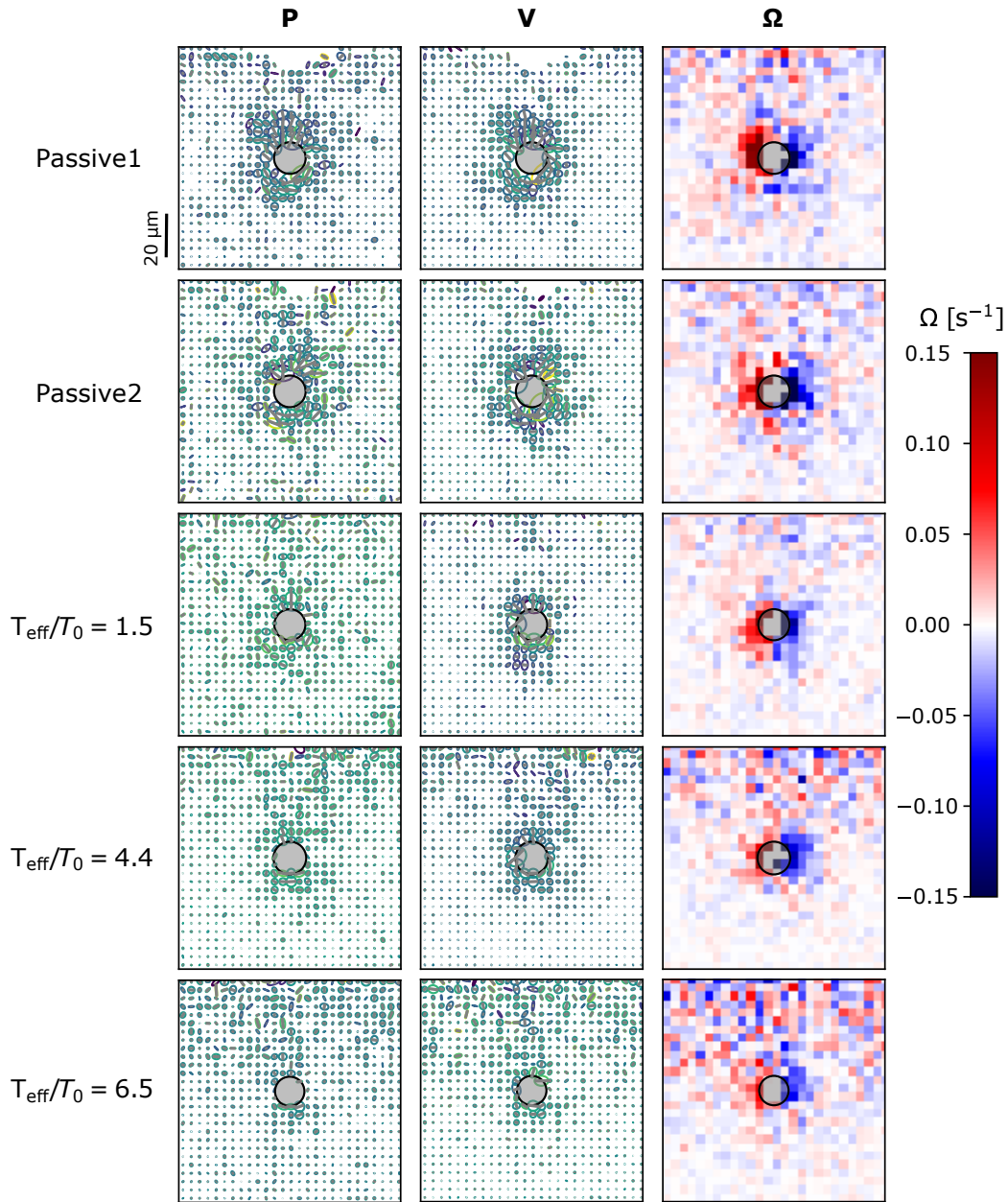


FIGURE 5.21: The map of texture analysis for different activity levels. The first column on the left shows the statistical topological change, or plastic behavior \mathbf{P} . The direction of links that have disappeared is indicated by a solid line of the coffee bean ellipse. The capsule ellipse indicates link appearing with its major axis. The center column displays the statistical velocity gradient \mathbf{V} . A major axis of the coffee bean ellipse indicates the direction and amplitude of stretching rate, while the compression is displayed by the major axis capsule ellipse. The last column on the right shows the statistical rotational rate Ω . The colors indicate the direction and amplitude of the rotational rate. All quantities are computed by coarsening the particle position into grid space of grid size $1.7 \mu\text{m} \times 1.7 \mu\text{m}$. The change is computed between two consecutive frames which are 0.2 s apart. The average is taken from the time when the the glass bead is at $x_{\text{GB}} = 50 \mu\text{m}$ until it has moved by one diameter.

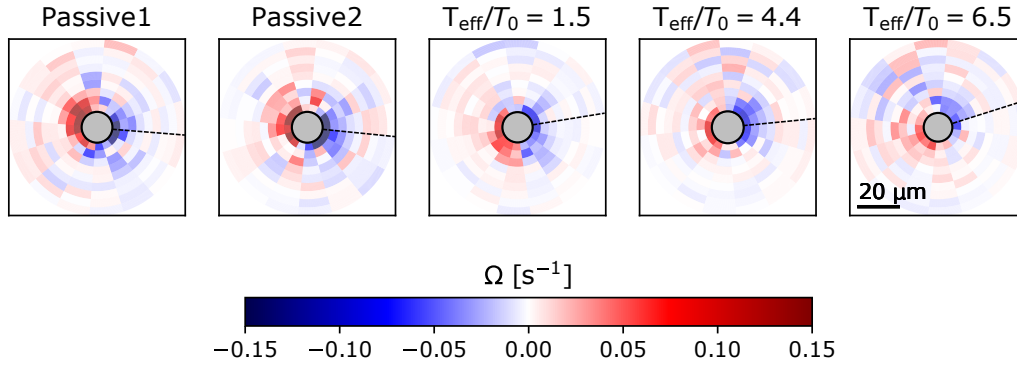


FIGURE 5.22: The statistical rotational rate Ω represented in a polar grid centred on the glass bead. The offset of angle of the grid is set to be the glass bead direction of motion, not the gravity. The dashed line represents the line $\theta = 0^\circ$, which is 90° from the glass bead direction of motion. Ω is computed in the same way as in Fig. 5.21.

We show the θ -dependence of Ω in Fig. 5.23. Let us first focus on one passive case, Fig. 5.23a displays $\Omega(\theta)$ at different distances from the glass bead. The curve is nearly fitted with the sine function (solid lines), which is an evidence of Stokes flow around a sphere [236, 237],

$$\Omega(\theta, r) = \frac{3}{4} \frac{U \sigma_{GB}}{r^2} \sin \theta, \quad (5.14)$$

where U is glass bead velocity. For a better statistics, we average $\Omega(\theta)$ among the first two shells (and ignore the other further shells because they are too far from the glass bead and thus noisy). In Fig. 5.23b we show the resulting $\Omega(\theta)$ of all activity levels and also fit the result with Eq. 5.14. From the fitting, we can extract the glass bead velocity U and make a comparison with the velocity obtained from the tracking. We summarize the comparison in Table. 5.3. The velocity extracted from the fitting is slightly lower than the velocity obtained from the tracking, however, they are still in the same order of magnitude and the deviation is the same for all activity levels. We note that the average between the first and the second shell may cause the drop of $\Omega(\theta)$ (but we need this average to gather enough statistics for the fit).

TABLE 5.3: Glass bead velocity in all experiments. The velocity is obtained from two different approaches. One from direct tracking of the bead (U_{tracked}), the other one from the fitting of $\Omega(\theta)$ (U_{fitted}). The comparison is made by the ratio $U_{\text{tracked}}/U_{\text{fitted}}$.

Exp No.	Marker	T_{eff}/T_0	U_{tracked} [$\mu\text{m/s}$]	U_{fitted} [$\mu\text{m/s}$]	$U_{\text{tracked}}/U_{\text{fitted}}$
1	▲	1.0	1.8 ± 0.1	1.1 ± 0.01	1.7
2	●	1.0	1.7 ± 0.1	1.1 ± 0.02	1.6
3	▼	1.5 ± 0.1	0.80 ± 0.1	0.50 ± 0.02	1.6
4	◆	4.4 ± 0.2	1.0 ± 0.1	0.63 ± 0.05	1.6
5	■	6.5 ± 0.3	0.9 ± 0.1	0.61 ± 0.03	1.5

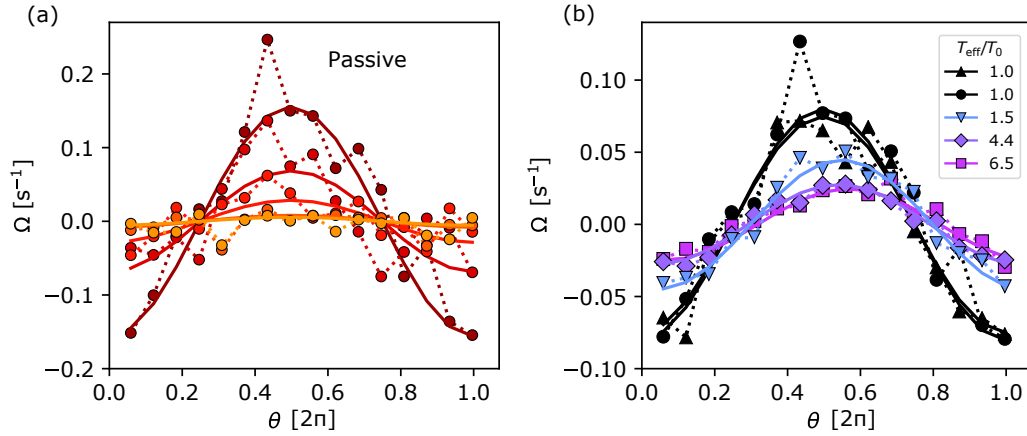


FIGURE 5.23: θ -dependence of Ω . The angle of reference $\theta = 0^\circ$ is 90° anti-clockwise from the glass bead direction of motion. (a) Focusing on one passive case, $\Omega(\theta)$ of different distance r from the glass bead center. From red to yellow color: 7.6, 11.7, 15.8, 19.9, and 28.1 μm . (b) The average of $\Omega(\theta)$ between two first shells of different activity levels. The solid lines are the fitting curve with Eq. 5.14.

To investigate the distance-dependence of Ω , we make a plot of $\Omega(r)$ at fixed θ . We choose θ such that $|\Omega|$ is maximized, which means $\theta = 0$ and π . For a better statistics, at each r , we average $\Omega(r)$ among eight grid elements: two on each side of $\theta = 0$ and π . Fig. 5.24 shows the resulting $\Omega(r)$ of each activity level divided by its corresponding U (from the tracking). All the curves collapse onto one master curve of exponent -2 . This also supports that the colloids around the glass bead are advected by a Stokes flow.

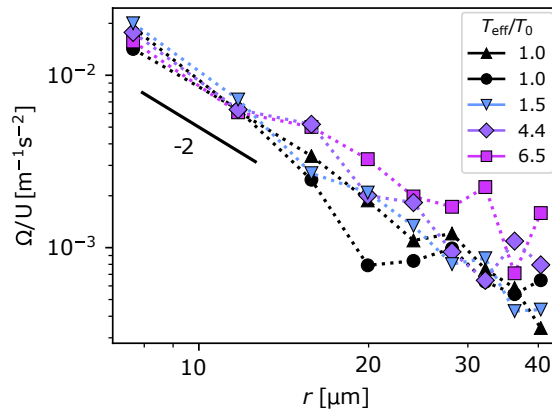


FIGURE 5.24: The distance-dependence of Ω averaging from the two sides of the glass beads ($\theta = 0$ and π and averaging among its two adjacent grid elements). $\Omega(r)$ normalized by U , glass bead instantaneous velocity obtained from the tracking, showing the collapse of different activity levels. The curve agrees with the exponent -2 reflecting a Stokes flow.

At this point, we have the evidence that at $x_{\text{GB}} = 50 \mu\text{m}$ the colloids around the falling bead are advected by a Stokes flow no matter the activity of the sediment. This opens the possibility of extracting an effective viscosity through a Stokes-like drag. To do this, what is required is a precise model of the other forces acting on the bead besides the viscous drag. Apart from gravitational force and Stokes drag, there

is a force from the colloids acting on the bead. The latter force could be obtained from an integral of pressure along the bead perimeter, which is complicated to define in active systems [238, 239], including the density gradient in our system. Whether this force would take the form of an effective Archimedes principle is an open question that would require a significant modelling effort to solve. However, unfortunately with this type of experiment, we cannot properly control important variables that are the bead diameter and velocity. Also, it is impractical to repeat the experiment. Therefore, instead of diving further into the analysis, we focused our efforts on a new experimental setup that could overcome those drawbacks.

To conclude this section, we investigated a falling glass bead into a colloidal sediment. We observed a difference in the bead motion when the colloidal sediment becomes active. We could explain the origin of this difference by analyzing the particle trajectories. The key difference comes from the flux of colloids above the glass bead. We continued our analysis using statistical tools to investigate bond deformations and we finally found that the flow of the colloids around the bead obeys the Stokes flow for all activity levels.

The setup of this experiment looks deceptively simple, but it has many uncontrolled parameters. In the next section, we will discuss our implementation of a new experimental setup. The goal is to properly control actuation force on the probe particle.

5.4 Perspective towards magnetic actuation

In the previous two sections, we applied force to the system using displacement of the probe particle, and we could extract some rheological properties of our active colloidal sediment. The next thing we would like to try is to apply rotational shear to the system using a magnetic field. One of the advantages of such an approach is that we can apply a large deformation without changing the environment inside the system (recall that our previous system always had a density gradient along the direction of gravity).

For the work in this section, I co-advised and collaborated with Mickaël Dos Santos, an engineering student from Institut Universitaire de Technologie (IUT) de Lyon 1. The design and fabrication of the magnetic microrheometer in our laboratory was the main objective of his internship from April to June 2018. With my supervisors, we provided him a concept of an electromagnet and magnetic microrheometer. The mechanical part and fabrication were supervised by Gilles Simon, a research engineer (ingénieur d'étude) of iLM. This was a great opportunity for me to work with people from different backgrounds, and I could learn a lot from them.

5.4.1 Key concept of magnetic microrheometer

We were inspired by Ref. [225] for the magnetic microrheometer. In brief, they used two pairs of aligned electromagnets that are placed orthogonally to each other (see Fig. 5.25). Their probe is a ferromagnetic microrotor that is magnetized to have a magnetic dipole moment. With this setup, it is possible to either translate or rotate the microrotor using magnetic force or torque, respectively. A force is induced by a gradient of the magnetic field. This can be done when a pair of electromagnets generates a magnetic field in the opposite direction to each other. When a pair of electromagnets generates a magnetic field in the same direction, it creates a relatively

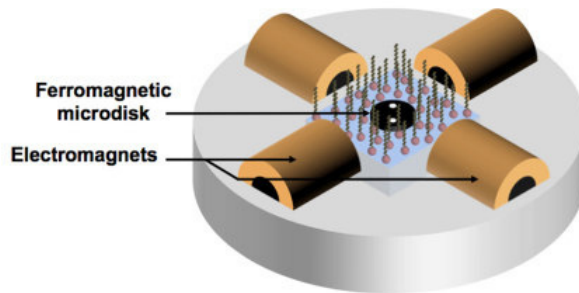


FIGURE 5.25: Schematic surface microrheometer using a magnetic field. Two aligned pairs of electromagnets are placed orthogonally to each other. At the center of the configuration is a ferromagnetic microrotor placed inside a sample. The pairs of electromagnets generate magnetic fields or magnetic field gradient which results in torques or forces on the microrotor. Therefore, the microrotor rotates or displaces according to the direction of the magnetic field/gradient. The image is retrieved from Ref. [225].

uniform magnetic field at the center of the configuration, and thus results in a magnetic torque on the microrotor. The microrotor, therefore, rotates until its magnetic dipole moment aligns with the applied magnetic field. With the use of two pairs of electromagnets, it is possible to continue the rotation or to make the microrotor oscillate.

5.4.2 Making of the magnetic microrheometer

Our goal setup is illustrated in Fig. 5.26. The objective and the sample holder are at the center of four electromagnets. It is important that the plane of the electromagnets is at the same level as the bottom of the experimental well, which is where the colloids are. The other important point is that the sample holder has to be movable while the electromagnets and the objective held fixed. This is to position a probe particle inside the colloidal sediment.

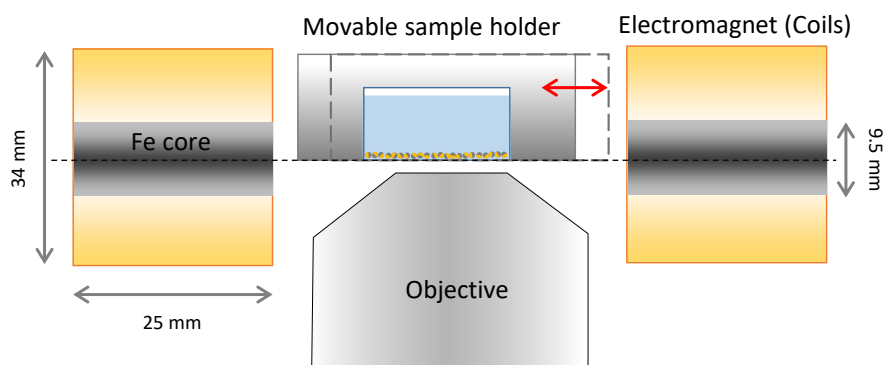


FIGURE 5.26: Schematic draft of our magnetic microrheometer (cross-section). Two pairs of aligned electromagnets are positioned orthogonally to each other with an objective and sample holder at the center. The plane of the electromagnets is supposed to be at the same level as the bottom of the experimental well. Importantly, the sample holder must be movable while the electromagnets and the objective are held fixed. Each electromagnet has an iron rod at the center to enhance the magnetic field.

For the electromagnets, we use a custom-designed solenoid made of copper wire of 0.37 mm diameter. Dimensions of the electromagnet are essential. This is because it is an important parameter for magnetic field strength, aside with a number of turns N of copper wire and applied electric current I . To calculate the dimension of a solenoid, we consider the relation between the magnetic field strength B and a distance x (measured from the center of one solenoid) as follows,

$$B(x) = \frac{\mu_0 N I R^2}{2(R^2 + x^2)^{3/2}}, \quad (5.15)$$

where $\mu_0 = 4\pi \times 10^{-7} \text{ T m A}^{-1}$ is the permeability constant and R is radius of a solenoid. However, another property that we also have to be concerned with is the inductance of a solenoid L ,

$$L = \frac{\mu_0 N^2 \pi R^2}{\ell}, \quad (5.16)$$

where ℓ is the length of the solenoid. Since the response time of a LR circuit is proportional to L/R , increasing N and R to gain more magnetic field strength will result in slower response time.

Due to the limitation of the space on our microscope stage, the solenoid length ℓ is set to be 25 mm. The radius of the solenoid is chosen at 17 mm. Therefore, the distance between two solenoids is $2R = 34$ mm. This is to have enough space for the objective and sample holder at the center. In each solenoid, there are double-layer 136 turns of copper wire (68 turns per each layer). From Eq. 5.15, if we applied current $I = 1$ A, we should obtain magnetic field at the center between two solenoids about 2 G with the corresponding response time 0.2 ms. Besides, the magnetic field can be enhanced by adding an iron rod at the center of the solenoid. We thus add an iron rod of 9.5 mm diameter into all solenoids. Note that this will also increase the response time of the solenoid.

We discussed and exchanged these ideas with Mickaël and Gilles, who did all the design and fabrication with the 3D printing technique. The microrheometer is composed of three main parts: a sample holder, electromagnet and cradles for the electromagnets. The sample holder is attached to the XY movable microscope stage. The experimental plate is the same as we always use throughout my PhD. We cut it to be able to fit it in this setup. The sample holder holds the cut plate from the above and leaves the side area for the electromagnets (see Fig. 5.27a). The design sketch of the electromagnet is shown in Fig. 5.27b. It is a solenoid made of copper wire and iron core. The cradles to hold the four electromagnets are attached to a fixed part of the microscope. They are positioned around the objective (see Fig. 5.27c). The final product after all the elements are put together is shown in Fig. 5.27d.

5.4.3 Preliminary output

We characterized the magnetic field from our custom-made electromagnets. We applied electric current of 0.7 A ⁴ to the solenoid and then measured the resultant magnetic field as shown in Fig. 5.28a. Without the iron core, the magnetic field at the center of the electromagnets pair is 3.5 G (measured from a hall effect sensor). This value increases to 16 G after the iron cores were inserted.

³This expression comes from the approximation of $R \gg \ell$ [240], which is not exactly our case.

⁴Note that the solenoid significantly heated up just a few seconds after we applied the current above this value. We are concerned about the degradation of the copper wire and also the deformation of the setup due to the heat. We, therefore, try not to put too high current.

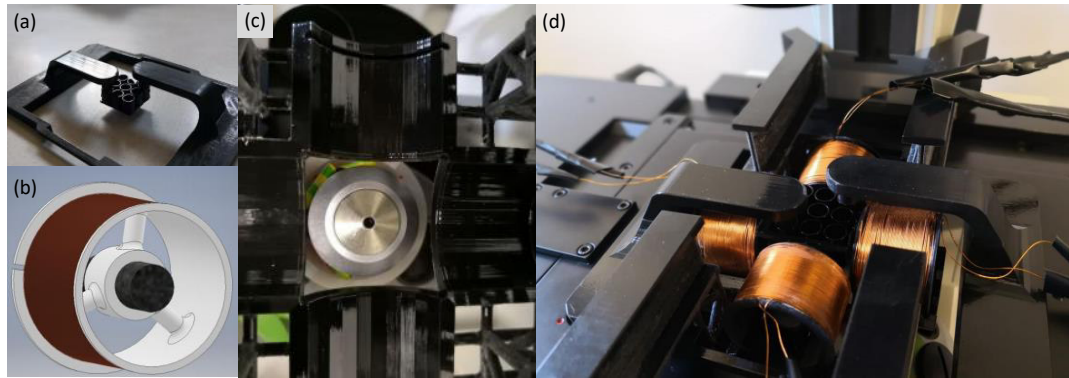


FIGURE 5.27: Our custom-made magnetic microrheometer. (a) Sample holder that is attached with XY movable stage of the microscope. The 96-well plate, which we always use as an experimental chamber, is cut into 3×3 well plate. Two wells at the diagonal are attached with the sample holder using a polymer screw from their bottom. We only use the well at the center for a further experiment. (b) Design sketch of the electromagnets: A solenoid made of copper wire (brown color) with an iron core (grey color). (c) Four cradles to support the electromagnets with the objective at the center. (d) The final system equipped on the microscope. Images were taken by Mickaël Dos Santos.

We used magnetized ferromagnetic beads ($12 \mu\text{m}$ in diameter) as an initial probe of the magnetic field inside the experimental chamber filled with deionized water. As soon as we applied current in one pair of the electromagnets, the beads moved closer to nearby beads and formed a short line of 2-3 beads. When we switched to apply the current to the orthogonal pair of the electromagnets, the lines rotate about 90° to the corresponding direction of the magnetic field (see Fig. 5.28b). These lines of the magnetic beads can be rotated back and forth by switching between pairs of electromagnets.

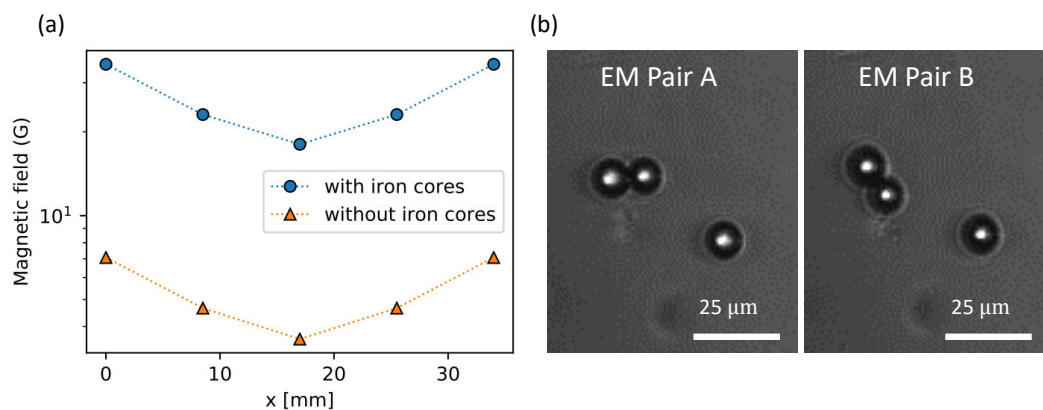


FIGURE 5.28: (a) Magnetic field characterization of one pair of electromagnets. The distance x is measured from the front of one electromagnet. Two electromagnets generate a magnetic field in the same direction from an electric current of 0.7 A . (b) Test of rotational mode with ferromagnetic beads of $12 \mu\text{m}$ diameter. We switched on each pair of electromagnets (EM) and observed the change of orientation of a pair of particles upon switching the EM pairs.

5.4.4 Further development

At this stage, most of the physical parts of the magnetic microrheometer have already been done. There are still two main points that we have to improve. The first point is the probe particles. We aim to use a ferromagnetic microrotor made by photolithographic techniques like in Ref. [225] and thus we could apply oscillatory shear to our colloidal suspension. The second point is to add dark-field microscopy into this setup. This is because the space below the objective is now occupied by the electromagnets. We thus cannot use our old LEDs ring for the dark-field microscopy. This point is crucial for a good resolution of the experimental images and particle tracking in a future work.

Apart from the physical components, we also aim to develop a circuit and software to properly control the magnetic field. For example in Ref. [225], they use a data acquisition (DAQ) to generate analog output and send it to an amplifier that drives a current to the solenoids. The mode of microrheology and motion parameters (amplitude and frequency) can be adjusted via a LabView code interface.

My work in this section is the first milestones for the development of a magnetic actuation for microrheology in our group. Going further in this direction is now the aim of the next PhD.

Key points of the chapter:

1. We discussed our microrheology investigation in the active colloid sediment.
2. The first actuation force we applied is a periodic motion of the probe particle using optical tweezers (SAOS).
 - (a) We obtained a hint that the active sediment is stiffer than the passive sediment. This is observed in both fluid and solid initial states of the sediment.
 - (b) Due to the light-induced attraction of the colloids to the probe, we suggest that optical tweezers may not be the right tool for our system.
3. The second actuation force we considered was using gravity to pull the probe particle through the sediment.
 - (a) We observed a difference in the probe motion among the passive and active sediment. The probe particle in the passive sediment first shows deceleration followed by constant velocity, acceleration and a second deceleration. The probe in the active sediment continues its deceleration then has a constant velocity, which happens much later than the second deceleration in the passive case.
 - (b) Analyzing the colloidal trajectory, we could explain that the origin of the difference comes from the difference in colloidal flux above the probe.
 - (c) We continued to analyze the colloids relative motion with their neighbors using the broken bonds and texture analysis.
 - (d) We found from texture analysis that the colloidal particles around the probe obey the Stokes flow.
4. Finally, we discussed the development of the magnetic microrheometer in our laboratory.

Chapter 6

Numerical simulation approach for the spontaneous dynamics of active Brownian particles

This chapter is an additional work with respect to the experimental core and methods of my PhD. It is motivated from our experimental result in Chapter 4. We investigated the spontaneous dynamics of the active sediment and found the *Deadlock from the Emergence of Active Directionality* (DEAD) phenomenon when the system becomes non-ergodic. In the experiment, we were limited by some constraints and properties that cannot be measured. For example, the density gradient, that we applied to confine the colloids and to vary the density, prevents us from measuring any long-range correlations. Another important point is that we cannot access to particle orientation, which could be the key to our explanation on the origin of the DEAD behavior.

Together with my intention to expand my research experience, I applied for a pre-doctoral fellowship from the Japan Society for the Promotion of Science (JSPS) and received the opportunity. From January to September 2020, I stayed in the Non-equilibrium physics group (R-lab) at Nagoya University and worked with Takeshi Kawasaki (lecturer, tenured). The goal of the fellowship is to construct the simulation and to reproduce my experimental system. With the simulation, we aim to better characterize and explore the minimum ingredient of the DEAD.

In the following sections, I will first introduce some relevant studies and then discuss what is still missing, which will lead to our plan to construct the simulation. Next, I will present our simulation setup starting from equations of motion to some relevant numerical techniques. The rest sections are the results of my simulation. I will discuss them in the order of density regime: individual particle, ergodic supercooled phase, and non-ergodic phase above the glass transition.

[Please note that at the moment of my writing, the work in the chapter is still in progress. The story will be fulfilled when the fellowship ends.]

6.1 Previous numerical studies

There are two popular models for artificial active colloids: Active Brownian Particle (ABP) [83, 241] and Active Ornstein-Uhlenbeck particle (AOUP) [77]. The equation of motion for ABP model is often presented by overdamped Langevin dynamics with an additional self-propulsion force, which is a force of constant amplitude and diffusive reorientation. For a simpler analytic expression, the AOUP model is proposed in terms of an overdamped equation comprising of an interaction term and

a self-propulsion velocity, which follows Ornstein-Uhlenbeck processes. However, unlike the ABP model, the thermal fluctuation is not written explicitly in the equation of motion. From our experimental realization, we believe that the DEAD behavior originates from a competition between Brownian translational and rotational diffusion. Therefore, the thermal fluctuation is a key ingredient that we need and we decide to model our experimental system with the ABP model.

A full-phase diagram for the 2D ABP model has reported by Digregorio et al. [155] using identical particles. They could locate the region of Motility Induced Phase Separation (MIPS) [86] on the phase diagram over a range of moderate densities and high enough self-propulsion force. This is similar to another phase diagram for an athermal polydispersed ABP model proposed by Fily et al. [156]. Both of the phase diagrams also include the solid/glass phase at high enough packing fraction. Besides, the glass transition line in the phase diagrams appears to be pushed towards higher packing fraction when the self-propulsion force is increased. This point is supported by Ni et al. [157], who used the framework of glassy physics to investigate a 3D ABP system focusing on the supercooled regime. Recall that we found the same behavior in our experiment (see Fig. 4.14a,b). We, therefore, believe that the ABP model is a good candidate to reproduce our experimental system.

While most of the ABP simulation works focus on the regime where the self-propulsion dominates Brownian motion, we observed the non-trivial phenomena in our experiment when the activity level is very low. This low activity regime has been overlooked and perhaps it is the reason why DEAD has never been reported in the previous simulations. This leads to the goal of this chapter: a simulation of a 2D ABP model at high density and low activity levels.

6.2 Setting up the simulation for Active Brownian particles

In this section, I will describe a general framework of simulation for an ABP system. I will start from the overdamped Langevin equation with an additional active force and follow by its dimensionless version, which is used for the numerical integration. After that, I will mention some numerical techniques that I use for the simulation.

6.2.1 Langevin equation for ABP

To mimic the active particles in our experiment, the closest model is the overdamped Langevin equation for Brownian particles with an additional active force. At temperature T , a position of particle i of diameter σ_0 at time t , $r_i(t)$ is governed by,

$$\frac{d}{dt}r_i(t) = \zeta^{-1} \left[\mathbf{F}_i^B(t) + \mathbf{F}_i^I(t) + \mathbf{F}_i^A(t) \right], \quad (6.1)$$

where $\zeta = 3\pi\eta\sigma_0$ is a drag coefficient. The first term stands for a Brownian random force which obeys,

$$\langle \mathbf{F}_i^B(t) \rangle = 0, \quad \langle \mathbf{F}_i^B(t) \cdot \mathbf{F}_j^B(t') \rangle = 2k_B T \zeta \delta_{ij} \delta(t - t') \mathbf{1}, \quad (6.2)$$

where δ_{ij} and $\delta(t - t')$ are the Kronecker and Dirac delta function, respectively, and $\mathbf{1}$ is an identity matrix. From the central limit theorem, $\mathbf{F}_i^B(t)$ shows a Gaussian distribution. Therefore, $\mathbf{F}_i^B(t)$ can be written as

$$\mathbf{F}_i^B(t) = \sqrt{2k_B T \zeta \delta(t)} \mathbf{R}_G \sim \sqrt{2k_B T \zeta / \Delta t} \mathbf{R}_G, \quad (6.3)$$

where R_G is a Gaussian random number of center 0 and variance 1. The approximation $\delta(t) \sim 1/\Delta t$ is made for a small time step Δt . The second term in Eq. 6.1 is an interaction term between particles, i.e., $F_i^I(t) = -\sum_j \frac{\partial U(r_{ij})}{\partial \mathbf{r}_i}$, where r_{ij} is a distance between particle i and j . In our simulation, we use Weeks-Chandler-Anderson (WCA) potential [161],

$$U(r_{ij}) = 4\epsilon \left[\left(\frac{a_{ij}}{r_{ij}} \right)^{12} - \left(\frac{a_{ij}}{r_{ij}} \right)^6 + \frac{1}{4} \right] \quad (r_{ij} < a_{\text{cut}}), \quad (6.4)$$

where $a_{ij} = (a_i + a_j)/2$ and $a_{\text{cut}} = 2^{1/6}a_{ij}$. Lastly, the additional active force is defined as

$$\mathbf{F}_i^A(t) = f\hat{\mathbf{u}}_i(t), \quad \frac{d}{dt}\theta_i(t) = \zeta_i(t) \sim \sqrt{\frac{2D_R}{\Delta t}}R_G, \quad (6.5)$$

where f represents constant magnitude of the self-propulsion force and $\hat{\mathbf{u}}_i(t) = (\cos\theta_i(t), \sin\theta_i(t))$ is a unit vector, in which $\langle \zeta_i(t)\zeta_j(t') \rangle = 2D_R\delta_{ij}\delta(t-t')$ and D_R is a rotational diffusion coefficient.

6.2.2 Nondimensionalized equation of motion

In a numerical simulation, it is better to use a dimensionless form of the equation of motion. One reason is to avoid numerical errors, for example, when adding small numbers to very large numbers. Another reason is that it is easier to identify significance of some parameters that govern important physics and thus simplify the parameter space. To nondimensionalize the equation of motion, we start by separating all variables into their physical units and dimensionless number. Here, we use a unit of length, time, and energy as particle diameter σ_0 , t_0 which will be defined shortly, and ϵ , respectively. Therefore, Eq. 6.1 can be rewritten as,

$$\frac{\sigma_0}{t_0} \frac{d}{d\tilde{t}} \tilde{\mathbf{r}}_i(\tilde{t}) = \zeta^{-1} \left[\sqrt{\frac{2k_B T \zeta}{t_0 \Delta \tilde{t}}} R_G + \frac{\epsilon}{\sigma_0} \tilde{\mathbf{F}}_i^I(\tilde{t}) + f\hat{\mathbf{u}}_i(\tilde{t}) \right], \quad \frac{1}{t_0} \frac{d}{d\tilde{t}} \theta_i(\tilde{t}) = \sqrt{\frac{2D_R}{t_0 \Delta \tilde{t}}} R_G \quad (6.6)$$

$$\frac{d}{d\tilde{t}} \tilde{\mathbf{r}}_i(\tilde{t}) = \sqrt{\frac{2k_B T}{\sigma_0^2 \zeta}} \frac{t_0}{\Delta \tilde{t}} R_G + \frac{\epsilon t_0}{\sigma_0^2 \zeta} \tilde{\mathbf{F}}_i^I(\tilde{t}) + \frac{f t_0}{\sigma_0 \zeta} \hat{\mathbf{u}}_i(\tilde{t}), \quad \frac{d}{d\tilde{t}} \theta_i(\tilde{t}) = \sqrt{\frac{2D_R t_0}{\Delta \tilde{t}}} R_G. \quad (6.7)$$

Now, $\tilde{\mathbf{r}}_i$ and \tilde{t} denote dimensionless position and time variables. We define the unit of time as $t_0 \equiv \sigma_0^2 \zeta / \epsilon$. For the parameters, we define dimensionless temperature, self-propulsion force and rotational coefficient as,

$$T^* \equiv k_B T / \epsilon, \quad f^* \equiv \sigma_0 f / \epsilon, \quad D_R^* = D_R t_0, \quad (6.8)$$

respectively. As a result, we obtain a dimensionless overdamped Langevin equation of an active particle as,

$$\frac{d}{d\tilde{t}} \tilde{\mathbf{r}}_i(\tilde{t}) = \sqrt{\frac{2T^*}{\Delta \tilde{t}}} R_G + \mathbf{F}_i^I(\tilde{t}) + f^* \hat{\mathbf{u}}_i(\tilde{t}), \quad \frac{d}{d\tilde{t}} \theta_i(\tilde{t}) = \sqrt{\frac{2D_R^*}{\Delta \tilde{t}}} R_G. \quad (6.9)$$

We can compare the parameters T^* , f^* and D_R^* in the simulation to the quantities that we can measure in our experiments. With this choice of the unit of time, we can see that the dimensionless temperature T^* is actually a dimensionless translational

diffusion coefficient D_T^* , i.e.,

$$T^* \equiv \frac{k_B T}{\epsilon} = \frac{k_B T}{\zeta} \frac{t_0}{\sigma_0^2} = D_T \frac{t_0}{\sigma_0^2} \equiv D_T^*. \quad (6.10)$$

In the same way, the dimensionless self-propulsion force f^* is thus a dimensionless propulsion velocity v_0^* ,

$$f^* \equiv \frac{\sigma_0 f}{\epsilon} = \frac{f}{\zeta} \frac{t_0}{\sigma_0} = v_0^*. \quad (6.11)$$

The dimensionless rotational diffusion coefficient D_R^* has the same physical meaning. For a spherical Brownian particle, one can find its relation with the translational diffusion coefficient such that $D_R^* = k_B T t_0 / \pi \eta \sigma_0^3 = 3D_T^* = 3T^*$. However, this relation holds for a 3D system. In our case, we aim to perform a 2D simulation. We thus take the factor 3 as an arbitrary constant in order to explore the significance of D_R^* compare to the translation thermal noise. Thinking more about this, our experimental system is a quasi-2D. The projected D_R into the plane should be less than the original 3D rotational diffusion. Some numerical studies on a 2D ABP system use the factor of 3 [155, 241], while some treat it independently from D_T [156]. In this work, we shall consider two cases in which $D_R^* = T^*$ and $D_R^* = 3T^*$.

6.2.3 Numerical integration of the equations of motion

For the numerical calculation, Eq. 6.9 is discretized and has the following form,

$$\begin{aligned} x_i(t + \Delta t) &= x_i(t) + \sqrt{2T^* \Delta t} R_G^x + F_i^{L,x}(t) \Delta t + f^* \cos \theta_i(t) \Delta t, \\ y_i(t + \Delta t) &= y_i(t) + \sqrt{2T^* \Delta t} R_G^y + F_i^{L,y}(t) \Delta t + f^* \sin \theta_i(t) \Delta t, \\ \theta_i(t + \Delta t) &= \theta_i(t) + \sqrt{2D_R^* \Delta t} R_G^\theta. \end{aligned} \quad (6.12)$$

Note that the variables (x, y, t) are dimensionless. We omit the tilde to make the equations easier to visualize. Eq. 6.12 is known as Euler integration method [242]. It is yet simple, but its accuracy is poor with an error at a given time of $\mathcal{O}(\Delta t)$. To avoid such an error, one can reduce Δt , which increases the simulation time, or use a more appropriate integration method.

We decided to use Heun method [243], which is a two-steps predictor-correction of the Euler method. The equations of motion for the simulation is in the following form,

$$\begin{aligned} x_i(t + \Delta t) &= x_i(t) + \sqrt{2T^* \Delta t} R_G^x + \frac{1}{2} \left[F_i^{L,x}(x, t) + F_i^{L,x}(x', t + \Delta t) \right] \\ &\quad + \frac{1}{2} [f \cos \theta_i(t) + f \cos \theta_i'(t + \Delta t)] \\ y_i(t + \Delta t) &= y_i(t) + \sqrt{2T^* \Delta t} R_G^y + \frac{1}{2} \left[F_i^{L,y}(y, t) + F_i^{L,y}(y', t + \Delta t) \right] \\ &\quad + \frac{1}{2} [f \sin \theta_i(t) + f \sin \theta_i'(t + \Delta t)] \\ \theta_i(t + \Delta t) &= \theta_i(t) + \sqrt{2D_R^* \Delta t} R_G^\theta, \end{aligned} \quad (6.13)$$

where x', y' and θ' are updated using Euler step in Eq. 6.12. At a given time step, the calculation of Heun method is doubled from Euler method. However, with better

accuracy of $\mathcal{O}((\Delta t)^2)$, we can use a larger time step compare to the Euler method and thus save on simulation time.

6.2.4 Relevant numerical simulation techniques

Box-Muller method for Gaussian random generator

Box-Muller method [244] is a trick to generate random numbers of Gaussian distribution from a uniform random generator. The basic form of this method states that given a pair of two independent uniform random numbers in a range $[0, 1]$, U_1 and U_2 , the following Z_1 and Z_2 are independent random variables with Gaussian distribution of variance 1,

$$Z_1 = \sqrt{-2 \log U_1} \cos(2\pi U_2), \text{ and } Z_2 = \sqrt{-2 \log U_1} \sin(2\pi U_2). \quad (6.14)$$

However, the sine and cosine functions are expensive for the computation, especially in the Brownian dynamics simulation where R_G is needed for every steps and every particles. To get rid of the trigonometric function, another form of the Box-Muller method is often used, which is known as a polar form [245, 246]. Given that u_1 and u_2 are uniform random numbers and (u_1, u_2) is a point on the unit disk. Its distance R from the origin is thus a uniform random number in a range $(0, 1)$. Therefore, let $R^2 = u_1^2 + u_2^2 = U_1$ and then, the trigonometric functions in Eq. 6.14 can be computed directly from $u_1/R = \cos(2\pi U_2)$ and $u_2/R = \sin(2\pi U_2)$.

Verlet list and cell lists method for neighbors search

For the interaction term $F_i^I(t) = -\sum_j \frac{\partial U(r_{ij})}{\partial r_i}$, one need to search for neighboring particles j that are within a cutoff distance a_{cut} from particle i and then calculate the interparticle distance r_{ij} . It is, of course, computationally expensive to loop over the particles at every time steps. The idea of the Verlet list [247] together with the cell lists method [248] is to consider only a few neighbors around a given particle.

The Verlet list is a list of neighboring particles j of particle i at one time. Once we create it, we can calculate r_{ij} by considering only particles j that are on the list. To create the Verlet list, the cell lists method is a trick that saves us from looping particles all over the simulation domain. In the cell lists method, the domain is divided into small cells of size R_{cell} such that $R_{\text{cell}} > a_{\text{cut}}$. All particles are assigned into a cell corresponding to their current position. Then, the Verlet list is created by looping particles j that are in the adjacent cells (3×3 cells) of particle i . If $r_{ij} > R_{\text{cell}}$, particle j is one of particle i 's neighbors. The Verlet list has to be updated during the simulation because particles can change neighbors. In this work, we update it automatically when any particle has displaced further than $(R_{\text{cell}} - a_{\text{cut}})/2$ from the last update. Determining the appropriate size of R_{cell} is important to optimize the simulation time. Smaller R_{cell} causes more frequently update of the Verlet list. On the other hand, larger R_{cell} results in more neighbors j to calculate r_{ij} in every steps.

Initial configuration

To initialize particle positions, one point to be concerned with is the divergence in our interaction potential $U(r_{ij})$. If two particles overlap and r_{ij} is too small, the interaction force thus blows up and causes an error. To avoid such a problem, there are two possible ways to initialize particle configuration. One way is to put particles in a lattice. The other way, which we are using, is putting particles randomly in

space and use an interaction potential that does not have a divergence to separate overlapped particles. In our case, we use a Harmonic sphere potential, $U(r_{ij}) = \epsilon(1 - r_{ij}/a_{ij})^2/2$ to perform this task. Once all particles are separated, we switch the potential to the desired one, which is WCA in our simulation. Fig. 6.1 shows the initial state of the simulation before and after we apply the harmonic sphere potential. Before we switch to WCA potential, we monitor the potential energy to verify that the harmonic sphere system has reached a stationary state, which means that particles are not overlapping anymore.

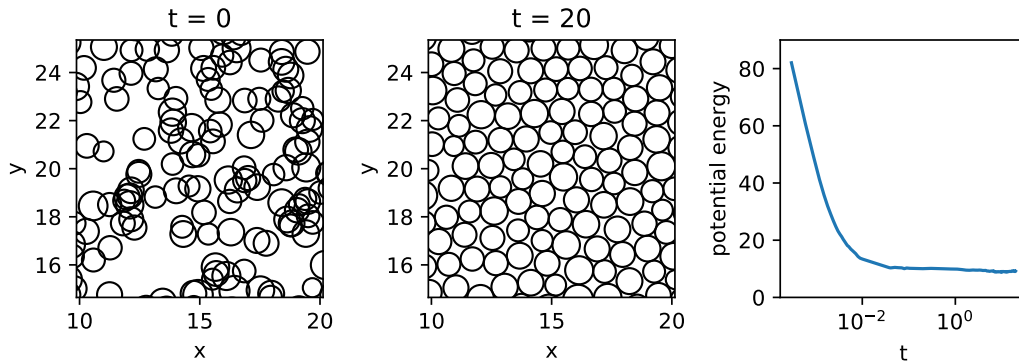


FIGURE 6.1: Initialize particle positions. At $t = 0$, particle positions are randomly distributed over the simulation domain. We apply the Harmonic sphere potential to make particles come out of each other as we can see from the snapshot at $t = 20$. Associated potential energy can be monitored to know whether the system has reached a stationary state or not. The unit of length and time in this representation is σ_0 and t_0 , respectively.

Logarithmic sampling

Since we want to capture the dynamics in a wide range of simulation time, it is better to save data (such as particle coordinate, potential energy, etc) with an increased time interval from the last saving. From this, we can capture both short-range and long-range time interval. In one file, we save the data in a logarithmic time interval. We repeat the sampling several times and save them into separated files. With this way of saving, the amount of the data is much lighter than the constant-interval sampling. Also, it is more efficient for the analysis since a pointer (in C++) takes a shorter time to scan the whole file with the Logarithmic sampling.

For statistics, there are two types of averages: time average and ensemble average. If the system can be equilibrated within a simulation time, the time average is recommended because static properties and dynamic properties remain unchanged in an equilibrated state. We can let the simulation run and repeatedly save the data at a longer time for more statistics (Fig. 6.2a) with no need to equilibrate the system again. The time average can be done at a low density and in an ergodic supercooled phase. On the other hand, in the non-ergodic phase, the system does not equilibrate within our time spare. In this regime, we aim to investigate the aging and its waiting time dependence. Therefore, we take an ensemble average by sampling at the same simulation time from the start (see Fig. 6.2b).

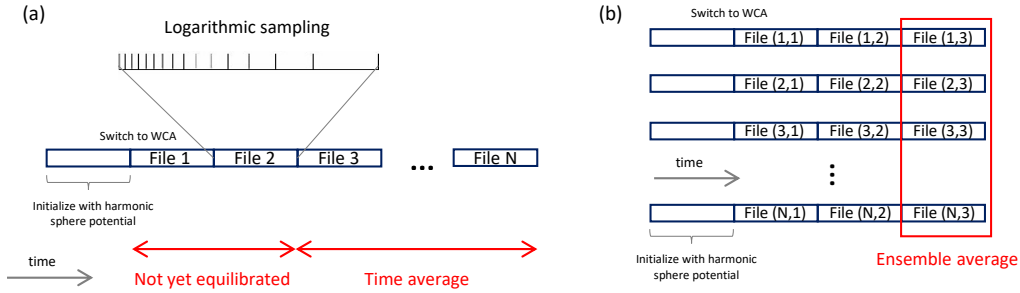


FIGURE 6.2: Schematic sampling diagram for (a) time average and (b) ensemble average. Data is saved in a separate file with a logarithmic time interval.

Zero-mode subtraction

Another point to be concerned in a simulation is infinite-wavelength fluctuation, which is known as zero-mode or Goldstone mode [249]. This zero-mode emerges from a periodic boundary condition, and results in a global movement of particles. In the simplest situation, it can be demonstrated as a zero-frequency solution of a periodic chain of harmonic oscillators. The resulting global motion indeed affects the investigation of any dynamical quantities. We, therefore, need to subtract the zero-mode in order to obtain the right relaxation dynamics.

We consider the zero-mode as the drift in the experiment because they both result in long-range collective motion. Therefore, to subtract the zero-mode, we apply the same procedure we have done for the drift subtraction mentioned in Section 3.1. In brief, we calculate a cumulative sum of the average particle displacement at each time step and subtract it from current particle positions. During the simulation, we always use the original particle positions. When we reach a time step at which we want to save current particle positions, we save the subtracted position and leave the original one untouched to continue the simulation.

We show the significance of the zero-mode subtraction in Fig. 6.3. The dynamics of the system is displayed by the mean square displacement (MSD). At low enough ϕ , the zero-mode weakly affects the dynamics as can be seen by the almost perfect overlapping of the MSD before and after the zero-mode subtraction. At such a high ϕ , without the zero-mode subtraction, the MSD shows higher dynamics than the actual relaxation.

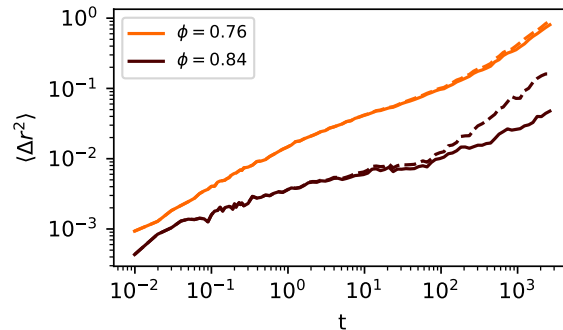


FIGURE 6.3: Mean square displacement (MSD) showing the significance of the zero-mode subtraction. The MSD before and after the subtraction is shown by the dashed and solid lines, respectively.

6.2.5 Our ABP simulation

In our simulation, we use $N = 1000$ particles (10% polydispersity with Gaussian distribution centered at $\sigma_0 = 1$) and their motion is governed by Eq. 6.13 with the step size $\Delta t = 10^{-4}$ and periodic boundary condition. The simulation program and analysis in this chapter are written in C++. We use the computer clusters of R-lab to run the programmes. Typically, it takes about 40 minutes to run one sample from $t = 0$ to 10^3 .

In the following sections, we will discuss our simulation results in different density regimes. Starting from a very dilute regime to investigate individual dynamics. Then, we will explore the supercooled regime by increasing packing fraction ϕ until we cannot equilibrate the system within a reasonable time because it approaches the glass transition density ϕ_g . Finally, we will investigate the density regime near and beyond ϕ_g using the ensemble average of aging systems. We note that all the simulations of different ϕ and Pe are run independently to each other. Unless stated otherwise, the results are averaged among 10 samples.

6.3 Dynamic of an individual ABP

We start with the simplest situation of individual particle dynamics with no interaction, i.e., $F_i^l(t) = 0$. In the first step, we verify our simulation by comparing the result with the literature and with the analytic expression. Verification is very important since the early steps. This is because, in simulation, it is easy to get data as well as easy to get the wrong one due to numerical errors (and also coding errors). Once we are confident with our simulation, we use it to simulate the systems of our interest and we try applying the same analysis that we did with our experimental system in the very dilute limit.

6.3.1 Verify the simulation

We compare our simulation with Volpe et al. [241], which is also a simulation of individual ABP. Without the nondimensionalization, their discrete equations of motion are,

$$\begin{aligned} x(t + \Delta t) &= x(t) + \sqrt{2D_T\Delta t}R_G^x + v_0 \cos \theta(t)\Delta t, \\ y(t + \Delta t) &= y(t) + \sqrt{2D_T\Delta t}R_G^y + v_0 \sin \theta(t)\Delta t, \\ \theta(t + \Delta t) &= \theta(t) + \sqrt{2D_R\Delta t}R_G^\theta. \end{aligned} \quad (6.15)$$

The parameter values were taken from the real situation. In a case of a particle of radius $1 \mu\text{m}$ immersed in water (viscosity $\eta = 0.001 \text{ N s m}^{-2}$) at temperature $T = 300 \text{ K}$, the corresponding translational and rotational diffusion coefficients are $D_R \sim 0.22 \mu\text{m}^2 \text{ s}^{-1}$ and $D_T \sim 0.16 \text{ s}^{-1}$, respectively.

We use our simulation to simulate the same condition by setting $D_R^* = 0.22$ and $T^* = 0.16$. The dimensionless propulsion force f^* is varied from 0 to 3 and is equivalent to the propulsion speed v_0 of the unit $\mu\text{m s}^{-1}$. The resulting MSD is shown in Fig. 6.4 in comparison with the result from Volpe et al. [241]. It can be seen that our simulation perfectly agrees with the previous study.

We can also compare our simulation with an analytic expression of MSD. Note that the rotational diffusion in our simulation is $2D$, unlike the quasi-2D experimental system. Therefore, we use the following expression obtained from Ref. [250], in

which $\tau_R = 1/D_R$,

$$\langle \Delta r^2 \rangle(t) = 4D_T t + 2v_0^2 \tau_R t + 2v_0^2 \tau_R^2 \left[e^{-t/\tau_R} - 1 \right]. \quad (6.16)$$

The solid lines in Fig. 6.4 represent the expression in Eq. 6.16 and they show a good agreement with our simulation result.

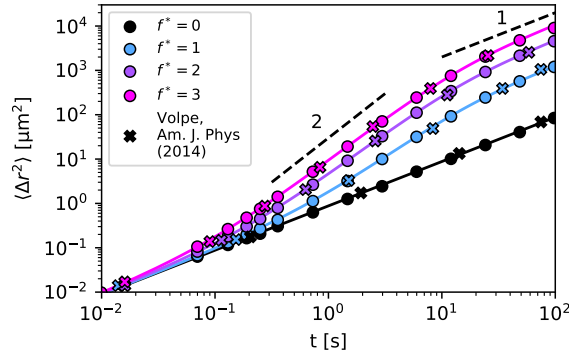


FIGURE 6.4: MSD of individual active Brownian particle compared with the result from Ref. [241] (crosses) at the same values of parameters. The solid lines represent the analytic expression in Eq. 6.16.

6.3.2 Individual dynamics of our system

At this point, we are confident with our simulation. We thus use it to simulate our system. Here we fix $T^* = 0.01$ and vary the activity levels, which is presented by a Péclet number $Pe = f^*/T^*$. For the value of D_R^* , we consider two cases such that $D_R^* = T^*$ and $D_R^* = 3T^*$. The resulting MSD is shown in Fig. 6.5a. In the ballistic regime at a short-time scale $t \ll \tau_R$, the two cases of D_R^* have no difference from one another. We can extract the dimensionless propulsion velocity v_0^* by fitting the MSD in this regime with $\langle \Delta r^2 \rangle(t) \approx (v_0^*)^2 t^2$. The difference in D_R^* is visible at the transition from the ballistic to the diffusive regime. The MSD of $D_R^* = 3T^*$ (shorter τ_R) reaches the diffusive regime before that of $D_R^* = T^*$ (longer τ_R). The dimensionless effective (translational) diffusion coefficient D_{eff}^* can be extracted at a long-time scale $t \gg \tau_R$, such that $\langle \Delta r^2 \rangle(t) \approx 4D_{\text{eff}}^* t$. In the passive case ($Pe = 0$) D_{eff}^* is actually T^* (recall that $D_T^* = T^*$). From the fitting of MSD at long-time scale, we obtain $D_{\text{eff}}^*(Pe = 0) = 0.01$, which is equal to $T^* = 0.01$ that we set for the simulation.

From Eq. 6.16, we can define D_{eff}^* as,

$$D_{\text{eff}}^* = D_T + \frac{1}{2} v_0^{*2} \tau_R = D_T + \frac{1}{2} \frac{v_0^{*2}}{D_R^*}. \quad (6.17)$$

We can verify this relation by plotting D_{eff}^* against $(v_0^*)^2$, which are obtained from a long-time and short-time MSD, respectively, as shown in Fig. 6.5b. Since there is no ballistic regime in the passive case ($Pe = 0$) and it is poorly visible at a low activity level ($Pe = 2$), we thus consider only high activity levels ($Pe \in [10, 50, 100, 200]$). The resulting plot shows a linear relation, which agrees with Eq. 6.17. We can also extract D_R^* by fitting the plot and compare with the value we set for the simulation. As a result, we obtain $D_R^* = 0.009 \pm 0.002$ for the case $D_R^* = T^*$, and $D_R^* = 0.027 \pm 0.002$

for $D_R^* = 3T^*$. This is, again, in agreement with the simulation parameters. Besides, we also verify the relation $v_0^* = f^*$ as shown in the inset of Fig. 6.5b.

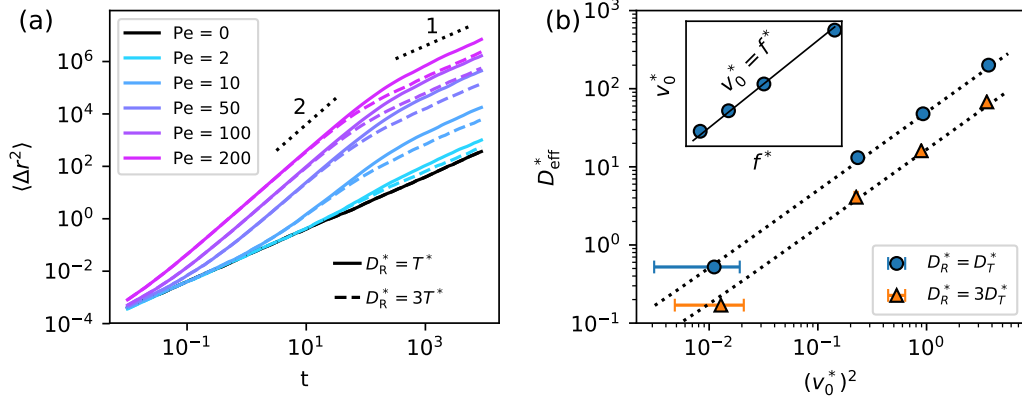


FIGURE 6.5: (a) MSD of individual active Brownian particle at $T^* = 0.01$ and different values of Pe. We consider D_R^* of two cases: $D_R^* = T^*$ and $D_R^* = 3T^*$. (b) Verification of the relation $D_{\text{eff}} = D_T + v_0^2/2D_R$ (dotted lines). We can extract D_R^* from the fit. We obtain $D_R^* = 0.009 \pm 0.002$ for the case $D_R^* = T^*$, and $D_R^* = 0.027 \pm 0.002$ for $D_R^* = 3T^*$. (Inset) Verification of $v_0^* = f^*$.

6.4 Ergodic supercooled regime

Now we extend our simulation by adding the interaction term $F_i^I(t) = -\sum_j \frac{\partial U(r_{ij})}{\partial \mathbf{r}_i}$, where $U(r_{ij})$ is the WCA potential defined in Eq. 6.4. We will first discuss the passive WCA systems, in which we investigate the relaxation time dependence on the packing fraction when approaching the glass transition. Then, we will turn on and increase the activity to investigate how it affects dynamics in the supercooled regime.

6.4.1 Passive WCA simulation

Effective hard sphere diameters in WCA system

WCA potential is widely used as an approximated hard sphere potential. However, we have to keep in mind that it is not a true hard sphere. The ‘softness’ of the potential modifies particle diameter from the bare diameter σ_0 that we defined in the simulation. This modification depends on the energy level $k_B T$ of the system (see Fig. 6.6). Mapping from σ_0 to an effective diameter σ_e can be done with the following expression [251, 252],

$$\sigma_e = \frac{2^{1/6}}{(1 + \sqrt{T^*})^{1/6}} \sigma_0, \quad (6.18)$$

which can be derived by solving the quadratic equation $T^* = 4X^2 - 4X + 1$, where $X = r^{-6}$. Consequently, the corresponding (effective) packing fraction is $\phi_e = \sum_j \pi(\sigma_e^j/2)^2/L^2$, where L is the size of the simulation domain.

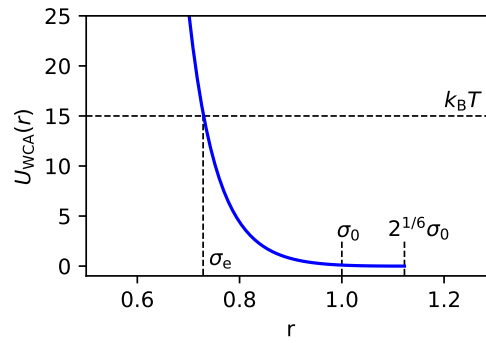


FIGURE 6.6: WCA potential as a function of distance r showing the map from a bare particle diameter σ_0 to an effective diameter σ_e .

In practice, we first define L from a bare particle diameter σ_0 to run the simulation and the corresponding packing fraction is a bare value ϕ_{bare} . Once the simulation is done, we present the result with a scaled packing fraction,

$$\phi_e = \frac{2^{1/3}}{(1 + \sqrt{T^*})^{1/3}} \phi_{\text{bare}}. \quad (6.19)$$

From this point, we always present our results with the scaled packing fraction ϕ_e and we simply refer it as ϕ until the end of the chapter.

Self-intermediate scattering function and relaxation time

We quantify the system relaxation using the self-intermediate scattering function $F_s(q, t)$ which is calculated from

$$F_s(q, t) = \frac{1}{N} \left\langle \sum_{i=1}^N e^{-i\mathbf{q} \cdot (\mathbf{r}_i(t) - \mathbf{r}_i(0))} \right\rangle \quad (6.20)$$

$$F_s(q, t) = \frac{1}{N} \left\langle \left(\sum_{i=1}^N \cos(\mathbf{q} \cdot \mathbf{r}_i(t)) \cos(\mathbf{q} \cdot \mathbf{r}_i(0)) \right) + \left(\sum_{i=1}^N \sin(\mathbf{q} \cdot \mathbf{r}_i(t)) \sin(\mathbf{q} \cdot \mathbf{r}_i(0)) \right) \right\rangle, \quad (6.21)$$

where $\langle \dots \rangle$ denotes the average among different samples, either time average or ensemble average. We choose $\mathbf{q} = 2\pi\hat{\mathbf{q}}$, and we also average among different four directions such that $\hat{\mathbf{q}} \in [\hat{\mathbf{q}}_x, (\hat{\mathbf{q}}_x + \hat{\mathbf{q}}_y)/\sqrt{2}, \hat{\mathbf{q}}_y, (\hat{\mathbf{q}}_y - \hat{\mathbf{q}}_x)/\sqrt{2}]$, where $\hat{\mathbf{q}}_x$ and $\hat{\mathbf{q}}_y$ are horizontal and vertical axes, respectively, in Fourier space.

In Fig. 6.7a, we show $F_s(q, t)$ of different samples from the same run but different initial time t_{ini} , where t_{ini} is a time after switching from harmonic sphere to WCA potential (please refer to Fig. 6.2a). It can be seen that the first sample ($t_{\text{ini}} = 0$) has not yet equilibrated and it relaxes faster than the others. For $t_{\text{ini}} > 100$, $F_s(q, t)$ does not change among samples, which means that the system has been equilibrated. We calculate the time average of $F_s(q, t)$ only among the equilibrated samples (in this example, from $t_{\text{ini}} > 100$), or when there is no time dependence. The resulting averaged $F_s(q, t)$ is shown in Fig. 6.7b with the standard deviation represented by the transparent region. The relaxation time τ_α is defined as a time when $F_s(q, t)$ has reached the threshold $1/e$.

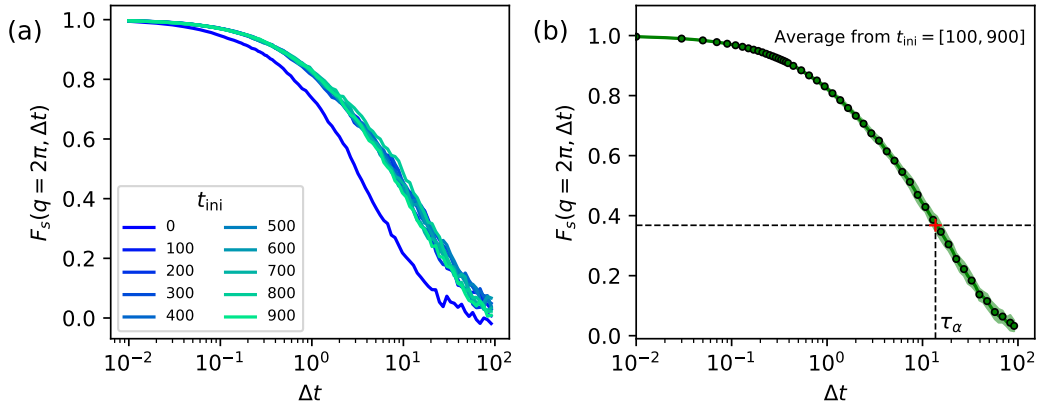


FIGURE 6.7: (a) The self-intermediate scattering function $F_s(q = 2\pi, \Delta t)$ of different samples at $\phi = 0.68$ from the same run but different initial time t_{ini} , where t_{ini} is a time after switching from harmonic sphere to WCA potential. For $t_{\text{ini}} > 100$, the samples have reached the equilibrium state, while the first sample ($t_{\text{ini}} = 0$) is still on the way. (b) Time average of $F_s(q = 2\pi, \Delta t)$ in which we only take the equilibrated samples ($t_{\text{ini}} > 100$) into account. The mean value is shown by the circles and solid lines. The transparent area behind represents the standard deviation among the time averages. The relaxation time τ_α is defined from the threshold value $1/e$, i.e., $F_s(q = 2\pi, \tau_\alpha) = 1/e$.

Approaching the glass transition from supercooled regime

We approach the glass transition by increasing the packing fraction ϕ . We show the self-intermediate scattering function $F_s(q = 2\pi, t)$ at $T^* = 0.01$ and various ϕ in Fig. 6.8a. The system relaxes slower and slower as ϕ increases. To obtain the relaxation time τ_α in the case where $F_s(q = 2\pi, \Delta t)$ has not reached the threshold $1/e$, we estimate τ_α by extrapolating with the stretched exponential function,

$$F_s(q = 2\pi, t) = A \exp \left[- (t/\tau)^\beta \right]. \quad (6.22)$$

The corresponding relaxation time τ_α is then obtained when the extrapolate line has reached $1/e$. At very high ϕ , $F_s(q = 2\pi, t)$ does not relax and we cannot obtain τ_α .

We show the relaxation time τ_α dependence of packing fraction ϕ in Fig. 6.8b. The resulting τ_α fits well with the the Vogel-Tamman-Fulcher (VTF) form,

$$\tau_\alpha = \tau_0 \exp \left[\frac{B\phi_0}{\phi_0 - \phi} \right], \quad (6.23)$$

where τ_0 is associated to the relaxation time at the limit $\phi \rightarrow 0$, B is the fragility index telling the strength of τ_α dependence on ϕ , and ϕ_0 is the divergence point. We obtain $\phi_0 = 0.81 \pm 0.01$ from the fit. This value is very close to the hard sphere glass transition point in 2D $\phi_g^{\text{HS}} \simeq 0.8$. Note that we only take the equilibrated samples (solid circles) into account for the fit.

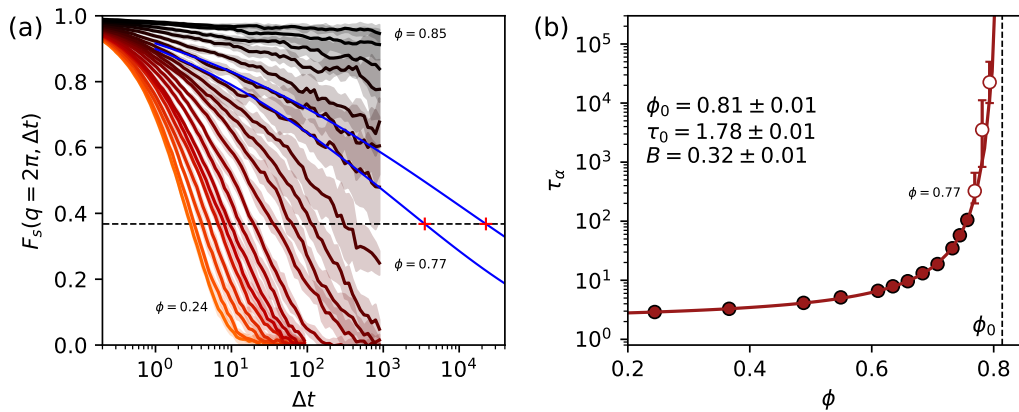


FIGURE 6.8: (a) The self-intermediate scattering function $F_s(q = 2\pi, \Delta t)$ of $T^* = 0.01$ at different packing fraction $\phi = [0.24, 0.85]$. The relaxation time τ_α is taken from the threshold $F_s(q = 2\pi, \tau_\alpha) = 1/e$. If $F_s(q = 2\pi, \tau_\alpha)$ has not reached the threshold within the time window, we extrapolate it using the stretched exponential function $F_s(q = 2\pi, t) = A \exp(-(t/\tau)^\beta)$ (blue lines) and obtain τ_α when the function has reached $1/e$. (b) The relaxation time τ_α as a function of packing fraction ϕ of our passive WCA polydisperse system. The filled circles are obtained from the completely relaxed systems. If the system has not yet equilibrated, the corresponding τ_α is shown by empty circles. The solid line is the VTF fit $\tau_\alpha = \tau_0 \exp[B\phi_0/(\phi_0 - \phi)]$, in which we only fit it with the equilibrated system (only solid circles). ϕ_0 is the divergence packing fraction.

Temperature dependence

We investigate the VTF relation for different temperature T^* as shown in Fig. 6.9. At the lowest temperature $T^* = 0.001$, we obtain only the initial rise of τ_α because the system at $\phi > 0.70$ has not equilibrated within the time window. As we increase T^* , the system relaxes faster as can be seen from the curves shifting towards lower τ_α . The higher T^* is, the more equilibrated points we obtain.

We fit the curve of each T^* with the VTF form and present the fitting parameters on the right panel. Note that we do not fit the lowest temperature because we have only a few points. It is worth noticing that the divergent point ϕ_0 remains unchanged for low T^* and it starts to increase from $T^* > 0.1$. Besides, this trend is the same for the fragility index B . We suggest that it is because WCA potential is a good approximation for the hard-sphere system only at low T^* . A larger deviation from the hard-sphere behavior could be expected as T^* is higher.

After investigating τ_α as a function of ϕ at different T^* , we decide to focus on only one temperature for the next step. This is because there will be two additional parameters when we introduce the self-propulsion, i.e., propulsion force f^* and rotational diffusion coefficient D_R^* . We thus need to scope our parameter space. For instance, we will only consider the system at $T^* = 0.01$.

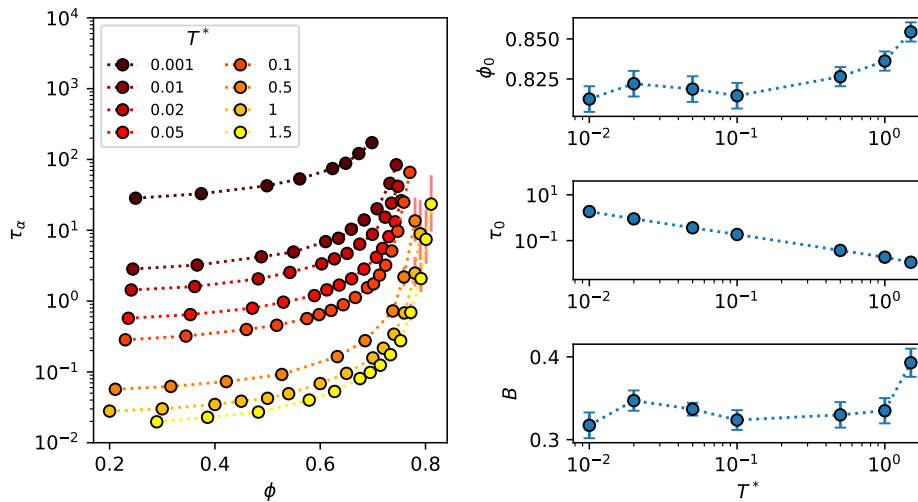


FIGURE 6.9: (Left panel) Temperature dependence of the relaxation time τ_α as a function of packing fraction ϕ . (Right panel) Fitting parameters from Eq. 6.23 at different temperature T^* : divergence of packing fraction ϕ_0 , relaxation time at $\phi \rightarrow 0$, τ_0 and fragility index B .

6.4.2 Active supercooled

We add the self-propulsion term by tuning the Péclet number $Pe = f^*/T^*$ from 0 (passive) to 200 (highly active). We show in Fig. 6.10 the influence of the activity on the relaxation at a density $\phi = 0.79$, at which the passive system has not equilibrated within our time window. Small activities ($Pe \in [1, 2]$) can help the relaxation as the estimated relaxation time gets smaller, but still not enough to equilibrate the system. With high enough activities, $Pe \geq 10$, the system has completely relaxed and it has entered the liquid phase. We can see that at such a high density, but still lower than $\phi_g^{\text{HS}} = 0.81 \pm 0.01$, the relaxation trend is monotonic with the activity levels.

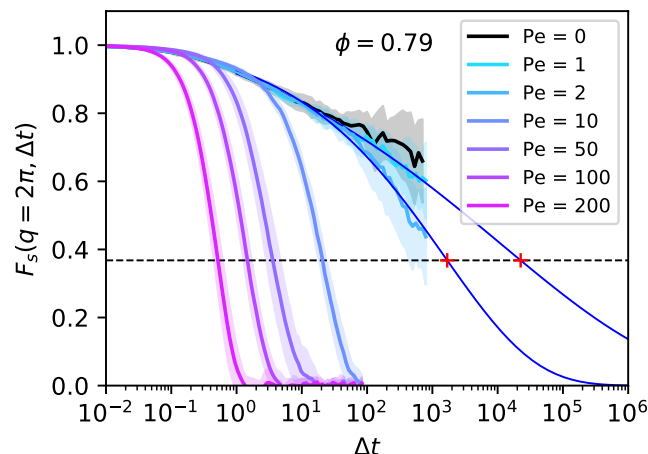


FIGURE 6.10: The self-intermediate scattering function $F_s(q = 2\pi, \Delta t)$ of $T^* = 0.01$ at $\phi = 0.79$. The activity level is varied from $Pe = 0$ to 200, in which $D_R^* = T^*$. The dark blue solid line is the extrapolation using the stretched exponential function. The relaxation time in this case is defined when the extrapolation has reached $1/e$ (red crosses).

How activity influences the glass transition?

We investigate how activity influences the glass transition by varying ϕ and measure the relaxation time τ_α for all activity levels. In Fig. 6.11, we present the VTF-like relation for self-propelled particles. Increasing Pe results in smaller τ_α as the whole curve shifts downward monotonically with Pe . Also, the divergence point ϕ_0 shifts towards higher ϕ . In the case of increasing T^* (Fig. 6.9), τ_0 got smaller by 3 orders of magnitude, while ϕ_0 increased by 0.04. By contrast, when increasing Pe , τ_0 decreases by 2 orders of magnitude, but ϕ_0 is significantly increased from 0.81 ($Pe = 0$) to more than 1.0 ($Pe = 200$). From this evidence, we can infer that ϕ_0 is more influenced by the self-propulsion force than by temperature.

Our plot in Fig. 6.11 reminds us the work from Ni et al. [157], in which they also investigate the glass transition of an ABP system but in 3D. Roughly speaking, we obtain the same conclusion: the self-propulsion pushes the glass transition towards higher ϕ . However, one significant difference in our result is the deviation from VTF form at moderate ϕ ($0.3 < \phi < 0.8$) and high Pe ($Pe \geq 10$). This deviation is not seen in Ni et al. [157] and it stands on our way to VTF fitting to obtain quantitatively ϕ_0 as a function of Pe . We, therefore, investigate this regime with a hypothesis of the Motility-Induced Phase Separation.

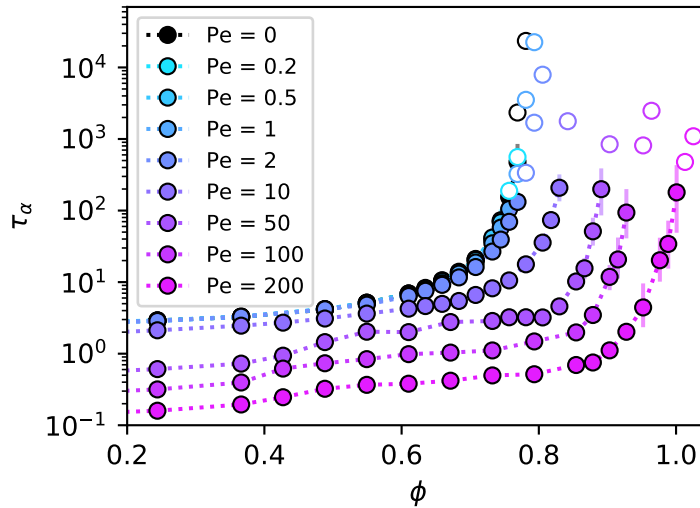


FIGURE 6.11: The relaxation time τ_α as a function of packing fraction ϕ of different activity levels Pe in the case of $D_R^* = T^*$. Completed equilibrate systems are shown by solid symbols. Empty symbols stand for nonequilibrated systems.

Motility-Induced Phase Separation

Motility-Induced Phase Separation or MIPS is a decrease of self-propulsion speed as the local density increases and the system displays a coexistence of dilute particles and dense aggregations [86]. MIPS is an emergent behavior in active systems even without alignment or attraction interaction. It has been investigated in 2D simulations and reported phase diagram show that MIPS occurs at high enough activity level [155, 156]. Besides, the critical density where the MIPS occurs is lower (and wider range) when the activity level is higher. When looking at the snapshots of our system at a fix density $\phi = 0.55$ and different activity levels (see Fig. 6.12a), the

phase separation is clearly seen at $Pe \geq 50$, while the passive system ($Pe = 0$) looks homogeneous. At $Pe = 10$, it is not obvious whether MIPS occurs or not.

Following Ref. [83], we probe MIPS by looking at the long-range correlation using static structure factor $S(q)$,

$$S(q) = \frac{1}{N} \left\langle \sum_{j=1}^N e^{-i\mathbf{q}\cdot\mathbf{r}_j} \sum_{k=1}^N e^{i\mathbf{q}\cdot\mathbf{r}_k} \right\rangle = \frac{1}{N} \left\langle \left(\sum_{j=1}^N \cos(\mathbf{q}\cdot\mathbf{r}_j) \right)^2 + \left(\sum_{j=1}^N \sin(\mathbf{q}\cdot\mathbf{r}_j) \right)^2 \right\rangle. \quad (6.24)$$

In Fig. 6.12b, we show $S(q)$ at a fix density $\phi = 0.55$ and different activity levels. For $Pe \geq 10$, $S(q)$ increases as q approaches zero indicating that there is a long-range correlation. By contrast for the passive case and $Pe \leq 2$, the curves remain flat at small q . We, therefore, infer that for $\phi = 0.55$, MIPS occurs at $Pe \geq 10$. In addition, the peak position of $S(q)$ shifts towards higher q as Pe increases indicating a shorter interparticle distance. This means that inside the dense liquid phase, the local density increases with activity levels.

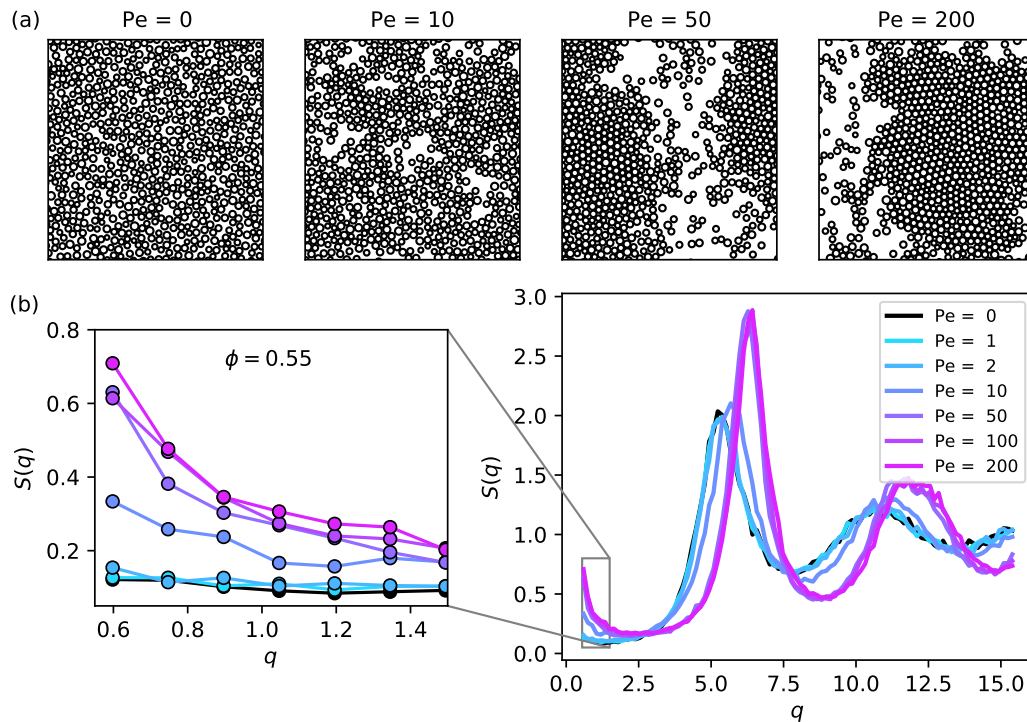


FIGURE 6.12: (a) Snapshots of the system at $\phi = 0.55$ and different Pe . (b) The static structure factor $S(q)$ calculated at $\phi = 0.55$ and different Pe . The rise of $S(q)$ at small q limit showing the long-range correlation, which is an indicator for MIPS. Such a long-range correlation starts to occur at $Pe \geq 10$.

To see the range of ϕ where MIPS occurs, we thus investigate the system at a fixed activity level. For instance, let us consider the system at $Pe = 200$. Fig. 6.13a shows snapshots from different ϕ showing an evolution of the system. Small clusters appear at $\phi = 20$ and then the phase separation at higher densities. The more ϕ increases, the more dense liquid phase dominates the domain. The system looks uniform at high enough density because the whole domain is occupied by the dense phase. $S(q)$ at small q also shows that the long-range correlation decreases with ϕ (see Fig. 6.13b) and disappears around $\phi \geq 0.85$.

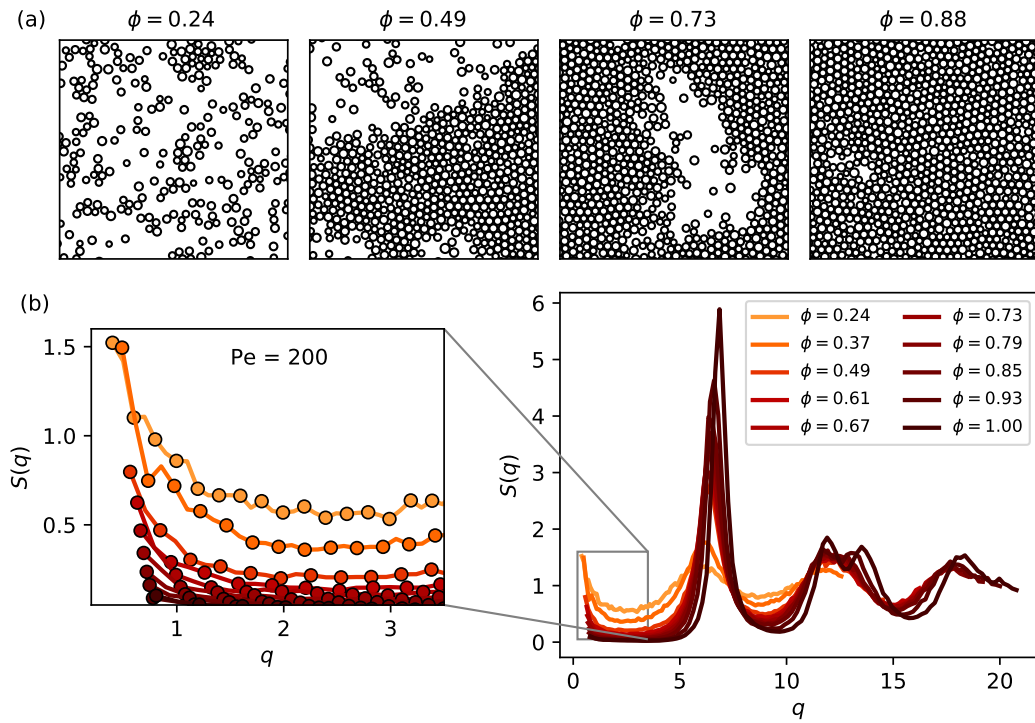


FIGURE 6.13: (a) Snapshots of the system at $Pe = 200$ and different ϕ . (b) The static structure factor $S(q)$ calculated at $Pe = 200$ and different ϕ . The long-range correlation can be probed at small q limit.

At this point, we know that MIPS occurs in our system at moderate density and high activity level. Therefore, the relaxation time obtained from $F_s(q, t)$ is not reliable when there is MIPS. This is because the system is in a coexistence state, and the relaxation time that we have obtained is an average between two groups of very fast (from the dilute gas phase) and very slow (from the dense liquid phase) particles. However, from this analysis, we can define a range of ϕ and Pe at which the relaxation time can be trusted. We, therefore, apply the VTF fit only for the reliable points.

VTF fitting

In Fig. 6.14, we show the VTF fits for different activity levels Pe . For $Pe < 10$, the VTF fits are made for the whole curve because no MIPS occurs in such low activities. At high activities $Pe \geq 10$, we exclude the MIPS region from the fit. We only trust the points in the supercooled regime (where τ_α is steeply rise) and the point in the very dilute limit $\phi = 0.01$, that we use to fix the parameter τ_0 . The fragility index B is difficult to obtain from the fit if there is MIPS. We thus use B of the passive case as a fixed parameter for $Pe \geq 10$ and this leaves ϕ_0 as the only fitting parameter. At low activities where no MIPS occur, we fit each curve with B and ϕ_0 as free parameters.

We also compare between two cases of $D_R = T^*$ (circles) and $D_R = 3T^*$ (triangles) and find no significant difference except in the MIPS region at $Pe = 50$. The $D_R = T^*$ case has larger relaxation time than the $D_R = 3T^*$ case. We suggest that this activity level is near the critical value where MIPS appears (please refer to Fig. 1.16). Changing rotational diffusion should affect the transition. This is a hint that increasing D_R may shift the MIPS transition line to higher Pe . We therefore see less influence

from the MIPS. The reason why we do not find such an obvious difference in other activity levels is because they are far away from the critical Pe . Anyway, in all activity levels, the two values of D_R^* induce little difference in the very dilute limit and the supercooled regime. Compared to Ni et al. [157] reporting that decreasing D_R results in an increment of ϕ_0 , in our case, we change D_R^* by only a factor of 3 while they varied D_R by a factor of 10. This could be a reason why we do not see clearly the dependence on the rotational diffusion.

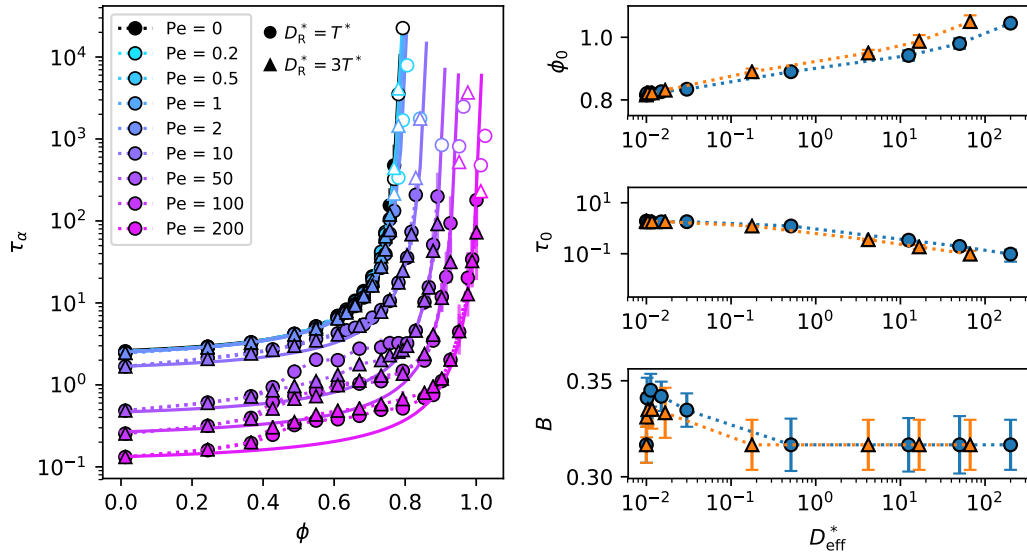


FIGURE 6.14: (Left panel) Relaxation time τ_α as a function of packing fraction ϕ at $T^* = 0.01$ and different activity levels Pe . The circles and triangles represent the cases $D_R^* = T^*$ and $D_R^* = 3T^*$, respectively. The filled symbols stand for the equilibrated systems and the empty symbols are for the non-equilibrated ones. The solid lines display the VTF fitting in which the MIPS region is excluded. (Right panel) Fitting parameters from Eq. 6.23 for different $D_{\text{eff}}^* = T^* + f^*/2D_R^*$.

The fitting parameters are shown on the right panel of Fig. 6.14. We display the fitting parameters as a function of dimensionless effective diffusion coefficient $D_{\text{eff}}^* = T^* + f^*/2D_R^*$ instead of Pe . It shows that ϕ_0 increases with D_{eff}^* , while τ_0 decreases. Both ϕ_0 and τ_0 have a monotonic trend with activity levels. What is worth noticing is the fragility index B . In the passive case, the fragility index is $B = 0.31 \pm 0.01$. At low activity levels ($D_{\text{eff}}^* \sim 0.01$, $Pe < 2$), B increases to 0.33 ± 0.01 . This could be a hint of the DEAD behavior in the supercooled regime that could not be observed in the experiment. Nevertheless, since the difference is very small $\Delta B = 0.02$ and within the error bars, we still need to carefully verify this point. We shall come back to this point after we investigate the dynamics above the glass transition, where the DEAD is obviously noticed in the experiment.

In the same spirit as the Fig. 4.14b, we scaled the relaxation time τ_α with τ_0 and the packing fraction ϕ with ϕ_0 . In Fig. 6.15, we show that all the curves collapse well onto one master curve, except for the MIPS region. At this point, we managed to reproduce our experimental systems from the very dilute limit to the ergodic supercooled regime. The simulation results support the mapping between the passive and active systems using $\tau_0(Pe)$ and $\phi_0(Pe)$ (except for the point of the fragility index at low activities that still needs to be verified).

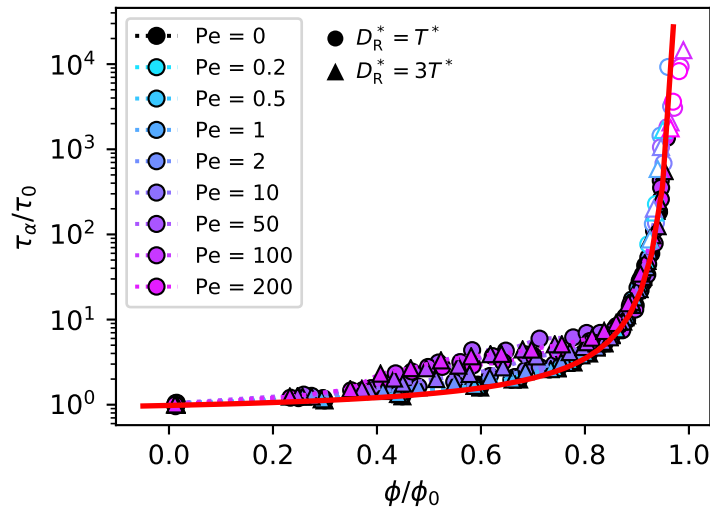


FIGURE 6.15: Scaled relaxation time τ_α/τ_0 as a function of scaled packing fraction ϕ/ϕ_0 of different activity levels Pe . The red line shows the collapse of the VTF relation (Eq. 6.23) except at the MIPS region.

6.5 Beyond the glass transition

Our next task is to investigate the relaxation dynamics in the glassy regime, where the passive system is nonergodic. This task is not straightforward because the system is stuck in one configuration and does not relax within our simulation time window. When thinking about our experiment, why were we able to obtain the relaxation time beyond the glass transition? And why was the relaxation time saturated at high packing fraction? One possibility is due to the softness of our particles (from the electrostatics repulsion) [150]. The other possibility is from the density gradient in our experimental setup. We varied the packing fraction by focusing on different slices in the sediment along the density gradient. Of course, these slices are not independent of each other. Particles in one slice can move to a less dense or a denser slice. This is why the system can relax even if the packing fraction is above the glass transition value. In other words, we can say that our dense system is aging.

To investigate the dynamics of the aging system in a simulation, we plan to quench the system and start the sampling after a given waiting time t_w . The simulation diagram is shown in Fig. 6.16. We first prepare the system in a liquid phase ϕ_{ini} . Like before, we randomize particle positions and use the Harmonic sphere potential to avoid the overlap. Then, we switch the potential to WCA and let the simulation run to equilibrate the system. The running time is about 10 times the relaxation time at ϕ_{ini} . This is to make sure that the system has already equilibrated. Then, we quench the system to a desired packing fraction ϕ_{final} by shrinking the simulation domain. To avoid particle overlap resulting from the periodic boundary condition, we also scale the particle coordinate with $L_{\text{final}}/L_{\text{ini}}$ (dilation transformation). After the quenching, we start the sampling after a waiting time t_w has passed. We repeat the simulation from the beginning 10 times with different random seeds for an ensemble average. We stress that the average is taken among totally independent sampling.

We show in Fig. 6.17 our first result from the quenching simulation in the passive system. With this procedure, we can continue investigating the system relaxation at

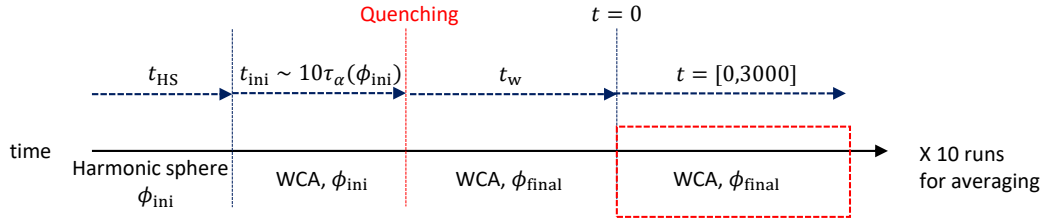


FIGURE 6.16: A simulation diagram to investigate the aging dynamics by quenching. The system is prepared at a packing fraction in a liquid phase ϕ_{ini} by using harmonic sphere potential to separate particles and then following by WCA potential to equilibrate the system. The time to equilibrate the system t_{ini} is set to be 10 times the relaxation time at ϕ_{ini} . Then, we quench the system by shrinking the simulation domain to a desired packing fraction ϕ_{final} and scale the particle coordinates by L_{final}/L_{ini} . After a waiting time t_w measured from the quenching, we start the sampling over a certain time window. We repeat this process 10 times with different random seeds to perform an ensemble average.

higher densities (even higher than ϕ_0 , where we are mostly interested in). We can notice the waiting time dependence of the relaxation time in Fig. 6.17a. The shorter the waiting time, the more deviation from the VTF relation. The initial packing fraction ϕ_{ini} affects the aging exponent δ , which is defined from $\tau_{\alpha} \sim t_w^{\delta}$, and the final packing fraction ϕ_{final} . The lower ϕ_{ini} results in a higher aging exponent and a lower upper bound of ϕ_{final} that we can obtain from the simulation. For the moment we choose $\phi_{ini} = 0.73$, which gives the aging exponent $\delta \in [0.14, 0.32]$ for $\phi_{final} \in [0.76, 0.78]$. The reason we choose such a relatively high ϕ_{ini} is because we aim to investigate the final system when it exits the liquid phase, which means that $\tau_{\alpha} < 10^2$. Nevertheless, the choice of a proper value of ϕ_{ini} is still an open question to be further investigated.

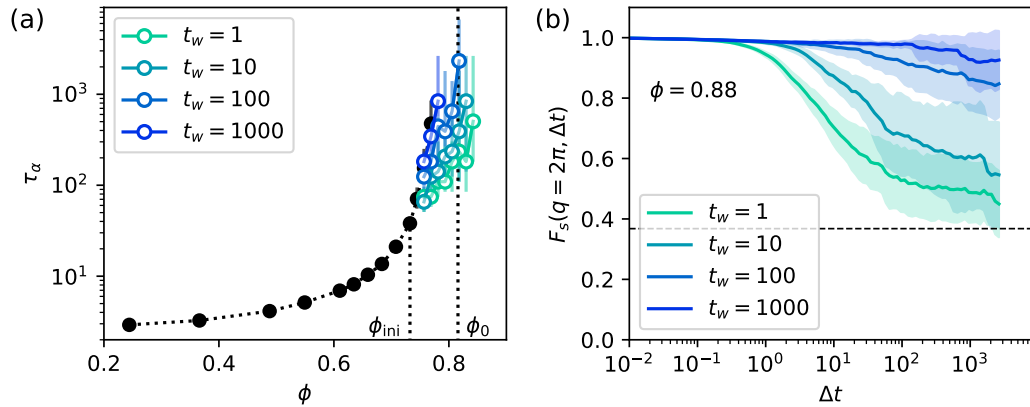


FIGURE 6.17: Results from the quenching simulation in the passive system ($Pe = 0$) at $T^* = 0.01$. (a) Relaxation time τ_{α} as a function of packing fraction ϕ . The results from the equilibrated systems (using time average) are shown by the filled circles. The open circles represent the relaxation time obtained from the ensemble average of the quenching simulation at different waiting time t_w . The initial packing fraction before the quenching is $\phi_{ini} = 0.73$. (b) The self-intermediate scattering function $F_s(q = 2\pi, \Delta t)$ at the final packing fraction $\phi = 0.88$ and different waiting time t_w after the quenching.

In Fig. 6.17a, we show τ_α only for the relaxed systems, i.e., $F_s(q, t)$ has decreased to $1/e$ within the simulation time window. However, we can still investigate the system relaxation at higher densities from $F_s(q, t)$ as shown in Fig. 6.17b. Depending on the waiting time t_w , the relaxation trend is clearly different: the exit from the initial plateau occurs earlier with lower t_w . The shape of $F_s(q, t)$ should be sufficient to capture the DEAD phenomenon that we are looking for. Therefore, our next task is to introduce the self-propulsion term and then compare $F_s(q, t)$ among different Pe , but with the same t_w . In a further step, when we would like to quantify the relaxation time, there would be other possible ways to define τ_α when it is too long to be measured as proposed in Refs. [253, 254].

In summary, we started exploring a system of active Brownian particles with numerical simulation. We explored the system in different density regimes. In a dilute regime, we could reproduce a persistent random motion and the relation of simulation parameters is in agreement with what we observed in our experiment. As we increased the density, the simulation exhibits MIPS at moderate density and high activity level, and this is not observed in our experimental system. Apart from the MIPS, in an ergodic supercooled regime, our simulation shows the VTF relation, in which the divergence shifts towards higher packing fraction when activity increases. By scaling with the relaxation time obtained from the dilute regime and the divergence, our simulation confirms the mapping from the passive to active system via the VTF relation, in which we have shown from our experimental investigation. We are now extending our simulation towards a nonergodic glass regime, where the experimental system displays the non-trivial DEAD phenomenon.

[At this moment, the work of in the last part is still in progress. The story of this part will be fulfilled after my JSPS fellowship ends in September 2020.]

Key points of the chapter:

1. We constructed a simulation model for Active Brownian Particles (ABP) with WCA interaction and developed our own C++ scripts for the simulation and analysis. We used our simulation to investigate the dynamics of the ABP system in a very dilute limit (without particle interaction). The resulting mean square displacement agrees with the previous work and analytic expression.
2. We explored the supercooled region by characterizing the relaxation time as a function of packing fraction in the passive supercooled system:
 - (a) At a fixed dimensionless temperature $T^* = 0.01$, we obtained the divergence of the VTF fit $\phi_0 = 0.81$, which agrees with the 2D hard sphere system.
 - (b) We varied T^* to investigate the temperature dependence on the relaxation and decided to first focus at $T^* = 0.01$ to continue the simulation for self-propelled particles
3. We added the activity in the supercooled simulation:
 - (a) The activity enhances the relaxation at constant packing fraction.
 - (b) The packing fraction dependence of the relaxation shows the deviation from the VTF form at moderate packing fraction and high activity levels. We thus investigated this regime and found Motility Induced Phase Separation (MIPS).
 - (c) We fitted our result with the VTF form discarding MIPS range. The fitting shows that ϕ_0 increases monotonically with activity levels. We showed the collapse of the VTF form from different activity levels when scaling the packing fraction with ϕ_0 and the relaxation time with $\tau(\phi \rightarrow 0)$.
4. At this moment, we are investigating the glassy regime where $\phi > \phi_0$. We quench the system to study its aging dynamics. The work in this part will be fulfilled when the fellowship ends.

Chapter 7

Conclusions and perspectives

During my PhD, we have tried to answer the question of "How activity influences relaxation dynamics and microrheology of a crowded system?" from the experimental approach. To tackle the question, the first task for me was to make a system of active colloids at high densities. To do so, I improved the procedure of making the colloids until we obtained a high-quality experimental sample. The next task was to design and perform experiments on the system to study, both spontaneous dynamics and microrheology. For the analysis part, I customized particle tracking algorithms and developed analysis tools specific to our dense system, which can be considered as big data.

Now, we manage to answer the first half of the question from our experiments on the self-propelled colloids. In brief, if the system packing fraction is lower than the glass transition value, the system dynamics is enhanced with increased activity level. The mapping from the passive to the active supercooled liquid can be done through activity-dependent effective temperature. However, such a mapping fails if the system is in a non-ergodic state (either glass or polycrystal). Beyond the glass transition, we have found that the system dynamics is non-monotonic with the activity level, i.e., more arrested and then more dynamical. The first regime is non-trivial and it is the most interesting behavior. We tried to investigate the relaxation mechanisms in this regime. We found that while the relaxation is dominated by collective motion at high activity levels, the relaxation is rather cooperative at low activity levels. Besides, the cooperative relaxation at such a low activity is less efficient than that of the passive system, and this is why the dynamics is more arrested. We come up with a model suggesting that the self-propulsion causes inefficient cage exploration for a weakly active particle, while a purely passive particle explores the cage via Brownian translational diffusion, which is more effective than the directed motion with rotational diffusion.

It would be interesting to carry on the analysis using a framework of glassy physics such as four-point correlation to characterize dynamic heterogeneity. However, we could not do this because our experiments always have a density gradient, which is good for the density variation but not for long-range correlation. To have a homogeneous dense system in the experiment, we would need a (very precisely) horizontal flat surface and a new way to confine the colloids. Some possible options would be a smaller experimental chamber, a chamber with a well-defined boundary, or a microfluidic chamber. We actually tried some of them, but the colloids did not move nicely on the bottom surface. Finding the right surface chemistry to reliably enable the movement of our particles, would definitely open up the possibilities of this experimental system.

Another experimental perspective that I could suggest is to use a binary-size system to avoid crystallization. For now, we are limited by the availability of micron-size gold particles, which are the base to make the Janus colloids. During my PhD,

we have tried using an alternative type of particles. We used latex particles covered by gold nanoparticles and then half-coated by platinum. The particles exhibited persistent random motion, just like our usual particles but with much longer persistence time. I see that this could be a new prospect to overcome the size limitation. With the latex particle as a base, it is much easier to change the size or even shape of active colloids. This could also lead to another kind of active systems such as active nematic.

A crucial ingredient to probe our cage exploration scenario is the particle orientation in the dense phase. Investigating time correlation of the orientation and its relation with the particle displacement with respect to the cage, would be an effective tool to look into cage exploration mechanisms. Unfortunately, this cannot be obtained easily from our current imaging method. In principle, it could be possible to distinguish the platinum side from the gold side of the colloids by using a color camera with a proper filter. However, one difficulty is that we always observe a 2D projection while particle reorientation is in 3D. Therefore, we also need the right image analysis tool that can detect the 3D orientation from the alternating appearance of the platinum side and the gold side, or their combination.

All the above three perspectives are yet possible, however, it is not straightforward to achieve them in experiments. The other way around is the simulation approach, in which most of the experimental limitations are gone and the particle orientation is known precisely. In the last period of my PhD, I have started the numerical investigation of a system of active Brownian particles. Until now, I can reproduce most of my experimental results up to the glass transition density *in silico*. Indeed, the simulation in the glassy phase should provide a better understanding of active glass, especially the non-monotonic behavior. Besides, we can freely adjust any simulation parameter to probe its influence on the system. For example, we could change the rotational diffusion time which is always coupled with the Brownian diffusion in experiments. From this point, we can explore the parameter space to find the minimal ingredients of the non-monotonic behavior and it could be a starting point for a theoretical approach.

On the second half of the question of my PhD, the microrheology, we are still on the way towards the answer. The results from our first investigation using optical tweezers show a hint that activity causes higher stiffness in the sediment. However, it is still not conclusive because of the unexpected interaction between the probe and the colloids. At least, we know that optical tweezers may not be the right tool for this system. We thus tried a new investigation using a falling probe inside the sediment. It revealed a significant difference in the velocity profile between the passive and active sediments. We found that the origin of the difference is the flux of colloids above the probe, i.e., the passive colloids result in more pushing flux compared to the active colloids. We carried on the analysis to investigate the relative motion of particles around the probe. As a result, we got a piece of evidence that the flow of the colloids around the probe follows a Stokes flow. This leads to a new possibility to extract an effective viscosity of the sediment. However, understanding the pressure of the active particles on the probe will require a significant modelling effort.

Even though the question cannot be clarified for now, our work has contributed some steps towards the goal. From the limitations we had during our experiments, we started to develop a magnetic microrheology setup for a better-controlled experiment in our future work.

In the bigger picture, I see that there are more and more experimental investigations on active dense systems in the past few years. Most of them focus on high activity levels where the self-propulsion is dominating. What is often overlooked is

the low activity regime, near the transition from passive to active systems. From a thermodynamic point of view, I think it would be interesting to investigate such a transition as well. Another perspective is to make a dense active system of abiotic microswimmers in a non-Newtonian medium. I think this would be a good model for biological active matter such as cells and tissues that live in complex intracellular fluid, and it could lead to a healthcare benefit in the long term.

Despite my research interest was starting from active matter, this PhD has opened up my knowledge and has introduced me to another field of non-equilibrium physics, which is glassy physics. I learned a lot in science and also analysis tools that involve condensed computational skills. Apart from that, doing experiments was also a new challenge for me as I had mostly a computational background from the beginning. Looking back from today, if I can evaluate myself, I have made huge progress so far. However, along the way, I have also realized a lot of things that I do not know. Even if my PhD has come to a finishing line, I believe that it is actually a starting point of my new progress.

Bibliography

- [1] Andrea Cavagna et al. “Flocking and Turning: a New Model for Self-organized Collective Motion”. In: *Journal of Statistical Physics* 158.3 (2015), pp. 601–627. ISSN: 1572-9613. DOI: [10.1007/s10955-014-1119-3](https://doi.org/10.1007/s10955-014-1119-3). URL: <https://doi.org/10.1007/s10955-014-1119-3>.
- [2] Tamás Vicsek et al. “Novel Type of Phase Transition in a System of Self-Driven Particles”. In: *Phys. Rev. Lett.* 75 (6 1995), pp. 1226–1229. DOI: [10.1103/PhysRevLett.75.1226](https://link.aps.org/doi/10.1103/PhysRevLett.75.1226). URL: <https://link.aps.org/doi/10.1103/PhysRevLett.75.1226>.
- [3] Natsuda Klongvessa. “Information transfer in a flock of birds: the inertial spin model with a blind area for an individual”. MA thesis. Mahidol University, 2016.
- [4] Andrea Cavagna et al. “The STARFLAG handbook on collective animal behaviour: 1. Empirical methods”. In: *Animal Behaviour* 76 (2008). Article, pp. 217–236. DOI: [10.1016/j.anbehav.2008.02.002](https://doi.org/10.1016/j.anbehav.2008.02.002).
- [5] A. Cavagna et al. “The STARFLAG handbook on collective animal behaviour: 2. Three-dimensional analysis”. In: *Animal Behaviour* 76.1 (2008), 237–248. URL: http://www.sciencedirect.com/science?_ob=ArticleURL&_udi=B6W9W-4SFHK8V-4&_user=10&_rdoc=1&_fmt=&_orig=search&_sort=d&_docanchor=&view=c&_searchStrId=1167726245&_rerunOrigin=scholar.google&_acct=C000050221&_version=1&_urlVersion=0&_userid=10&md5=68fcf040af.
- [6] Alessandro Attanasi et al. “Information transfer and behavioural inertia in starling flocks”. In: *Nature Physics* 10 (2014). Article, 691 EP –. URL: <https://doi.org/10.1038/nphys3035>.
- [7] Jérémie Palacci et al. “Sedimentation and Effective Temperature of Active Colloidal Suspensions”. In: *Phys. Rev. Lett.* 105 (8 2010), p. 088304. DOI: [10.1103/PhysRevLett.105.088304](https://link.aps.org/doi/10.1103/PhysRevLett.105.088304). URL: <https://link.aps.org/doi/10.1103/PhysRevLett.105.088304>.
- [8] Félix Ginot et al. “Nonequilibrium Equation of State in Suspensions of Active Colloids”. In: *Phys. Rev. X* 5 (1 2015), p. 011004. DOI: [10.1103/PhysRevX.5.011004](https://link.aps.org/doi/10.1103/PhysRevX.5.011004). URL: <https://link.aps.org/doi/10.1103/PhysRevX.5.011004>.
- [9] Felix Ginot et al. “Sedimentation of self-propelled Janus colloids: polarization and pressure”. In: *New Journal of Physics* 20.11 (2018), p. 115001. DOI: [10.1088/1367-2630/aae732](https://doi.org/10.1088/1367-2630/aae732). URL: <https://doi.org/10.1088/1367-2630/aae732>.
- [10] I. Theurkauff et al. “Dynamic Clustering in Active Colloidal Suspensions with Chemical Signaling”. In: *Phys. Rev. Lett.* 108 (26 2012), p. 268303. DOI: [10.1103/PhysRevLett.108.268303](https://link.aps.org/doi/10.1103/PhysRevLett.108.268303). URL: <https://link.aps.org/doi/10.1103/PhysRevLett.108.268303>.

- [11] F. Ginot et al. "Aggregation-fragmentation and individual dynamics of active clusters". In: *Nature Communications* (2018). ISSN: 2041-1723. DOI: [10.1038/s41467-017-02625-7](https://doi.org/10.1038/s41467-017-02625-7).
- [12] Sriram Ramaswamy. "The Mechanics and Statistics of Active Matter". In: *Annual Review of Condensed Matter Physics* 1.1 (2010), pp. 323–345. DOI: [10.1146/annurev-conmatphys-070909-104101](https://doi.org/10.1146/annurev-conmatphys-070909-104101). eprint: <https://doi.org/10.1146/annurev-conmatphys-070909-104101>. URL: <https://doi.org/10.1146/annurev-conmatphys-070909-104101>.
- [13] Tamás Vicsek and Anna Zafeiris. "Collective motion". en. In: *Physics Reports* 517.3-4 (Aug. 2012), pp. 71–140. ISSN: 03701573. DOI: [10.1016/j.physrep.2012.03.004](https://doi.org/10.1016/j.physrep.2012.03.004). URL: <https://linkinghub.elsevier.com/retrieve/pii/S0370157312000968>.
- [14] M. C. Marchetti et al. "Hydrodynamics of soft active matter". In: *Reviews of Modern Physics* 85.3 (2013), pp. 1143–1189. DOI: [10.1103/revmodphys.85.1143](https://doi.org/10.1103/revmodphys.85.1143). URL: <https://doi.org/10.1103/revmodphys.85.1143>.
- [15] Jasper van der Gucht. "Grand Challenges in Soft Matter Physics". In: *Frontiers in Physics* 6 (2018), p. 87. ISSN: 2296-424X. DOI: [10.3389/fphy.2018.00087](https://doi.org/10.3389/fphy.2018.00087). URL: <https://www.frontiersin.org/article/10.3389/fphy.2018.00087>.
- [16] Daniel Needleman and Zvonimir Dogic. "Active matter at the interface between materials science and cell biology". In: *Nature Reviews Materials* 2.9 (2017), p. 17048. ISSN: 2058-8437. DOI: [10.1038/natrevmats.2017.48](https://doi.org/10.1038/natrevmats.2017.48). URL: <https://doi.org/10.1038/natrevmats.2017.48>.
- [17] D A Harris. "The vital force — A study of bioenergetics by Franklin M Harold. pp 577, WH Freeman, New York. 1986. £19.95: ISBN 0-7167-1734-4". In: *Biochemical Education* 15.2 (1987), pp. 94–94. DOI: [10.1016/0307-4412\(87\)90102-6](https://doi.org/10.1016/0307-4412(87)90102-6). eprint: <https://onlinelibrary.wiley.com/doi/pdf/10.1016/0307-4412%2887%2990102-6>. URL: <https://onlinelibrary.wiley.com/doi/abs/10.1016/0307-4412%2887%2990102-6>.
- [18] Zsuzsanna Környei et al. "Proliferative and migratory responses of astrocytes to in vitro injury". In: *Journal of Neuroscience Research* 61.4 (2000), pp. 421–429. DOI: [10.1002/1097-4547\(20000815\)61:4<421::AID-JNR8>3.0.CO;2-4](https://doi.org/10.1002/1097-4547(20000815)61:4<421::AID-JNR8>3.0.CO;2-4). eprint: <https://onlinelibrary.wiley.com/doi/pdf/10.1002/1097-4547%2820000815%2961%3A4%3C421%3A%3AAID-JNR8%3E3.0.CO%3B2-4>. URL: <https://onlinelibrary.wiley.com/doi/abs/10.1002/1097-4547%2820000815%2961%3A4%3C421%3A%3AAID-JNR8%3E3.0.CO%3B2-4>.
- [19] Antonio Jacinto, Alfonso Martinez-Arias, and Paul Martin. "Mechanisms of epithelial fusion and repair". In: *Nature Cell Biology* 3.5 (2001), E117–E123. ISSN: 1476-4679. DOI: [10.1038/35074643](https://doi.org/10.1038/35074643). URL: <https://doi.org/10.1038/35074643>.
- [20] Roberto Mayor and Sandrine Etienne-Manneville. "The front and rear of collective cell migration". In: *Nature Reviews Molecular Cell Biology* 17 (2016). Review Article, 97 EP –. URL: <https://doi.org/10.1038/nrm.2015.14>.
- [21] Pernille Rørth. "Collective guidance of collective cell migration". English. In: *Trends in Cell Biology* 17.12 (Dec. 2007), pp. 575–579. ISSN: 0962-8924, 1879-3088. DOI: [10.1016/j.tcb.2007.09.007](https://doi.org/10.1016/j.tcb.2007.09.007). URL: [https://www.cell.com/trends/cell-biology/abstract/S0962-8924\(07\)00246-2](https://www.cell.com/trends/cell-biology/abstract/S0962-8924(07)00246-2).

- [22] Thomas S. Deisboeck and Iain D. Couzin. “Collective behavior in cancer cell populations”. In: *BioEssays* 31.2 (2009), pp. 190–197. DOI: [10.1002/bies.200800084](https://doi.org/10.1002/bies.200800084). eprint: <https://onlinelibrary.wiley.com/doi/pdf/10.1002/bies.200800084>. URL: <https://onlinelibrary.wiley.com/doi/abs/10.1002/bies.200800084>.
- [23] David Gonzalez-Rodriguez et al. “Soft Matter Models of Developing Tissues and Tumors”. In: *Science* 338.6109 (2012), pp. 910–917. ISSN: 0036-8075. DOI: [10.1126/science.1226418](https://doi.org/10.1126/science.1226418). eprint: <https://science.sciencemag.org/content/338/6109/910.full.pdf>. URL: <https://science.sciencemag.org/content/338/6109/910>.
- [24] Jessica L. Ouderkirk and Mira Krendel. “Non-muscle myosins in tumor progression, cancer cell invasion, and metastasis”. In: *Cytoskeleton* 71.8 (2014), pp. 447–463. DOI: [10.1002/cm.21187](https://doi.org/10.1002/cm.21187). eprint: <https://onlinelibrary.wiley.com/doi/pdf/10.1002/cm.21187>. URL: <https://onlinelibrary.wiley.com/doi/abs/10.1002/cm.21187>.
- [25] Carlos Pérez-González et al. “Active wetting of epithelial tissues”. In: *Nature Physics* 15.1 (2019), pp. 79–88. ISSN: 1745-2481. DOI: [10.1038/s41567-018-0279-5](https://doi.org/10.1038/s41567-018-0279-5). URL: <https://doi.org/10.1038/s41567-018-0279-5>.
- [26] Lu Chen et al. “Engineering controllable bidirectional molecular motors based on myosin”. In: *Nature nanotechnology* 7.4 (2012). 22343382[pmid], pp. 252–256. ISSN: 1748-3395. DOI: [10.1038/nnano.2012.19](https://doi.org/10.1038/nnano.2012.19). URL: <https://www.ncbi.nlm.nih.gov/pubmed/22343382>.
- [27] Muneaki Nakamura et al. “Remote control of myosin and kinesin motors using light-activated gearshifting”. In: *Nature nanotechnology* 9.9 (2014). 25086603[pmid], pp. 693–697. ISSN: 1748-3395. DOI: [10.1038/nnano.2014.147](https://doi.org/10.1038/nnano.2014.147). URL: <https://www.ncbi.nlm.nih.gov/pubmed/25086603>.
- [28] Tony D. Schindler et al. “Engineering myosins for long-range transport on actin filaments”. In: *Nature nanotechnology* 9.1 (2014), pp. 33–38. ISSN: 1748-3395. DOI: [10.1038/nnano.2013.229](https://doi.org/10.1038/nnano.2013.229). URL: <https://www.ncbi.nlm.nih.gov/pubmed/24240432>.
- [29] Jesse L. Silverberg et al. “Collective Motion of Humans in Mosh and Circle Pits at Heavy Metal Concerts”. In: *Phys. Rev. Lett.* 110 (22 2013), p. 228701. DOI: [10.1103/PhysRevLett.110.228701](https://doi.org/10.1103/PhysRevLett.110.228701). URL: <https://link.aps.org/doi/10.1103/PhysRevLett.110.228701>.
- [30] H. P. Zhang et al. “Collective motion and density fluctuations in bacterial colonies”. In: *Proceedings of the National Academy of Sciences* 107.31 (2010), pp. 13626–13630. ISSN: 0027-8424. DOI: [10.1073/pnas.1001651107](https://doi.org/10.1073/pnas.1001651107). eprint: <https://www.pnas.org/content/107/31/13626.full.pdf>. URL: <https://www.pnas.org/content/107/31/13626>.
- [31] Thomas E. Angelini et al. “Glass-like dynamics of collective cell migration”. In: *Proceedings of the National Academy of Sciences* 108.12 (2011), pp. 4714–4719. ISSN: 0027-8424. DOI: [10.1073/pnas.1010059108](https://doi.org/10.1073/pnas.1010059108). eprint: <https://www.pnas.org/content/108/12/4714.full.pdf>. URL: <https://www.pnas.org/content/108/12/4714>.
- [32] R. Di Leonardo et al. “Bacterial ratchet motors”. In: *Proceedings of the National Academy of Sciences* 107.21 (2010), pp. 9541–9545. ISSN: 0027-8424. DOI: [10.1073/pnas.0910426107](https://doi.org/10.1073/pnas.0910426107). eprint: <https://www.pnas.org/content/107/21/9541.full.pdf>. URL: <https://www.pnas.org/content/107/21/9541>.

- [33] Gaszton Vizsnyiczai et al. "Light controlled 3D micromotors powered by bacteria". In: *Nature Communications* 8.1 (2017), p. 15974. ISSN: 2041-1723. DOI: [10.1038/ncomms15974](https://doi.org/10.1038/ncomms15974). URL: <https://doi.org/10.1038/ncomms15974>.
- [34] Claudio Maggi et al. "Self-Assembly of Micromachining Systems Powered by Janus Micromotors". In: *Small* 12.4 (2016), pp. 446–451. DOI: [10.1002/smll.201502391](https://doi.org/10.1002/smll.201502391). eprint: <https://onlinelibrary.wiley.com/doi/pdf/10.1002/smll.201502391>. URL: <https://onlinelibrary.wiley.com/doi/abs/10.1002/smll.201502391>.
- [35] Antoine Aubret et al. "Targeted assembly and synchronization of self-spinning microgears". In: *Nature Physics* 14.11 (2018), pp. 1114–1118. ISSN: 1745-2481. DOI: [10.1038/s41567-018-0227-4](https://doi.org/10.1038/s41567-018-0227-4). URL: <https://doi.org/10.1038/s41567-018-0227-4>.
- [36] Wayne K. Potts. "The chorus-line hypothesis of manoeuvre coordination in avian flocks". In: *Nature* 309.5966 (1984), pp. 344–345. ISSN: 1476-4687. DOI: [10.1038/309344a0](https://doi.org/10.1038/309344a0). URL: <https://doi.org/10.1038/309344a0>.
- [37] M. Ballerini et al. "Interaction ruling animal collective behavior depends on topological rather than metric distance: Evidence from a field study". In: *Proceedings of the National Academy of Sciences* 105.4 (2008), pp. 1232–1237. ISSN: 0027-8424. DOI: [10.1073/pnas.0711437105](https://doi.org/10.1073/pnas.0711437105). eprint: <https://www.pnas.org/content/105/4/1232.full.pdf>. URL: <https://www.pnas.org/content/105/4/1232>.
- [38] Andrea Cavagna et al. "Scale-free correlations in starling flocks". In: *Proceedings of the National Academy of Sciences* 107.26 (2010), pp. 11865–11870. ISSN: 0027-8424. DOI: [10.1073/pnas.1005766107](https://doi.org/10.1073/pnas.1005766107). eprint: <https://www.pnas.org/content/107/26/11865.full.pdf>. URL: <https://www.pnas.org/content/107/26/11865>.
- [39] Nicholas C. Makris et al. "Critical Population Density Triggers Rapid Formation of Vast Oceanic Fish Shoals". In: *Science* 323.5922 (2009), pp. 1734–1737. ISSN: 0036-8075. DOI: [10.1126/science.1169441](https://doi.org/10.1126/science.1169441). eprint: <https://science.sciencemag.org/content/323/5922/1734.full.pdf>. URL: <https://science.sciencemag.org/content/323/5922/1734>.
- [40] Ch. Becco et al. "Experimental evidences of a structural and dynamical transition in fish school". In: *Physica A: Statistical Mechanics and its Applications* 367 (2006), pp. 487–493. ISSN: 0378-4371. DOI: <https://doi.org/10.1016/j.physa.2005.11.041>. URL: <http://www.sciencedirect.com/science/article/pii/S0378437105012689>.
- [41] J. Buhl et al. "From Disorder to Order in Marching Locusts". In: *Science* 312.5778 (2006), pp. 1402–1406. ISSN: 0036-8075. DOI: [10.1126/science.1125142](https://doi.org/10.1126/science.1125142). eprint: <https://science.sciencemag.org/content/312/5778/1402.full.pdf>. URL: <https://science.sciencemag.org/content/312/5778/1402>.
- [42] Alessandro Attanasi et al. "Collective Behaviour without Collective Order in Wild Swarms of Midges". In: *PLOS Computational Biology* 10.7 (July 2014), pp. 1–10. DOI: [10.1371/journal.pcbi.1003697](https://doi.org/10.1371/journal.pcbi.1003697). URL: <https://doi.org/10.1371/journal.pcbi.1003697>.

- [43] Yael Katz et al. "Inferring the structure and dynamics of interactions in schooling fish". In: *Proceedings of the National Academy of Sciences* 108.46 (2011), pp. 18720–18725. ISSN: 0027-8424. DOI: [10.1073/pnas.1107583108](https://doi.org/10.1073/pnas.1107583108). eprint: <https://www.pnas.org/content/108/46/18720.full.pdf>. URL: <https://www.pnas.org/content/108/46/18720>.
- [44] Iain D Couzin and Jens Krause. "Self-Organization and Collective Behavior in Vertebrates". In: vol. 32. *Advances in the Study of Behavior*. Academic Press, 2003, pp. 1–75. DOI: [https://doi.org/10.1016/S0065-3454\(03\)01001-5](https://doi.org/10.1016/S0065-3454(03)01001-5). URL: <http://www.sciencedirect.com/science/article/pii/S0065345403010015>.
- [45] A. Garcimartín et al. "Flow and clogging of a sheep herd passing through a bottleneck". In: *Phys. Rev. E* 91 (2 2015), p. 022808. DOI: [10.1103/PhysRevE.91.022808](https://doi.org/10.1103/PhysRevE.91.022808). URL: <https://link.aps.org/doi/10.1103/PhysRevE.91.022808>.
- [46] Caesar Saloma et al. "Self-organized queuing and scale-free behavior in real escape panic". In: *Proceedings of the National Academy of Sciences* 100.21 (2003), pp. 11947–11952. ISSN: 0027-8424. DOI: [10.1073/pnas.2031912100](https://doi.org/10.1073/pnas.2031912100). eprint: <https://www.pnas.org/content/100/21/11947.full.pdf>. URL: <https://www.pnas.org/content/100/21/11947>.
- [47] D. J. McCafferty et al. "Emperor penguin body surfaces cool below air temperature". In: *Biology Letters* 9.3 (2013), p. 20121192. DOI: [10.1098/rsbl.2012.1192](https://doi.org/10.1098/rsbl.2012.1192). eprint: <https://royalsocietypublishing.org/doi/pdf/10.1098/rsbl.2012.1192>. URL: <https://royalsocietypublishing.org/doi/abs/10.1098/rsbl.2012.1192>.
- [48] S. Richter et al. "Phase transitions in huddling emperor penguins". In: *Journal of physics D: Applied physics* 51.21 (2018). 30416209[pmid], p. 214002. ISSN: 0022-3727. DOI: [10.1088/1361-6463/aabb8e](https://doi.org/10.1088/1361-6463/aabb8e). URL: <https://www.ncbi.nlm.nih.gov/pubmed/30416209>.
- [49] Daniel P. Zitterbart et al. "Coordinated Movements Prevent Jamming in an Emperor Penguin Huddle". In: *PLOS ONE* 6.6 (June 2011), pp. 1–3. DOI: [10.1371/journal.pone.0020260](https://doi.org/10.1371/journal.pone.0020260). URL: <https://doi.org/10.1371/journal.pone.0020260>.
- [50] R C Gerum et al. "The origin of traveling waves in an emperor penguin huddle". In: *New Journal of Physics* 15.12 (2013), p. 125022. DOI: [10.1088/1367-2630/15/12/125022](https://doi.org/10.1088/1367-2630/15/12/125022). URL: <https://doi.org/10.1088/1367-2630/15/12/125022>.
- [51] Nicolas Bain and Denis Bartolo. "Dynamic response and hydrodynamics of polarized crowds". In: *Science* 363.6422 (2019), pp. 46–49. ISSN: 0036-8075. DOI: [10.1126/science.aat9891](https://doi.org/10.1126/science.aat9891). eprint: <https://science.sciencemag.org/content/363/6422/46.full.pdf>. URL: <https://science.sciencemag.org/content/363/6422/46>.
- [52] E. M. Purcell. "Life at low Reynolds number". In: *American Journal of Physics* 45.1 (1977), pp. 3–11. DOI: [10.1119/1.10903](https://doi.org/10.1119/1.10903). eprint: <https://doi.org/10.1119/1.10903>. URL: <https://doi.org/10.1119/1.10903>.

- [53] J Elgeti, R G Winkler, and G Gompper. “Physics of microswimmers—single particle motion and collective behavior: a review”. In: *Reports on Progress in Physics* 78.5 (May 2015), p. 056601. ISSN: 0034-4885, 1361-6633. DOI: [10.1088/0034-4885/78/5/056601](https://doi.org/10.1088/0034-4885/78/5/056601). URL: <http://stacks.iop.org/0034-4885/78/i=5/a=056601?key=crossref.098e1dfca7db8f1f68a5a86fca9219b5>.
- [54] Matthew F. Copeland and Douglas B. Weibel. “Bacterial swarming: a model system for studying dynamic self-assembly”. In: *Soft Matter* 5 (6 2009), pp. 1174–1187. DOI: [10.1039/B812146J](https://doi.org/10.1039/B812146J). URL: <http://dx.doi.org/10.1039/B812146J>.
- [55] Előd Méhes and Tamás Vicsek. “Collective motion of cells: from experiments to models”. In: *Integrative Biology* 6.9 (July 2014), pp. 831–854. ISSN: 1757-9708. DOI: [10.1039/c4ib00115j](https://doi.org/10.1039/c4ib00115j). eprint: <http://oup.prod.sis.lan/ib/article-pdf/6/9/831/27283783/c4ib00115j.pdf>. URL: <https://doi.org/10.1039/c4ib00115j>.
- [56] Wouter-Jan Rappel et al. “Self-organized Vortex State in Two-Dimensional Dictyostelium Dynamics”. In: *Phys. Rev. Lett.* 83 (6 1999), pp. 1247–1250. DOI: [10.1103/PhysRevLett.83.1247](https://doi.org/10.1103/PhysRevLett.83.1247). URL: <https://link.aps.org/doi/10.1103/PhysRevLett.83.1247>.
- [57] A. Szabó et al. “Collective cell motion in endothelial monolayers”. en. In: *Physical Biology* 7.4 (Nov. 2010), p. 046007. ISSN: 1478-3975. DOI: [10.1088/1478-3975/7/4/046007](https://doi.org/10.1088/1478-3975/7/4/046007). URL: <https://doi.org/10.1088%2F1478-3975%2F7%2F4%2F046007>.
- [58] Peter Friedl and Darren Gilmour. “Collective cell migration in morphogenesis, regeneration and cancer”. In: *Nature Reviews Molecular Cell Biology* 10.7 (2009), pp. 445–457. ISSN: 1471-0080. DOI: [10.1038/nrm2720](https://doi.org/10.1038/nrm2720). URL: <https://doi.org/10.1038/nrm2720>.
- [59] B. Szabó et al. “Phase transition in the collective migration of tissue cells: Experiment and model”. In: *Phys. Rev. E* 74 (6 2006), p. 061908. DOI: [10.1103/PhysRevE.74.061908](https://doi.org/10.1103/PhysRevE.74.061908). URL: <https://link.aps.org/doi/10.1103/PhysRevE.74.061908>.
- [60] Linda Oswald et al. “Jamming transitions in cancer”. en. In: *Journal of Physics D: Applied Physics* 50.48 (Oct. 2017), p. 483001. ISSN: 0022-3727. DOI: [10.1088/1361-6463/aa8e83](https://doi.org/10.1088/1361-6463/aa8e83). URL: <https://doi.org/10.1088%2F1361-6463%2Faa8e83>.
- [61] Simon Garcia et al. “Physics of active jamming during collective cellular motion in a monolayer”. In: *Proceedings of the National Academy of Sciences* 112.50 (2015), pp. 15314–15319. ISSN: 0027-8424. DOI: [10.1073/pnas.1510973112](https://doi.org/10.1073/pnas.1510973112). eprint: <https://www.pnas.org/content/112/50/15314.full.pdf>. URL: <https://www.pnas.org/content/112/50/15314>.
- [62] T. J. Pedley and J. O. Kessler. “Hydrodynamic Phenomena in Suspensions of Swimming Microorganisms”. In: *Annual Review of Fluid Mechanics* 24.1 (1992), pp. 313–358. DOI: [10.1146/annurev.fl.24.010192.001525](https://doi.org/10.1146/annurev.fl.24.010192.001525). eprint: <https://doi.org/10.1146/annurev.fl.24.010192.001525>. URL: <https://doi.org/10.1146/annurev.fl.24.010192.001525>.
- [63] Luis H. Cisneros et al. “Fluid dynamics of self-propelled microorganisms, from individuals to concentrated populations”. In: *Experiments in Fluids* 43.5 (2007), pp. 737–753. ISSN: 1432-1114. DOI: [10.1007/s00348-007-0387-y](https://doi.org/10.1007/s00348-007-0387-y). URL: <https://doi.org/10.1007/s00348-007-0387-y>.

- [64] Avraham Be'er and Gil Ariel. "A statistical physics view of swarming bacteria". In: *Movement Ecology* 7.1 (2019), p. 9. ISSN: 2051-3933. DOI: [10.1186/s40462-019-0153-9](https://doi.org/10.1186/s40462-019-0153-9). URL: <https://doi.org/10.1186/s40462-019-0153-9>.
- [65] John Toner and Yuhai Tu. "Long-Range Order in a Two-Dimensional Dynamical XY Model: How Birds Fly Together". In: *Phys. Rev. Lett.* 75 (23 1995), pp. 4326–4329. DOI: [10.1103/PhysRevLett.75.4326](https://doi.org/10.1103/PhysRevLett.75.4326). URL: <https://link.aps.org/doi/10.1103/PhysRevLett.75.4326>.
- [66] Eric Lauga and Thomas R Powers. "The hydrodynamics of swimming microorganisms". In: *Reports on Progress in Physics* 72.9 (2009), p. 096601. DOI: [10.1088/0034-4885/72/9/096601](https://doi.org/10.1088/0034-4885/72/9/096601). URL: <https://doi.org/10.1088/0034-4885/72/9/096601>.
- [67] Mark J. Schnitzer. "Theory of continuum random walks and application to chemotaxis". In: *Phys. Rev. E* 48 (4 1993), pp. 2553–2568. DOI: [10.1103/PhysRevE.48.2553](https://doi.org/10.1103/PhysRevE.48.2553). URL: <https://link.aps.org/doi/10.1103/PhysRevE.48.2553>.
- [68] Howard C. Berg. *E. coli in Motion*. 2003.
- [69] HOWARD C. BERG and DOUGLAS A. BROWN. "Chemotaxis in Escherichia coli analysed by Three-dimensional Tracking". In: *Nature* 239.5374 (1972), pp. 500–504. ISSN: 1476-4687. DOI: [10.1038/239500a0](https://doi.org/10.1038/239500a0). URL: <https://doi.org/10.1038/239500a0>.
- [70] Raymond E. Goldstein, Marco Polin, and Idan Tuval. "Noise and Synchronization in Pairs of Beating Eukaryotic Flagella". In: *Phys. Rev. Lett.* 103 (16 2009), p. 168103. DOI: [10.1103/PhysRevLett.103.168103](https://doi.org/10.1103/PhysRevLett.103.168103). URL: <https://link.aps.org/doi/10.1103/PhysRevLett.103.168103>.
- [71] Lutz Schimansky-Geier et al. "Structure formation by active Brownian particles". In: *Physics Letters A* 207.3 (1995), pp. 140–146. ISSN: 0375-9601. DOI: [https://doi.org/10.1016/0375-9601\(95\)00700-D](https://doi.org/10.1016/0375-9601(95)00700-D). URL: <http://www.sciencedirect.com/science/article/pii/037596019500700D>.
- [72] P. Romanczuk et al. "Active Brownian particles". In: *The European Physical Journal Special Topics* 202.1 (2012), pp. 1–162. ISSN: 1951-6401. DOI: [10.1140/epjst/e2012-01529-y](https://doi.org/10.1140/epjst/e2012-01529-y). URL: <https://doi.org/10.1140/epjst/e2012-01529-y>.
- [73] Karl b. Przibram. "Über die ungeordnete Bewegung niederer Tiere. II". In: *Archiv für Entwicklungsmechanik der Organismen* 153 (1913), pp. 401–405. DOI: <https://doi.org/10.1007/BF01686480>.
- [74] Joakim Stenhammar et al. "Phase behaviour of active Brownian particles: the role of dimensionality". In: *Soft Matter* 10 (10 2014), pp. 1489–1499. DOI: [10.1039/C3SM52813H](https://doi.org/10.1039/C3SM52813H). URL: <http://dx.doi.org/10.1039/C3SM52813H>.
- [75] M. E. Cates and J. Tailleur. "When are active Brownian particles and run-and-tumble particles equivalent? Consequences for motility-induced phase separation". In: *EPL (Europhysics Letters)* 101.2 (2013), p. 20010. DOI: [10.1209/0295-5075/101/20010](https://doi.org/10.1209/0295-5075/101/20010). URL: <https://doi.org/10.1209/0295-5075/101/20010>.
- [76] Claudio Maggi et al. "Multidimensional stationary probability distribution for interacting active particles". In: *Scientific Reports* 5 (2015). Article, 10742 EP -. URL: <https://doi.org/10.1038/srep10742>.

- [77] Étienne Fodor et al. “How Far from Equilibrium Is Active Matter?” In: *Phys. Rev. Lett.* 117 (3 2016), p. 038103. DOI: [10.1103/PhysRevLett.117.038103](https://doi.org/10.1103/PhysRevLett.117.038103). URL: <https://link.aps.org/doi/10.1103/PhysRevLett.117.038103>.
- [78] T. F. F. Farage, P. Krinninger, and J. M. Brader. “Effective interactions in active Brownian suspensions”. In: *Phys. Rev. E* 91 (4 2015), p. 042310. DOI: [10.1103/PhysRevE.91.042310](https://doi.org/10.1103/PhysRevE.91.042310). URL: <https://link.aps.org/doi/10.1103/PhysRevE.91.042310>.
- [79] Grzegorz Szamel. “Self-propelled particle in an external potential: Existence of an effective temperature”. In: *Phys. Rev. E* 90 (1 2014), p. 012111. DOI: [10.1103/PhysRevE.90.012111](https://doi.org/10.1103/PhysRevE.90.012111). URL: <https://link.aps.org/doi/10.1103/PhysRevE.90.012111>.
- [80] Grzegorz Szamel, Elijah Flenner, and Ludovic Berthier. “Glassy dynamics of athermal self-propelled particles: Computer simulations and a nonequilibrium microscopic theory”. In: *Phys. Rev. E* 91 (6 2015), p. 062304. DOI: [10.1103/PhysRevE.91.062304](https://doi.org/10.1103/PhysRevE.91.062304). URL: <https://link.aps.org/doi/10.1103/PhysRevE.91.062304>.
- [81] John Toner and Yuhai Tu. “Flocks, herds, and schools: A quantitative theory of flocking”. In: *Phys. Rev. E* 58 (4 1998), pp. 4828–4858. DOI: [10.1103/PhysRevE.58.4828](https://doi.org/10.1103/PhysRevE.58.4828). URL: <https://link.aps.org/doi/10.1103/PhysRevE.58.4828>.
- [82] Melissa B. Miller and Bonnie L. Bassler. “Quorum Sensing in Bacteria”. In: *Annual Review of Microbiology* 55.1 (2001). PMID: 11544353, pp. 165–199. DOI: [10.1146/annurev.micro.55.1.165](https://doi.org/10.1146/annurev.micro.55.1.165). eprint: <https://doi.org/10.1146/annurev.micro.55.1.165>. URL: <https://doi.org/10.1146/annurev.micro.55.1.165>.
- [83] Yaouen Fily and M. Cristina Marchetti. “Athermal Phase Separation of Self-Propelled Particles with No Alignment”. In: *Phys. Rev. Lett.* 108.23 (2012). DOI: [10.1103/physrevlett.108.235702](https://doi.org/10.1103/physrevlett.108.235702). URL: <https://doi.org/10.1103/physrevlett.108.235702>.
- [84] Demian Levis and Ludovic Berthier. “Clustering and heterogeneous dynamics in a kinetic Monte Carlo model of self-propelled hard disks”. In: *Phys. Rev. E* 89 (6 2014), p. 062301. DOI: [10.1103/PhysRevE.89.062301](https://doi.org/10.1103/PhysRevE.89.062301). URL: <https://link.aps.org/doi/10.1103/PhysRevE.89.062301>.
- [85] J. Tailleur and M. E. Cates. “Statistical Mechanics of Interacting Run-and-Tumble Bacteria”. In: *Phys. Rev. Lett.* 100 (21 2008), p. 218103. DOI: [10.1103/PhysRevLett.100.218103](https://doi.org/10.1103/PhysRevLett.100.218103). URL: <https://link.aps.org/doi/10.1103/PhysRevLett.100.218103>.
- [86] Michael E. Cates and Julien Tailleur. “Motility-Induced Phase Separation”. In: *Annual Review of Condensed Matter Physics* 6.1 (2015), pp. 219–244. DOI: [10.1146/annurev-conmatphys-031214-014710](https://doi.org/10.1146/annurev-conmatphys-031214-014710). eprint: <https://doi.org/10.1146/annurev-conmatphys-031214-014710>. URL: <https://doi.org/10.1146/annurev-conmatphys-031214-014710>.
- [87] Michael E Cates. “Active Field Theories”. In: 2019.
- [88] Clemens Bechinger et al. “Active Brownian Particles in Complex and Crowded Environments”. In: *Rev. Mod. Phys.* 88.1 (2016), p. 045006.

- [89] S.J. Ebbens. "Active colloids: Progress and challenges towards realising autonomous applications". In: *Current Opinion in Colloid & Interface Science* 21 (2016), pp. 14–23. ISSN: 1359-0294. DOI: <https://doi.org/10.1016/j.cocis.2015.10.003>. URL: <http://www.sciencedirect.com/science/article/pii/S1359029415000679>.
- [90] A. Aubret, S. Ramanarivo, and J. Palacci. "Eppur si muove, and yet it moves: Patchy (phoretic) swimmers". In: *Current Opinion in Colloid & Interface Science* 30 (2017), pp. 81–89. ISSN: 1359-0294. DOI: <https://doi.org/10.1016/j.cocis.2017.05.007>. URL: <http://www.sciencedirect.com/science/article/pii/S1359029417300468>.
- [91] Jeffrey L. Moran and Jonathan D. Posner. "Phoretic Self-Propulsion". In: *Annual Review of Fluid Mechanics* 49.1 (2017), pp. 511–540. DOI: [10.1146/annurev-fluid-122414-034456](https://doi.org/10.1146/annurev-fluid-122414-034456). eprint: <https://doi.org/10.1146/annurev-fluid-122414-034456>. URL: <https://doi.org/10.1146/annurev-fluid-122414-034456>.
- [92] Jeffrey Moran and Jonathan Posner. "Microswimmers with no moving parts". In: *Physics Today* 72.5 (2019), pp. 44–50. DOI: [10.1063/PT.3.4203](https://doi.org/10.1063/PT.3.4203). eprint: <https://doi.org/10.1063/PT.3.4203>. URL: <https://doi.org/10.1063/PT.3.4203>.
- [93] Julien Deseigne et al. "Vibrated polar disks: spontaneous motion, binary collisions, and collective dynamics". In: *Soft Matter* 8 (20 2012), pp. 5629–5639. DOI: [10.1039/C2SM25186H](https://doi.org/10.1039/C2SM25186H). URL: <http://dx.doi.org/10.1039/C2SM25186H>.
- [94] Antoine Bricard et al. "Emergence of macroscopic directed motion in populations of motile colloids". In: *Nature* 503.7474 (2013), pp. 95–98. DOI: [10.1038/nature12673](https://doi.org/10.1038/nature12673). URL: <https://doi.org/10.1038/nature12673>.
- [95] Sumit Gangwal et al. "Induced-Charge Electrophoresis of Metallo-dielectric Particles". In: *Phys. Rev. Lett.* 100 (5 2008), p. 058302. DOI: [10.1103/PhysRevLett.100.058302](https://doi.org/10.1103/PhysRevLett.100.058302). URL: <https://link.aps.org/doi/10.1103/PhysRevLett.100.058302>.
- [96] Renfeng Dong et al. "Highly Efficient Light-Driven TiO₂-Au Janus Micromotors". In: *ACS Nano* 10.1 (2016), pp. 839–844. ISSN: 1936-0851. DOI: [10.1021/acsnano.5b05940](https://doi.org/10.1021/acsnano.5b05940). URL: <https://doi.org/10.1021/acsnano.5b05940>.
- [97] Hong-Ren Jiang, Natsuhiko Yoshinaga, and Masaki Sano. "Active Motion of a Janus Particle by Self-Thermophoresis in a Defocused Laser Beam". In: *Phys. Rev. Lett.* 105 (26 2010), p. 268302. DOI: [10.1103/PhysRevLett.105.268302](https://doi.org/10.1103/PhysRevLett.105.268302). URL: <https://link.aps.org/doi/10.1103/PhysRevLett.105.268302>.
- [98] Ivo Buttinoni et al. "Active Brownian motion tunable by light". In: *Journal of Physics: Condensed Matter* 24.28 (July 2012), p. 284129. ISSN: 0953-8984, 1361-648X. DOI: [10.1088/0953-8984/24/28/284129](https://doi.org/10.1088/0953-8984/24/28/284129). URL: <http://stacks.iop.org/0953-8984/24/i=28/a=284129?key=crossref.f1ef1c86534435edc06d22f7c0cc35ff>.
- [99] Julien Deseigne, Olivier Dauchot, and Hugues Chaté. "Collective Motion of Vibrated Polar Disks". In: *Phys. Rev. Lett.* 105 (9 2010), p. 098001. DOI: [10.1103/PhysRevLett.105.098001](https://doi.org/10.1103/PhysRevLett.105.098001). URL: <https://link.aps.org/doi/10.1103/PhysRevLett.105.098001>.

- [100] G. Quincke. "Ueber Rotationen im constanten electrischen Felde". In: *Annalen der Physik* 295.11 (1896), pp. 417–486. DOI: [10.1002/andp.18962951102](https://doi.org/10.1002/andp.18962951102). eprint: <https://onlinelibrary.wiley.com/doi/pdf/10.1002/andp.18962951102>. URL: <https://onlinelibrary.wiley.com/doi/abs/10.1002/andp.18962951102>.
- [101] Antoine Bricard et al. "Emergent vortices in populations of colloidal rollers". In: *Nature Communications* 6.1 (2015), p. 7470. ISSN: 2041-1723. DOI: [10.1038/ncomms8470](https://doi.org/10.1038/ncomms8470). URL: <https://doi.org/10.1038/ncomms8470>.
- [102] TODD M. SQUIRES and MARTIN Z. BAZANT. "Induced-charge electro-osmosis". In: *Journal of Fluid Mechanics* 509 (2004), 217–252. DOI: [10.1017/S0022112004009309](https://doi.org/10.1017/S0022112004009309).
- [103] TODD M. SQUIRES and MARTIN Z. BAZANT. "Breaking symmetries in induced-charge electro-osmosis and electrophoresis". In: *Journal of Fluid Mechanics* 560 (2006), 65–101. DOI: [10.1017/S0022112006000371](https://doi.org/10.1017/S0022112006000371).
- [104] Daiki Nishiguchi and Masaki Sano. "Mesoscopic turbulence and local order in Janus particles self-propelling under an ac electric field". In: *Phys. Rev. E* 92 (5 2015), p. 052309. DOI: [10.1103/PhysRevE.92.052309](https://doi.org/10.1103/PhysRevE.92.052309). URL: <https://link.aps.org/doi/10.1103/PhysRevE.92.052309>.
- [105] Ming Han et al. "Effective temperature concept evaluated in an active colloid mixture". In: *Proceedings of the National Academy of Sciences* 114.29 (2017), pp. 7513–7518. DOI: [10.1073/pnas.1706702114](https://doi.org/10.1073/pnas.1706702114). eprint: <http://www.pnas.org/content/114/29/7513.full.pdf>. URL: <http://www.pnas.org/content/114/29/7513.abstract>.
- [106] Jonathan R. Howse et al. "Self-Motile Colloidal Particles: From Directed Propulsion to Random Walk". In: *Phys. Rev. Lett.* 99 (4 2007), p. 048102. DOI: [10.1103/PhysRevLett.99.048102](https://doi.org/10.1103/PhysRevLett.99.048102). URL: <https://link.aps.org/doi/10.1103/PhysRevLett.99.048102>.
- [107] Jeremie Palacci et al. "Living Crystals of Light-Activated Colloidal Surfers". In: *Science* 339.February (2013), pp. 936–939. ISSN: 0036-8075. DOI: [10.1126/science.1230020](https://doi.org/10.1126/science.1230020). URL: <http://www.sciencemag.org/content/339/6122/936.full.pdf>.
- [108] J. Palacci et al. "Light-activated self-propelled colloids". In: *Philosophical Transactions of the Royal Society A: Mathematical, Physical and Engineering Sciences* 372.2029 (2014), p. 20130372. DOI: [10.1098/rsta.2013.0372](https://doi.org/10.1098/rsta.2013.0372). eprint: <https://royalsocietypublishing.org/doi/pdf/10.1098/rsta.2013.0372>. URL: <https://royalsocietypublishing.org/doi/abs/10.1098/rsta.2013.0372>.
- [109] Giovanni Volpe et al. "Microswimmers in patterned environments". In: *Soft Matter* 7 (19 2011), pp. 8810–8815. DOI: [10.1039/C1SM05960B](https://doi.org/10.1039/C1SM05960B). URL: <http://dx.doi.org/10.1039/C1SM05960B>.
- [110] Walter F. Paxton et al. "Catalytic Nanomotors: Autonomous Movement of Striped Nanorods". In: *Journal of the American Chemical Society* 126.41 (2004), pp. 13424–13431. DOI: [10.1021/ja047697z](https://doi.org/10.1021/ja047697z).
- [111] Jean Perrin. "Mouvement Brownien et réalité moléculaire". In: *Ann. Chim. Phys.* 18 (1 1909), pp. 5–104. URL: http://hermes.ffn.ub.es/luisnavarro/nuevo_maletin/Perrin_1909.pdf.

- [112] Wilson Poon. "Colloids as Big Atoms". In: *Science* 304.5672 (2004), pp. 830–831. ISSN: 0036-8075. DOI: [10.1126/science.1097964](https://doi.org/10.1126/science.1097964). URL: <http://science.sciencemag.org/content/304/5672/830>.
- [113] Roberto Piazza, Tommaso Bellini, and Vittorio Degiorgio. "Equilibrium sedimentation profiles of screened charged colloids: A test of the hard-sphere equation of state". In: *Phys. Rev. Lett.* 71 (25 1993), pp. 4267–4270. DOI: [10.1103/PhysRevLett.71.4267](https://doi.org/10.1103/PhysRevLett.71.4267). URL: <https://link.aps.org/doi/10.1103/PhysRevLett.71.4267>.
- [114] John C. Crocker and David G. Grier. "Methods of Digital Video Microscopy for Colloidal Studies". In: *Journal of Colloid and Interface Science* 179.1 (1996), pp. 298–310. ISSN: 0021-9797. DOI: <https://doi.org/10.1006/jcis.1996.0217>. URL: <http://www.sciencedirect.com/science/article/pii/S0021979796902179>.
- [115] J. Tailleur and M. E. Cates. "Sedimentation, trapping, and rectification of dilute bacteria". In: *EPL* 86.6 (2009), p. 60002. URL: <http://stacks.iop.org/0295-5075/86/i=6/a=60002>.
- [116] Sophie Ramananarivo, Etienne Ducrot, and Jeremie Palacci. "Activity-controlled annealing of colloidal monolayers". In: *Nature Communications* 10.1 (2019), p. 3380. ISSN: 2041-1723. DOI: [10.1038/s41467-019-11362-y](https://doi.org/10.1038/s41467-019-11362-y). URL: <https://doi.org/10.1038/s41467-019-11362-y>.
- [117] Guillaume Briand, Michael Schindler, and Olivier Dauchot. "Spontaneously Flowing Crystal of Self-Propelled Particles". In: *Phys. Rev. Lett.* 120.20 (2018). DOI: [10.1103/physrevlett.120.208001](https://doi.org/10.1103/physrevlett.120.208001). URL: <https://doi.org/10.1103/physrevlett.120.208001>.
- [118] Delphine Geyer et al. "Freezing a Flock: Motility-Induced Phase Separation in Polar Active Liquids". In: *Phys. Rev. X* 9 (3 2019), p. 031043. DOI: [10.1103/PhysRevX.9.031043](https://doi.org/10.1103/PhysRevX.9.031043). URL: <https://link.aps.org/doi/10.1103/PhysRevX.9.031043>.
- [119] Delphine Geyer, Alexandre Morin, and Denis Bartolo. "Sounds and hydrodynamics of polar active fluids". In: *Nature Materials* 17.9 (2018), pp. 789–793. ISSN: 1476-4660. DOI: [10.1038/s41563-018-0123-4](https://doi.org/10.1038/s41563-018-0123-4). URL: <https://doi.org/10.1038/s41563-018-0123-4>.
- [120] Andrea Cavagna. "Supercooled liquids for pedestrians". In: *Physics Reports* 476.4-6 (2009), pp. 51–124. DOI: [10.1016/j.physrep.2009.03.003](https://doi.org/10.1016/j.physrep.2009.03.003). URL: <https://doi.org/10.1016/j.physrep.2009.03.003>.
- [121] P. N. Pusey and W. van Megen. "Phase behaviour of concentrated suspensions of nearly hard colloidal spheres". In: *Nature* 320.6060 (1986), pp. 340–342. ISSN: 1476-4687. DOI: [10.1038/320340a0](https://doi.org/10.1038/320340a0). URL: <https://doi.org/10.1038/320340a0>.
- [122] Walter Kob and Hans C. Andersen. "Scaling Behavior in the β -Relaxation Regime of a Supercooled Lennard-Jones Mixture". In: *Phys. Rev. Lett.* 73 (10 1994), pp. 1376–1379. DOI: [10.1103/PhysRevLett.73.1376](https://doi.org/10.1103/PhysRevLett.73.1376). URL: <https://link.aps.org/doi/10.1103/PhysRevLett.73.1376>.
- [123] S. R. Williams and W. van Megen. "Motions in binary mixtures of hard colloidal spheres: Melting of the glass". In: *Phys. Rev. E* 64 (4 2001), p. 041502. DOI: [10.1103/PhysRevE.64.041502](https://doi.org/10.1103/PhysRevE.64.041502). URL: <https://link.aps.org/doi/10.1103/PhysRevE.64.041502>.

- [124] Gary L Hunter and Eric R Weeks. "The physics of the colloidal glass transition". In: *Reports on Progress in Physics* 75.6 (2012), p. 066501. DOI: [10.1088/0034-4885/75/6/066501](https://doi.org/10.1088/0034-4885/75/6/066501). URL: <https://doi.org/10.1088%2F0034-4885%2F75%2F6%2F066501>.
- [125] P. N. Pusey et al. "Hard spheres: crystallization and glass formation". In: *Philosophical Transactions of the Royal Society A: Mathematical, Physical and Engineering Sciences* 367.1909 (2009), pp. 4993–5011. DOI: [10.1098/rsta.2009.0181](https://royalsocietypublishing.org/doi/pdf/10.1098/rsta.2009.0181). eprint: <https://royalsocietypublishing.org/doi/pdf/10.1098/rsta.2009.0181>. URL: <https://royalsocietypublishing.org/doi/abs/10.1098/rsta.2009.0181>.
- [126] B. J. Alder and T. E. Wainwright. "Phase Transition for a Hard Sphere System". en. In: *The Journal of Chemical Physics* 27.5 (Nov. 1957), pp. 1208–1209. ISSN: 0021-9606, 1089-7690. DOI: [10.1063/1.1743957](http://aip.scitation.org/doi/10.1063/1.1743957). URL: <http://aip.scitation.org/doi/10.1063/1.1743957>.
- [127] William G. Hoover and Francis H. Ree. "Melting Transition and Communal Entropy for Hard Spheres". en. In: *The Journal of Chemical Physics* 49.8 (Oct. 1968), pp. 3609–3617. ISSN: 0021-9606, 1089-7690. DOI: [10.1063/1.1670641](http://aip.scitation.org/doi/10.1063/1.1670641). URL: <http://aip.scitation.org/doi/10.1063/1.1670641>.
- [128] N. D. Mermin and H. Wagner. "Absence of Ferromagnetism or Antiferromagnetism in One- or Two-Dimensional Isotropic Heisenberg Models". In: *Phys. Rev. Lett.* 17 (22 1966), pp. 1133–1136. DOI: [10.1103/PhysRevLett.17.1133](https://link.aps.org/doi/10.1103/PhysRevLett.17.1133). URL: <https://link.aps.org/doi/10.1103/PhysRevLett.17.1133>.
- [129] B. J. Alder and T. E. Wainwright. "Phase Transition in Elastic Disks". In: *Phys. Rev.* 127 (2 1962), pp. 359–361. DOI: [10.1103/PhysRev.127.359](https://link.aps.org/doi/10.1103/PhysRev.127.359). URL: <https://link.aps.org/doi/10.1103/PhysRev.127.359>.
- [130] Katherine J. Strandburg. "Two-dimensional melting". In: *Rev. Mod. Phys.* 60 (1 1988), pp. 161–207. DOI: [10.1103/RevModPhys.60.161](https://link.aps.org/doi/10.1103/RevModPhys.60.161). URL: <https://link.aps.org/doi/10.1103/RevModPhys.60.161>.
- [131] S. T. Chui. "Grain-Boundary Theory of Melting in Two Dimensions". In: *Phys. Rev. Lett.* 48 (14 1982), pp. 933–935. DOI: [10.1103/PhysRevLett.48.933](https://link.aps.org/doi/10.1103/PhysRevLett.48.933). URL: <https://link.aps.org/doi/10.1103/PhysRevLett.48.933>.
- [132] J M Kosterlitz and D J Thouless. "Ordering, metastability and phase transitions in two-dimensional systems". In: *Journal of Physics C: Solid State Physics* 6.7 (Apr. 1973), pp. 1181–1203. ISSN: 0022-3719. DOI: [10.1088/0022-3719/6/7/010](http://stacks.iop.org/0022-3719/6/i=7/a=010?key=crossref.f2d443370878b9288c142e398ad429b1). URL: <http://stacks.iop.org/0022-3719/6/i=7/a=010?key=crossref.f2d443370878b9288c142e398ad429b1>.
- [133] B. I. Halperin and David R. Nelson. "Theory of Two-Dimensional Melting". In: *Phys. Rev. Lett.* 41 (2 1978), pp. 121–124. DOI: [10.1103/PhysRevLett.41.121](https://link.aps.org/doi/10.1103/PhysRevLett.41.121). URL: <https://link.aps.org/doi/10.1103/PhysRevLett.41.121>.
- [134] A. P. Young. "Melting and the vector Coulomb gas in two dimensions". In: *Phys. Rev. B* 19 (4 1979), pp. 1855–1866. DOI: [10.1103/PhysRevB.19.1855](https://link.aps.org/doi/10.1103/PhysRevB.19.1855). URL: <https://link.aps.org/doi/10.1103/PhysRevB.19.1855>.
- [135] Etienne P. Bernard and Werner Krauth. "Two-Step Melting in Two Dimensions: First-Order Liquid-Hexatic Transition". In: *Phys. Rev. Lett.* 107 (15 2011), p. 155704. DOI: [10.1103/PhysRevLett.107.155704](https://link.aps.org/doi/10.1103/PhysRevLett.107.155704). URL: <https://link.aps.org/doi/10.1103/PhysRevLett.107.155704>.

- [136] Alice L. Thorneywork et al. "Two-Dimensional Melting of Colloidal Hard Spheres". In: *Phys. Rev. Lett.* 118 (15 2017), p. 158001. DOI: [10.1103/PhysRevLett.118.158001](https://doi.org/10.1103/PhysRevLett.118.158001). URL: <https://link.aps.org/doi/10.1103/PhysRevLett.118.158001>.
- [137] Antara Pal, Md Arif Kamal, and V. A. Raghunathan. "Observation of the Chiral and Achiral Hexatic Phases of Self-assembled Micellar polymers". In: *Scientific Reports* 6 (2016). Article, 32313 EP -. URL: <https://doi.org/10.1038/srep32313>.
- [138] Neil W Ashcroft and N David Mermin. *Solid State Physics. The Science of Microfabrication*. 1976.
- [139] M.A. Meyers, A. Mishra, and D.J. Benson. "Mechanical properties of nanocrystalline materials". In: *Progress in Materials Science* 51.4 (2006), pp. 427–556. ISSN: 0079-6425. DOI: <https://doi.org/10.1016/j.pmatsci.2005.08.003>. URL: <http://www.sciencedirect.com/science/article/pii/S0079642505000447>.
- [140] W. T. Laughlin and D. R. Uhlmann. "Viscous flow in simple organic liquids". In: *The Journal of Physical Chemistry* 76.16 (1972), pp. 2317–2325. ISSN: 0022-3654. DOI: [10.1021/j100660a023](https://doi.org/10.1021/j100660a023). URL: <https://doi.org/10.1021/j100660a023>.
- [141] R Edgeworth, B J Dalton, and T Parnell. "The pitch drop experiment". In: *European Journal of Physics* 5.4 (1984), pp. 198–200. DOI: [10.1088/0143-0807/5/4/003](https://doi.org/10.1088/0143-0807/5/4/003). URL: <https://doi.org/10.1088/0143-0807/5/4/003>.
- [142] C. A. Angell. "Formation of Glasses from Liquids and Biopolymers". In: *Science* 267.5206 (1995), pp. 1924–1935. ISSN: 0036-8075. DOI: [10.1126/science.267.5206.1924](https://doi.org/10.1126/science.267.5206.1924). eprint: <https://science.sciencemag.org/content/267/5206/1924.full.pdf>. URL: <https://science.sciencemag.org/content/267/5206/1924>.
- [143] Frank H. Stillinger. "A Topographic View of Supercooled Liquids and Glass Formation". In: *Science* 267.5206 (1995), pp. 1935–1939. ISSN: 0036-8075. DOI: [10.1126/science.267.5206.1935](https://doi.org/10.1126/science.267.5206.1935). eprint: <https://science.sciencemag.org/content/267/5206/1935.full.pdf>. URL: <https://science.sciencemag.org/content/267/5206/1935>.
- [144] Pablo G. Debenedetti and Frank H. Stillinger. "Supercooled liquids and the glass transition". In: *Nature* 410.6825 (2001), pp. 259–267. ISSN: 1476-4687. DOI: [10.1038/35065704](https://doi.org/10.1038/35065704). URL: <https://doi.org/10.1038/35065704>.
- [145] Patrick Charbonneau et al. "Fractal free energy landscapes in structural glasses". In: *Nature Communications* 5.1 (2014), p. 3725. ISSN: 2041-1723. DOI: [10.1038/ncomms4725](https://doi.org/10.1038/ncomms4725). URL: <https://doi.org/10.1038/ncomms4725>.
- [146] H. Vogel. "Das Temperaturabhängigkeitsgesetz der Viskosität von Flüssigkeiten". In: *Zeitschrift für Phys* 22 (1921), pp. 645–646.
- [147] Gordon S. Fulcher. "ANALYSIS OF RECENT MEASUREMENTS OF THE VISCOSITY OF GLASSES". In: *Journal of the American Ceramic Society* 8.6 (1925), pp. 339–355. DOI: [10.1111/j.1151-2916.1925.tb16731.x](https://doi.org/10.1111/j.1151-2916.1925.tb16731.x). eprint: <https://ceramics.onlinelibrary.wiley.com/doi/pdf/10.1111/j.1151-2916.1925.tb16731.x>. URL: <https://ceramics.onlinelibrary.wiley.com/doi/abs/10.1111/j.1151-2916.1925.tb16731.x>.

- [148] G. Tammann and W. Hesse. "Die Abhängigkeit der Viscosität von der Temperatur bei unterkühlten Flüssigkeiten". In: *Zeitschrift für anorganische und allgemeine Chemie* 156.1 (1926), pp. 245–257. DOI: 10.1002/zaac.19261560121. eprint: <https://onlinelibrary.wiley.com/doi/pdf/10.1002/zaac.19261560121>. URL: <https://onlinelibrary.wiley.com/doi/abs/10.1002/zaac.19261560121>.
- [149] Elisa Tamborini, C Patrick Royall, and Pietro Cicuta. "Correlation between crystalline order and vitrification in colloidal monolayers". In: *Journal of Physics: Condensed Matter* 27.19 (2015), p. 194124. DOI: 10.1088/0953-8984/27/19/194124. URL: <https://doi.org/10.1088/0953-8984/27/19/194124>.
- [150] Adrian-Marie Philippe et al. "Glass Transition of Soft Colloids". In: *Phys. Rev. E* 97.4 (Apr. 2018), p. 040601. DOI: 10.1103/PhysRevE.97.040601.
- [151] G Petekidis, D Vlassopoulos, and P N Pusey. "Yielding and flow of sheared colloidal glasses". In: *Journal of Physics: Condensed Matter* 16.38 (2004), S3955–S3963. DOI: 10.1088/0953-8984/16/38/013. URL: <https://doi.org/10.1088/0953-8984/16/38/013>.
- [152] Winslow H. Herschel and Ronald Bulkley. "Konsistenzmessungen von Gummi-Benzollösungen". In: *Kolloid-Zeitschrift* 39.4 (1926), pp. 291–300. ISSN: 1435-1536. DOI: 10.1007/BF01432034. URL: <https://doi.org/10.1007/BF01432034>.
- [153] Daniel Bonn et al. "Yield stress materials in soft condensed matter". In: *Rev. Mod. Phys.* 89 (3 2017), p. 035005. DOI: 10.1103/RevModPhys.89.035005. URL: <https://link.aps.org/doi/10.1103/RevModPhys.89.035005>.
- [154] Julian Bialké, Thomas Speck, and Hartmut Löwen. "Crystallization in a Dense Suspension of Self-Propelled Particles". In: *Phys. Rev. Lett.* 108 (16 2012), p. 168301. DOI: 10.1103/PhysRevLett.108.168301. URL: <https://link.aps.org/doi/10.1103/PhysRevLett.108.168301>.
- [155] Pasquale Digregorio et al. "Full Phase Diagram of Active Brownian Disks: From Melting to Motility-Induced Phase Separation". In: *Phys. Rev. Lett.* 121 (9 2018), p. 098003. DOI: 10.1103/PhysRevLett.121.098003. URL: <https://link.aps.org/doi/10.1103/PhysRevLett.121.098003>.
- [156] Yaouen Fily, Silke Henkes, and M. Cristina Marchetti. "Freezing and phase separation of self-propelled disks". In: *Soft Matter* 10 (13 2014), pp. 2132–2140. DOI: 10.1039/C3SM52469H. URL: <http://dx.doi.org/10.1039/C3SM52469H>.
- [157] Ran Ni, Martien A Cohen Stuart, and Marjolein Dijkstra. "Pushing the Glass Transition towards Random Close Packing Using Self-Propelled Hard Spheres." en. In: *Nature communications* 4 (Oct. 2013), p. 2704. ISSN: 2041-1723. DOI: 10.1038/ncomms3704. URL: <http://www.nature.com/ncomms/2013/131028/ncomms3704/full/ncomms3704.html>.
- [158] Ludovic Berthier and Jorge Kurchan. "Non-equilibrium glass transitions in driven and active matter". In: *Nature Physics* 9 (2013). Article, 310 EP –. URL: <https://doi.org/10.1038/nphys2592>.
- [159] Ludovic Berthier. "Nonequilibrium Glassy Dynamics of Self-Propelled Hard Disks". In: *Phys. Rev. Lett.* 112 (22 2014), p. 220602. DOI: 10.1103/PhysRevLett.112.220602. URL: <https://link.aps.org/doi/10.1103/PhysRevLett.112.220602>.

- [160] Elijah Flenner, Grzegorz Szamel, and Ludovic Berthier. "The nonequilibrium glassy dynamics of self-propelled particles". In: *Soft Matter* 12 (34 2016), pp. 7136–7149. DOI: [10.1039/C6SM01322H](https://doi.org/10.1039/C6SM01322H). URL: <http://dx.doi.org/10.1039/C6SM01322H>.
- [161] John D. Weeks, David Chandler, and Hans C. Andersen. "Role of Repulsive Forces in Determining the Equilibrium Structure of Simple Liquids". In: *The Journal of Chemical Physics* 54.12 (1971), pp. 5237–5247. DOI: [10.1063/1.1674820](https://doi.org/10.1063/1.1674820). eprint: <https://doi.org/10.1063/1.1674820>. URL: <https://doi.org/10.1063/1.1674820>.
- [162] Ludovic Berthier, Elijah Flenner, and Grzegorz Szamel. "How active forces influence nonequilibrium glass transitions". In: *New J. Phys.* 19.12 (2017), p. 125006. URL: <http://stacks.iop.org/1367-2630/19/i=12/a=125006>.
- [163] Saroj Kumar Nandi et al. "A random first-order transition theory for an active glass". In: *Proceedings of the National Academy of Sciences* (2018). ISSN: 0027-8424. URL: <http://www.pnas.org/content/early/2018/07/06/1721324115>.
- [164] Walter F. Paxton, Ayusman Sen, and Thomas E. Mallouk. "Motility of Catalytic Nanoparticles through Self-Generated Forces". In: *Chemistry – A European Journal* 11.22 (2005), pp. 6462–6470. DOI: [10.1002/chem.200500167](https://doi.org/10.1002/chem.200500167). eprint: <https://onlinelibrary.wiley.com/doi/pdf/10.1002/chem.200500167>. URL: <https://onlinelibrary.wiley.com/doi/abs/10.1002/chem.200500167>.
- [165] Walter F. Paxton et al. "Catalytically Induced Electrokinetics for Motors and Micropumps". In: *Journal of the American Chemical Society* 128.46 (2006), pp. 14881–14888. ISSN: 0002-7863. DOI: [10.1021/ja0643164](https://doi.org/10.1021/ja0643164). URL: <https://doi.org/10.1021/ja0643164>.
- [166] Yang Wang et al. "Bipolar Electrochemical Mechanism for the Propulsion of Catalytic Nanomotors in Hydrogen Peroxide Solutions". In: *Langmuir* 22.25 (2006), pp. 10451–10456. ISSN: 0743-7463. DOI: [10.1021/la0615950](https://doi.org/10.1021/la0615950). URL: <https://doi.org/10.1021/la0615950>.
- [167] JEFFREY L. MORAN and JONATHAN D. POSNER. "Electrokinetic locomotion due to reaction-induced charge auto-electrophoresis". In: *Journal of Fluid Mechanics* 680 (2011), 31–66. DOI: [10.1017/jfm.2011.132](https://doi.org/10.1017/jfm.2011.132).
- [168] Aidan Brown and Wilson Poon. "Tonic effects in self-propelled Pt-coated Janus swimmers". In: *Soft Matter* 10 (22 2014), pp. 4016–4027. DOI: [10.1039/C4SM00340C](https://doi.org/10.1039/C4SM00340C). URL: <http://dx.doi.org/10.1039/C4SM00340C>.
- [169] Aidan T. Brown et al. "Ionic screening and dissociation are crucial for understanding chemical self-propulsion in polar solvents". In: *Soft Matter* 13 (6 2017), pp. 1200–1222. DOI: [10.1039/C6SM01867J](https://doi.org/10.1039/C6SM01867J). URL: <http://dx.doi.org/10.1039/C6SM01867J>.
- [170] Shaltiel Eloul et al. "Reactive Momentum Transfer Contributes to the Self-Propulsion of Janus Particles". In: *Phys. Rev. Lett.* 124 (18 2020), p. 188001. DOI: [10.1103/PhysRevLett.124.188001](https://doi.org/10.1103/PhysRevLett.124.188001). URL: <https://link.aps.org/doi/10.1103/PhysRevLett.124.188001>.
- [171] Sébastien Michelin and Eric Lauga. "Phoretic self-propulsion at finite Péclet numbers". In: *Journal of Fluid Mechanics* 747 (2014), 572–604. DOI: [10.1017/jfm.2014.158](https://doi.org/10.1017/jfm.2014.158).

- [172] Sébastien Michelin and Eric Lauga. “Geometric tuning of self-propulsion for Janus catalytic particles”. In: *Scientific Reports* 7 (2017). Article, 42264 EP –. URL: <https://doi.org/10.1038/srep42264>.
- [173] Jinxing Li et al. “Self-Propelled Nanomotors Autonomously Seek and Repair Cracks”. In: *Nano Letters* 15.10 (2015), pp. 7077–7085. ISSN: 1530-6984. DOI: [10.1021/acs.nanolett.5b03140](https://doi.org/10.1021/acs.nanolett.5b03140). URL: <https://doi.org/10.1021/acs.nanolett.5b03140>.
- [174] Daniel Allan et al. *trackpy: Trackpy v0.3.2*. Aug. 2016. DOI: [10.5281/zenodo.60550](https://doi.org/10.5281/zenodo.60550). URL: <https://doi.org/10.5281/zenodo.60550>.
- [175] Léon Van Hove. “Correlations in Space and Time and Born Approximation Scattering in Systems of Interacting Particles”. In: *Phys. Rev.* 95 (1 1954), pp. 249–262. DOI: [10.1103/PhysRev.95.249](https://doi.org/10.1103/PhysRev.95.249). URL: <https://link.aps.org/doi/10.1103/PhysRev.95.249>.
- [176] Dan V. Goia and Egon Matijević. “Tailoring the particle size of monodispersed colloidal gold”. In: *Colloids and Surfaces A: Physicochemical and Engineering Aspects* 146.1 (1999), pp. 139–152. ISSN: 0927-7757. DOI: [https://doi.org/10.1016/S0927-7757\(98\)00790-0](https://doi.org/10.1016/S0927-7757(98)00790-0). URL: <http://www.sciencedirect.com/science/article/pii/S0927775798007900>.
- [177] Anaconda Software Distribution. *Computer software. Vers. 2-2.4.0. Anaconda*. Nov. 2016. URL: <https://anaconda.com>.
- [178] Travis Oliphant. *NumPy: A guide to NumPy*. USA: Trelgol Publishing. [Online; accessed <today>]. 2006–. URL: <http://www.numpy.org/>.
- [179] Eric Jones, Travis Oliphant, Pearu Peterson, et al. *SciPy: Open source scientific tools for Python*. [Online; accessed 2019-09-12]. 2001–. URL: <http://www.scipy.org/>.
- [180] Wes McKinney et al. “Data structures for statistical computing in python”. In: *Proceedings of the 9th Python in Science Conference*. Vol. 445. Austin, TX. 2010, pp. 51–56.
- [181] Aric A. Hagberg, Daniel A. Schult, and Pieter J. Swart. “Exploring Network Structure, Dynamics, and Function using NetworkX”. In: *Proceedings of the 7th Python in Science Conference*. Ed. by Gaël Varoquaux, Travis Vaught, and Jarrod Millman. Pasadena, CA USA, 2008, pp. 11–15.
- [182] J. D. Hunter. “Matplotlib: A 2D graphics environment”. In: *Computing in Science & Engineering* 9.3 (2007), pp. 90–95. DOI: [10.1109/MCSE.2007.55](https://doi.org/10.1109/MCSE.2007.55).
- [183] C. Patrick Royall, Ard A. Louis, and Hajime Tanaka. “Measuring colloidal interactions with confocal microscopy”. In: *The Journal of Chemical Physics* 127.4 (2007), p. 044507. DOI: [10.1063/1.2755962](https://doi.org/10.1063/1.2755962). eprint: <https://doi.org/10.1063/1.2755962>. URL: <https://doi.org/10.1063/1.2755962>.
- [184] Adam Edward Stones, Roel P. A. Dullens, and Dirk G. A. L. Aarts. “Model-Free Measurement of the Pair Potential in Colloidal Fluids Using Optical Microscopy”. In: *Phys. Rev. Lett.* 123 (9 2019), p. 098002. DOI: [10.1103/PhysRevLett.123.098002](https://doi.org/10.1103/PhysRevLett.123.098002). URL: <https://link.aps.org/doi/10.1103/PhysRevLett.123.098002>.

- [185] Jean-Pierre Hansen and Ian R. McDonald. "Chapter 3 - Static Properties of Liquids: Thermodynamics and Structure". In: *Theory of Simple Liquids (Fourth Edition)*. Ed. by Jean-Pierre Hansen and Ian R. McDonald. Fourth Edition. Oxford: Academic Press, 2013, pp. 61–104. ISBN: 978-0-12-387032-2. DOI: <https://doi.org/10.1016/B978-0-12-387032-2.00003-9>. URL: <http://www.sciencedirect.com/science/article/pii/B9780123870322000039>.
- [186] Mathieu Leocmach. *The colloid toolkit*. 2015. DOI: [10.5281/zenodo.31286](https://doi.org/10.5281/zenodo.31286). URL: <http://dx.doi.org/10.5281/zenodo.31286>.
- [187] Lester Hedges. *Structural order parameters (the easy way)*. URL: <http://lesterhedges.net/miscellanea/structural/>.
- [188] Elijah Flenner, Min Zhang, and Grzegorz Szamel. "Analysis of a growing dynamic length scale in a glass-forming binary hard-sphere mixture". In: *Phys. Rev. E* 83.5 (May 2011), p. 051501. ISSN: 1539-3755. DOI: [10.1103/PhysRevE.83.051501](https://doi.org/10.1103/PhysRevE.83.051501). URL: <http://link.aps.org/doi/10.1103/PhysRevE.83.051501> (visited on 04/03/2012).
- [189] M. D. Ediger. "Spatially Heterogeneous Dynamics in Supercooled Liquids". In: *Annual Review of Physical Chemistry* 51.1 (2000). PMID: 11031277, pp. 99–128. DOI: [10.1146/annurev.physchem.51.1.99](https://doi.org/10.1146/annurev.physchem.51.1.99). eprint: <https://doi.org/10.1146/annurev.physchem.51.1.99>. URL: <https://doi.org/10.1146/annurev.physchem.51.1.99>.
- [190] Elijah Flenner and Grzegorz Szamel. "Dynamic heterogeneities above and below the mode-coupling temperature: Evidence of a dynamic crossover". In: *The Journal of Chemical Physics* 138.12 (2013), 12A523. DOI: [10.1063/1.4773321](https://doi.org/10.1063/1.4773321). eprint: <https://doi.org/10.1063/1.4773321>. URL: <https://doi.org/10.1063/1.4773321>.
- [191] N. Lačević et al. "Spatially heterogeneous dynamics investigated via a time-dependent four-point density correlation function". In: *The Journal of Chemical Physics* 119.14 (2003), pp. 7372–7387. DOI: [10.1063/1.1605094](https://doi.org/10.1063/1.1605094). eprint: <https://doi.org/10.1063/1.1605094>. URL: <https://doi.org/10.1063/1.1605094>.
- [192] Sharon C. Glotzer, Vladimir N. Novikov, and Thomas B. Schröder. "Time-dependent, four-point density correlation function description of dynamical heterogeneity and decoupling in supercooled liquids". In: *The Journal of Chemical Physics* 112.2 (2000), pp. 509–512. DOI: [10.1063/1.480541](https://doi.org/10.1063/1.480541). eprint: <https://doi.org/10.1063/1.480541>. URL: <https://doi.org/10.1063/1.480541>.
- [193] N. Lačević et al. "Growing correlation length on cooling below the onset of caging in a simulated glass-forming liquid". English. In: *Physical Review E* 66.3 (2002). Paper id.: 030101. ISSN: 2470-0045. DOI: [10.1103/PhysRevE.66.030101](https://doi.org/10.1103/PhysRevE.66.030101).
- [194] L. Berthier et al. "Direct Experimental Evidence of a Growing Length Scale Accompanying the Glass Transition". In: *Science* 310.5755 (2005), pp. 1797–1800. ISSN: 0036-8075. DOI: [10.1126/science.1120714](https://doi.org/10.1126/science.1120714). eprint: <https://science.sciencemag.org/content/310/5755/1797.full.pdf>. URL: <https://science.sciencemag.org/content/310/5755/1797>.
- [195] L. Berthier. "Dynamic Heterogeneity in Amorphous Materials". In: *Physics Online Journal* 4, 42 (May 2011), p. 42. DOI: [10.1103/Physics.4.42](https://doi.org/10.1103/Physics.4.42). arXiv: [1106.1739](https://arxiv.org/abs/1106.1739) [cond-mat.stat-mech].

- [196] Songrit Maneewongvatana and David M. Mount. "Analysis of approximate nearest neighbor searching with clustered point sets". In: *Data Structures, Near Neighbor Searches, and Methodology*. 1999.
- [197] Jon Louis Bentley. "Multidimensional Binary Search Trees Used for Associative Searching". In: *Commun. ACM* 18.9 (Sept. 1975), pp. 509–517. ISSN: 0001-0782. DOI: [10.1145/361002.361007](https://doi.org/10.1145/361002.361007). URL: <http://doi.acm.org/10.1145/361002.361007>.
- [198] C.B. Barber, D.P. Dobkin, and H.T. Huhdanpaa. "The Quickhull algorithm for convex hulls". In: *ACM Trans. on Mathematical Software* 4.22 (Dec. 1996), pp. 469–483. ISSN: 0001-0782. URL: <http://www.qhull.org>.
- [199] Keiji Watanabe and Hajime Tanaka. "Direct Observation of Medium-Range Crystalline Order in Granular Liquids Near the Glass Transition". In: *Phys. Rev. Lett.* 100 (15 2008), p. 158002. DOI: [10.1103/PhysRevLett.100.158002](https://doi.org/10.1103/PhysRevLett.100.158002). URL: <https://link.aps.org/doi/10.1103/PhysRevLett.100.158002>.
- [200] Claudio Donati et al. "Stringlike Cooperative Motion in a Supercooled Liquid". In: *Phys. Rev. Lett.* 80 (11 1998), pp. 2338–2341. DOI: [10.1103/PhysRevLett.80.2338](https://doi.org/10.1103/PhysRevLett.80.2338). URL: <https://link.aps.org/doi/10.1103/PhysRevLett.80.2338>.
- [201] Andrew H. Marcus, Jeremy Schofield, and Stuart A. Rice. "Experimental observations of non-Gaussian behavior and stringlike cooperative dynamics in concentrated quasi-two-dimensional colloidal liquids". In: *Phys. Rev. E* 60 (5 1999), pp. 5725–5736. DOI: [10.1103/PhysRevE.60.5725](https://doi.org/10.1103/PhysRevE.60.5725). URL: <https://link.aps.org/doi/10.1103/PhysRevE.60.5725>.
- [202] Raffaele Pastore, Antonio Coniglio, and Massimo Pica Ciamarra. "From cage-jump motion to macroscopic diffusion in supercooled liquids". In: *Soft Matter* 10 (31 2014), pp. 5724–5728. DOI: [10.1039/C4SM00739E](https://doi.org/10.1039/C4SM00739E). URL: <http://dx.doi.org/10.1039/C4SM00739E>.
- [203] G. Briand and O. Dauchot. "Crystallization of Self-Propelled Hard Discs". In: *Phys. Rev. Lett.* 117 (9 2016), p. 098004. DOI: [10.1103/PhysRevLett.117.098004](https://doi.org/10.1103/PhysRevLett.117.098004). URL: <https://link.aps.org/doi/10.1103/PhysRevLett.117.098004>.
- [204] Borge ten Hagen, Sven van Teeffelen, and Hartmut Löwen. "Brownian Motion of a Self-Propelled Particle". en. In: *Journal of Physics: Condensed Matter* 23.19 (May 2011), p. 194119. ISSN: 0953-8984, 1361-648X. DOI: [10.1088/0953-8984/23/19/194119](https://doi.org/10.1088/0953-8984/23/19/194119). arXiv: [1005.1343](https://arxiv.org/abs/1005.1343). URL: <http://arxiv.org/abs/1005.1343> (visited on 02/25/2019).
- [205] Natsuda Klongvessa et al. "Active Glass: Ergodicity Breaking Dramatically Affects Response to Self-Propulsion". In: *Phys. Rev. Lett.* 123 (24 2019), p. 248004. DOI: [10.1103/PhysRevLett.123.248004](https://doi.org/10.1103/PhysRevLett.123.248004). URL: <https://link.aps.org/doi/10.1103/PhysRevLett.123.248004>.
- [206] Natsuda Klongvessa et al. "Nonmonotonic behavior in dense assemblies of active colloids". In: *Phys. Rev. E* 100 (6 2019), p. 062603. DOI: [10.1103/PhysRevE.100.062603](https://doi.org/10.1103/PhysRevE.100.062603). URL: <https://link.aps.org/doi/10.1103/PhysRevE.100.062603>.
- [207] Daphne Weihs, Thomas G. Mason, and Michael A. Teitell. "Bio-Microrheology: A Frontier in Microrheology". In: *Biophysical Journal* 91.11 (2006), pp. 4296 – 4305. ISSN: 0006-3495. DOI: <https://doi.org/10.1529/biophysj.106.081109>. URL: <http://www.sciencedirect.com/science/article/pii/S0006349506721439>.

- [208] Denis Wirtz. “Particle-Tracking Microrheology of Living Cells: Principles and Applications”. In: *Annual Review of Biophysics* 38.1 (2009). PMID: 19416071, pp. 301–326. DOI: [10.1146/annurev.biophys.050708.133724](https://doi.org/10.1146/annurev.biophys.050708.133724). eprint: <https://doi.org/10.1146/annurev.biophys.050708.133724>. URL: <https://doi.org/10.1146/annurev.biophys.050708.133724>.
- [209] Kenji Nishizawa et al. “Feedback-tracking microrheology in living cells”. In: *Science Advances* 3.9 (2017). DOI: [10.1126/sciadv.1700318](https://doi.org/10.1126/sciadv.1700318). eprint: <https://advances.sciencemag.org/content/3/9/e1700318.full.pdf>. URL: <https://advances.sciencemag.org/content/3/9/e1700318>.
- [210] G. L. Miño et al. “Induced diffusion of tracers in a bacterial suspension: theory and experiments”. In: *Journal of Fluid Mechanics* 729 (2013), 423–444. DOI: [10.1017/jfm.2013.304](https://doi.org/10.1017/jfm.2013.304).
- [211] T. V. Kasyap, Donald L. Koch, and Mingming Wu. “Hydrodynamic tracer diffusion in suspensions of swimming bacteria”. In: *Physics of Fluids* 26.8 (2014), p. 081901. DOI: [10.1063/1.4891570](https://doi.org/10.1063/1.4891570). eprint: <https://doi.org/10.1063/1.4891570>. URL: <https://doi.org/10.1063/1.4891570>.
- [212] Eric W. Burkholder and John F. Brady. “Tracer diffusion in active suspensions”. In: *Phys. Rev. E* 95 (5 2017), p. 052605. DOI: [10.1103/PhysRevE.95.052605](https://doi.org/10.1103/PhysRevE.95.052605). URL: <https://link.aps.org/doi/10.1103/PhysRevE.95.052605>.
- [213] Eric W. Burkholder and John F. Brady. “Nonlinear microrheology of active Brownian suspensions”. In: *Soft Matter* 16 (4 2020), pp. 1034–1046. DOI: [10.1039/C9SM01713E](https://doi.org/10.1039/C9SM01713E). URL: <http://dx.doi.org/10.1039/C9SM01713E>.
- [214] Howard A. Barnes. *A handbook of elementary rheology*. Aberystwyth Univ. of Wales, Institute of Non-Newtonian Fluid Mechanics 2000, 2000.
- [215] P. Coussot. “Yield stress fluid flows: A review of experimental data”. In: *Journal of Non-Newtonian Fluid Mechanics* 211 (2014), pp. 31–49. ISSN: 0377-0257. DOI: <https://doi.org/10.1016/j.jnnfm.2014.05.006>. URL: <http://www.sciencedirect.com/science/article/pii/S0377025714000895>.
- [216] Gargallo Ligia and Radić Deodato. “Viscoelastic Behaviour of Polymers”. In: *Physicochemical Behavior and Supramolecular Organization of Polymers*. Dordrecht: Springer Netherlands, 2009, pp. 43–162. ISBN: 978-1-4020-9372-2. DOI: [10.1007/978-1-4020-9372-2_2](https://doi.org/10.1007/978-1-4020-9372-2_2). URL: https://doi.org/10.1007/978-1-4020-9372-2_2.
- [217] Naoki Sasaki. “Viscoelastic Properties of Biological Material”. In: *Viscoelasticity - From Theory to Biological Applications*. IntechOpen, 2012. DOI: [10.5772/49979](https://doi.org/10.5772/49979). URL: www.intechopen.com/books/viscoelasticity-from-theory-to-biological-applications/viscoelastic-properties-of-biological-materials.
- [218] Pierre Lidon, Louis Villa, and Sébastien Manneville. “Power-law creep and residual stresses in a carbopol gel”. In: *Rheologica Acta* 56.3 (2017), pp. 307–323. ISSN: 1435-1528. DOI: [10.1007/s00397-016-0961-4](https://doi.org/10.1007/s00397-016-0961-4). URL: <https://doi.org/10.1007/s00397-016-0961-4>.
- [219] T. G. Mason and D. A. Weitz. “Linear Viscoelasticity of Colloidal Hard Sphere Suspensions near the Glass Transition”. In: *Phys. Rev. Lett.* 75 (14 1995), pp. 2770–2773. DOI: [10.1103/PhysRevLett.75.2770](https://doi.org/10.1103/PhysRevLett.75.2770). URL: <https://link.aps.org/doi/10.1103/PhysRevLett.75.2770>.

- [220] Todd M. Squires and Thomas G. Mason. “Fluid Mechanics of Microrheology”. In: *Annual Review of Fluid Mechanics* 42.1 (2010), pp. 413–438. DOI: [10.1146/annurev-fluid-121108-145608](https://doi.org/10.1146/annurev-fluid-121108-145608). eprint: <https://doi.org/10.1146/annurev-fluid-121108-145608>. URL: <https://doi.org/10.1146/annurev-fluid-121108-145608>.
- [221] Alexander Meyer et al. “Laser tweezer microrheology of a colloidal suspension”. In: *Journal of Rheology* 50.1 (2006), pp. 77–92. DOI: [10.1122/1.2139098](https://doi.org/10.1122/1.2139098). eprint: <https://doi.org/10.1122/1.2139098>. URL: <https://doi.org/10.1122/1.2139098>.
- [222] Rae M. Robertson-Anderson. “Optical Tweezers Microrheology: From the Basics to Advanced Techniques and Applications”. In: *ACS Macro Letters* 7.8 (2018), pp. 968–975. DOI: [10.1021/acsmacrolett.8b00498](https://doi.org/10.1021/acsmacrolett.8b00498). URL: <https://doi.org/10.1021/acsmacrolett.8b00498>.
- [223] S. Q. Choi et al. “Active microrheology and simultaneous visualization of sheared phospholipid monolayers”. In: *Nature Communications* 2.1 (2011), p. 312. ISSN: 2041-1723. DOI: [10.1038/ncomms1321](https://doi.org/10.1038/ncomms1321). URL: <https://doi.org/10.1038/ncomms1321>.
- [224] Ivo Buttinoni et al. “Colloidal binary mixtures at fluid–fluid interfaces under steady shear: structural, dynamical and mechanical response”. In: *Soft Matter* 11 (42 2015), pp. 8313–8321. DOI: [10.1039/C5SM01693B](https://doi.org/10.1039/C5SM01693B). URL: <http://dx.doi.org/10.1039/C5SM01693B>.
- [225] Zachary A. Zell et al. “Linear and nonlinear microrheometry of small samples and interfaces using microfabricated probes”. In: *Journal of Rheology* 60.1 (2016), pp. 141–159. DOI: [10.1122/1.4937931](https://doi.org/10.1122/1.4937931). eprint: <https://doi.org/10.1122/1.4937931>. URL: <https://doi.org/10.1122/1.4937931>.
- [226] Torsten Jähnke and Philipp Rauch. *Optical Tweezers for Single-Cell, Multicellular Investigations in the Life Sciences*. 2015. URL: <https://www.americanlaboratory.com/914-Application-Notes/180081-Optical-Tweezers-for-Single-Cell-Multicellular-Investigations-in-the-Life-Sciences/> (visited on 07/04/2020).
- [227] Pietro Cicuta and Athene M. Donald. “Microrheology: a review of the method and applications”. In: *Soft Matter* 3 (12 2007), pp. 1449–1455. DOI: [10.1039/B706004C](https://doi.org/10.1039/B706004C). URL: <http://dx.doi.org/10.1039/B706004C>.
- [228] Manuel Sickert and Francis Rondelez. “Shear Viscosity of Langmuir Monolayers in the Low-Density Limit”. In: *Phys. Rev. Lett.* 90 (12 2003), p. 126104. DOI: [10.1103/PhysRevLett.90.126104](https://doi.org/10.1103/PhysRevLett.90.126104). URL: <https://link.aps.org/doi/10.1103/PhysRevLett.90.126104>.
- [229] A. Ashkin et al. “Observation of a single-beam gradient force optical trap for dielectric particles”. In: *Opt. Lett.* 11.5 (1986), pp. 288–290. DOI: [10.1364/OL.11.000288](https://doi.org/10.1364/OL.11.000288). URL: <http://ol.osa.org/abstract.cfm?URI=ol-11-5-288>.
- [230] Manlio Tassieri. “Microrheology with optical tweezers”. In: *Microrheology with Optical Tweezers: Principles and Applications*. Ed. by Manlio Tassieri. CRC Press, 2016. URL: <http://eprints.gla.ac.uk/136237/>.
- [231] M T Valentine, L E Dewalt, and H D Ou-Yang. “Forces on a colloidal particle in a polymer solution: a study using optical tweezers”. In: *Journal of Physics: Condensed Matter* 8.47 (1996), pp. 9477–9482. DOI: [10.1088/0953-8984/8/47/048](https://doi.org/10.1088/0953-8984/8/47/048). URL: <https://doi.org/10.1088/0953-8984/8/47/048>.

- [232] Cole D. Chapman et al. "Onset of Non-Continuum Effects in Microrheology of Entangled Polymer Solutions". In: *Macromolecules* 47.3 (2014), pp. 1181–1186. ISSN: 0024-9297. DOI: [10.1021/ma401615m](https://doi.org/10.1021/ma401615m). URL: <https://doi.org/10.1021/ma401615m>.
- [233] Todd M. Squires. "Nonlinear Microrheology: Bulk Stresses versus Direct Interactions". In: *Langmuir* 24.4 (2008), pp. 1147–1159. ISSN: 0743-7463. DOI: [10.1021/la7023692](https://doi.org/10.1021/la7023692). URL: <https://doi.org/10.1021/la7023692>.
- [234] F. Graner et al. "Discrete rearranging disordered patterns, part I: Robust statistical tools in two or three dimensions". In: *The European Physical Journal E* 25.4 (2008), pp. 349–369. ISSN: 1292-895X. DOI: [10.1140/epje/i2007-10298-8](https://doi.org/10.1140/epje/i2007-10298-8). URL: <https://doi.org/10.1140/epje/i2007-10298-8>.
- [235] Miguel Aubouy et al. "A texture tensor to quantify deformations". In: *Granular Matter* 5.2 (2003), pp. 67–70. ISSN: 1434-5021. DOI: [10.1007/s10035-003-0126-x](https://doi.org/10.1007/s10035-003-0126-x). URL: <https://doi.org/10.1007/s10035-003-0126-x>.
- [236] George K. Batchelor. *An Introduction to Fluid Dynamics*. Cambridge University Press, 1967.
- [237] Chiang C. Mei. *Lecture Notes on Fluid Dynamics*. 2007. URL: http://web.mit.edu/1.63/www/Lec-notes/chap2_slow/2-5Stokes.pdf.
- [238] Wen Yan and John F. Brady. "The swim force as a body force". In: *Soft Matter* 11 (31 2015), pp. 6235–6244. DOI: [10.1039/C5SM01318F](https://doi.org/10.1039/C5SM01318F). URL: <http://dx.doi.org/10.1039/C5SM01318F>.
- [239] A. P. Solon et al. "Pressure is not a state function for generic active fluids". In: *Nature Physics* 11.8 (2015), pp. 673–678. ISSN: 1745-2481. DOI: [10.1038/nphys3377](https://doi.org/10.1038/nphys3377). URL: <https://doi.org/10.1038/nphys3377>.
- [240] David Jiles. *Introduction to Magnetism and Magnetic Materials 3rd edition*. Boca Raton: CRC Press, 2015. DOI: <https://doi.org/10.1201/b18948>.
- [241] Giorgio Volpe, Sylvain Gigan, and Giovanni Volpe. "Simulation of the active Brownian motion of a microswimmer". In: *American Journal of Physics* 82.7 (2014), pp. 659–664. DOI: [10.1119/1.4870398](https://doi.org/10.1119/1.4870398). eprint: <https://doi.org/10.1119/1.4870398>. URL: <https://doi.org/10.1119/1.4870398>.
- [242] J. C. Butcher. *The Numerical Analysis of Ordinary Differential Equations: Runge-Kutta and General Linear Methods*. USA: Wiley-Interscience, 1987. ISBN: 0471910465.
- [243] W. Paul and D. Y. Yoon. "Stochastic phase space dynamics with constraints for molecular systems". In: *Phys. Rev. E* 52 (2 1995), pp. 2076–2083. DOI: [10.1103/PhysRevE.52.2076](https://doi.org/10.1103/PhysRevE.52.2076). URL: <https://link.aps.org/doi/10.1103/PhysRevE.52.2076>.
- [244] George E. P. Box and Mervin E. Muller. "A Note on the Generation of Random Normal Deviates". In: 1958.
- [245] James R. Bell. "Algorithm 334: Normal Random Deviates". In: *Commun. ACM* 11.7 (July 1968), p. 498. ISSN: 0001-0782. DOI: [10.1145/363397.363547](https://doi.org/10.1145/363397.363547). URL: <https://doi.org/10.1145/363397.363547>.
- [246] R. Knop. "Remark on Algorithm 334 [G5]: Normal Random Deviates". In: *Commun. ACM* 12.5 (May 1969), p. 281. ISSN: 0001-0782. DOI: [10.1145/362946.362996](https://doi.org/10.1145/362946.362996). URL: <https://doi.org/10.1145/362946.362996>.

- [247] Loup Verlet. "Computer "Experiments" on Classical Fluids. I. Thermodynamical Properties of Lennard-Jones Molecules". In: *Phys. Rev.* 159 (1 1967), pp. 98–103. DOI: [10.1103/PhysRev.159.98](https://doi.org/10.1103/PhysRev.159.98). URL: <https://link.aps.org/doi/10.1103/PhysRev.159.98>.
- [248] William Mattson and Betsy M. Rice. "Near-neighbor calculations using a modified cell-linked list method". In: *Computer Physics Communications* 119.2 (1999), pp. 135–148. ISSN: 0010-4655. DOI: [https://doi.org/10.1016/S0010-4655\(98\)00203-3](https://doi.org/10.1016/S0010-4655(98)00203-3). URL: <http://www.sciencedirect.com/science/article/pii/S0010465598002033>.
- [249] N.W. Ashcroft and N.D. Mermin. *Solid State Physics*. Holt, Rinehart and Winston, 1976. ISBN: 9788131500538. URL: <https://books.google.bs/books?id=r8SPYgEACAAJ>.
- [250] Isabella Petrelli et al. "Effective temperatures in inhomogeneous passive and active bidimensional Brownian particle systems". In: *arXiv e-prints*, arXiv:2005.02303 (May 2020), arXiv:2005.02303. arXiv: [2005.02303](https://arxiv.org/abs/2005.02303) [[cond-mat.stat-mech](https://arxiv.org/abs/2005.02303)].
- [251] Dor Ben-Amotz and Dudley R. Herschbach. "Estimation of effective diameters for molecular fluids". In: *The Journal of Physical Chemistry* 94.3 (1990), pp. 1038–1047. ISSN: 0022-3654. DOI: [10.1021/j100366a003](https://doi.org/10.1021/j100366a003). URL: <https://doi.org/10.1021/j100366a003>.
- [252] Dor Ben-Amotz and George Stell. "Reformulation of Weeks-Chandler-Andersen Perturbation Theory Directly in Terms of a Hard-Sphere Reference System". In: *The Journal of Physical Chemistry B* 108.21 (2004), pp. 6877–6882. ISSN: 1520-6106. DOI: [10.1021/jp037810s](https://doi.org/10.1021/jp037810s). URL: <https://doi.org/10.1021/jp037810s>.
- [253] Takeshi Kawasaki and Akira Onuki. "Slow relaxations and stringlike jump motions in fragile glass-forming liquids: Breakdown of the Stokes-Einstein relation". In: *Phys. Rev. E* 87 (1 2013), p. 012312. DOI: [10.1103/PhysRevE.87.012312](https://doi.org/10.1103/PhysRevE.87.012312). URL: <https://link.aps.org/doi/10.1103/PhysRevE.87.012312>.
- [254] Ludovic Berthier and Mark D. Ediger. *How to measure a structural relaxation time that is too long to be measured?* 2020. arXiv: [2005.06520](https://arxiv.org/abs/2005.06520) [[cond-mat.stat-mech](https://arxiv.org/abs/2005.06520)].